UNIVERSITÀ
degli STUDI
di CATANIA

Investigation of Structure, Stability and Forces of Nanoparticles Assembled at Liquid Interfaces

From Ionic Surfactants to Proteins: Interfacial Assembly and Non-Equilibrium Behavior of Silica Nanoparticles

Pascal Tomasella

Supervisor: Giovanni Calogero Li Destri Nicosia
Associate Professor, University of Catania

Ph.D. coordinator: Salvatore Scirè
Full Professor, University of Catania

University of Catania
Department of Chemical Sciences
International Ph.D. in Chemical Sciences
Academic year: 2024/25

Dissertation

Catania, November 2025

This page intentionally left blank.

Investigation of Structure, Stability and Forces of Nanoparticles Assembled at Liquid Interfaces

Copyright © 2025 - Pascal Tomasella, University of Catania.

This dissertation is original work, written solely for this purpose, and all the authors whose studies and publications contributed to it have been duly cited. Partial reproduction is allowed with acknowledgment of the author and reference to the degree, academic year, institution - *University of Catania* - and public defense date.

This page intentionally left blank.

Abstract

This Ph.D. project focused on the fundamental study of the structure and interactions in monolayers of nanoparticles irreversibly adsorbed at the water-air interface. These systems, generally formed by the presence of additives that promote the interfacial assembly of nanoparticles, are of great scientific interest because of the potential they offer for the creation of nanostructured surfaces for applications in areas such as sensing, catalysis, and functional and "smart" materials engineering. The thesis is divided into two main parts.

In the first part, it was investigated a model system in which the adsorption of Silicon Oxide Nanoparticles (NPs) was promoted by the addition of Cetyltrimethylammonium bromide (CTAB), a cationic surfactant that promotes assembly through electrostatic interactions. In particular, a new experimental procedure using X-ray scattering techniques as Grazing Incidence Small Angle X-ray Scattering (GISAXS) was developed to analyze the adsorption mechanisms in detail and to obtain kinetic and thermodynamic information on these out-of-equilibrium systems. Subsequently, I focused on studying the specific effect of ion and ionic strength on the adsorption and structure of monolayers and interparticle interactions. The results showed that the assembly is governed by non-DLVO interactions related to the specific nature of the cation, and that the density and stability of the monolayers are mainly determined by the long-range electrostatic repulsive forces established between the nanoparticles at the interface. In this context, I also analyzed how the ionic nature and ionic strength condition the ability of monolayers to recover their structure after non-elastic deformation, *i.e.*, in the regime of non-reversible monolayer deformation.

In the second part, we focus on studying the role of proteins as additives in the promotion of the assembly of silica nanoparticles at the water-air interface. Proteins, which are intrinsically amphiphilic, biocompatible, and biodegradable macromolecules, are ideal candidates for the development of green and environmentally sustainable formulations. In fact, they are widely used and studied agents for the stabilization of large interphase systems such as foams and emulsions. During my Ph.D., I specifically investigated the influence of the type of protein on the structure and mechanical stability of hybrid monolayers (organic-inorganic) using three well-characterized model proteins such as Bovine Serum Albumin (BSA), β-Casein (BCN) and β-Lactoglobulin (BLG). The experimental approach combined advanced X-ray scattering and neutron scattering as GISAXS and Neutron Reflectometry (NR) techniques, dynamic surface tension

studies to monitor NP-induced changes, and Sum Frequency Generation (SFG) spectroscopy to obtain molecular information on the change in protein interfacial structure caused by interaction with NPs. This fundamental study provides new insights into the mechanisms of stabilization of complex interfaces through the synergy between nanoparticles and proteins, opening the way to the possibility of creating more effective and environmentally friendly formulations.

Keywords: Out-of-equilibrium adsorption, interfaces, nanoparticles, surfactant, proteins, monolayer structure.

This page intentionally left blank.

Contents

This page intentionally left blank.

Acronyms

μ_e	electrophoretic mobility. (*p. 42, 43*)
ζ	Zeta-potential. (*p. 134, 138*)
2D	two-dimensional. (*p. 2, 12, 13, 15, 17, 21, 28, 133, 139, 159, 195*)
AFM	Atomic Force Microscopy. (*p. 8, 62, 190*)
AzoTAB	azobenzene trimethylammonium bromide. (*p. 14*)
BCN	β-Casein. (*p. i, 21, 76*)
BLG	β-Lactoglobulin. (*p. i, 21, 76*)
BSA	Bovine Serum Albumin. (*p. i, 21, 76*)
CMC	critical micellar concentration. (*p. 13*)
CTAB	Cetyltrimethylammonium bromide. (*p. i, 12, 20, 29, 32, 132, 133, 136, 138*)
DLS	Dynamic Light Scattering. (*p. 35, 134*)
DLVO	Derjaguin, Landau, Verwey, and Overbeek. (*p. 5, 15–17*)
DST	dynamic surface tension. (*p. 19, 21, 37, 134*)
DTAB	dodecyltrimethylammonium bromide. (*p. 12, 29, 34, 132, 136*)
EDL	Electric Double Layer. (*p. 6, 7*)
EOR	Enhanced Oil Recovery. (*p. 12, 17*)
GISAXS	Grazing Incidence Small Angle X-ray Scattering. (*p. i, 21, 29, 31, 40, 46, 52, 58, 133, 190, 191*)
IEP	isoelectric point. (*p. 16*)
KCl	potassium chloride. (*p. 15*)
NaCl	sodium chloride. (*p. 15, 133*)
NPs	Silicon Oxide Nanoparticles. (*p. i, ii, 2, 17, 40, 133, 136–138, 157*)
NR	Neutron Reflectometry. (*p. i, 19, 21, 205*)

PDMA poly[2-(dimethylamino)ethyl methacrylate]. (*p. 16*)
PS polystyrene. (*p. 14, 16*)

SANS Small Angle Neutron Scattering. (*p. 138, 157*)
SFA Surface Force Apparatus. (*p. 8*)
SFG Sum Frequency Generation. (*p. ii, 21*)
SIE specif ion effect. (*p. 1, 40*)
SLD scattering length density. (*p. 205, 207*)

XRR X-Ray Reflectometry. (*p. 19*)

This page intentionally left blank.

1 Introduction

Liquid interfaces are environments of unique physical and chemical complexity, where molecular interactions, adsorption phenomena, and self-assembly processes are governed by forces and constraints distinct from those operating in bulk phases. Among these, the air–water interface has been extensively investigated as a model system to study interfacial phenomena with molecular resolution. In recent years, scientific and technological interest has been growing in the development of nanoparticle monolayers at such interfaces, particularly those formed upon their irreversible adsorption. These systems offer a highly versatile platform for creating nanostructured surfaces with tunable properties, making them attractive for a wide range of applications including chemical sensing, heterogeneous catalysis, and the fabrication of "smart" materials with responsive or adaptive functionalities. Thanks to the high mechanical and chemical stability, colloid-stabilized liquid interfaces are useful for many different applications such as food industry (Dickinson, 2010a), oil-recovery (J. G. Lee et al., 2018), pharmaceuticals and drug-delivery (T. N. Hunter et al., 2008), energy harvesting (Kundu et al., 2017) and sensing (Giner-Casares et al., 2016).

A key feature of these interfacial assemblies is their sensitivity to external parameters such as ionic strength, pH, or the presence of additives that mediate particle–interface and particle–particle interactions (Vialetto et al., 2021).

Although surfactants and amphiphilic molecules have long been used to modulate the behavior of interfaces, their use in combination with colloidal particles opened up new avenues for tuning the structural organization and stability at the nanoscale.

Despite significant progress in this field, a comprehensive understanding of the mechanisms that govern nanoparticle adsorption, interparticle interactions, and the resulting interfacial structure remains incomplete. In particular, the dynamic and out-of-equilibrium nature of these assemblies poses significant experimental and theoretical challenges, requiring advanced analytical tools capable of probing structural and kinetic aspects with high spatial and temporal resolution.

Moreover, addressing how the ionic strength and the specif ion effect (SIE) modulate the assembly and the interaction between nanoparticles within the monolayer can

pave the way to a more rational design of functional monolayers. Addressing these open questions is not only fundamental from a physicochemical standpoint but also essential for the rational design of functional materials. By gaining deeper insight into the forces driving the assembly at liquid interfaces, we can develop more efficient, sustainable, and customizable formulations for emerging technologies.

In this context, the present doctoral work focuses on the experimental investigation of nanoparticle monolayers formed at the air–water interface, with a particular emphasis on the role of additives, both molecular and macromolecular, in directing interfacial assembly and determining structural and mechanical properties.

1.1 Out-of-equilibrium thermodynamics of colloids at fluid interfaces

The first groundbreaking observation of emulsions and foams stabilized by colloidal particles trapped at the interface dates back to the 20th century with the studies made first by Ramsden and then Pickering (Ramsden, 1904; Pickering, 1907). Since then, numerous studies have been carried out in order to understand and study the layer properties of particles or nanoparticles confined at the interface between two immiscible liquids. In fact, the self-assembly of colloidal particles allows us to produce a hierarchical design of new functional materials (Vogel et al., 2015). However, the fine-tuning of NPs layers properties is possible only by understanding and mastering the fundamental physicochemical aspects of the energetic beyond their assembly. In this perspective, it is essential to identify two types of forces: *i*) forces driving the adsorption at the interface, *ii*) interparticle forces acting within the monolayer.

1.1.1 Forces driving the particles assembly

The driving force for the segregation of species at the interface is the minimization of the Gibbs free energy of the interface, which can be expressed by the variation of the interfacial surface tension (γ_{12}) between the two immiscible fluids. In fact, when particles accumulate at the interface, they reduce the contact area between the two fluids, leading to a reduction of the free energy of the systems. However, since the particle dimensions usually exceed the interface thickness, the standard thermodynamic description of the surface tension cannot be applied (Garbin, 2013).

In this case, the interfacial tension must be considered as an effective magnitude. Specifically, particle adsorption at the interface creates a two-dimensional (2D) lateral pressure (Π) that opposes the reduction of the contact area between the two fluids guided by the interfacial tension (γ_{12}) and effectively decreases the total surface energy (γ)

$$\gamma = \gamma_{12} - \Pi \tag{1.1}$$

The lateral pressure exerted by the particles adsorbed at the interface is related to the particle surface excess (Γ) and the so-called trapping energy (ΔE_P), according to (Forth

et al., 2019)

$$\Pi(\Gamma) = \Gamma * \Delta E_P \tag{1.2}$$

The trapping energy ΔE_P, can be defined as the energy required to move an isolated particle from its equilibrium position at the interface to the bulk continuum, and so $\Delta E_P = E_{interface} - E_{bulk}$ where $E_{interface}$ and E_{bulk} are the energy of the particle at the interface and in the bulk dispersion, respectively (A. e. a. Maestro, 2014; Zanini et al., 2016).

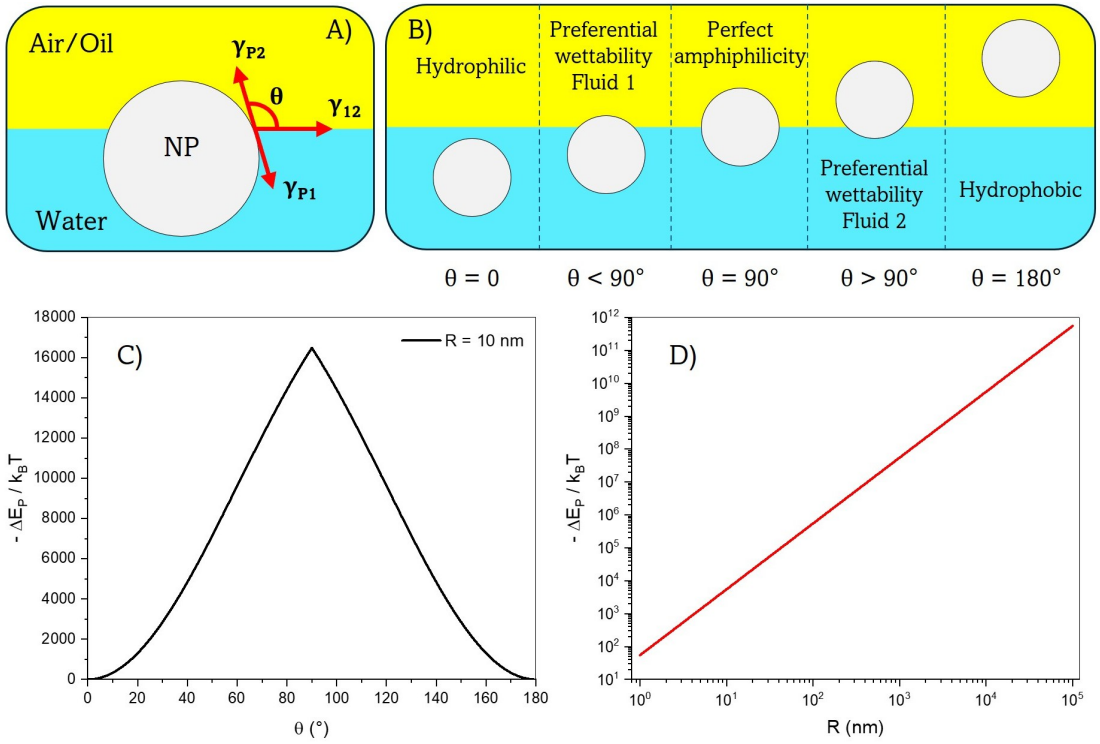

Figure 1.1: *A) Sketch of the mechanical equilibrium of a particle adsorbed at the interface between two immiscible liquids (Guzmán et al., 2022b; G. B. Davies et al., 2014). θ is the particle contact angle, γ_{p1} and γ_{P2} are the surface tension between the particle and the fluids 1 and 2, respectively, and γ_{12} is the surface tension between fluids 1 and 2. B) Contact angle evolution as function of the position with respect the fluid/fluid interface for particles with different affinity for the two fluids. C) Trapping energy evolution with contact angle for a particle of radius $R = 10$ nm, surface tension $\gamma_{12} = 72$ mN/m and temperature of 25 °C. Evolution of the trapping energy with respect to the particle radius, for contact angle $\theta = 90°$, $\gamma_{12} = 72$ mN/m and temperature of 25 °C. Curves in C) and D) were obtained with Equation 1.4.*

A more rigorous description of the trapping energy can be obtained by applying the Young's law to the geometrical sketch reported in Figure 1.1*A*. Once the equilibrium condition has been reached, the sum of the forces (interfacial tensions) acting on the system must be zero (McBride et al., 2012), and so

$$\gamma_{P1} + \gamma_{P2} - \gamma_{12} cos\theta = 0 \tag{1.3}$$

where γ_{P1} and γ_{P2} are the surface energy between the particle and fluids 1 and 2, respectively, and θ is the three-phase contact angle. In the case of a spherical particle of

radius R embedded between the two immiscible fluids 1 and 2, it can be possible to provide an analytic description of the ΔE_P by using geometrical consideration, obtaining that (Ballard et al., 2019)

$$\Delta E_P = -\pi R^2 \gamma_{12} (1 \pm \cos\theta)^2 \tag{1.4}$$

The symbol ± accounts for the different affinity of the particles for the two fluids, suggesting that in the most general case, the mechanical equilibrium condition does not correspond to equal immersion of the particle in both fluid phases. In fact, for more hydrophilic particles the center of the sphere will be located in the water phase, corresponding to $\theta < 90°$ and ΔE_P is calculated by using the sign + in the Equation 1.4. In contrast, for highly oleophilic particles, the center of the sphere will be located in the more hydrophobic fluid and thus at $\theta > 90°$ and the sign − must be used. Finally, it should be mentioned that Equation 1.4 is valid only for particles characterized by low roughness and dimensions significantly higher than the capillary wave of the fluid interface (Ballard et al., 2019).

A critical aspect that arises from this peculiar behavior is that for particles with a radius larger than 10 nm, the trapping energy can be hundreds or thousands of times higher than $k_B T$ as shown in Figure 1.1 C and D. Such a high-energy barrier implies that thermal fluctuations alone are insufficient to detach the particle once it has reached the interface, even in the absence of attractive surface–interface interactions. As a result, the system becomes kinetically trapped in a metastable state, where the observed structures and dynamics are governed not by equilibrium thermodynamics, but by the history of assembly and local energy landscapes (Guzmán et al., 2022b). This kinetic trapping has profound implications for the system comprehension and description. In practice, the non-equilibrium nature of the interface means that its structure and properties evolve over time and depend on how the system was prepared. Once nanoparticles are adsorbed, their desorption or large-scale rearrangement becomes energetically inaccessible, so the resulting monolayer reflects the kinetic pathway of adsorption rather than a true thermodynamic equilibrium. Consequently, quantities such as surface pressure, surface coverage, or interparticle distance cannot be regarded as equilibrium state variables but as transient or history-dependent observables that capture metastable configurations of the interface. This perspective highlights that out-of-equilibrium behavior is not an anomaly but an intrinsic characteristic of nanoparticle-laden interfaces, where the balance between energy barriers and relaxation times defines the structures that can be experimentally observed.

1.1.2 Interparticle forces acting within the monolayer

Once the particles reach the interface, several forces and interactions start to act on them, modulating and controlling the final structure and density, in terms of surface coverage, of the particle monolayer (Guzmán et al., 2022b; A. Maestro et al., 2018; A. Maestro, 2019). A general description of these interactions can be obtained by splitting them into two main groups: *i*) direct interaction, and *ii*) interaction mediated by the

interface itself. The first type of forces are always present in the bulk phase and only slightly modified by the presence of the interface. On the other hand, the seconds arise as a result of the confinement of the particles at the interface. Some of these interactions are represented in a simplified model in Figure 1.2.

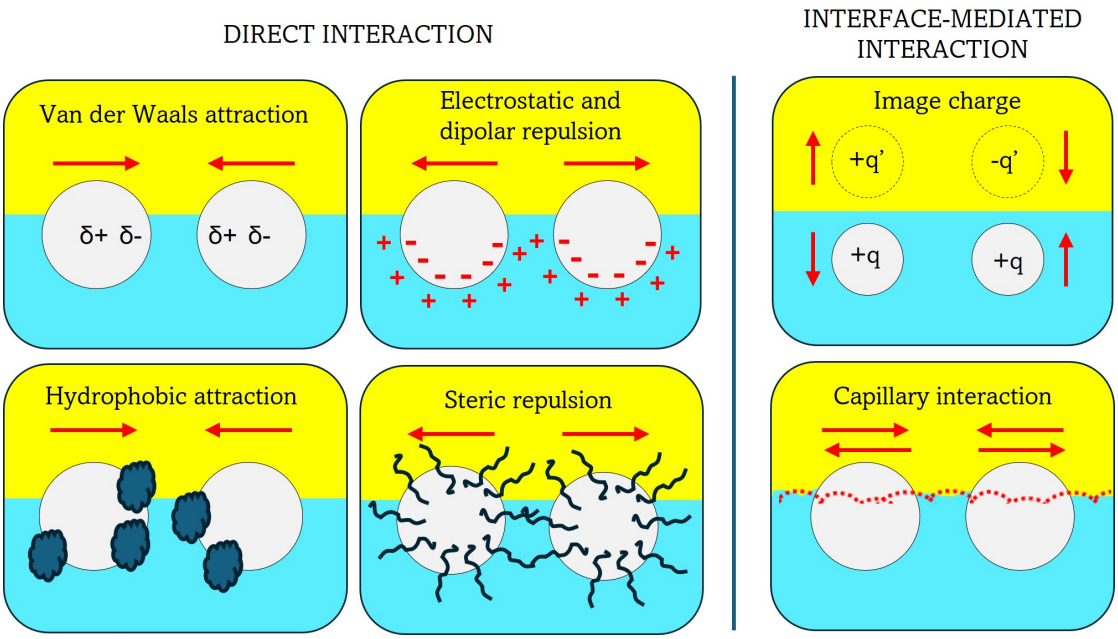

Figure 1.2: *Simplified illustration of interactions between particles trapped at the interface.*

In the framework of direct forces, the first to be mentioned are van der Waals attractions and electrostatic repulsions, which are generally expressed in the most approximated form in the classical Derjaguin, Landau, Verwey, and Overbeek (DLVO) theory (B. V. Derjaguin et al., 1987; J. N. Israelachvili, 2011). The DLVO theory, initially developed by Derjaguin and Landau (1941) (B. Derjaguin et al., 1941), who analyzed the repulsive electrostatic interactions between charged surfaces, and later extended by Verwey and Overbeek (1948) through the inclusion of attractive van der Waals forces and the formulation of the total interaction potential (Verwey, 1947), is widely used to describe the stability of colloidal dispersions. The theory considers the balance between two fundamental forces acting between particles in a liquid medium: van der Waals attraction and electrostatic repulsion, which are assumed to be independent of each other. The van der Waals contribution of two particles interacting through a medium is always attractive as stated by the combination rule (Hamaker, 1937), and thus the Hamaker constant A_{P1P}, which describes the magnitude of the interaction between two identical particles P through medium 1, is always positive. However, for particles trapped at the interface, which could also be partially immersed in fluid 2, the magnitude of the interaction depends on the Hamaker constant A_{P2P}, which has the same meaning as A_{P1P}, but considering fluid 2 (Berg, 2009). An estimation of the overall interacting potential can be obtained by assuming the existence of an effective

Hamaker constant (Williams et al., 1992), defined as follows:

$$A_{interface} = A_{P1P} + f^2(3 - 2f)(A_{P2P} - A_{P1P}) \tag{1.5}$$

where f is the volume fraction of the sphere immersed in fluid 2 and therefore depends on the contact angle θ as explained in Equation 1.4. The interaction potential between two particles of radius R at center-to-center separation distance r can be approximated as (J. N. Israelachvili, 2011):

$$U_{vdW}(r) \approx \frac{A_{interface}}{12} \frac{R}{r - 2R} \tag{1.6}$$

When a colloidal particle is immersed in a fluid, its surface may acquire a charge due to dissociation of surface groups, *e.g.* acid, basic or ionizable moieties, or by the adsorption of charged molecules, such as the electrolytes from the bulk solution. As a result, the surface will attract oppositely charged ions from the solution and repel the co-ion. This leads to the formation of the so-called Electric Double Layer (EDL) (Berg, 2009; J. N. Israelachvili, 2011). The most complex, but non-exhaustive, model to describe the EDL is the Stern model, which accounts for the presence of hard bound counter-ion at the interface in the Helmholtz layer, and the presence of a diffusive layer of tightly bound ions. The formation of the EDL causes an electrostatic screening of the surface potential, modulating the interparticle interaction (Grahame, 1947). Specifically, a quantity that can help describe how and in which magnitude the electrolyte in solution can screen the surface potential is the Debye length. The Debye length (λ_D) is the distance from the interface at which the surface potential is effectively screened by the surrounding electrolytes, and thus is generally considered the thickness of the diffuse layer. In the Poisson-Boltzmann mean-field theory (Lamm, 2003) and in the framework of the Debye-Hückel approximation (Debye, 1923), the inverse of the Debye length (k) is equal to

$$k = \lambda_D^{-1} = \sqrt{\frac{\sum_i \rho_{\infty_i} Z_i^2 e^2}{\epsilon_0 \epsilon_r k_B T}} \tag{1.7}$$

where the numerator describes the total ionic strength of the electrolyte in solution, defined by the sum of the product of the number density ρ_{∞_i} and the charge eZ_i of each ion i^{th}, while the denominator takes into account the bulk electric properties by its dielectric constant $\epsilon = \epsilon_0 \epsilon_r$ and the thermal energy $k_B T$ where k_B is the Boltzmann constant and T is the temperature.

As defined, the formation of the EDL guides the electrostatic repulsion interaction between two spherical charged particles of radius R by means of the approximated linearized Poisson-Boltzmann potential (J. N. Israelachvili, 2011; Verwey, 1947), as follows.

$$U_{EDL}(r) = \frac{aR}{kr} e^{-kr} \tag{1.8}$$

where a is a constant that takes into account the dipole magnitude and the dielectric properties of the two bulk phases.

However, when a particle is trapped at the interface between two fluids characterized by different dielectric constants ϵ_{r1} and ϵ_{r2}, the EDL formed at the interfaces immersed in the two fluids will differ both due to the different propensity of the interface to be ionized, leading to a different surface potential, and because of a different distribution of the ions around them. These asymmetries in the charge distribution result in the development of an effective dipole moment. Consequently, particles at the interface interact via dipole–dipole interactions. In the far-field limit, where the interparticle distance satisfies $kr \gg 10$, this interaction can be approximated as:

$$U_{dipolar}(r) = \frac{a k_B T}{r^3} \tag{1.9}$$

where a is a constant that takes into account the dipole magnitude and the dielectric properties of the two bulk phases (Zigelman et al., 2020). Notably, since the electrostatic repulsion potential $U_{EDL}(r)$ decays exponentially with distance, it becomes negligible beyond a few Debye lengths. In contrast, the dipolar interaction $U_{dipolar}(r)$ exhibits a slower algebraic decay as r^{-3}, and therefore governs the long-range interactions between particles trapped at fluid interfaces. However, this dipolar interaction becomes significant only in the presence of a real asymmetry in the electrostatic environment surrounding the particle, and thus arises when the particle is substantially exposed to both fluid phases, resulting in distinct electric double layers on either side and thus in the emergence of a non-negligible dipole moment. Conversely, if the particle is almost entirely immersed in one of the two fluids, the asymmetry is reduced, and the induced dipole interaction becomes negligible. In this case, the interaction is primarily governed by the EDL repulsion.

A well-known strategy for stabilizing colloidal suspension is the functionalization of the particle surface with polymers or long-tailed surfactants by chemical grafting or physical adsorption. This leads to the appearance of a steric repulsion interaction that becomes important at short interparticle distances. The analytical solution for this interaction is not so trivial, but a good estimation of the repulsion interaction between two planar surfaces grafted with polymer chains of effective length equal to L and number surface density equal to σ is given by the Alexander - de Gennes equation that takes into account the emergence of a repulsive osmotic pressure that arises when the surface-to-surface distance D < 2L and for an entropic loss caused by the polymer chain extension in highly grafted polymer brushes (Gennes, 1980). The general repulsive pressure can be expressed as follows.

$$P_{steric}(D) = k_B T \sigma^{3/2} [(2L/D)^{9/4} - (2L/D)^{-3/4}] \quad \text{for} \quad D < 2L \tag{1.10}$$

In the Derjaguin approximation, it is possible to obtain an approximate interaction potential between two spherical particles of radius R grafted with a polymer brush of

thickness L and surface number density σ at the center-to-center distance r, as reported in the following (J. N. Israelachvili, 2011).

$$U_{steric}(r) \approx RL^2\sigma^{3/2}\frac{2L}{r-2R} \quad \text{for} \quad r < 2L \tag{1.11}$$

However, the experimental or theoretical determination of the steric potential is not as straightforward as may appear. In fact, when a particle is trapped at the interface between two different fluids, the effective brush length L is generally not uniform. This is because the polymer chains experience different solvent qualities in the two fluid phases, leading to asymmetric swelling. As a result, the segments of the brush immersed in each fluid may adopt different conformations, depending on whether the corresponding liquid acts as a good or poor solvent for the polymer. This asymmetry complicates the accurate modeling of steric repulsion.

The last direct forces that must be mentioned are those driven by hydrophobic interactions. Hydrophobic interactions arise from the effective attraction between hydrophobic surfaces in water. Despite their importance, a systematic theoretical framework is still lacking, making their quantitative modeling particularly challenging. These interactions become increasingly relevant at small particle sizes, where molecular-scale solvent structuring and interface effects cannot be neglected. In such cases, hydrophobic forces minimize unfavorable particle–solvent contacts in the aqueous phase, playing a key role in the overall interaction balance. Experimental surface-force measurements have shown that the corresponding free-energy gain can reach values of 10–100 mJ/m^2, corresponding to interaction energies of several k_BT per particle for nanoparticles with radii of tens of nanometers (J. Israelachvili et al., 1982; Donaldson Jr et al., 2015). The hydrophobic potential of mean force is often expressed empirically as an exponentially decaying function of the surface-to-surface distance

$$U_{hydrophobic} = -A_{hyd} \cdot e^{-\frac{r}{\lambda_{hyd}}}, \tag{1.12}$$

where A_{hyd} is the interaction strength (typically 0.01-0.1 mJ/m^2) and λ_{hyd} is the characteristic decay length (1–3 nm). Although this representation is phenomenological, it captures the main experimental trends observed in Surface Force Apparatus (SFA) and Atomic Force Microscopy (AFM) studies (Craig et al., 1998; J. N. Israelachvili, 2011). Under certain electrolyte or surfactant conditions, longer-ranged hydrophobic attractions up to tens of nanometers have been reported, suggesting a strong coupling between solvent structure and interfacial chemistry. Overall, the magnitude of these interactions is comparable to electrostatic and van der Waals contributions, emphasizing their central role in determining particle aggregation and stability at fluid interfaces.

We can now approach the surface-mediated forces, thus interactions that arise from the asymmetry introduced by the confinement of a particle at the fluid/fluid interface. Among others, the capillary interaction probably plays a major role in the definition of the energetic landscape governing the behavior of particles at the interface. Capil-

lary forces arise from the particle-induced deformation of the interface, increasing the lateral interaction between particles. Specifically, capillary forces are caused by two independent, but sometimes coexisting, effects: *i*) the so-called flotation forces due to the gravitational modification of the interface shape by large particles, and *ii*) the immersion forces due to the existence of a non-smooth contact line mostly caused by the roughness or irregularity of particle shape (Kralchevsky et al., 2000). Although the first play a role only for particles with diameter comparable to that of the capillary length ($l_c = \sqrt{(\gamma_{12}/\Delta\rho g)}$, where $\Delta\rho$ is the difference in the mass density of the two fluids), and thus negligible for particles with dimensions smaller than 5-10 μm, the seconds are always present and strictly depend on the wettability, roughness, and shape of the particles (Stamou et al., 2000). These forces can cause both attractive and repulsive potentials depending on the local curvature of the interface. However, at low interparticle distances, the capillary interaction always produces a net attractive potential. The following is a simplistic expression of the magnitude of the capillary potential.

$$U_{capillary}(r) = -12\pi\gamma_{12}K^2\zeta\frac{r^4}{R^4} \tag{1.13}$$

where R is the particle size, ζ is a factor that takes into account the shape and orientation of the particle, and K depends on the deformation amplitude of the interface (Stamou et al., 2000).

The last phenomenon that will be discussed in this section is the formation of the image charge at the interface. Although image charge interactions are not strictly interparticle forces, they emerge due to the presence of a dielectric discontinuity at the interface between the two fluids and are therefore included in this discussion. These interactions originate from the dielectric mismatch between the two fluid phases: when a charged particle approaches the interface, the difference in permittivity induces an electrostatic response that can be described, in classical terms, as the induction of an image charge on the opposite side of the interface. The polarity of the image charge can be equal to or opposite the charge of the particle approaching the interface as can be expressed in a first instance by the following approximated equation (Hatlo et al., 2008).

$$q^{'} = q\frac{\epsilon_1 - \epsilon_2}{\epsilon_1 + \epsilon_2} \tag{1.14}$$

where $q^{'}$ is the induced image charge and ϵ_1 and ϵ_2 are the dielectric constants of fluids 1 and 2, respectively. As can be easily calculated, for a particle dispersed in the medium 1 such that $\epsilon_1 > \epsilon_2$, as in the most general case the colloids are dispersed in the aqueous phase which has a much higher dielectric constant than that of oil or air, the induced image charge will have the same polarity as the inducting particle. Noteworthy, in the case of the air-water interface, since the dielectric constant of water is $\epsilon_1 \approx 80$ (Malmberg et al., 1956) and that of the air is $\epsilon_2 \approx 1$ (Hughes et al., 1952), the magnitude of $q^{'}$ will be around 97% of the inducting charge q. This leads to a strong repulsive potential acting in the direction perpendicular to the interface that

alters the free energy of the particle near the surface hindering its adsorption. Despite the fact that the induction of an image charge is fundamentally a single-particle effect, its macroscopic consequence is the modulation of the particle packing density at the interface, favoring or disfavoring adsorption in a similar manner to the interparticle interactions described above. This makes it relevant in the overall balance of forces governing the interfacial assembly.

In summary, the assembly of colloidal particles at fluid interfaces results from a delicate interplay between the forces driving particle adsorption, namely the trapping energy ΔE_P, and those acting between particles once they are confined at the interface that can be expressed in a first approximation as the sum of the individual interactions above mentioned, such that $U_{TOT} = U_{DLVO} + U_{dipolar} + U_{hydrophobic} + U_{steric} + U_{interface}$, with the last term accounting for the interface-mediated interactions.

The interplay between these interactions has been clearly demonstrated in a number of experimental systems, spanning from micrometer-sized colloids to nanoparticles. For instance, capillary attraction between partially immersed latex or silica microspheres has been directly visualized by optical and confocal microscopy, revealing the formation of linear or hexagonal aggregates whose geometry depends on the particle size and wetting asymmetry (Aveyard et al., 2000; Stamou et al., 2000). In contrast, electrostatic repulsion dominates in charged systems, where well-ordered, quasi-crystalline domains can form when the screening length in water is comparable to the interparticle spacing. Such behavior has been observed for charged polystyrene and silica particles at the air–water interface, and the degree of ordering can be tuned by adjusting the ionic strength or pH of the subphase (Isa et al., 2011). For nanoparticles of a few tens of nanometers, van der Waals and hydrophobic interactions become increasingly relevant. Hydrophobically modified or partially coated nanoparticles often display irreversible clustering and network formation once the interfacial film is compressed beyond a critical surface coverage (G. Kim et al., 2002; Guzmán et al., 2022a). These irreversible transitions are a direct manifestation of the kinetic trapping that characterizes out-of-equilibrium interfaces. Overall, these examples illustrate how the balance between attractive and repulsive forces governs both the structure and stability of colloidal monolayers. Depending on the system composition and interfacial conditions, the same physical mechanisms can lead to long-range ordering, aggregation, or disordered arrested states. Recognizing these experimental signatures is essential for interpreting the behavior of nanoparticle-laden interfaces discussed in the following sections.

While these interactions can be classified and distinguished from each other for conceptual clarity, they are intrinsically coupled; in fact, the extent of immersion, governed by particle wettability, not only determines the adsorption energy but also modulates the nature and magnitude of interparticle forces and *vice versa*. Understanding and controlling this balance is thus essential for driving the structural and mechanical properties of interfacial assemblies.

To achieve such control, one of the most effective strategies is the use of additives, such as small molecules, ions, surfactants, or macromolecules, that can finely tune the physicochemical properties of the particles and the environment at the interface. The following section explores in detail how selected additives were employed in the literature to modulate interfacial interactions, with particular attention to their role in directing particle assembly, monolayer structure, and the resulting interaction potentials.

1.2 Additives-driven particles assembly at the air-water interface

Colloidal monolayers at fluid interfaces can generally be fabricated using two distinct methodologies. The first involves the direct spreading of particles that possess intrinsic interfacial activity, typically amphiphilic or highly hydrophobic particles, at the interface between two immiscible fluids. These particles are often insoluble in the aqueous phase and are deposited using methods such as drop-casting from volatile organic solvents or solvent-spreading protocols, leading to the formation of Langmuir monolayers (Schultz et al., 2006; Wen et al., 2011). In such cases, adsorption occurs spontaneously due to the favorable balance of interfacial energies.

The second approach, which is particularly relevant for hydrophilic or charge-stabilized particles dispersed in aqueous media, and thus relevant for the development of this doctoral thesis, involves their induced adsorption at the fluid interface, leading to the formation of Gibbs monolayers. Because these colloids exhibit negligible interfacial affinity under native conditions, often due to strong hydration shells or repulsive particle-particle and interface-particle electrostatic barriers (Vialetto et al., 2021), external intervention is required to enable their adsorption. This is achieved through the incorporation of additives into the suspension. Such additives may include electrolytes, ionic or nonionic surfactants, polymers, or cosolvents, and act either by the *in situ* modification of the physicochemical properties of the particle surface (e.g., wettability, surface charge) or by altering the interaction potential between the particles and the interface (Yuan et al., 2022).

In practical terms, the main difference between Langmuir and Gibbs monolayers lies in how the surface density of the adsorbed species is controlled. In Langmuir monolayers, a known amount of material, either molecular or particulate, is deposited directly onto the interface, allowing the surface coverage to be tuned externally by compression or by varying the spreading quantity. In Gibbs monolayers, on the other hand, the steady-state surface density results from the spontaneous adsorption of molecules or particle from the bulk to the interface and is governed by the interactions between the adsorbing species and the subphase and the adsorbing species themselves at the interface.

The use of additives thus provides a versatile and widely applicable route for guid-

ing colloidal adsorption and tuning the structure and stability of interfacial assemblies. Beyond static structural control, additives also modulate the dynamic behavior and mechanical response of particle-laden interfaces, influencing interfacial rheology, adsorption/desorption kinetics, and the ability of monolayers to withstand and recover from external mechanical perturbations (Liggieri et al., 2011; Yu et al., 2018; Deshmukh et al., 2015). Such effects become particularly relevant when designing reconfigurable or stress-responsive soft interfaces, where the interplay between interparticle forces and interfacial rheology governs the structural resilience and reversibility of the colloidal monolayer.

1.2.1 Surfactants

Among the additives that modulate interfacial assembly of colloids at fluid interfaces, surfactants have become the model system par excellence for studying nanoparticle adsorption at fluid interfaces. Owing to their well-defined amphiphilic character and their ability to modify interfacial tension, surface charge, and wettability, surfactants provide a highly controllable platform to mediate interactions between colloidal particles and fluid–fluid interfaces. Their effectiveness in promoting or suppressing nanoparticle adsorption is derived from mechanisms such as electrostatic complexation, hydrophobization via surface adsorption, and the generation of Marangoni flows, all of which directly impact the assembly of 2D colloidal monolayers (Vialetto et al., 2021; Bernard P. Binks et al., 2000; A. e. a. Maestro, 2014). As a result, surface stabilization by surfactant-coated particles has become the benchmark for investigating fundamental interfacial phenomena, such as adsorption kinetics, contact angle modulation, and 2D crystallization.

Beyond their role as academic model systems, surfactants are also of major industrial relevance in applications where controlling nanoparticle adsorption at fluid interfaces is critical. For instance, in emulsion polymerization, surfactants guide the interfacial localization of growing polymer particles, influencing the size distribution and colloidal stability (Gilbert, 1995). In the fabrication of nanostructured coatings and interfacial films, the surfactant-assisted assembly enables the creation of highly ordered nanoparticle layers with tunable spacing and interfacial coverage (Bigioni, 2006). In addition, surfactant-driven adsorption is widely exploited in Enhanced Oil Recovery (EOR) and Pickering emulsions, where the interfacial localization of nanoparticles is key to system stability and performance (Chevalier et al., 2013; Nguyen et al., 2011). In these contexts, the knowledge derived from model surfactant–particle systems provides essential design principles for scaling up interfacial self-assembly processes in applied technologies.

The adsorption of a nanoparticle to a fluid interface strongly depends on its wettability and surface charge. Surfactants, especially ionic ones such as Cetyltrimethylammonium bromide (CTAB) or dodecyltrimethylammonium bromide (DTAB), adsorb electrostatically onto oppositely charged particle surfaces, altering their interfacial be-

havior. For instance, anionic silica (SiO_2) nanoparticles, which are highly hydrophilic and carry a strong negative surface charge at neutral pH, do not spontaneously adsorb at oil-water or air-water interfaces. However, when CTAB is added to the suspension, it electrostatically binds to the particle surface, reducing the surface charge and consequently the image charge (Equation 1.14) and increasing the hydrophobicity of the particle affecting the contact angle (θ) at the interface (Vialetto et al., 2021). Taken together, these two effects cooperate to simultaneously decrease the energy barrier for the adsorption and increase the trapping energy (Equation 1.1), promoting the out-of-equilibrium assembly of 2D nanoparticle layer at the interface.

The effect of cationic surfactants on the particle adsorption shows a concentration-dependent effect that can be generalized by identifying three different regimes: *1*) at very low concentration compared to that of nanoparticle, the amount of surfactant is not sufficient to modify the physicochemical properties of the particle and thus to promote their adsorption; *ii*) at intermediate concentration, usually below the critical micellar concentration (CMC), the surfactant adsorbs on the particle surface forming a monolayer that alters the hydrophilicity of the particle and its surface charge promoting the formation of a particle monolayer at the interface; finally *iii*) at very high concentration, generally above the CMC, surfactant forms a bilayer around the particle producing a surface charge inversion and restoring its hydrophilicity, thus re-stabilizing the colloidal aqueous suspension and hindering the adsorption at the interface (Bernard P Binks et al., 2007; A. e. a. Maestro, 2014; A. Maestro et al., 2012).

Beyond concentration effects, the molecular structure of the surfactant also plays a key role in tuning the adsorption. In particular, increasing the hydrophobic chain length of the surfactant leads to stronger particle–interface interactions and more robust trapping. In fact, it was demonstrated that, under identical conditions of particle and surfactant concentration, surfactants with longer alkyl chains yield monolayers with higher particle density and enhanced stability at the interface. This effect is attributed to a more pronounced hydrophobization of the nanoparticles, which increases the contact angle θ and thus the trapping energy, as indicated by Equation 1.4 (Ruffino et al., 2022).

Further, it is important to note that ionic surfactants interacting with oppositely charged colloidal particles not only affect their adsorption behavior, but also significantly influence the structural organization of the resulting monolayer. Experimental observations have shown that monolayers exhibiting high crystallinity and long-range order can be obtained only at low surfactant concentrations, where the screening of the particle surface charge is minimal. In this regime, electrostatic and dipolar repulsive interactions between particles remain dominant, promoting well-defined interparticle spacing and ordered arrangements. In contrast, increasing the surfactant concentration leads to progressive surface charge neutralization and enhanced hydrophobicity of the particles. These combined effects suppress the repulsive interactions that typically prevent particle aggregation and, simultaneously, promote short-range hydrophobic attractions. As a result, the interfacial assembly becomes increasingly disordered, with

a tendency toward the formation of amorphous monolayers (Vialetto et al., 2020; C. Li et al., 2020). In extreme cases, this can even lead to coagulation or irreversible aggregation of the particles, both in the bulk phase and at the fluid interface, thereby undermining the formation of uniform and ordered colloidal films.

In addition, the surfactant-induced modulation of interparticle interactions and monolayer packing density plays a crucial role in determining the interfacial viscoelasticity, with direct implications for the rheological behavior and stress response of the assembled films (Ravera et al., 2006; Safouane et al., 2007). Specifically, the combined use of nanoparticles and surfactants at fluid interfaces enhances both shear and dilatational viscoelastic properties of the interfacial film, due to the synergistic interplay between surfactant-mediated adsorption and nanoparticle-induced structural reinforcement, that can be tuned by a proper bulk formulation (Yu et al., 2018). This increase in interfacial elasticity and rigidity has been directly correlated with improved foam and emulsion stability, as it reduces film thinning, coalescence, and drainage under stress (Liggieri et al., 2011; Mendoza et al., 2014; Beltramo et al., 2017; Thijssen et al., 2017).

A particularly intriguing class of surfactants that has recently gained attention for interfacial colloidal assembly is that of photoswitchable surfactants. These molecules incorporate a light-responsive moiety, typically an azobenzene unit, that enables reversible conformational switching between trans (E) and cis (Z) isomers upon light irradiation. The two isomers exhibit markedly different physicochemical properties: the trans form is more linear, apolar, hydrophobic, and surface active, whereas the cis isomer adopts a bent geometry and possesses a significant dipole moment, making it more polar and less surface active. As a consequence, these surfactants allow remote, optical modulation of interfacial tension and particle–interface interactions, offering a unique handle for out-of-equilibrium control (Anyfantakis et al., 2014).

One of the most illustrative examples is azobenzene trimethylammonium bromide (AzoTAB), which has been used to design photosensitive colloidal systems capable of light-tunable particle adsorption and structural rearrangement at the air–water interface. Vialetto et al. (2019) demonstrated that AzoTAB can reversibly tune the surface charge of anionic polystyrene (PS) microparticles through its light-dependent isomerization state. In the trans state, the surfactant interacts with the particles at relatively low concentrations, leading to their partial neutralization and enhanced interfacial trapping. Upon UV irradiation, AzoTAB isomerizes to the more hydrophilic cis state, which requires a significantly higher concentration to achieve the same level of particle surface coverage and charge neutralization. This shift in surface affinity can be used to optically modulate the adsorption behavior of the particles. More notably, by working at very low AzoTAB concentrations, it was possible to exploit this mechanism to reversibly switch the packing order of PS particles at the interface. In the dark, weakly interacting particles formed disordered aggregates due to weak residual repulsions. Upon light activation, the desorption of cis-AzoTAB from the interface increased the electrostatic confinement, triggering rapid crystallization of the colloidal monolayer. Turning off the light allowed trans-AzoTAB to re-adsorb, weakening repulsion, and

restoring disorder. This process, driven by the dynamic adsorption-desorption of the surfactant, provides a compelling demonstration of dissipative, stimuli-responsive 2D crystallization.

Although the system discussed here is not the focus of this thesis, it represents an excellent conceptual example of how multiple interparticle and particle–interface potentials can be modulated simultaneously through a single external stimulus. By coupling molecular-scale switching to collective colloidal behavior, photoswitchable surfactants illustrate in a simple yet powerful way how the balance of electrostatic, capillary, and hydrophobic contributions can be dynamically tuned. This idea directly resonates with the general aim of this work: to understand how interfacial additives control the energetic landscape and drive out-of-equilibrium organization in nanoparticle-laden interfaces

1.2.2 Electrolytes

Another widely studied and effective class of additives used to promote the adsorption of colloidal particles at fluid interfaces is that of aqueous soluble electrolytes. Unlike surfactants, which directly modify the surface chemistry of the particles through molecular adsorption, electrolytes act primarily by tuning the electrostatic environment of the system. Their main effect arises from the modulation of the ionic strength of the aqueous phase, which influences the interaction potentials between particles, as well as between particles and the fluid interface. In systems composed of charge-stabilized nanoparticles, such as silica or latex particles dispersed in water, strong repulsive interactions prevent particles from approaching each other, due to the long-range electrostatic double-layer forces described by the DLVO theory in Equation 1.8, or the interface due to the high repulsive charge image (Equation 1.14). By adding electrolytes, the Debye screening length is reduced, compressing the double layer around each particle and thereby weakening the repulsive barrier. This facilitates both particle aggregation in the bulk and adsorption at the air–water or oil–water interface. Furthermore, electrolyte-induced screening can lower the image charge repulsion between particles and the dielectric discontinuity at the fluid interface. As a result, even highly hydrophilic and charged colloids may adsorb irreversibly at fluid interfaces in the presence of sufficient ionic strength. This strategy has been widely applied to enable the formation of colloidal monolayers from otherwise non-interfacially active particles and to control the assembly dynamics by tuning the salt concentration, valency, or pH of the suspension.

The influence of electrolytes on colloidal adsorption is strongly dependent on the valency and concentration of the ions added. In the case of monovalent salts, such as sodium chloride (NaCl) or potassium chloride (KCl), the main effect is a gradual compression of the electrical double layer surrounding the colloidal particles. As the ionic strength increases, the Debye screening length κ^{-1} decreases, reducing the range of electrostatic repulsion and allowing particles to approach the fluid interface more

closely. For instance, it has been shown that the addition of NaCl to aqueous suspensions of anionic PS nanoparticles enables their irreversible adsorption at the air–water interface, which is otherwise energetically unfavorable under low-salt conditions (Williams et al., 1992).

In contrast, the addition of multivalent counterions, such as Ca^{2+}, Mg^{2+}, or Al^{3+}, produces much stronger effects. These ions not only screen electrostatic repulsion more effectively but can also bind directly to negatively charged particle surfaces, inducing partial or complete charge neutralization and even bridging (J. N. Israelachvili, 2011). Hence, interfacial adsorption and flocculation can occur at substantially lower concentrations than in monovalent salts (Tian et al., 2014). However, under these conditions, the classical DLVO framework breaks down and cannot be reliably used for quantitative modeling. This failure arises because multivalent ions introduce strong ion–ion correlations, surface-specific adsorption, charge regulation, and short-range attractions that are not captured by the mean-field approximation of DLVO theory (Bakhshandeh et al., 2022; Silvera Batista et al., 2015). As a result, developing an analytical treatment of their effect becomes non-tractable, one must instead rely on empirical observations or more complex theoretical models that incorporate ionic correlations and specific adsorption phenomena.

Finally, particles whose surface charge is governed by ionizable moieties, such as carboxylate or ammonium functionalized particles or metal oxide particles such as silica (SiO_2) or alumina (Al_2O_3), show a dependency on the pH of the solution, adding another layer of complexity. In this framework, the adsorption behavior of these systems can be properly tuned by modifying the pH. For example, for oxide particles such as silica, whose surface charge arises from the dissociation of surface silanol groups. At high pH, deprotonation increases the negative surface charge, requiring higher ionic strengths to achieve effective screening. Conversely, lowering the pH toward the isoelectric point (IEP) reduces the surface charge density, decreasing the energy barrier for interfacial adsorption (Park et al., 2012). Another example comes from Fujii et al. (2017) where the adsorption at the air-water interface of PS nanoparticles functionalized with poly[2-(dimethylamino)ethyl methacrylate] (PDMA) can be activated or deactivated by controlling the solution pH. In this specific case, PDMA is a pH-sensitive poly-electrolyte, which is highly hydrophilic and positively charged at pH < 3 due to the protonation of methacrylate groups and highly hydrophobic at pH > 10 where the polymer is deprotonated. Thus, the particle adsorption occurred only at pH > 10.

Moreover, the presence of electrolytes critically influences not only the equilibrium adsorption of colloidal particles but also the kinetics of interfacial capture and the rheological response of the adsorbed layer. Since common fluid interfaces such as air–water or oil–water are effectively characterized by a negative surface charge (Gragson et al., 1997; Jungwirth et al., 2006), the addition of electrolytes mitigates electrostatic repulsion between negatively charged particles, the negatively charged interface, and the image charge, allowing particles to approach more easily and adsorb faster. This results in increased adsorption rates, particularly at higher ionic strengths or with mul-

tivalent counterions, as demonstrated by faster adsorption curves in salt-rich systems (Dugyala et al., 2016; Tomasella et al., 2025; Williams et al., 1992). In addition, change in the ionic strength allows to modulate interfacial rheology and relaxation behavior. In fact, the increase in the interfacial elastic modulus is promoted by tighter nanoparticle packing and stronger lateral interactions (Chai et al., 2020). At high ionic strength or in the presence of multivalent cations, both dilatational and shear moduli increase, reflecting stiffer, more mechanically resilient interfacial films (Kirby et al., 2018; Da et al., 2021; Van Den Berg et al., 2018). Understanding these electrolyte-mediated effects is essential for controlling the dynamic assembly and mechanical resilience of colloidal monolayers, particularly in applications where interfacial films must withstand cyclic or large-scale mechanical perturbations.

In summary, these examples show that electrolyte composition, concentration, and pH can be exploited as precise control parameters for tuning particle–interface and particle-particle interactions and directing the formation of stable colloidal monolayers. On the other hand, the effects of multivalent ions are beyond the predictive reach of classical DLVO theory. Thus, future work must integrate advanced models and tailored experiments to fully harness these effects for the controlled assembly of colloidal monolayers.

1.2.3 Macromolecules and Proteins

Besides surfactants and electrolytes, another important class of additives used to control interfacial colloidal assembly includes macromolecules, such as synthetic polymers and biopolymers. Hydrophilic polymers, *e.g.*, PEG, PVA, were extensively used to promote the adsorption of hydrophilic silica particles at the fluid-fluid interface to stabilize foams and emulsions or for EOR applications (Son et al., 2015; Qing et al., 2020; Srivastava et al., 2017; ShamsiJazeyi et al., 2014). Another class of widely used macromolecules is poly-electrolytes, thus polymers containing charged repeating units that confer them high charge density and unique properties. Xue et al. (2016) demonstrated how a mixture of silica nanoparticles and a cationic polyelectrolyte has a synergistic effect in the stabilization of foams. In fact, they demonstrated how the presence of NPs led to a higher stability against Ostwald ripening due to an increased surface elasticity, while the polymer increased the stability against coalescence and lamella drainage. Additional examples further underscore these effects: the 2D confining of mixed responsive hydrogels - inorganic particles layer at the fluid interfaces not only reinforces their stiffness, but also enables tunable phase-transition with modulated rheology (Loescher et al., 2025; El-Tawargy et al., 2018; Abgarjan et al., 2025). Moreover, entropic and enthalpic interactions at the polymer–NP interface can modulate dynamic fragility and heterogeneity, offering further levers to tune mechanical behavior under external stimuli (Begam et al., 2018; Guzmán et al., 2022a).

Despite the use of macromolecules being by now a well-established strategy for stabilizing nanoparticles at fluid interfaces, and although many additional examples

could be cited beyond those already discussed, the use of proteins as functional additives to guide nanoparticle adsorption and interfacial assembly remains a largely untapped opportunity. From a physicochemical perspective, proteins are macromolecules that exhibit intrinsic amphiphilicity, as they are composed of both hydrophilic and hydrophobic amino acid residues (Foster, 1977). Typically, these residues are present in comparable proportions, enabling proteins to behave as macrosurfactants. Their ability to adsorb and accumulate at air–water and oil–water interfaces has been recognized since the 19th century (Gochev et al., 2016; Ramsden, 1904), when early investigations began to uncover their role in stabilizing foams and emulsions. Thanks to the development of increasingly sensitive experimental techniques for probing interfacial films, our mechanistic understanding of protein behavior at fluid interfaces has advanced significantly in recent years (G. G. Gochev et al., 2024; Damodaran, 2005; Enders et al., 2023).

From a structural and interfacial perspective, proteins can be classified into three broad categories, globular, intrinsically disordered, and fibrillar, whose solubility and adsorption behavior differ markedly (Alberts et al., 2002). Globular proteins, such as bovine serum albumin (BSA), β-lactoglobulin (BLG), or lysozyme, are typically well soluble in water due to their compact tertiary structure, where hydrophilic residues are outwardly exposed while hydrophobic domains remain buried. Their adsorption at fluid interfaces usually involves partial unfolding, which allows the exposure of hydrophobic groups to the air phase while maintaining an overall stable core (Noskov et al., 2010; Braunschweig et al., 2017). Intrinsically disordered proteins (IDPs), exemplified by caseins, lack a fixed tertiary structure and possess both hydrophilic and hydrophobic blocks distributed along the chain. This amphiphilic character promotes self-association into micelles and gives rise to macrosurfactant-like behavior: IDPs are moderately soluble, rapidly adsorb to interfaces, and can rearrange extensively to minimize interfacial energy. Their flexible nature makes them efficient stabilizers of emulsions and foams, capable of covering large surface areas at relatively low bulk concentrations (Horvath et al., 2022; Bhat et al., 2016). In contrast, fibrillar proteins, such as collagen or amyloid assemblies, are often poorly soluble or even insoluble in water due to their extensive intermolecular β-sheet or triple-helix organization. They tend to precipitate and form network-like, rigid interfacial layers with limited capacity for rearrangement or desorption (Qiao et al., 2022; T. Li et al., 2023). These insoluble protein films typically behave as Langmuir-type monolayers, whereas the more soluble globular and disordered proteins display Gibbs-like dynamic exchange with the subphase.

Nevertheless, while much is known about protein–interface interactions in food and pharmaceutical formulations, their role in modulating nanoparticle adsorption, interfacial trapping energy, and the structure of assembled monolayers remains poorly characterized. Only a limited number of studies have investigated how proteins can promote or direct nanoparticle adsorption at fluid interfaces and influence the morphology and packing of the resulting monolayers.

Although the interaction between proteins and nanoparticles in the bulk phase is

now relatively well understood and documented, their behavior at fluid interfaces remains almost entirely unexplored. Proteins can interact with nanoparticles through electrostatic forces, hydrophobic interactions, or specific binding mechanisms, potentially altering their surface charge, wettability, and steric profile (Galdino et al., 2020; Halder et al., 2023; Lundqvist et al., 2004; Yadav et al., 2016). These changes could, in principle, be exploited to fine-tune both particle adsorption and interparticle interactions, enabling the design of tailored hybrid monolayers. However, the structural complexity, conformational flexibility, and environmental sensitivity of proteins (e.g., to pH and ionic strength) may open avenues for developing dynamically reconfigurable interfaces, where both structure and mechanical response can be actively modulated. In this perspective, protein-based interfacial films often exhibit limited mechanical strength and fast stress relaxation, and are prone to denaturation under perturbation (Dickinson, 2010b; Dickinson, 1999). The incorporation of colloidal nanoparticles could, in principle, enhance interfacial elasticity, slow down relaxation dynamics, and provide structural reinforcement in mixed interfacial films, as evidenced in surfactant–particle systems (Ravera et al., 2006).

Only a few experimental studies can currently be found in the literature. Among them, Gahtori et al. (2023) investigated the interaction between human serum albumin and gold nanoparticles at both air–water and lipid–water interfaces, showing that protein-mediated adsorption was strongly pH-dependent. Further, Shourni et al., 2022 demonstrated that the absorption of BSA onto non surface-active silica nanoparticles renders them surface-active, altering both the dynamic surface tension and interfacial rheology. The authors showed that these effects strongly depend on protein concentration, especially for the interfacial monolayer elasticity which, although enhanced by the presence of nanoparticles compared to the bare protein, exhibits a clear maximum in the hard corona regime before decreasing as soft corona layers develop. Moreover, (Rey et al., 2018) observed that, analogously to polymers or hydrogels, proteins can direct the assembly of microparticles into unconventional phases. In particular, BSA has been reported to promote chain-like and square arrangements of spherical microcolloids at the air–water interface, instead of the hexagonal lattices typically observed. This behavior has been attributed to BSA-mediated modifications of the interparticle interaction potential, consistent with the formation of hard core–soft shell complexes. Finally, Ang et al. (2010) conducted what is, to the best of the author's knowledge, the first structural investigation of silica nanoparticles in the presence of a β-casein monolayer at the air–water interface, employing neutron reflectometry (NR) and X-ray reflectometry (XRR) techniques.

Exploiting the natural diversity of proteins, their molecular recognition capabilities, and their conformational responsiveness to external stimuli could unlock new strategies for the fabrication of dynamic, biocompatible interfacial materials. Moreover, from both scientific and technological perspectives, the development of next-generation interfacial materials that are biodegradable, biocompatible, and environmentally sustainable is of paramount importance. Despite the widespread use of synthetic surfactants

and polymers in colloidal systems, concerns regarding their toxicity and persistence in the environment call for the urgent development of greener and more sustainable alternatives. In the author's view, proteins offer one of the most promising routes toward this goal.

To fully realize this potential, however, rigorous and systematic studies combining colloidal science, protein biophysics, and interfacial characterization are urgently needed to move beyond anecdotal observations and establish a robust design framework for protein-mediated nanoparticle assembly at fluid interfaces.

1.3 Objectives, experimental approach and thesis structure

This doctoral research focuses on the structural organization, interparticle interactions, and mechanical response of monolayers composed of colloidal silica nanoparticles, approximately 25 nm in diameter, irreversibly adsorbed at the air–water interface. These nanometric monolayers are investigated as model systems for understanding interfacial assembly under non-equilibrium conditions, with particular attention to the role of surface-active additives in directing their adsorption and collective behavior. The overall objective is to develop a quantitative and mechanistic framework that links the microscopic forces at play to the macroscopic properties of the resulting interfacial films.

Beyond their fundamental scientific interest, these systems also have clear practical relevance in a variety of technological fields. For example, gaining a better understanding of how nanoparticles organize and interact at liquid interfaces can help improve the design of optical and plasmonic sensors, where ordered interfacial layers can act as tunable diffraction gratings or enhance light–matter interactions for more sensitive detection (M. Li et al., 2015). Similarly, in heterogeneous catalysis, interfacial nanoparticle films can serve as efficient and easily recoverable catalytic platforms for reactions occurring in bi-phasic environments (Juan Liu et al., 2024). The same principles are valuable for developing stimuli-responsive coatings and adaptive membranes, where the mechanical and chemical stability of the nanoparticle layer determines the surface functionality (Ramesh et al., 2022; Heo et al., 2024; Yi et al., 2024). Finally, exploring the use of proteins and other biocompatible additives opens new possibilities for sustainable formulations in areas such as food, cosmetics, and pharmaceuticals, where environmentally friendly interfacial stabilizers are becoming increasingly important.

The thesis is organized into two main parts. The first part investigates a well-established model system composed of negatively charged silica nanoparticles and the cationic surfactant CTAB. The choice of this system is motivated by its widespread use in the literature as a benchmark platform for probing surfactant-mediated nanoparticle adsorption. Its relatively simple electrostatic framework provides a solid basis for exploring adsorption kinetics, interparticle interactions, and monolayer mechanics with a high degree of control and reproducibility.

This part of the project, detailed reported in **section 1**, is structured around three fundamental questions:

1. What is the mechanism governing the adsorption kinetics of silica nanoparticles at the air–water interface, and how are these kinetics modulated by surfactant concentration and ionic strength?

While indirect, by dynamic surface tension (DST), or direct observations, with microscopy and optical tweezers, have been successfully employed to study the mechanisms behind the dynamics of the adsorption of micron-sized particles, nanoscale systems require more refined methods. To this end, in Chapter 2 a new experimental approach based on time-resolved Grazing Incidence Small Angle X-ray Scattering (GISAXS) was employed to monitor the *in situ* adsorption process and structural evolution of the monolayer with high temporal and spatial resolution.

2. How do ionic strength and cationic valency influence the interparticle interactions within the monolayer?

By confining nanoparticles at a 2D interface, the measurement of interparticle potentials becomes more easily characterized compared to bulk suspensions, where no equivalent high-resolution technique exists for nanocolloids. In Chapter 3, a custom experimental protocol combining GISAXS with simultaneous Langmuir trough compression is used to extract interaction potentials as a function of interparticle distance, and to investigate the influence of electrolyte composition and nature on the NP monolayer structure.

3. How does the bulk composition, in terms of ionic strength, cationic identity, and surfactant concentration, affect the monolayer ability to reorganize and recover the structure upon large deformations?

By linking the insights gained from adsorption kinetics and interaction forces, in Chapter 4, the structural resilience of the monolayers is assessed following mechanical perturbations. Compression–expansion cycles are used to probe plasticity, hysteresis, and the degree of structural recovery under various bulk conditions.

The second part of the thesis, developed in **section 2** shifts focus toward the use of proteins as biocompatible and amphiphilic additives capable of promoting nanoparticle adsorption at fluid interfaces. Specifically, three model proteins, Bovine Serum Albumin (BSA), β-Casein (BCN) and β-Lactoglobulin (BLG), were investigated. These proteins are widely studied, and their behavior at the air–water interface is well documented, providing a reliable foundation for exploring their ability to mediate the formation of hybrid organic–inorganic monolayers.

In Chapter 5 a systematic study is conducted to evaluate how protein concentration affects the structure of nanoparticle monolayers under static conditions. In the static regime, techniques such as DST, GISAXS, Neutron Reflectometry (NR), and vibrational Sum Frequency Generation (SFG) spectroscopy are employed to characterize the interfacial structure at multiple length scales and probe protein conformation.

In Chapter 6 the dynamic properties of the hybrid monolayers were investigated. The structural evolution of the films was evaluated during lateral compression in a Langmuir trough by *in situ* GISAXS and NR to investigate how the mechanical response of the monolayer is related to changes in structure and interfacial composition.

By combining these two complementary experimental strategies, one centered on a classical surfactant-based model system and the other on structurally complex and environmentally relevant biomolecules, this doctoral thesis aims to deliver a comprehensive understanding of nanoparticle monolayer assembly at fluid interfaces. The findings contribute to the development of tunable, responsive, and sustainable interfacial materials, bridging fundamental interfacial science with practical applications in coatings, encapsulation, and biointerface design.

This page intentionally left blank.

Section 1

This page intentionally left blank.

2

Time-resolved investigation of nanoparticle adsorption at the air-water interface

The formation of self-assembled nanoparticle monolayers at the fluid interfaces is a consolidated and versatile tool for the production of 2D films with unique properties, whose applications span a wide range of technologically relevant processes, as extensively described in Chapter 1. In this dissertation, special attention was given to the formation of Gibbs monolayers in which spontaneous adsorption of nanoparticles at the air-water interface is promoted by the addition of additives such as ionic surfactants and electrolytes (Section 1.2).

However, given the non-equilibrium conditions of the particle adsorption (Ballard et al., 2019), the determination of the static surface excess upon monolayer equilibration is not straightforward, limiting our possibility of ultrafine tuning of the monolayer structure. In this framework, our understanding of the adsorption kinetics and mechanisms is even more limited, due to the experimental difficulties in tracking particle adsorption especially when dealing with sub-micron or even nanoparticles, which cannot be monitored with standard optical techniques. This presents a challenge for designing and engineering particle-decorated liquid surfaces capable of responding to external stimuli, such as in the emerging field of structured liquids (Ghaffarkhah et al., 2024), or more broadly in applications where external deformations of the nanoparticle monolayer may induce particle adsorption or desorption. Thus, an in-depth understanding of particle adsorption kinetics is essential to optimize the response rate to external signals. In recent decades, important information on nanoparticle adsorption kinetics and reconfiguration has been obtained by employing real-space investigations using optical microscopy (Chai et al., 2020) or indirect techniques such as tensiometry (Garbin et al., 2012; Jafarlou et al., 2021) and interfacial rheology (Liggieri et al., 2011). However, while optical microscopy studies have provided information on the structural evolution

of monolayers over time during microparticle adsorption, indirect techniques can only provide a macroscale view of the interface, offering no insight into the nanoscale assembly and reorganization of nanoparticles at interfaces. Furthermore, Eftekhari et al., 2024 recently observed that surfactant-decorated nanoparticles form variable-density monolayers at the air/water interface without reducing surface tension. This hinders the possibility of using these conventional investigative methodologies without ambiguous interpretations.

In this perspective, GISAXS may overcome these limitations by providing sub-nm structural information on the assembly of nanoparticles at the air/water interface (Vorobiev et al., 2015). These measurements might also be performed with high temporal resolution, thanks to the fast response rate of 2D X-ray detectors. However, GISAXS experiments at liquid interfaces are generally performed with synchrotron radiation, and thus the associated safety and technical requirements, namely the safety search and the sample alignment, do not allow for investigating the nanoparticle adsorption occurring in the first minutes after the sample preparation.

In this chapter, a new experimental methodology that overcomes the practical limitations imposed by synchrotron-radiation experiments will be discussed, allowing us to follow the real-time surfactant-induced nanoparticle adsorption at the air/water interface with GISAXS. This new approach consists of spreading, with a remotely-controlled syringe (please refer to Section A.1 for further details), the surfactant solution on the pre-aligned nanoparticle dispersion. We used this methodology on a model system consisting of negatively charged silica nanoparticles, which are known to adsorb at the air/water interface upon the addition of a cationic surfactant such as DTAB and CTAB (A. Maestro et al., 2012). We employed monodisperse NPs having a diameter of approximately 25 nm, ensuring good GISAXS contrast and high sensitivity to any variation in the interparticle distance (Ruffino et al., 2022). We will demonstrate that the obtained GISAXS patterns evolution with time is diagnostic of the formation of a nanoparticle monolayer having progressively increasing surface density. The direct comparison of surface tension and GISAXS pattern temporal evolution will shed further light on the mechanism behind the role played by the surfactant in promoting the nanoparticle adsorption. Finally, we will perform, for the first time, the out-of-equilibrium thermodynamic analysis, in terms of the steady-state nanoparticle surface excess, and kinetic analysis of the nanoparticle adsorption process and the role played by both surfactant and ionic strength.

2.1 Results and Discussion

Figure 2.1 shows the evolution of the surface pressure following the spreading of equal volumes of CTAB solutions at various concentrations onto the aqueous subphase. These concentrations were selected to yield final bulk surfactant concentrations of 10^{-6} M, 4×10^{-6} M, and 10^{-5} M upon complete dissolution in the aqueous phase (see Section A.1 for further details). Throughout the manuscript, these bulk surfactant concen-

trations are used as references. The concentrations were chosen to maximize nanoparticle adsorption (Ruffino et al., 2022) while minimizing the adsorption of free surfactant molecules (Eftekhari et al., 2024). As a result, the maximum density of surfactant per nanoparticle area reached is 0.043 nm^{-2}, significantly lower than the critical surfactant-to-NP ratio of 0.6–0.74 nm^{-2} required to saturate the NP surface and initiate free surfactant adsorption (Eftekhari et al., 2024).

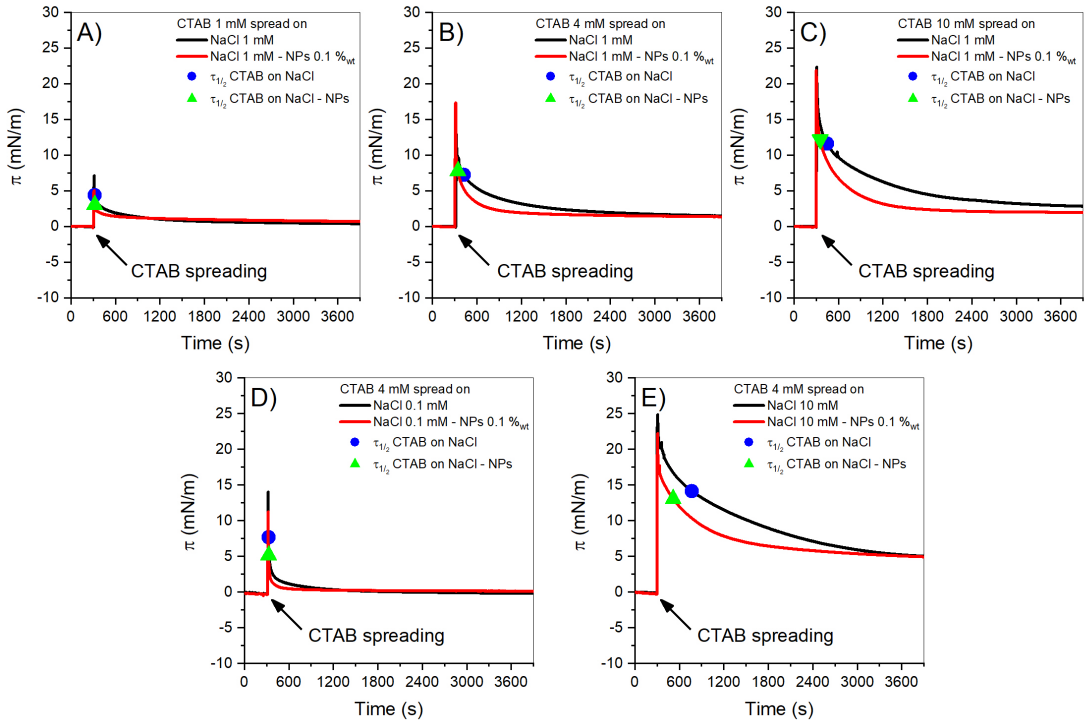

Figure 2.1: *Surface pressure variations with time upon spreading of 375 µL of CTAB solution (see arrow) having concentration equal to 1 mM (A), 4 mM (B, D, E), 10 mM (C) on NaCl solutions (black curves) and on dispersions containing NaCl and 0.1 %wt of silica nanoparticles (red curves). The NaCl concentration was 1 mM in A, B and C, 0.1 mM in D and 10 mM in E. The final CTAB bulk concentration is 10^{-6} M in A, $4x10^{-6}$ M in B, D and E, and is 10^{-5} M in C. The blue circles and green triangles are placed halfway between the maximum surface pressure value and the lowest final one for CTAB solutions spread on NaCl solutions and on mixed NaCl/silica nanoparticles dispersions, respectively.*

When a water-soluble surfactant is deposited onto a water surface, spreading occurs within seconds (K. Lee et al., 2007). Accordingly, as shown in Figure 2.1, the surface pressure rapidly rises to a peak due to the formation of a dense surfactant layer, then gradually decreases over 10–10^3 seconds as the surfactant dissolves into the subphase. The characteristic time to reach a surface pressure midway between the maximum and final values (denoted $\tau_{1/2}$ in Figure 2.2) increases with CTAB concentration (Figure 2.2*A*), reflecting both higher initial surface pressures and a greater number of molecules dissolving. Additionally, $\tau_{1/2}$ increases with ionic strength (Figure 2.2*B*), supporting the notion that surfactant dissolution governs surface pressure dynamics. In fact, the presence of salt screens electrostatic repulsion between surfactant headgroups, thereby stabilizing the interfacial layer (Eftekhari et al., 2020). In the

presence of nanoparticles, the surface pressure decreases faster, but $\tau_{1/2}$ retains the same dependence on CTAB concentration and ionic strength. This likely results from a lower probability of CTAB resorption after dissolution. Dissolved CTAB interacts with negatively charged silica nanoparticles, reducing its chemical potential in bulk. Furthermore, silica nanoparticles spontaneously adsorb to the air–water interface even at very low CTAB concentrations (Ruffino et al., 2022; Li-Destri et al., 2019). Although this adsorption does not significantly raise surface pressure, it reduces the available interfacial area, thereby lowering the probability of further CTAB adsorption.

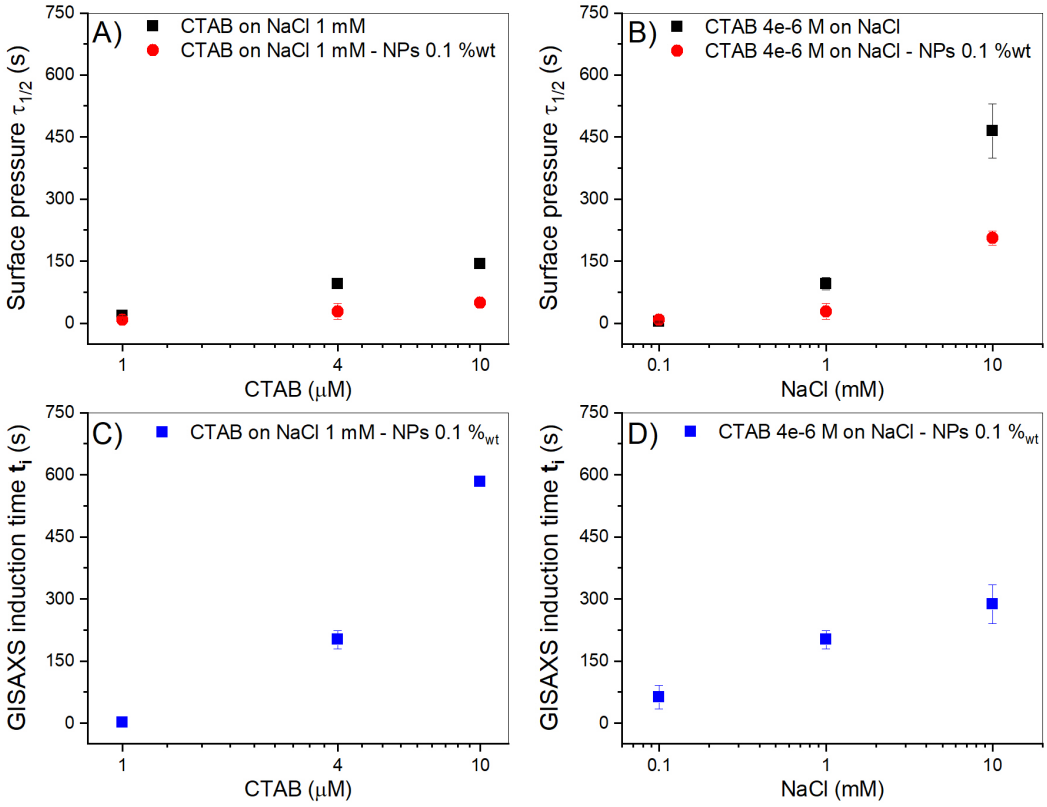

Figure 2.2: *Time after spreading required to reach a surface pressure value halfway between the maximum one and the lowest final one ($\tau_{1/2}$ for CTAB spread on NaCl solutions (black squares) and on dispersions containing NaCl and 0.1 %wt of silica nanoparticles (red circles) as a function of the final CTAB bulk concentration (A) and of the ionic strength (B). Time required for the appearance of the first Bragg GISAXS rods upon spreading CTAB solutions as a function of the final CTAB bulk concentration (C) and of the ionic strength (D). In A and C the bulk ionic strength of NaCl is 1 mM, while in B and D, the final CTAB bulk concentration is 4x10^{-6} M.*

Following surfactant spreading, nanoparticle adsorption at the air–water interface was monitored via Grazing Incidence Small Angle X-ray Scattering (GISAXS). The resulting patterns feature two symmetric structure factor rods, indicative of correlated interfacial nanoparticles (Costa et al., 2016) (see Figure 2.3).

Since the position of these rods relates to interparticle distance, the time evolution of the GISAXS pattern (Tomasella et al., 2025) provides insight into both the onset of nanoparticle adsorption and the increase in NP surface density. By considering the hexagonal packing, the structure factor rod position (q_c) can be related to the interpar-

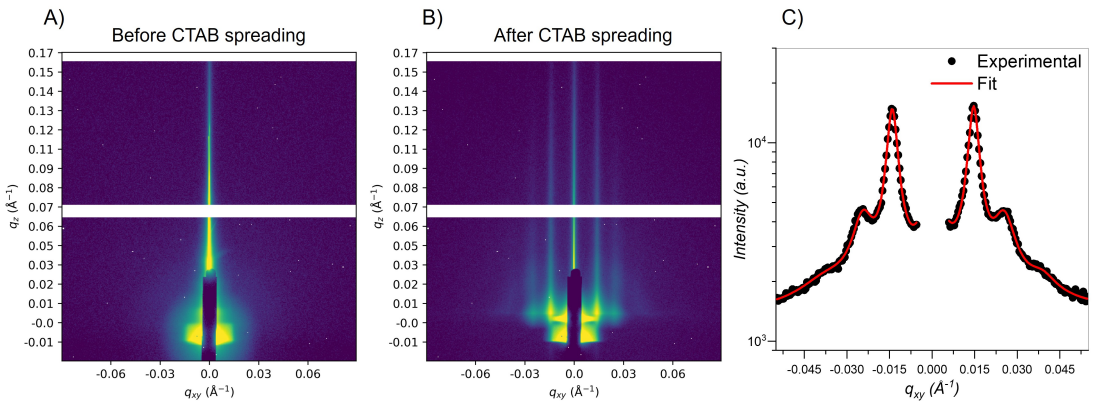

Figure 2.3: *GISAXS pattern of the NP dispersion before (A) and after (B) CTAB spreading. The absence of diagnostic structure factor rods in (A) demonstrates that i) the surfactant is indispensable to promote the NP adsorption and ii) the NP is of high purity, no contaminants promoting the NP adsorption are present. In C it is reported an exemplificative GISAXS experimental cut (black dots) with the corresponding fit (red curve). Please refer to the Section A.1 and Appendix G for further details.*

ticle spacing (d) through the following relationship:

$$d = \frac{4\pi}{q_c\sqrt{3}} \tag{2.1}$$

By fitting the time-resolved 1D GISAXS patterns profiles (see Section A.1 for details), the evolution of interparticle distance over time was obtained. In Figure 2.4, the time-dependent interparticle distance is shown together with the dynamic surface tension, illustrating that variations in surface tension do not directly reflect the assembly of nanoparticles at the air–water interface.

For negatively charged silica nanoparticles to adsorb, appropriate additives must be introduced to render the particles surface-active and to overcome electrostatic repulsion due to the interfacial image charges (Hatlo et al., 2008). In this context, the lack of GISAXS signals prior to CTAB addition (Figure 2.3) confirms the absence of contaminants and demonstrates that nanoparticle adsorption is solely driven by interactions with the CTAB.

After the CTAB spreading, GISAXS rods become visible after a concentration-dependent induction time (t_i), as shown in Figure 2.2 and 2.4. This induction time increases with both CTAB concentration and ionic strength, indicating that a dense interfacial CTAB layer initially inhibits nanoparticle adsorption. Adsorption occurs only after a sufficient amount of CTAB has dissolved, freeing up interfacial area. The trend in t_i closely mirrors that of $\tau_{1/2}$, despite t_i is consistently longer, especially at higher CTAB concentrations. While $\tau_{1/2}$ reaches its maximum at high ionic strength, t_i peaks at high CTAB concentrations, suggesting that more surfactant must dissolve before nanoparticle adsorption can begin.

Further insight is provided by the surface tension values measured at the onset of GISAXS rod appearance. Except in the case of the highest ionic strength, nanopar-

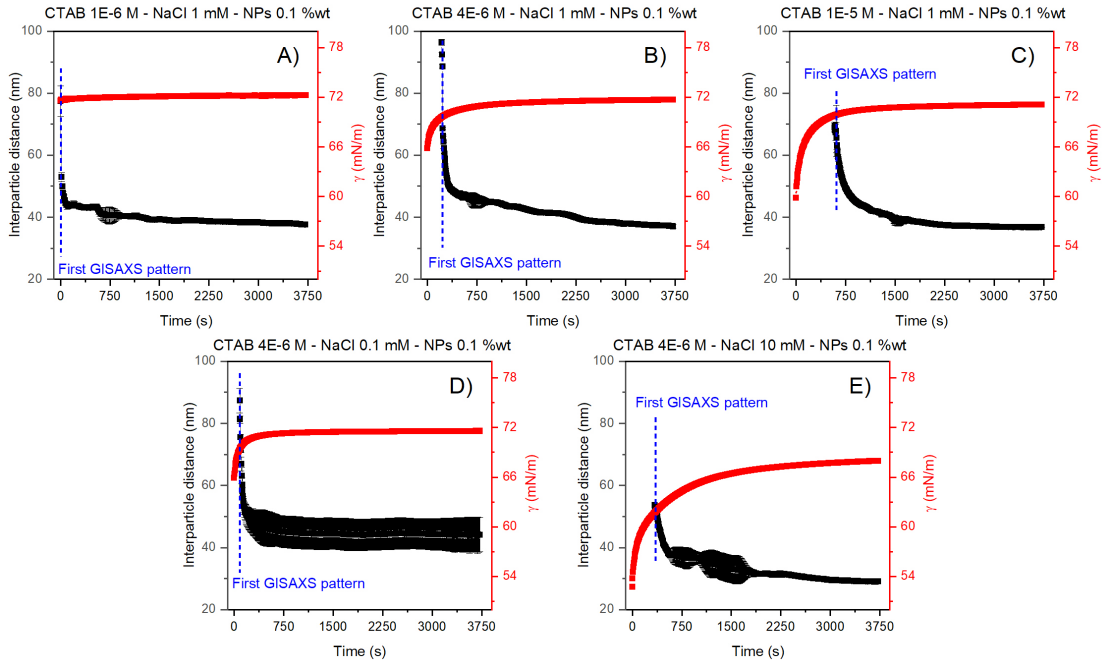

Figure 2.4: *Surface tension evolution with time (red curves) upon spreading of 375 µL of CTAB solution having concentration equal to 1 mM (A), 4 mM (B, D, E), 10 mM (C) on dispersions containing NaCl and 0.1 %wt of silica nanoparticles. Interfacial silica NP inter-particle distance variation with time (black curves) upon spreading of 375 µL of CTAB solution having concentration equal to 1 mM (A), 4 mM (B, D, E), 10 mM (C) on dispersions containing NaCl and 0.1 %wt of silica nanoparticles. The final CTAB bulk concentration is 10^{-6} M in A, $4x10^{-6}$ M in B, D and E, and 10^{-5} M in C. The ionic strength is 1 mM in A, B and C, 0.1 mM in D and 10 mM in E.*

ticles begin to adsorb only when the surface tension is $\gtrsim$ 70 mN/m, indicating that CTAB forms only a sparse layer at the interface. This supports the idea that CTAB primarily facilitates nanoparticle adsorption through direct bulk interactions, forming amphiphilic, surfactant-coated nanoparticles (A. Maestro et al., 2012).

However, prior studies conducted by C. Li et al. (2020) proposed that at low CTAB concentrations, adsorption of free cationic surfactant at the interface could screen the negative charge of the water surface (Mishra et al., 2012), thereby enabling the adsorption of negatively charged nanoparticles. In such cases, where electrostatic screening drives adsorption without direct NP-surfactant interaction, CTAB is described as a promoter. Conversely, when adsorption involves direct surfactant-NP interactions forming amphiphilic particles, CTAB acts as a modifier. The current findings, together with prior work on surfactant effects on interfacial interparticle repulsions (Ruffino et al., 2022), indicate that CTAB functions as a modifier across all concentrations tested. Although electrostatic screening by NaCl (present in mM amounts) is more efficient than the CTAB (Figure A.2), salt alone is not sufficient to induce NP adsorption (Figure 2.3). Thus, even at μM concentrations, CTAB enhances nanoparticle surface activity and acts as a true modifier.

As nanoparticle adsorption progresses, the number of particles at the interface increases, leading to a gradual decrease in interparticle distance. A similar experiment

was carried out using DTAB. However, due to its higher solubility, compositional inhomogeneities arose in both the bulk and interfacial phases (K. Lee et al., 2007), resulting in inconsistent and non-systematic variation in interparticle spacing with time (Figure A.3).

Notably, the interparticle distances measured one hour after CTAB spreading are systematically shorter than those observed in monolayers formed from "mixed" dispersions, i.e., dispersions containing both NP and CTAB from the beginning. Nonetheless, both sets of data show the same dependence on bulk CTAB concentration (Ruffino et al., 2022) and ionic strength (Figure A.4). Since the adsorbed NP are not at equilibrium in either case, the discrepancy probably arises from kinetic factors. We hypothesize that the method of monolayer formation influences the final number of adsorbed nanoparticles. In particular, CTAB spreading may lead to an inhomogeneous assembly process, with NP domains characterized by reduced interparticle spacing. Evidence for domain formation comes from measurements of interparticle distance under lateral compression (Figure A.5). While monolayers formed from "mixed" dispersions display a continuous, linear decrease in inter-particle distance with compression, those formed by CTAB spreading exhibit step-like variations and discontinuities, indicative of a non-uniform NP distribution at the interface.

To gain quantitative physicochemical insight, we calculated the nanoparticle surface excess, Γ, by converting the time-dependent interparticle distance (d) using the following equation:

$$\Gamma = \frac{N_{NP}}{A} = \frac{\frac{A}{A_{NP}}}{A} = \frac{1}{A_{NP}} = \frac{1}{\pi(\frac{d}{2})^2} \tag{2.2}$$

Here, A is the macroscopic trough area, N_{NP} is the number of adsorbed nanoparticles, and A_{NP} is the average area per nanoparticle, approximated as circular.

The resulting time evolution of the surface excess is shown in Figure 2.5, where each curve represents an average of at least two independent experiments. The surface excess evolution with time reveal two distinct adsorption regimes, accounting for two different adsorption mechanisms. In the early stage (approximately the first 100 seconds), the surface excess increases linearly with the square root of time, indicative of a diffusion-controlled adsorption regime (Ter Minassian-Saraga, 1956). This regime can be described by the equation:

$$\Gamma(t) = D_{\text{app}}\sqrt{t} + c \tag{2.3}$$

where D_{app} is the apparent diffusion coefficient and c is the surface excess at $t = 0$. Fitting this expression to the experimental data allows extraction of D_{app}, which is found to increase with CTAB concentration, while remaining relatively unaffected by ionic strength (Table 2.1). Noteworthy, the parameter c offers limited physical meaning in this context, as GISAXS rods only appear at $t > 0$. Consequently, fitting often yields negligible or non-physical (negative) values for c.

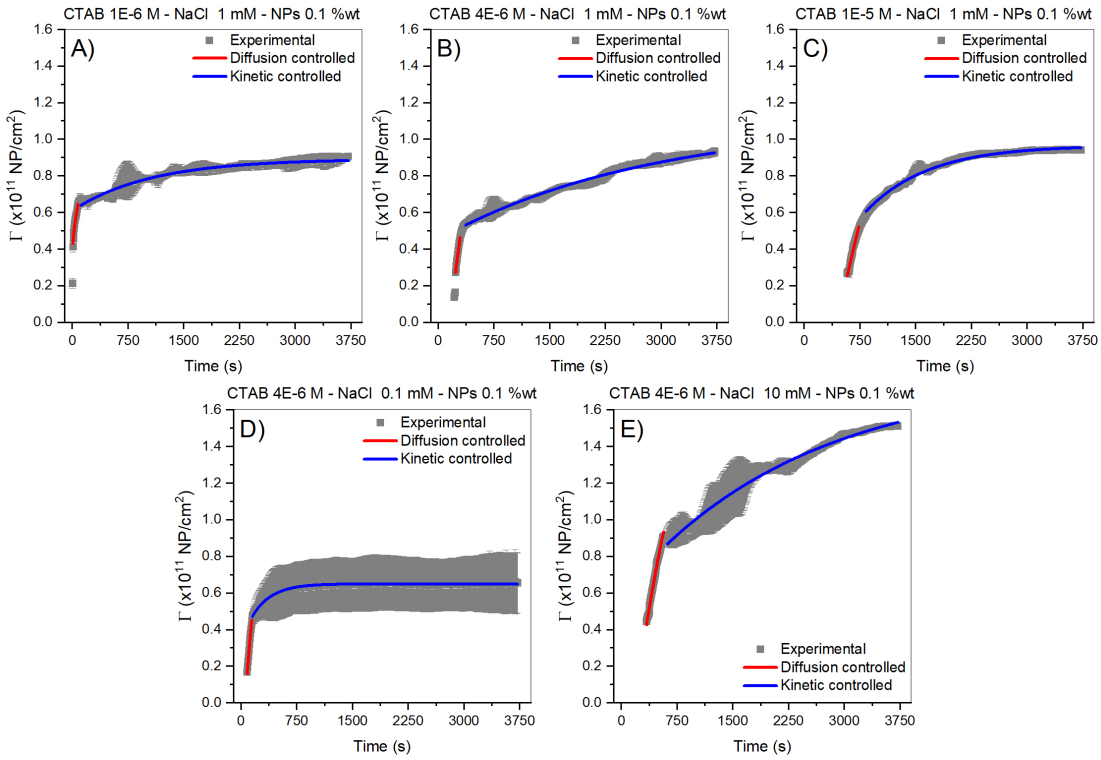

Figure 2.5: *Nanoparticle surface excess evolution with time (grey squares) upon spreading of 375 µL of CTAB solution having concentration equal to 1 mM (A), 4 mM (B, D, E), 10 mM (C) on dispersions containing NaCl and 0.1 %wt of silica nanoparticles. The final CTAB bulk concentration is 10^{-6} M in A, $4x10^{-6}$ M in B, D and E, and 10^{-5} M in C. The ionic strength is 1 mM in A, B and C, 0.1 mM in D and 10 mM in E. The red curves are the results of the diffusion-based fitting, with equation $\Gamma(t) = D_{app} * \sqrt{t} + c$, while the blue curves arise from the kinetics-based fitting, with equation $\Gamma(t) = y_0 + A(1 - e^{-kt})$.*

Interestingly, the trend observed for D_{app} is opposite to that obtained from bulk diffusion measurements via Dynamic Light Scattering (DLS) reported in Figure A.2. This suggests that, during the initial adsorption stage, the process is governed not by nanoparticle diffusion but by CTAB back diffusion from the interface to the bulk. Since diffusion depends on the concentration of the diffusing species, higher CTAB concentrations near the interface lead to increased D_{app}. However, as previously shown, nanoparticle adsorption begins only when the surface concentration of CTAB is low. Therefore, under the different experimental conditions tested, the interfacial CTAB density should remain fairly constant at the onset of NP adsorption, while the subsurface CTAB concentration may vary significantly. This implies that the rate-limiting step in the early regime is the formation of surface-active, surfactant-decorated nanoparticles, dependent on CTAB diffusion from the subsurface to the bulk. This further supports CTAB role as a modifier.

The second, slower adsorption stage follows a first-order kinetic model, well described by the exponential function:

$$\Gamma(t) = y_0 + A\left(1 - e^{-kt}\right) \tag{2.4}$$

Table 2.1: *Parameters obtained from the fit of the experimental curves of the surface excess.*

	First adsorption step [a]		Second adsorption step [b]		
Sample	D_{app} $(\times 10^{11} NP/cm^2 s^{1/2})$	R_a^2	Γ_∞ $(\times 10^{11} NP/cm^2)$	k_{kin} $(\times 10^{-4}\ s^{-1})$	R_b^2
CTAB 1E-6M – NaCl 1mM – NPs 0.1%wt	0.039±0.001	0.996	0.089±0.005	9.5±0.2	0.999
CTAB 4E-6M – NaCl 0.1 mM – NPs 0.1%wt	0.103±0.001	0.999	0.649±0.006	38.9±0.4	0.991
CTAB 4E-6M – NaCl 1mM – NPs 0.1%wt	0.102±0.001	0.999	1.305±0.026	2.2±0.1	0.984
CTAB 4E-6M – NaCl 10mM – NPs 0.1%wt	0.094±0.001	0.996	1.781±0.018	4.2±0.1	0.988
CTAB 1E-5M – NaCl 1mM – NPs 0.1%wt	0.088±0.002	0.987	0.965±0.001	11.9±0.1	0.989

[a] Fit parameters obtained from Equation 2.3
[b] Fit parameters obtained from Equation 2.4 and 2.5

Here, k is the kinetic rate constant, y_0 is the surface excess at $t = 0$ (for this stage), and A is the increase in surface excess during this phase. Thus, the steady-state surface excess can be obtained as follows:

$$\Gamma_\infty = y_0 + A \tag{2.5}$$

Values of Γ_∞ as functions of CTAB concentration and ionic strength are shown in Figure 2.6. To our knowledge, this constitutes the first quantitative experimental investigation into how composition and ionic strength affect the final density of nanoparticle monolayers.

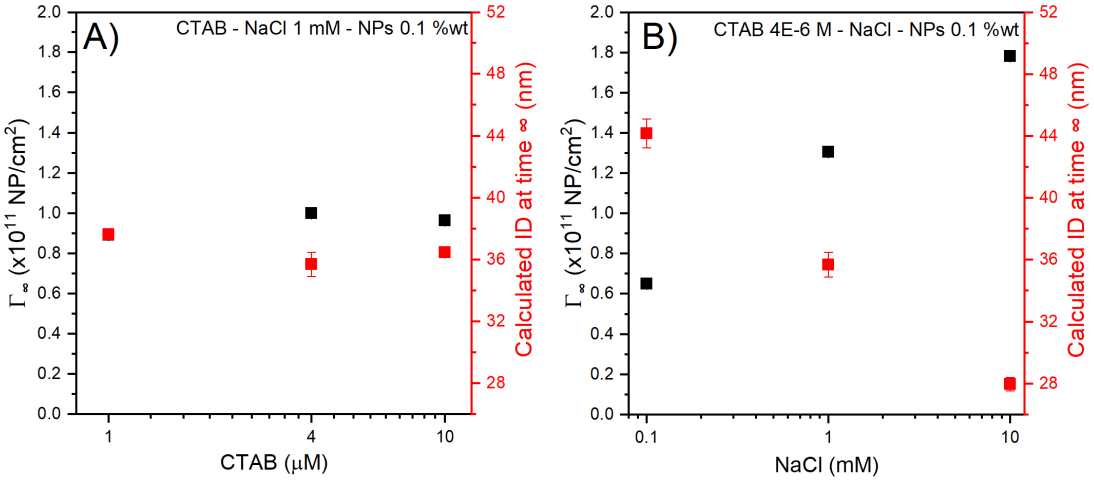

Figure 2.6: *Nanoparticle surface excess at an infinite time (black squares) and the corresponding interparticle distance (red squares) as a function of the CTAB bulk concentration (A) and of the ionic strength (B).*

CTAB concentration has only a modest effect on the final number of adsorbed nanoparticles, which remains in the range of 9.0×10^{10} to 1.0×10^{11} particles/cm^2. In contrast, ionic strength significantly influences the monolayer density, varying from $\sim 6 \times 10^{10}$ to 1.8×10^{11} particles/cm^2. This suggests that interfacial repulsions, rather than amphiphilicity, predominantly determine NP coverage.

At low ionic strengths, the interparticle separations are ~20–10 nm, while 10 mM NaCl reduces them to ~2 nm (Figure 2.6). These distances, calculated from Γ_∞ via

Equation 2.5, are larger than the mean NP diameter, validating the physical meaning of the model.

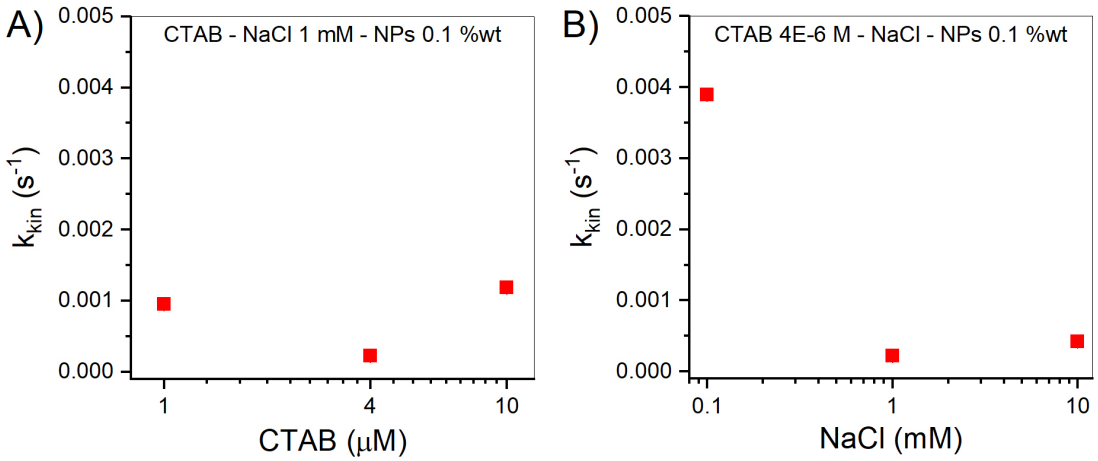

Figure 2.7: *Adsorption kinetic constant obtained from the fitting with Equation 2.4 as a function of the CTAB bulk concentration (A) and of the ionic strength (B).*

The effect of ionic strength is easily appreciable also in the kinetics of the second adsorption phase. Figure 2.7 shows that k is highest at low ionic strength, where weak screening allows long-range electrostatic repulsions to dominate, resulting in early arrest of adsorption. As ionic strength increases, k decreases by roughly one order of magnitude. The relationship between k and CTAB concentration is less straightforward, exhibiting a minimum at intermediate concentrations. At low CTAB levels, fewer decorating molecules lead to stronger repulsions and early arrest. At high concentrations, better NP decoration enhances surface activity, promoting faster adsorption kinetics.

2.2 Conclusion

We have established a GISAXS-based strategy capable of monitoring, in real time, the irreversible adsorption of surfactant-decorated nanoparticles, overcoming the intrinsic limitations of conventional indirect techniques (Jafarlou et al., 2021; Eftekhari et al., 2024). This method is based on the spreading of a cationic surfactant onto pre-aligned dispersions that already contain nanoparticles. By combining GISAXS with DST measurements, we demonstrate that nanoparticle adsorption begins only after most of the spread surfactant has dissolved. These findings reinforce the interpretation that, even at μM concentrations, the surfactant binds directly to the nanoparticles, acting as a true modifier rather than merely a promoter that screens electrostatic repulsion (C. Li et al., 2020).

For the first time, the time-resolved surface excess profiles of adsorbed nanoparticles enabled a quantitative determination of the steady-state surface excess (Γ_∞). This quantity was shown to be primarily governed by ionic strength, highlighting that while nanoparticle amphiphilicity induced by the interaction with the surfactant is crucial to

enable adsorption, the extent of adsorption is primarily dictated by interfacial electrostatic repulsions. Accordingly, these repulsive forces also determine the timescale for adsorption arrest, which becomes shorter as the repulsions grow stronger.

3

Effect of Ion Valence on Nanoparticle-Laden Interfaces

The study of specific ion effects (SIE) in colloidal and interfacial systems can be traced back to the pioneering work of Franz Hofmeister in 1888, who first demonstrated that different ions can have dramatically distinct impacts on protein solubility and interfacial phenomena (Hofmeister, 1888). Since then, interest in understanding how the chemical identity of ions influences interfacial behavior has steadily grown, revealing that electrolyte effects cannot be explained solely by bulk ionic strength. In the traditional frameworks of the DLVO theory, ions are treated as point charges (Debye, 1923); due to this, the theory often fails to capture the non-additive and non-linear effects arising from multivalent ions, where charge correlations, ion bridging, and specific adsorption play significant roles (Silvera Batista et al., 2015; Quesada-Pérez et al., 2004; Cacace et al., 1997; Hunger et al., 2022).

Understanding how different ionic compositions modulate interparticle forces is not only of fundamental scientific interest but also has practical implications in numerous fields where colloidal behavior is highly sensitive to electrolyte composition. Examples include water treatment, where multivalent cations are known to induce rapid flocculation (S. Lee et al., 2007; H. Lee et al., 2021), fertilizers (Fageria et al., 2009), batteries (Aurbach et al., 2004), emulsions (Frith et al., 2008), foam (Gao et al., 2015), coating (Jeschull et al., 2024), enhanced oil recovery (EOR) (ShamsiJazeyi et al., 2014) where electrolyte composition directly affects interfacial stability and particle assembly, and even biological systems, where ion specificity influences protein and membrane interactions (Vasquez-Montes et al., 2022) or nanoparticle behavior in biological systems (Carrillo-Carrion et al., 2014).

In this perspective, we decided to focus our attention on the behavior of nanoparticles (NPs) at fluid interfaces in the presence of monovalent and multivalent cations. In fact, while the effect of ionic strength and ion charge on colloidal stability has been extensively investigated in bulk suspensions (López-León et al., 2003; Alkan et al., 2005),

comparatively few studies have examined how ionic strength and specific cation identity and valence modulate nanoparticle interactions once adsorbed at fluid interfaces (Asao et al., 2016; Kirby et al., 2018; Matheus et al., 2016).

This chapter aims to fill a critical gap in the literature by providing one of the first systematic experimental investigations into how both ionic strength and cation valence influence nanoparticle interaction potentials in interfacial monolayers, an area that remains underexplored compared to bulk colloidal systems. We investigated the impact of three representative cations, K^+, Ca^{2+}, and La^{3+}, on nanoparticle assembly and interactions at fluid interfaces. The choice of these salts, namely KCl, $CaCl_2$ and $LaCl_3$, was motivated by several reasons. First, they have been extensively studied in bulk colloidal systems, providing a robust reference framework from the literature to identify possible discrepancies or confirm observed behaviors also at the interface (Son et al., 2015; Z. Liu et al., 2020). Moreover, they are all highly soluble in the tested concentration range (Charykov et al., 2021), do not induce hydrolysis under the experimental neutral pH conditions used, and do not undergo complex speciation in solution (Hinz, 2015; Meier et al., 1990). This ensures that variations in interparticle interactions can be confidently attributed to ion valence and ionic strength, rather than pH fluctuations, precipitation, or secondary chemical reactions.

3.1 Results and Discussion

The investigation of the valence-dependent specif ion effect (SIE) and the effect of the bulk ionic strength on the assembly of silica nanoparticles (NPs) at the air-water interface was carried out by using cations with increasing charge, namely K^+, Ca^{2+} and La^{3+}, obtained by the corresponding chloride salts, at ionic strength of 0.1, 1, and 10 mM.

The mixed CTAB-NP-salt solutions were poured into a Langmuir trough and let equilibrate for 30 minutes to ensure the complete formation of the nanoparticle layer at the air-water interface as already demonstrated elsewhere (Li-Destri et al., 2019). After this equilibration time, the formation of a nanoparticle monolayer was confirmed by GISAXS. In Figure 3.1 is reported an example of a 2D GISAXS pattern and the corresponding horizontal cut (see Section B.1 for further details), showing the characteristic Bragg peaks associated with the formation of a hexagonally packed NP monolayer. The 2D GISAXS patterns of the monolayer under all investigated bulk conditions are shown in Figure B.2, B.3, and B.4.

The main Bragg peak position (q_c) in reciprocal space is related to the interparticle distance in real space, as described in Equation G.14 and further detailed in Section G.3. From the interparticle distance values, the nanoparticle surface excess at steady-state can be estimated using Equation 2.2. The resulting surface excess values are shown in Figure 3.2.

A clear linear positive correlation is observed between surface excess and both the ionic strength of the bulk solution and the nominal cation charge. This indicates that

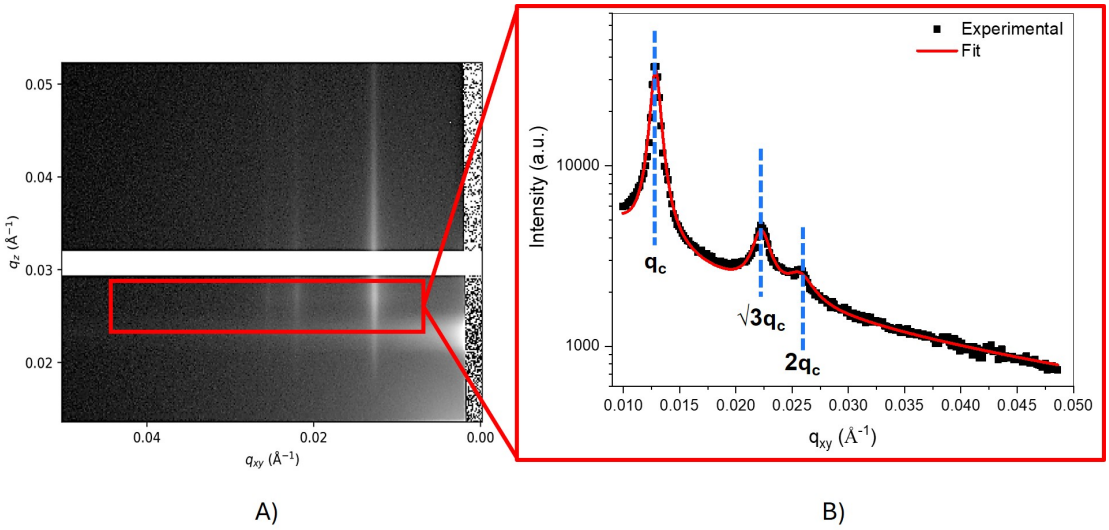

Figure 3.1: *A) Example of 2D GISAXS pattern associated with the formation of silica nanoparticle monolayer at the air-water interface. B) Horizontal cut obtained by the integration of the scattering intensity along q_z in the range 0.0237- 0.0291 Å^{-1} defined inside the red box. The pattern clearly shows three intense Bragg peaks at the position q_c, $\sqrt{3}q_c$ and $2q_c$ associated with the formation of a hexagonally packed nanoparticle monolayer. Black squares are the experimental value and the red line is the associated fitting (detailed information can be found in Section B.1).*

increasing either parameter leads to the formation of denser nanoparticle monolayers. Regarding the dependence on ionic strength, an increase in this parameter leads to a higher nanoparticle monolayer density, with a particularly strong effect observed in the case of KCl.In fact, while the surface excess increases from approximately 3.8×10^{10} NP/cm^2 at 0.1 mM to about 1.2×10^{11} NP/cm^2 at 10 mM, and thus showing a 3-fold increase in monolayer density, in the presence of $CaCl_2$ and $LaCl_3$, the increase in monolayer density with ionic strength is smoother (Figure 3.2*A*), showing only a ~ 1.3-fold and ~ 1.2-fold increase, respectively, going from 0.1 mM to 10 mM. This different effect of ionic strength can be attributed to the specific role of the cation species. The more pronounced increase in monolayer density observed for KCl compared to $CaCl_2$ and $LaCl_3$ is related to the fact that, at a given ionic strength, divalent and trivalent cations already promote the formation of denser monolayers. For example, at an ionic strength of 0.1 mM, the monolayer density increases by a factor of approximately 3.7 when moving from K^+ to La^{3+} (Figure 3.2*B*).

As a result, in the presence of Ca^{2+} and La^{3+}, the monolayers are already tightly packed even at low ionic strength, limiting the extent to which further increases in ionic strength can enhance packing. Conversely, for K^+, the initial monolayer density is lower, allowing a more pronounced effect of the increasing ionic strength on the final monolayer density. As a proof of that, it can be observed that at the higher ionic strength, 1 mM and 10 mM, also the cation charge effect became smoother, producing respectively a ~2-fold and ~1.5-fold peaking density increase moving from KCl to $LaCl_3$.

From a theoretical perspective, the effect of ionic strength on monolayer density

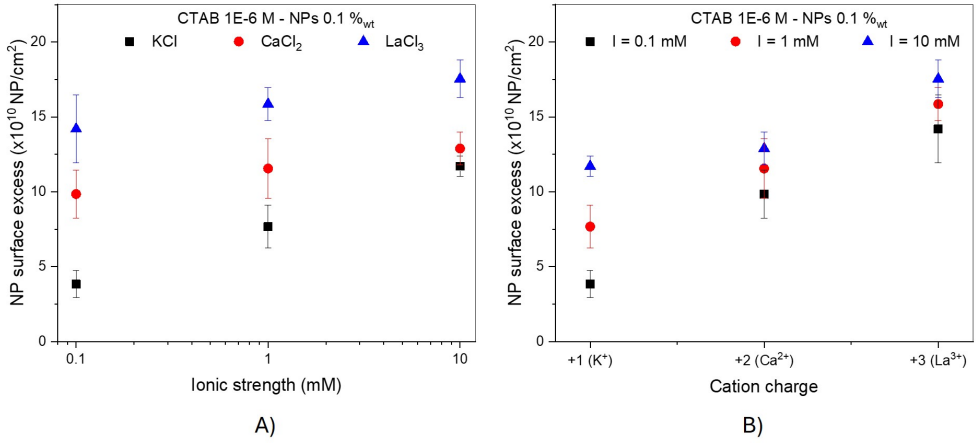

Figure 3.2: *Nanoparticle surface excess after 30 minutes for monolayer equilibration as function of A) the bulk ionic strength and B) the cations nominal charge. The bulk concentration was* $1 \times 10^{-6} M$ *in CTAB and* $0.1\%_{wt}$ *in nanoparticles for all the tested conditions.*

can, in the first instance, be attributed to the electrostatic screening of the nanoparticle surface charge, in agreement with DLVO theory (B. V. Derjaguin et al., 1987; J. N. Israelachvili, 2011). Increasing the ionic strength of the solution leads, on one hand, to a reduction in repulsive electrostatic interactions (Williams et al., 1992), and on the other, to the screening of interfacial image charges (Hatlo et al., 2008). Both effects act cooperatively to facilitate the trapping of a greater number of nanoparticles at the interface.

Conversely, the cation charge effect cannot be addressed within the framework of classical DLVO theory as extensively described in the introduction to this chapter. Thus, specific non-DLVO interactions between the multivalent cations and the silica nanoparticle surface must be taken into account. As already demonstrated elsewhere, multi-charged cations can interact specifically with deprotonated $Si{-}O^-$ moieties exposed on the silica surface, often leading to the covalent coordination of the cations (Dishon et al., 2011; Z. Liu et al., 2020). This causes the decrease in the electrostatic repulsive interactions between particles not because of the increased electrostatic screening due to the Electric Double Layer compression, as the DLVO would predict, but rather because of the neutralization of the surface charge (J. N. Israelachvili, 2011; Hsu et al., 1997).

To evaluate whether these previously observed phenomena also apply to our system, the electrophoretic mobility (μ_e) of the silica nanoparticles in the presence of 1μM of CTAB and different salts and ionic strengths was investigated. The results are reported in Figure 3.3.

The electrophoretic mobility evolution with the increase in the suspension ionic strength shows the expected trend. Higher salt concentrations induce the lowering of the effective nanoparticle potential (Figure 3.3*A*). However, the most remarkable effect comes out by comparing the NP electrophoretic mobility as a function of the cation

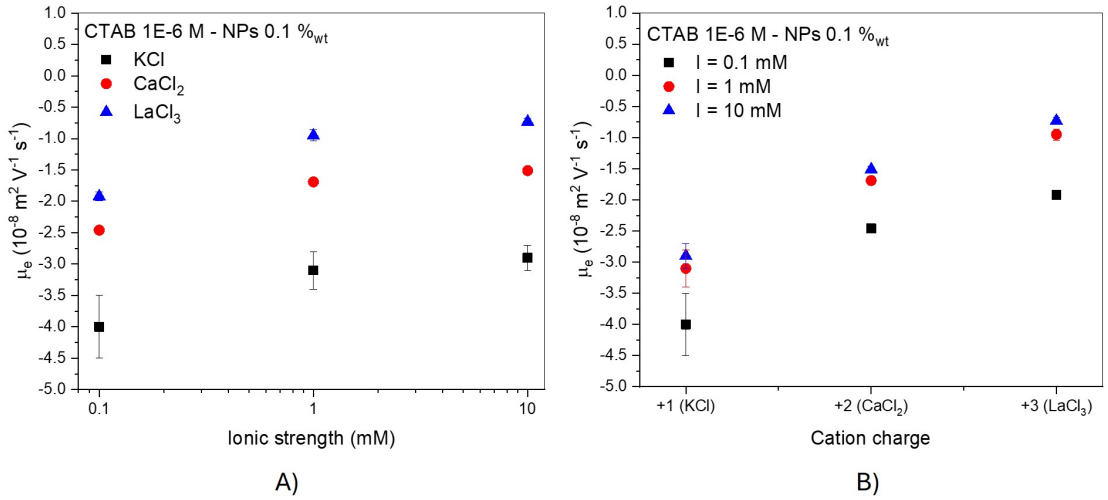

Figure 3.3: *Evolution of the nanoparticle electrophoretic mobility (μ_e) in mixed CTAB-NP-salts suspension reported as function of A) the bulk ionic strength and B) the cations nominal charge. The bulk concentration was $1 \times 10^{-6} M$ in CTAB and $0.1\%_{wt}$ in nanoparticles for all the tested conditions.*

charge at fixed bulk ionic strength (Figure 3.3*B*). In fact, multivalent cations, namely Ca^{2+} and La^{3+}, always show a stronger screening of the NP surface charges, inducing a more pronounced decrease (*i.e.*,less negative) in μ_e. This effect is clearly visible even at low ionic strength: for instance, at 0.1 mM, μ_e is –4 $\times 10^{-8} m^2 \cdot V^{-1} \cdot s^{-1}$ in KCl, –2.5 $\times 10^{-8} m^2 \cdot V^{-1} \cdot s^{-1}$ in $CaCl_2$, and –1.9 $\times 10^{-8} m^2 \cdot V^{-1} \cdot s^{-1}$ in $LaCl_3$. Despite the significantly lower cation molar concentrations for the multivalent salts, as it will be discussed below,the NP surface potential is markedly reduced, confirming their stronger charge screening ability of higher valency cations. This trend continues at higher ionic strengths: at 10 mM, μ_e becomes –2.9 $\times 10^{-8} m^2 \cdot V^{-1} \cdot s^{-1}$ in KCl, –1.5 $\times 10^{-8} m^2 \cdot V^{-1} \cdot s^{-1}$ in $CaCl_2$, and as low as –0.7 $\times 10^{-8} m^2 \cdot V^{-1} \cdot s^{-1}$ in $LaCl_3$. This effect, already observed several times in the literature (Dishon et al., 2011; Z. Liu et al., 2020; Hsu et al., 1997), was always associated with the stronger absorption of multi-charge cations to the silica surface compared to monovalent cations (K^+) (Quesada-Pérez et al., 2004; Tiraferri et al., 2015), which induces an actual screening of the NP surface charge (Kobayashi, 2008). The electrophoretic mobility (μ_e) results we obtained are in perfect agreement with the ones reported in the literature, suggesting that the main contribution to the marked differences in the NP surface excess observed has an electrostatic nature.

Moreover, it must be pointed out how the affinity between the NP surface and the cation increases concomitantly with its charge. In fact, by taking into account the relationship between the ionic strength and the actual molar concentration for the various salts, we can calculate the cations molar concentration. By assuming we want to obtain a solution with ionic strength I, the salt concentrations required are $C_{KCl} = I$, $C_{CaCl_2} = I/3$ and $C_{LaCl_3} = I/6$, and so the actual cations concentrations in the suspension are $[K^+] = I$, $[Ca^{2+}] = I/3$ and $[La^{3+}] = I/6$. This demonstrated that, despite the molar concentration of the multivalent cations are always lower than the K^+, their higher affinity with the silica surface, usually associated with the cations chemisorp-

tion rather than a simple physisorption as expected for monovalent species, lead to a stronger surface charge screening effect.

Finally, further support for the above conclusions comes from a qualitative analysis of the GISAXS patterns acquired after 30 minutes for monolayer equilibration, shown in Figure B.2, B.3 and B.4. Specifically, as the ionic strength or cation valency increases, the GISAXS patterns reveal a progressive weakening, and in some cases complete disappearance, of higher-order scattering peaks. These high-order Bragg peaks are clearly observed for KCl at 0.1 mM and 1 mM, as well as for $CaCl_2$ at the same ionic strength, while they disappear at higher ionic strength and for $LaCl_3$. At the same time, a noticeable broadening of the main Bragg peak occurs. Both of these trends indicate a loss of long-range lateral order, which, as previously discussed (Roach et al., 2022), is primarily governed by long-range electrostatic repulsion between the particles.

To further explore whether, beyond the clear electrostatic effects already demonstrated, there could be an additional contribution coming from a specific CTAB-NP interaction, we examined the variation of the surface tension as a function of bulk CTAB concentration. The main motivation behind this analysis was to investigate whether the presence of different salts could alter the amphiphilicity of the system, potentially via specific cation–surfactant interactions that go beyond simple charge screening.

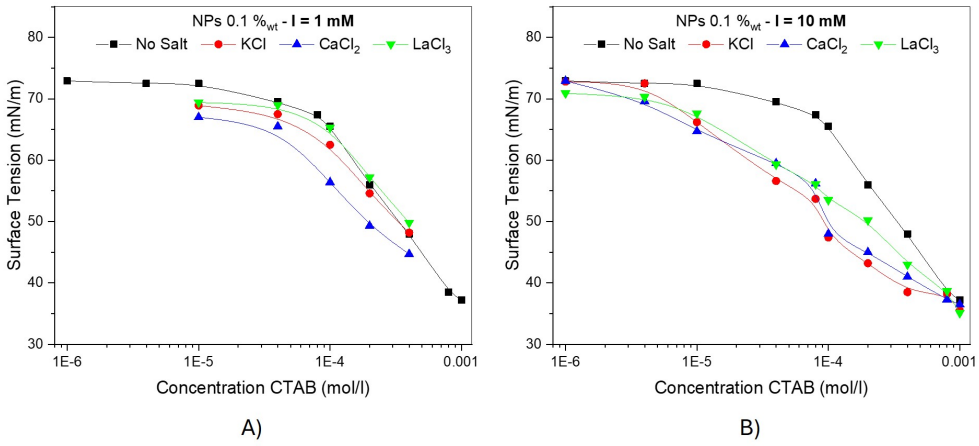

Figure 3.4: *Surface tension variation with respect to the bulk CTAB concentration for suspension contain 0.1 $\%_{wt}$ of silica nanoparticle in the presence of KCl, $cacl_2$ and $lacl_3$ at ionic strength of a) 1 mM and B) 10 mM. Solid lines are included as a guide to the eye only.*

The results reported in Figure 3.4 show a clear trend. In the presence of salt, the surface tension begins to decrease at lower CTAB concentrations compared to salt-free conditions. Moreover, the higher the ionic strength, the more pronounced this decrease becomes. This indicates that the presence of ions facilitates the adsorption of CTAB at the interface. What is particularly interesting, however, is that this trend is largely independent of the cation type. Despite the significant differences in nanoparticle surface excess observed in the previous experiments, the shape and position of the adsorption isotherms seem to be independent of the cation nature at a fixed ionic

strength. This firstly suggests that the NP-CTAB interaction is primarily driven by ionic strength, rather than by any specific interaction mediated by different cations, and secondly that the decrease of the surface tension should be related to the adsorption of free CTAB molecules at the interface. In fact, as previously demonstrated, upon a surfactant threshold concentration we move from a cooperative adsorption regime, where increasing the surfactant concentration promotes the adsorption of an higher number of nanoparticle, to a competitive one characterized by the adsorption of free CTAB molecules that induces a decrease in the nanoparticle surface excess (Ruffino et al., 2022; Eftekhari et al., 2020; Jafarlou et al., 2021).

Furthermore, at the low CTAB concentration used in the GISAXS experiment ($1 \times 10^{-6} M$), the surface tension remained equal to that of the pure air-water interface across all conditions of salts and ionic strength, despite the marked difference in the nanoparticle surface excess. This once again supports what has already been discussed in Chapter 2 and in previous literature (Eftekhari et al., 2024), so that surface tension is not a reliable parameter to obtain quantitative information on the nanoparticle assembly at the air–water interface.

The fact that the surface tension variation shows different trends with increasing ionic strength, but not with cation identity, can be rationalized by considering the stoichiometry of the salts used. Since we used 1:1 (KCl), 1:2 ($CaCl_2$), and 1:3 ($LaCl_3$) electrolytes, achieving the same ionic strength required adjusting the salt concentrations accordingly, as previously explained. As a result, the effective concentration of Cl^- ions in solution remains relatively similar across different salts at a fixed ionic strength, namely $[Cl^-]_{KCl} = I$, $[Cl^-]_{CaCl_2} = 2I/3$ and $[Cl^-]_{LaCl_3} = I/2$. This is a crucial point because it has been shown, somewhat counterintuitively, that increasing ionic strength can enhance CTAB–NP interactions (Siegel et al., 2025; Qazi et al., 2020). This is attributed to the higher concentration of negative ions, which facilitates tighter packing of the cationic surfactant on the NP surface. Therefore, given that the Cl^- concentration is comparable among the different salts at a given ionic strength, it is reasonable to conclude that the observed surface tension trends are not dictated by the nature of the salt, but rather by this common background of ionic strength and anion concentration. Finally, since the bulk Cl^- concentration slightly decreases with increasing cation valence at a fixed ionic strength, if the nanoparticle assembly were driven by chloride ions, the monolayer density would be expected to decrease accordingly.

Further experiments were conducted to investigate the interparticle potential as a function of the in-plane interparticle distance. To this aim, the nanoparticle monolayers were compressed in a Langmuir trough. The compression isotherms reported in Figure 3.5 show the characteristic compression-induced surface pressure increase, which is associated with the work required to bring the nanoparticles closer together, in opposition to the long-range electrostatic repulsion and short-range steric repulsions, induced by the presence of CTAB molecules on the NP surface, acting between them (Li-Destri et al., 2019; Ruffino et al., 2022).

In-depth information on the monolayer structural evolution during compression

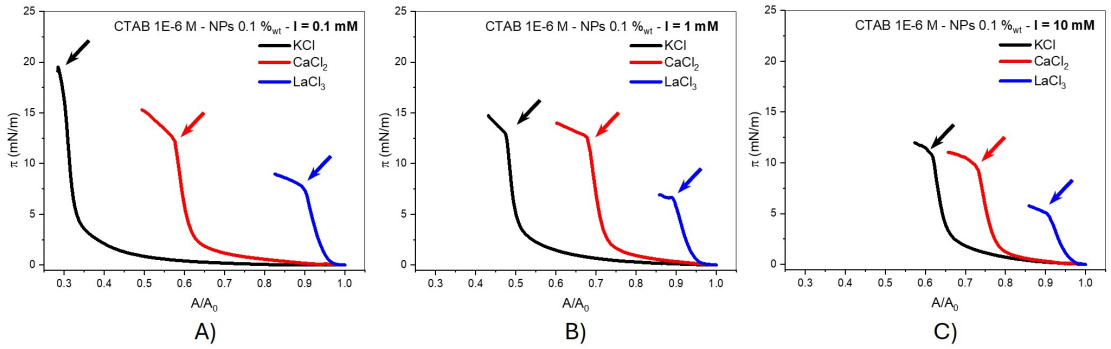

Figure 3.5: *Compression isotherm of CTAB-coated NP monolayer in the presence of KCl (black lines), $CaCl_2$ (red lines) and $LaCl_3$ (blue lines) at the bulk ionic strength of A) 0.1 mM, B) 1 mM, and C) 10 mM. The bulk concentration was $1 \times 10^{-6} M$ in CTAB and $0.1\%_{wt}$ in nanoparticles for all the tested conditions. Arrows indicate the monolayer collapse.*

were obtained by *in-situ* GISAXS experiments. GISAXS allows us to follow the interparticle distance variation within the monolayer during compression and thus, to estimate the number of adsorbed nanoparticles in dynamic conditions. In fact, once obtained the interparticle distance (ID), the number of adsorbed nanoparticles (N_{NP}) can be calculated by considering the macroscopic trough surface area (A) and the NP microscopic area (A_{NP}) with the following equation.

$$N_{NP} = \frac{A}{A_{NP}} = \frac{A}{\pi(\frac{ID}{2})^2} \tag{3.1}$$

where A_{NP} is considered as the circular area of radius equal to half the interparticle distance.

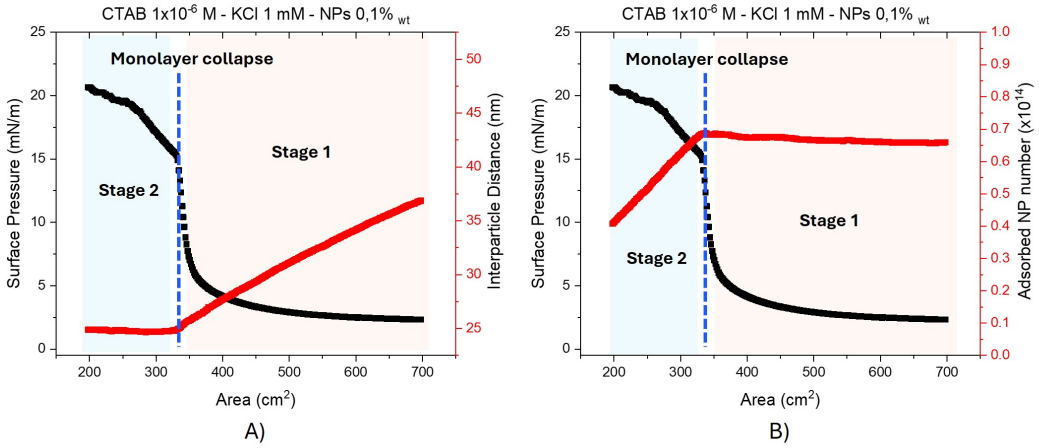

Figure 3.6: *Example of the interparticle distance evolution (red square in A) and the corresponding number of adsorbed nanoparticle (red square in B) together with the associate variation in the surface pressure (black line in A and B).The two characteristic compression stage associated with the formation of a homogeneous irreversibly adsorbed nanoparticle monolayer are highlighted. In **stage 1** the monolayer compression induces a progressive reduction of the in-plane interparticle distance associated with a constant number of nanoparticles. On the contrary, in **stage 2** a constant interparticle distance is associated with a progressive decrease in the nanoparticle number caused by the particle desorption toward bulk, namely the monolayer collapse (vertical dashed blue line).*

An example of a dynamic GISAXS experiment is shown in Figure 3.6, while the curves corresponding to the other tested conditions are reported in Figure B.5, B.6, and B.7. The compression behavior of all the tested monolayers reveals two distinct stages, labeled as stage 1 and stage 2 in Figure 3.6.

In stage 1, compression induces a progressive reduction of the interparticle distance within the monolayer, while the number of adsorbed nanoparticles remains constant. This behavior is typical of monolayers composed of irreversibly adsorbed nanoparticles (Li-Destri et al., 2019; Ruffino et al., 2022). In fact, in the presence of Gibbs monolayers at thermodynamic equilibrium, a reduction in macroscopic area generally triggers desorption of molecules at the interface to maintain a constant surface excess (J. Davies, 1952). However, in out-of-equilibrium systems where the monolayer consists of particles with a trapping energy much greater than thermal energy ($\Delta E_p \gg k_B T$), compression does not cause desorption. Instead, the particles are forced to pack closer together, leading to a reduction in available area per particle without altering their overall number at the interface. Noteworthy, the linear decrease of the interparticle distance with the compression provides evidence for the homogeneity of the obtained monolayers, which are formed by well-separated NPs rather than isolated clusters. Please, see Figure A.5 and the related comment for comparison.

This behavior persists until the interparticle distance reaches a critical threshold, beyond which the repulsive interparticle interaction potentials overcome the trapping energy. At this point, the monolayer undergoes a collapse. This phenomenon is clearly reflected in the trend observed during stage 2, where the interparticle distance remains constant while the corresponding number of nanoparticles progressively decreases. In fact, for hydrophilic nanoparticles, such as those used in this work, the collapse manifests as the desorption of the nanoparticles from the interface toward bulk, rather than the formation of nanoparticles multi-layers at the interface. This is supported by the GISAXS patterns acquired after the monolayer collapse, reported in Figure B.2, B.3 and B.4, which do not show any scattering features along q_x that would appear in case of multilayered structures formed at the air-water interface (Vegso et al., 2011).

In addition to the evolution of the interparticle distance and the number of adsorbed nanoparticles described above, the analysis of the surface pressure (π) during compression reveals the existence of three main regimes (Figure 3.6). In stage 1, the surface pressure initially increases in a gradual and smooth manner, reflecting the progressive densification of the monolayer. As compression proceeds toward the collapse point, a marked pressure peak is observed, reaching very high values. Once the monolayer collapses, in stage 2, the surface pressure continues to increase but with a lower slope compared to the steepest portion preceding the collapse, indicating the change in the mechanical response of the interface.

The most interesting observation concerns the first, smoother part of the surface pressure curve: here, the evolution of the surface pressure is strongly dependent on both the ionic strength of the aqueous subphase and the charge of the cations present, as suggested in the trends reported in Figure B.8. At a fixed interparticle distance,

higher ionic strength or higher valence ions lead to a less pronounced increase in surface pressure. This behavior can be interpreted as evidence of a higher compressibility of the monolayer under these conditions, suggesting a correlation with the electrostatic screening obtained in the different bulk compositions. In fact, reducing the repulsive electrostatic interactions between nanoparticles requires less mechanical work to bring them closer together, thereby leading to a smaller rise in pressure upon compression. This trend is consistent with previous experimental studies on nanoparticle and mixed lipid–nanoparticle monolayers, where the subphase ionic strength strongly influences the surface pressure–area isotherm and the mechanical dilatability of the film. At low ionic strength, electrostatic repulsions keep the particles more separated, resulting in a steeper increase in surface pressure upon compression. Conversely, at higher ionic strength, electrostatic screening facilitates particle packing, producing a smoother pressure increase (Bykov et al., 2022).

Thus, as the surface pressure–area isotherm acts not only as an indicator of mechanical densification but also as a sensitive probe of the interactions acting between NPs within the monolayer, we decided to employ an already used strategy to obtain microscopic information on the interparticle interaction potential as a function of the particle-particle distance (Li-Destri et al., 2019; Ruffino et al., 2022).

Briefly, since the number of adsorbed nanoparticles remains constant during stage 1 of compression, the macroscopic compression work (ΔW) performed before the onset of collapse, defined as the product of the change in surface pressure ($\Delta\pi$) and the corresponding change in macroscopic area (ΔA), as expressed in Equation 3.2, can be directly associated with the mechanical work required to bring the nanoparticles closer together at the interface (Santini et al., 2011; Li-Destri et al., 2019).

$$\Delta W = \frac{\Delta\pi \cdot \Delta A}{2} \tag{3.2}$$

Moreover, since GISAXS allowed us to count the number of nanoparticles during compression, the compression work per single nanoparticle (ΔW_{NP}), corresponding to the single particle potential, can be calculated as follows:

$$\Delta W_{NP} = U_{NP} = \frac{\Delta\pi \cdot \Delta A}{2 \cdot N_{NP}} \tag{3.3}$$

and, by considering Equation 3.1, Equation 3.3 can be rewritten as follows.

$$U_{NP} = \frac{\Delta\pi \cdot \Delta A_{NP}}{2} \tag{3.4}$$

The outcome of this calculation is presented in Figure 3.7, where the interparticle repulsive potential is plotted as a function of the interparticle distance. The calculated interaction potentials span approximately three orders of magnitude and exhibit two distinct regimes: a long-range repulsive regime, observed at interparticle distances of about 46–30 nm with corresponding potentials in the range of $U_{NP} \sim 10^{-23}$–10^{-21} J, and a short-range regime, occurring at distances of approximately 30–28 nm with potentials

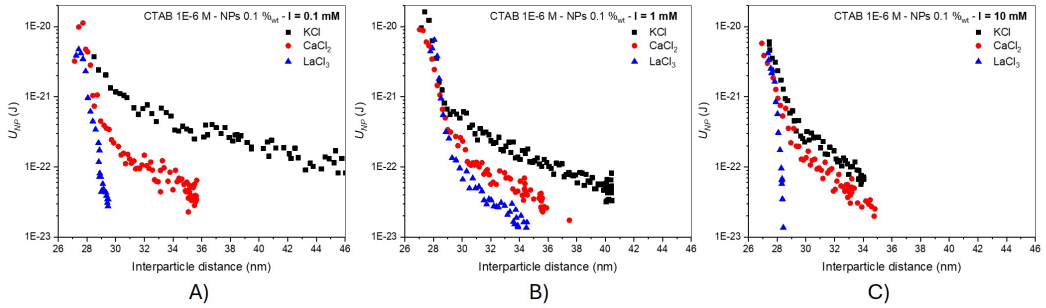

Figure 3.7: *Evolution of the single particle potential vs particle-particle distance ($U_{NP}vsID$) for monolayer at the bulk ionic strength of A) 0.1 mM, B) 1 mM and, C) 10 mM in KCl (black square), $CaCl_2$ (red circles) and $LaCl_3$ (blue triangles). The bulk concentration was 1×10^{-6} M in CTAB and 0.1 $\%_{wt}$ in NPs for all the tested conditions.*

of $U_{NP} \sim 10^{-21} - 10^{-20}$ J. The transition between these two regimes is highlighted by the change in slope of the U_{NP} versus ID curves.

Concerning the short-range interactions, these can be attributed to steric repulsion arising from the contact, or eventual interpenetration, of the chains of the surfactant molecules adsorbed on the nanoparticle surface, as previously demonstrated (Ruffino et al., 2022). Interestingly, both the dependence on the interparticle distance and the magnitude of these interactions, which is in agreement with previous literature reports (Min et al., 2008), appear to be unaffected by the ionic strength or the nature of the counterions. It has been consistently observed that such steric forces are primarily governed by the chemical nature and surface concentration of the adsorbed surfactant or polymer layer. Therefore, since all our experiments were carried out in the presence of CTAB at the same bulk concentration (1×10^{-6} M), no significant differences in the short-range interaction behavior were expected.

As previously discussed, the collapse of the monolayer, systematically observed at an interparticle distance of around $27.2 \pm 0.2nm$ irrespective of the bulk composition, occurs when the lateral repulsive forces become comparable to or exceed the nanoparticle desorption energy (ΔE_P). Considering that the interaction potential curves were derived only from the compression isotherm up to the collapse point, the maximum measured repulsive potential can be regarded as a reliable estimate of the nanoparticle desorption energy in our monolayers. This value is found to be in the range of $7 - 12 \times 10^{-21}$ J, corresponding to approximately $1.7 - 2.9\, k_B T$ at 25 °C and a particle radius of 11.6 nm. Although this desorption energy may appear surprisingly low, it is in good agreement, in terms of order of magnitude, with previously reported values for CTAB-coated silica nanoparticles at fluid interfaces (Calzolari et al., 2012). From this estimate, we can infer the contact angle of our nanoparticles using Equation 1.4, yielding values in the range of 10.6 - 12.1°, and corresponding to an immersion depth of ~ 11.4 nm, thus 99.9 % of the particle volume is in the aqueous phase. These results indicate a highly hydrophilic character of the nanoparticles, which provides a clear explanation for their tendency to re-disperse into the bulk phase once expelled from the

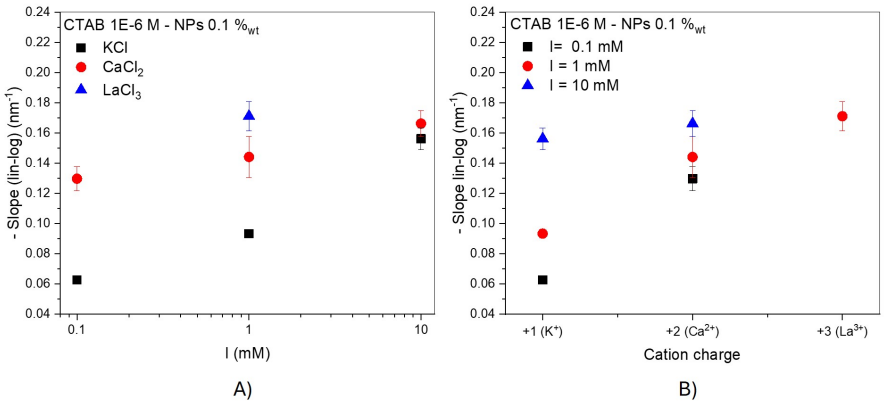

Figure 3.8: *Negative of the slope of the linear fit of the long-range repulsive potential as a function of A) the bulk ionic strength for in KCl (black square), $CaCl_2$ (red circles) and $LaCl_3$ (blue triangles) and B) the cation charge at the ionic strength of 0.1 mM (black squares), 1 mM (red circles), and 10 mM (blue triangles). The bulk concentration was 1×10^{-6} M in CTAB and $0.1\%_{wt}$ in NPs.*

monolayer as a consequence of the collapse.

Regarding the long-range interactions, their magnitude is in good agreement with previously reported values for similar colloidal systems (J. N. Israelachvili, 2011). These interactions display a strong dependence on both the ionic strength and the nature of the cation present in solution. Specifically, at a fixed interparticle distance, the repulsive potential consistently decreases with increasing ionic strength or with the presence of multivalent cations, as expected by observing the π vs ID curves in Figure B.8. The linear trend observed in the lin-log representation of these interactions suggests an exponential decay of the repulsive potential with distance, which is typically associated with electrostatic repulsion mechanisms. To further quantify these long-range interactions and relate them to bulk solution conditions, the negative of the slopes of the linear fits in the 46–30 nm interparticle distance range (see Figure B.9) was extracted and reported in Figure 3.8, as a function of the bulk composition. Unfortunately, for the $LaCl_3$ samples at ionic strengths of 0.1 mM and 10 mM, it was not possible to perform the same analysis. In these cases, the force–distance curves captured only the short-range repulsive regime due to the high surface density of the obtained monolayers, resulting in a steady-state interparticle distance of about 29-30 nm after 30 minutes of monolayer formation.

The data clearly show an overall trend where increasing both the ionic strength and the cation charge results in higher slope values (more negative), indicating a progressive reduction of the effective interparticle repulsion. For monovalent cations (K^+), the slope remains comparatively low at 0.1 mM, while increasing the ionic strength to 1 and 10 mM leads to a smoother decay of the potential. A similar trend is observed for divalent (Ca^{2+}) and trivalent (La^{3+}) ions, but the slope is already larger at low ionic strengths, proving once again that multivalent ions are more effective in screening electrostatic interactions between CTAB-coated nanoparticles. This behavior is consistent with general electrostatic theory for colloidal systems, where multivalent cations are known to induce stronger double layer compression and, in some cases, charge corre-

lation effects, enhancing particle attraction or reducing repulsion (J. N. Israelachvili, 2011; Tian et al., 2014; Matheus et al., 2016).

Further, as we estimate 99.9 % of the particle volume is immersed in the water phase, we can assume that the dipolar contribution to the long range electrostatic repulsion is negligible. Thus, by taking into account only the double layer repulsion potential, reported in Equation 1.8, and ignoring in a first instance all the other potentials that could act on the nanoparticles (Section 1.1), the slope obtained with the linear fit should be the inverse of the Debye length. For monovalent (1:1) salt, the Debye length at ionic strengths equal to 0.1 mM, 1 mM, and 10 mM are respectively 30.4, 9.6, and 3.04 nm, as obtained with Equation 1.7. The putative Debye lengths calculated with the inverse of the slope for KCl are 15.9, 10.7, and 6.4 nm, thus significantly different from the expected values. This observation suggests that, in addition to the electrostatic contribution, other surface-induced interaction potentials (*i.e.*, van der Waals attraction, capillary interactions, image charges, etc.) play a non-negligible role in determining the effective interparticle forces.

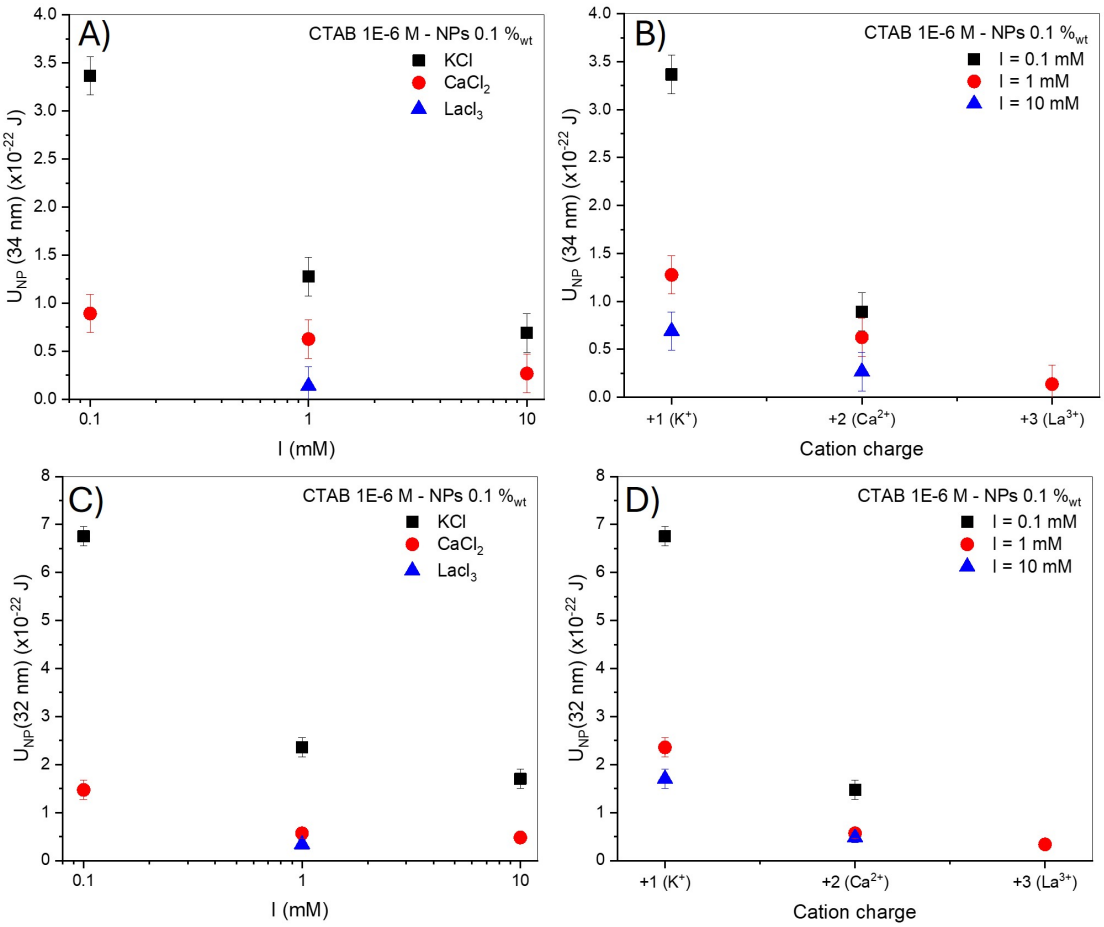

Figure 3.9: *Interparticle interaction potential at the interparticle distance of (A,B) 34 nm ($U_{NP}(34nm)$) and (C,D) 32 nm ($U_{NP}(32nm)$) reported as a function of the bulk ionic strength (A,C) and of the cation charge (B,D). The bulk concentration was 1×10^{-6} M in CTAB and $0.1\%_{wt}$ in NPs.*

Additional support for this interpretation arises from a qualitative comparison be-

tween the electrophoretic mobility trends and the particle-particle repulsive potential at the arbitrarily chosen interparticle distance of 34 nm, $U_{NP}(34nm)$, and 32 nm, $U_{NP}(32nm)$, reported in Figure 3.9. As already discussed, increasing ionic strength shifts the electrophoretic mobility towards less positive values (Figure 3.3), reflecting a progressive screening of the nanoparticle surface charge. However, at any given ionic strength, the dependence of μ_e on cation valence remains essentially unchanged, with comparable slopes of the μ_e versus cation charge relationship across the explored electrolyte concentrations. In contrast, the effect of cation valence on the long-range repulsive forces becomes progressively weaker as the ionic strength increases with a non-linear relationship. A similar attenuation has been observed for the interfacial excess, reinforcing the notion that purely electrostatic interactions cannot fully capture the static or dynamic behavior of nanoparticles at the interface. These results, corroborated by theoretical simulation (Matheus et al., 2016), suggest that additional contributions, beyond classical double layer repulsion described by the DLVO theory that primarily govern the interaction both in the bulk phase and the interface, likely play a significant role in governing the interfacial organization and interactions of the adsorbed particles.

3.2 Conclusion

In summary, this chapter provides one of the few systematic experimental investigations into how both ionic strength and cation valence shape the interparticle interaction potentials of CTAB-coated nanoparticles adsorbed at the air-water interface.

By combining compression isotherms with *in situ* GISAXS measurements, we have quantitatively characterized both short-range steric repulsions, that were found to be largely insensitive to both ionic strength and cation valence, and long-range electrostatic interactions, their magnitude and decay length vary as a function of the bulk ionic environment. Our results demonstrate that multivalent cations are significantly more efficient than monovalent ions in screening electrostatic repulsion, leading to denser interfacial packing and ultimately lower interparticle distances. Interestingly, the dependence of electrophoretic mobility on both ionic strength and cation valence follows a markedly different trend compared to that observed for the interfacial excess and the long-range interparticle repulsion. This contrasting behavior highlights that the mechanisms governing nanoparticle adsorption and long-range interactions at the interface cannot be fully captured by electrostatic considerations alone.

Furthermore, by comparing interfacial excess measurements with the corresponding surface tension data, we show that surface tension alone is not a reliable estimator of nanoparticle adsorption or packing density. Our findings confirm earlier observations that the apparent equation of state of nanoparticle monolayers can be strongly decoupled from their actual interfacial coverage. This underlines the need for direct quantification of interfacial excess when studying particle-laden interfaces, as relying solely on surface tension may lead to misinterpretations of adsorption phenomena.

Overall, this work reveals the key role of cation valence in governing nanoparticle interactions and assembly at fluid interfaces. The analysis presented here focuses on valence-dependent effects, which represent an essential component of the broader class of specific ion effects. A full understanding of chemical specificity would, however, require a systematic comparison among ions with the same nominal charge but different hydration and polarizability. Such investigations, extending beyond the scope of the present study, would provide valuable insight into how subtle ion–water correlations and surface affinity determine the effective interfacial potentials of nanoparticles.

4

Impact of bulk composition on the recovery and reconfiguration of nanoparticle monolayer

Understanding and controlling the dynamic behavior of particle-laden interfaces is essential for the development of advanced soft materials and interfacial technologies. From reconfigurable Pickering emulsions to regenerable membranes and adaptive liquid-based devices, many applications rely not only on the spontaneous assembly of nanoparticles into stable interfacial layers and monolayers, but also on their ability to respond, adapt, and reorganize under external mechanical stimuli (Forth et al., 2019; Tran et al., 2019). In these contexts, the ability of interfacial nanoparticles to adsorb, desorb, and collectively rearrange is a key factor that determines the mechanical resilience, structural integrity, and functional lifetime of the interfacial layer. For example, emulsions used in encapsulation or drug delivery must be robust enough to resist shear forces (Cui, 2011), while remaining responsive to programmed triggers. Similarly, nanoparticle-stabilized films in filtration or sensing devices must recover their interfacial structure after mechanical stress to maintain performance over multiple cycles (González et al., 2022; D. Xie et al., 2022).

While the adsorption behavior of silica nanoparticles functionalized with cationic surfactants such as CTAB has been extensively investigated under quasi-static conditions, their response to large-scale mechanical deformations, such as those induced by interfacial compression and expansion, remains poorly understood. This is primarily due to the scarcity of studies, particularly at low surfactant-to-nanoparticle ratios (Santini et al., 2011). Although some works have addressed structural changes induced by compression/expansion, these are typically limited to studies on spread nanoparticle monolayers (Langmuir monolayers). Due to the intrinsic nature of such systems, little attention has been paid to the fate of particles ejected during monolayer collapse or to their potential for re-adsorption. In most cases, highly hydrophobic particles tend

to form multilayers or complex aggregates upon collapse, which can relax during expansion without necessarily undergoing true re-adsorption from the bulk phase to the interface (Abgarjan et al., 2025; Garbin, 2019; Razavi et al., 2015). Moreover, a systematic investigation into how ionic strength and cation valence affect the dynamic recovery of such systems after large mechanical perturbation is still lacking.

This chapter addresses these open questions by investigating how the bulk composition, specifically CTAB concentration, ionic strength, and cation valence, affects the dynamic reconfiguration of nanoparticle monolayers at the air–water interface. Using a Langmuir trough, we apply multiple controlled compression–expansion protocols designed to test both the extent and the mechanism of monolayer recovery following collapse. *In situ* GISAXS investigation allowed the quantification of both particle desorption during collapse and subsequent re-adsorption during the following expansion. By comparing results across a matrix of compositions and protocols, we derive a quantitative recovery metric and identify how interfacial dynamics are governed by the interplay between the bulk composition and interparticle forces.

Through this analysis, we aim not only to shed light on the fundamental processes governing monolayer resilience but also to provide a rational framework for designing reconfigurable, reusable, and composition-tunable soft interfaces. Moreover, this work lays the groundwork for future investigations seeking to correlate dynamic behavior with intrinsic nanoparticle properties, such as size, surface charge, and hydrophobicity, modulated by the bulk medium.

4.1 Results and Discussion

The dynamic and recovery capability of silica nanoparticle monolayers was investigated by employing simple and effective protocols based on multiple compression/expansion cycles in a Langmuir trough. In order to link the capability of structure recovery with the bulk composition, we prepared silica dispersions at the concentration of 0.1 $\%_{wt}$ in the presence of micromolar CTAB concentration (1×10^{-6} M and 4×10^{-6} M), combined with either 1 mM KCl, 10 mM KCl, 1 mM $CaCl_2$, or 1 mM $LaCl_3$ to modulate both the bulk ionic strength and cation charge. The salt concentrations just reported must be considered as suspension ionic strength and not as molar concentration (see Section B.1 for further details).

Each dispersion was poured into a Langmuir trough and allowed to adsorb at the water/air interface for 30 minutes at the controlled temperature of 25 °C. We then performed two sequential compression/expansion cycles reaching complete monolayer collapse. Both the compressions and expansions were performed at the constant speed of $\sim 22\ cm^2/min$. Three procedural variants were implemented:

- **Subphase Cleaning (SC)**: After 30 min of adsorption, the subphase was exchanged with pure water using a dual-channel peristaltic pump operating at a flow rate of approximately 10 mL/min, in order to remove excess non-adsorbed

nanoparticles. Compression/expansion cycles were then performed. To ensure complete subphase renewal, a water volume corresponding to three times the capacity of the Langmuir trough was flushed through the system.

- **Two Consecutive Compressions (2CC)**: Without subphase exchange, we executed back-to-back full compression/expansion cycles.
- **Intermediate adsorption (IA)**: Following the first compression, the monolayer was fully expanded and allowed to rest for 30 min before a second comp/exp cycle.

The rationale behind these experimental protocols lies in the intrinsic behavior of nanoparticle monolayers when subjected to progressive area reduction during compression. As extensively described in Chapters 2 and 3, under our experimental conditions silica nanoparticles, once adsorbed, are essentially irreversibly trapped at the air–water interface. However, during compression the available interfacial area decreases, forcing the particles to approach each other until a critical monolayer density is reached. Beyond this point, the monolayer can no longer sustain the lateral pressure and undergoes collapse, leading to the ejection of nanoparticles back into the bulk phase by keeping the monolayer bidimensionality (Figure 3.6). However, some of these desorbed nanoparticles may diffuse back to the interface during the subsequent expansion phase, partially restoring interfacial coverage. The extent of this recovery process depends on the kinetics of adsorption, the interparticle interactions modulated by ionic strength and counterion valence, and the mechanical history of the interface itself, all of which we aim to disentangle with our experimental protocols.

Specifically, the SC protocol provides a reference scenario to test whether recovery is solely attributable to particles that are at the interface after the 30 min of adsorption. By replacing the subphase with pure water, any excess non-adsorbed nanoparticles are removed, ensuring that only those particles ejected during monolayer collapse can potentially re-adsorb and contribute to the second compression cycle. A zero recovery percentage under these conditions would therefore indicate negligible recruitment from residual bulk particles. The 2CC protocol, on the other hand, retains the bulk reservoir of dispersed nanoparticles, allowing us to evaluate the extent to which particles can immediately re-adsorb following desorption, without any additional time for monolayer rearrangement. Finally, the IA protocol introduces a 30-minute resting time at full expansion, corresponding to the time given for the formation of a homogeneously packed monolayer, providing additional time for nanoparticles at the interface to rearrange and for particles in the bulk to diffuse to the interface and re-establish dense coverage before the second compression.

The results of these measurements are presented in Appendix C, from Figure C.1 to C.5, while Figure 4.1 displays a single bulk condition as a representative example to facilitate the discussion. The compression/expansion isotherms obtained with the three different protocols exhibit similar features. In both the 1^{st} and 2^{nd} compression cycles, the compression/expansion isotherms show a marked hysteresis, characteris-

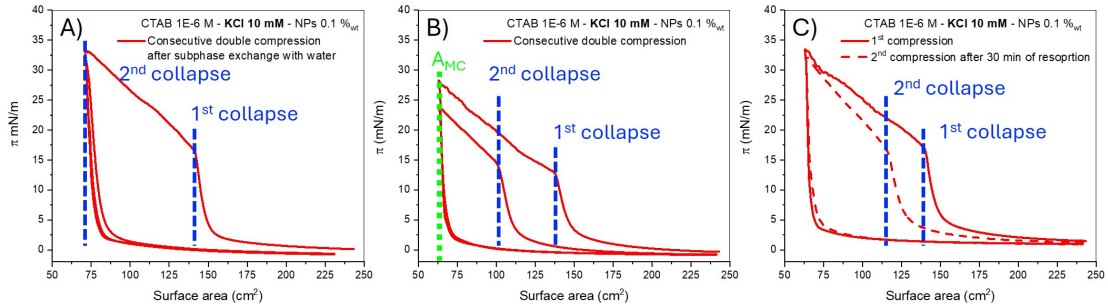

Figure 4.1: *Example of compression/expansion isotherms for nanoparticles monolayer at the air-water interface obtained with protocol A) subphase cleaning (SC), B) two consecutive compression (2CC), and C) Intermediate adsorption (IA). The dashed blue lines indicates the first and the second monolayer collapse area, while the green lines indicates the macroscopic area of maximum compression (A_{MC}).*

tic of non-reversible processes. The compression curves show the trend of the π-A isotherm associated with the nanoparticle monolayer described in the previous chapter, with the collapse area of the first compression consistently larger than that of the second. Specifically, the macroscopic area at the 2^{nd} collapse follows the order IA > 2CC >> SC. The expansion curves, on the other hand, are marked by an abrupt decrease in surface pressure with increasing area, which suddenly drops to zero without any specific feature. This behavior was previously associated with the monolayer rupture with fast relaxation processes and without any appreciable reconfiguration effect of the surfactant at the interface (Santini et al., 2011).

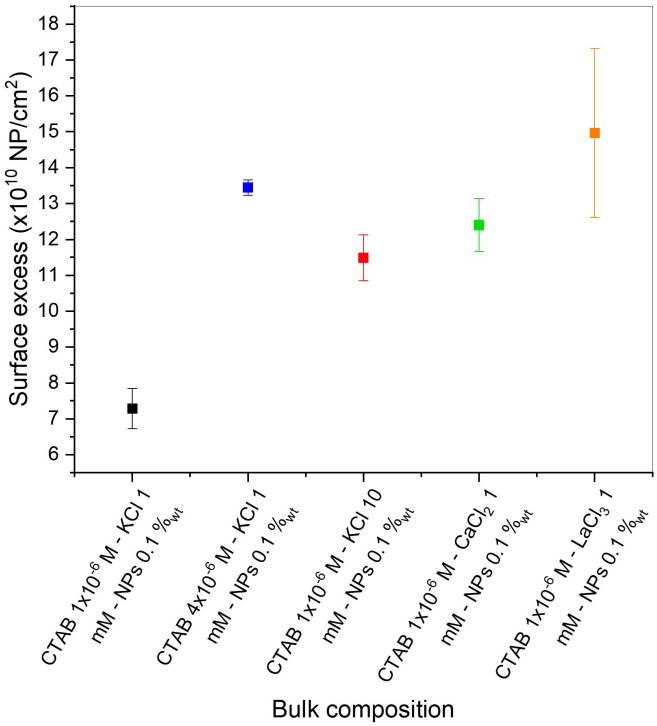

Figure 4.2: *Nanoparticle surface excess estimated from the interparticle distance at the steady state as a function of the bulk composition.*

To obtain in-depth information on the structural evolution during the compres-

sion/expansion cycles we performed *in situ* GISAXS characterization obtaining information on the interparticle distance (ID) and number of adsorbed nanoparticles (N) during the dynamic experiments, as detailed explained in Chapter 3. We firstly estimated the nanoparticle surface excess from the interparticle distance value after 30 min of adsorption. The obtained results, reported in Figure 4.2 are in perfect agreement with that reported in the previous chapters and elsewhere (Ruffino et al., 2022).

Then, we investigated the effect of subphase exchange on the monolayer structure. As shown in Figure 4.3, both the interparticle distance and the surface pressure evolution during compression are comparable for monolayers with and without subphase exchange, with only minor deviations that can be attributed to experimental variability. This suggests that the overall monolayer structure remains unaffected by the water flux beneath the interface and that the removal of the bulk nanoparticle reservoir does not trigger nanoparticle desorption, providing additional evidence of the irreversible nature of the adsorption process.

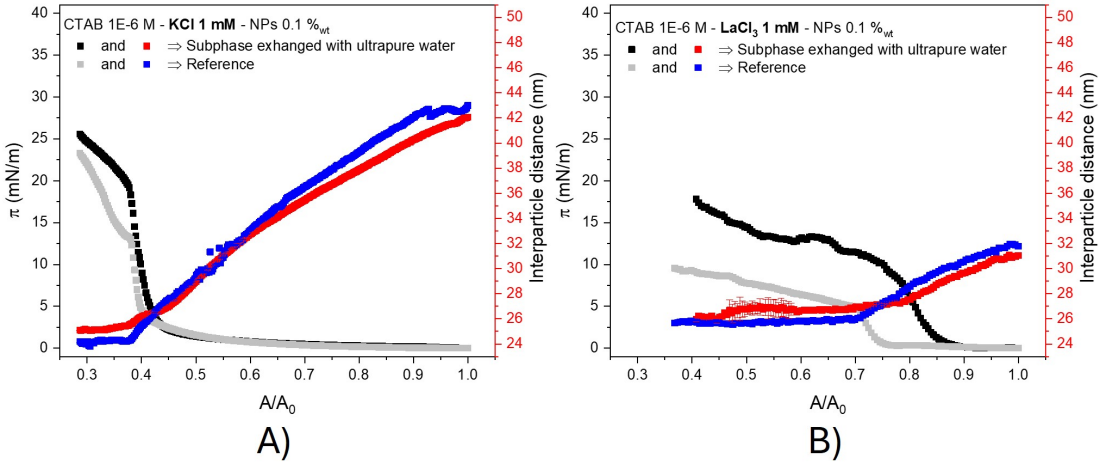

Figure 4.3: *Interparticle distance and the corresponding surface pressure evolution during compression for nanoparticle monolayer obtained with subphase exchange with ultrapure water after 30 min of adsorption (black squares π and red squares ID) in comparison with the monolayer obtained at the same bulk composition, but without subphase exchange (gray squares π and blue squares ID). The bulk composition was 0.1 $\%_{wt}$ NPs, 1×10^{-6} M CTAB and ionic strength 1 mM in A) KCl and B) $LaCl_3$.*

Further, we performed a complete characterization of the structural evolution during the compression/expansion cycle for the 2CC and IA protocols. The results of the interparticle distance evolution are shown in Figure 4.4, while in Figure C.6 to C.10 are also reported the corresponding surface pressure and number of adsorbed nanoparticles. The interparticle distance and adsorbed nanoparticle number evolution during the first compression step is the characteristic one for irreversibly adsorbed NP monolayer, with features already described in the previous chapter (see Figure 3.6 and related comments). Notably, a distinct behavior was observed for the expansion curves. Except for the sample prepared at CTAB 1×10^{-6} M and KCl 1 mM, the variation of the interparticle distance with macroscopic area expansion is characterized by an initial increase followed by a plateau, with the plateau value depending on the system composition. This response can be associated with two distinct phenomena:

- *i*) The initial increase in interparticle distance corresponds to a uniform spreading of the monolayer, until the particle density is sufficiently low to allow additional nanoparticles from the bulk to adsorb at the interface without significantly altering the average interparticle spacing. Thus, once a critical interparticle distance is reached, a further increase in the macroscopic area promotes the adsorption of nanoparticles from the bulk. This adsorption occurs at constant surface excess.
- *ii*) Alternatively, the monolayer undergoes a uniform expansion up to a threshold interparticle distance, beyond which isolated nanoparticle clusters detach and float freely at the interface. In this regime, while the overall macroscopic area increases and the mean separation distance between clusters increases, the average interparticle distance within each cluster remains essentially constant. This finding indicates that the internal packing density of the clusters is preserved and unaffected by the large-scale rearrangement of the monolayer. In this framework, any eventual nanoparticle adsorption from the bulk is associated with the increase in the size of the clusters without any change in their packing density.

Interestingly, for the sample with composition $1{\times}10^{-6}$ M - KCl 1 mM (Figure 4.4 *A*, *B* and Figure C.6), the evolution of the interparticle distance during both the first expansion and the second compression exhibits a nearly linear increase/decrease, with only minor deviations. These small variations are likely associated with monolayer heterogeneities, probably caused by amorphization induced during the first compression, as indicated by the broadening of the GISAXS peaks reported in Figure C.11 (Li-Destri et al., 2019). This behavior suggests that, during expansion, the monolayer spreads uniformly at the interface, leading to an increase in the interparticle distance proportional to the increase in the macroscopic area. Under these conditions, the monolayer remains relatively homogeneous after expansion, so the subsequent compression shows a correspondingly linear decrease in the interparticle distance. Both the expansion and the second compression indicate a constant number of adsorbed nanoparticles, implying that only a very small fraction of nanoparticles adsorb during both the 2CC and IA protocols.

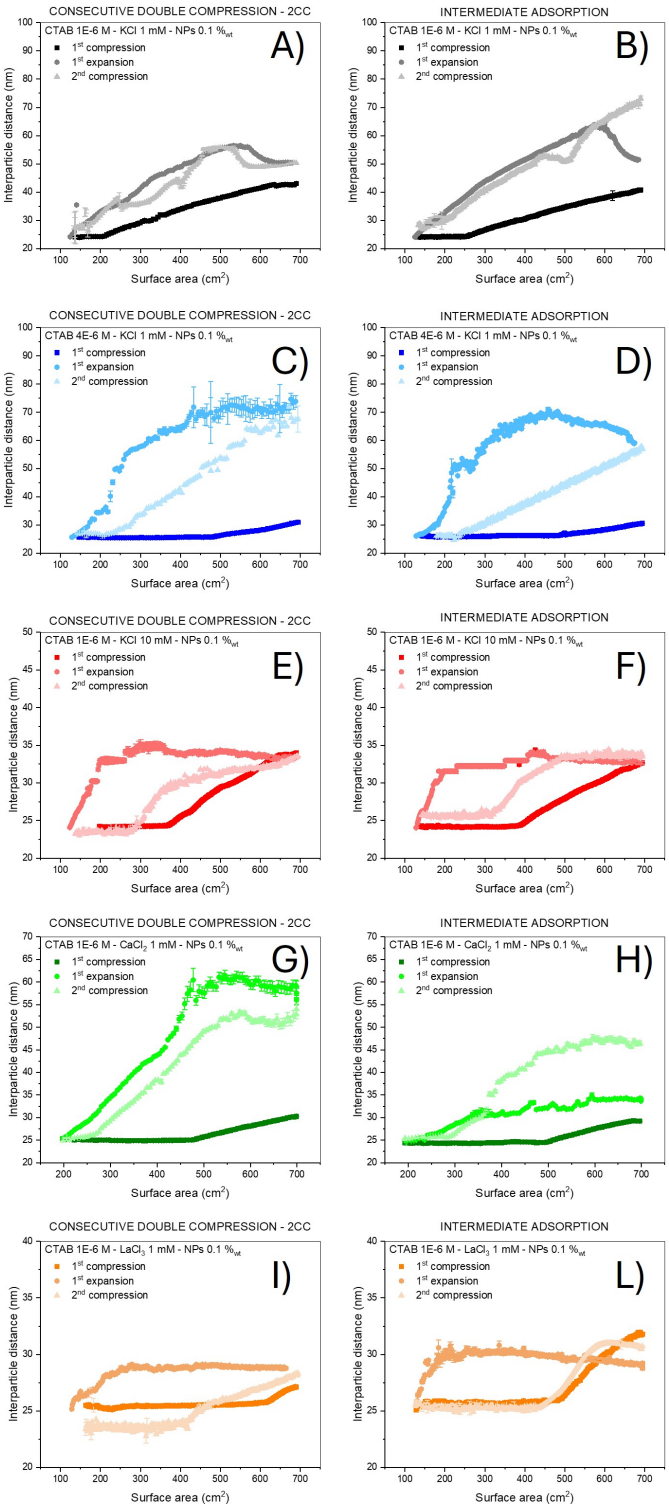

Figure 4.4: *Interparticle distance evolution during the compression/expansion experiment performed with protocol two consecutive compression (2CC) in (A, C, E, G, I) and intermediate adsorption (IA) in (B, D, F, H, L) for sample with bulk composition equal to (A,B) CTAB* $1 \times 10^{-6}M$ *– KCl 1 mM – NPs 0.1%*$_{wt}$*; (C,D) CTAB* $4 \times 10^{-6}M$ *– KCl 1 mM – NPs 0.1%*$_{wt}$*; (E,F) CTAB* $1 \times 10^{-6}M$ *– KCl 10 mM – NPs 0.1%*$_{wt}$*; (G,H) CTAB* $1 \times 10^{-6}M$ *– CaCl*$_2$ *1 mM – NPs 0.1%*$_{wt}$*; (I,L) CTAB* $1 \times 10^{-6}M$ *– LaCl*$_3$ *1 mM – NPs 0.1%*$_{wt}$*.*

To verify that the hysteresis observed in both surface pressure and interparticle distance arises from nanoparticle desorption triggered by monolayer compression beyond the collapse point, we conducted a compression/expansion cycle targeting a macroscopic area prior to collapse. As shown in Figure 4.5, the compression/expansion cycles performed before the collapse are fully reversible, both in terms of surface pressure and interparticle distance.

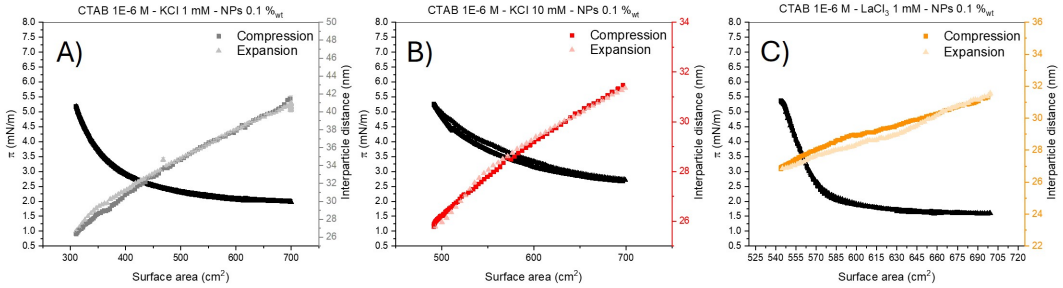

Figure 4.5: *Compression/expansion cycle performed to a target area prior to monolayer collapse for sample at bulk composition CTAB* 1×10^{-6}*, NPs 0.1* $\%_{wt}$ *and A) KCl 1 mM, B) KCl 10 mM, and C)* $LaCl_3$ *1 mM. The perfect match between both the surface pressure and the interparticle distance of the compression and expansion curves demonstrated monolayer reversibility.*

The interparticle evolution during the second compression helps distinguish between the two possible mechanisms. Indeed, if scenario *i*) applies, the second compression step would display a trend analogous to the first one, namely a linear decrease in the interparticle distance with decreasing macroscopic area. This behavior is characteristic of a homogeneously distributed monolayer in which compression progressively brings nanoparticles closer together, as previously discussed. Conversely, if scenario *ii*) applies, the second compression would initially show a constant interparticle distance, reflecting the fact that floating clusters are pushed closer to one another without altering their internal packing. The interparticle distance would then decrease only once the clusters come into contact with each other.

Based on the above consideration, we can immediately observe how the sample at bulk composition CTAB 4×10^{-6} M - KCl 1 mM (Figure 4.4 *C*, *D* and Figure C.7) follows the first scenario proposed, showing a linear and constant decrease in the interparticle distance during the second compression, both in the 2CC and IA protocols. On the contrary, the samples with composition CTAB 1×10^{-6} M - KCl 10 mM (Figure 4.4 *E*, *F* and Figure C.8), 1×10^{-6} M - $CaCl_2$ 1 mM (Figure 4.4 *G*, *H* and Figure C.9) and 1×10^{-6} M - $LaCl_3$ 1 mM (Figure 4.4 *I*, *L* Figure C.10), evolve as for the second scenario, with the second compression characterized by a first step at constant interparticle distance followed by a linear decrease till the monolayer collapse. It is worth noting that the sample containing $LaCl_3$ 1 mM in the 2CC protocol (Figure 4.4 *I*) exhibits a linear decrease in interparticle distance during the second compression. However, the collapse occurs at a significantly smaller area than would be expected. Since the interparticle distance at the onset of the second compression matches that reached at the steady state, one would anticipate that, if the monolayer were densely packed, the collapse point dur-

ing the second compression should closely align with that of the first. The fact that this is not observed indicates that the resulting monolayer is less densely packed. The apparent linear decrease in interparticle distance during the second compression may arise from the combined effect of structural heterogeneity and the limited precision of GISAXS peak position determination. The monolayer likely consists of locally dense domains embedded in more loosely packed or defective regions. These well-packed domains, although spatially separated, dominate the measured q_c response during compression, producing an apparent linear trend even when the global packing is inhomogeneous. At the same time, the broad GISAXS peaks observed in this sample Figure C.14, indicative of short lateral correlation lengths and small or highly disordered domains, introduce an averaging effect over a wide distribution of local spacings. This can smooth out non-linear variations and further reinforce the apparent linearity. The reduced collapse area is then consistent with the overall lower packing efficiency and limited mechanical connectivity of the film. These limitations could be mitigated by combining GISAXS with complementary real-space imaging techniques. *In situ* Brewster Angle Microscopy (BAM) could provide direct visualization of domain formation and lateral heterogeneities during compression, while *ex situ* AFM measurements on transferred monolayers would help correlate local topography and packing with the averaged scattering response. Such combined approaches would allow distinguishing genuine structural rearrangements from instrumental broadening effects and yield a more complete picture of nanoparticle organization at the interface.

Further, the interparticle distance values reached during the expansion are in the range 60-70 nm for the sample at CTAB 1×10^{-6} M - KCl and $CaCl_2$ 1 mM and CTAB 4×10^{-6} M - KCl 1 mM, thus an interparticle spacing significantly higher than that reached at the steady state after 30 min of monolayer formation. This indicates that the eventual adsorption of nanoparticles from the bulk occurs only when a very sparse layer is formed. On the contrary, the samples at CTAB 1×10^{-6} M - KCl 10 mM and $LaCl_3$ 1 mM show that the increase in the interparticle distance during the expansion arrests when values in the range 30-35 nm are reached. These interparticle distance values are comparable with those observed at the steady state. Upon this threshold being reached, further expansion induces the detachment of isolated clusters, as previously proposed, thus the adsorption may occur also in the presence of densely packed islands.

This last observation suggests that high ionic strength or the presence of highly charged cations promotes the formation of densely packed clusters in which the interparticle distance matches that at steady state. This implies the existence of a net attractive force between particles, despite their retaining a negative surface charge, as confirmed by electrophoretic mobility measurements even at the highest ionic strengths tested (Figure 3.3). This surprising result provides a rationale for the formation of highly compact monolayers within 30 minutes and is the only plausible explanation for the stability of densely packed clusters during expansion, a process that would otherwise, by entropic considerations alone, favor particle separation. Furthermore, when viewed in the broader context of the results discussed in Chapter 3, this finding reveals

that, particularly in the presence of La^{3+}, the attractive interaction is strong enough to bring nanoparticles at the minimum distance (~30 nm), below which short-range steric repulsion becomes dominant. This interpretation is consistent with previous reports showing that multivalent cations can significantly modify the interaction forces between like-charged surfaces. (Dishon et al., 2011) demonstrated that increasing the valence and size of counterions can strongly suppress the electrostatic repulsion between negatively charged silica surfaces in bulk aqueous electrolytes, and in some cases even lead to net attractive interactions, an effect attributed to ion–ion correlations and specific adsorption beyond the predictions of classical DLVO theory. Complementary to this, (Matheus et al., 2016) compared the interaction forces between charged colloidal particles in bulk and at the air–water interface, showing that, at ionic strength higher than 25 mM and in the presence of multivalent cations, the interfacial interactions are significantly less repulsive than their bulk counterparts. This enhanced screening at the interface suggests that multivalent counterions are even more effective in reducing electrostatic repulsion under interfacial confinement, potentially allowing the emergence of short-range attractive components. Taken together, these findings support the hypothesis that both bulk ion–correlation effects and interface-specific electrostatic modifications contribute to the formation and stability of densely packed nanoparticle clusters under high ionic strength and high valence cations.

To quantitatively assess the extent of nanoparticle re-adsorption during the expansion phase and the eventual subsequent resting period, we introduced the Recovery % (R%) parameter. The recovery % was arbitrarily defined as the ratio between the number of nanoparticles that re-adsorb during the expansion and the eventual 30 min rest in the intermediate adsorption protocol (N_R), and the number of nanoparticles lost with the first compression (N_D), as follows:

$$\text{Recovery } \% = \frac{N_R}{N_D} \tag{4.1}$$

As discussed in Chapter 3, the number of nanoparticles can be calculated using Equation 3.1. Thus, the number of nanoparticles desorbed during the first compression is equal to the difference between the number of nanoparticles at the first collapse (N_{C1}) and the number of particles remaining at the point of maximum compression of the monolayer (N_{MC}). By applying Equation 3.1 and considering that, after the collapse, the interparticle distance, and thus the area per particle, remains constant, we can express N_D as follows:

$$N_D = N_{C1} - N_{MC} = \frac{A_{C1}}{a_{collapse}} - \frac{A_{MC}}{a_{collapse}} \tag{4.2}$$

Here, A_{C1} is the macroscopic trough area at the point of the first monolayer collapse, A_{MC} is the minimum macroscopic area reached during compression (*i.e.*, the point of maximum compression), and $a_{collapse}$ is the area per nanoparticle, which remains constant after collapse, as demonstrated. Moreover, it must be mentioned that the

collapse interparticle distance is the same for both the first and second compression, independently of the bulk composition and the protocol used.

Furthermore, the number of nanoparticles that re-adsorb during the expansion phase, including any possible intermediate adsorption, is defined as the difference between the number of nanoparticles calculated at the second collapse (N_{C2}) and the number of nanoparticles remaining at the end of the first compression (N_{MC}). In this calculation, it is assumed that during the second compression the number of nanoparticles in the monolayer remains constant until the second collapse is reached, meaning that no compression-induced desorption occurs.

$$N_R = N_{C2} - N_{MC} = \frac{A_{C2}}{a_{collapse}} - \frac{A_{MC}}{a_{collapse}} \tag{4.3}$$

Here, A_{C2} is the macroscopic trough area at the second collapse, while all the others have the same meaning as in Equation 4.2. Specifically, as the interparticle distance at which the monolayer collapse occurs is the same both in the first and in the second cycle, $a_{collapse}$ has exactly the same value in Equation 4.2 and 4.3.

Thus, by combining all the equations written above, we can conclude that the Recovery % is equal to:

$$\text{Recovery \%} = \frac{N_R}{N_D} = \frac{\frac{A_{C2}}{a_{collapse}} - \frac{A_{MC}}{a_{collapse}}}{\frac{A_{C1}}{a_{collapse}} - \frac{A_{MC}}{a_{collapse}}} = \frac{A_{C2} - A_{MC}}{A_{C1} - A_{MC}} \tag{4.4}$$

The results of these calculations are reported in Figure 4.6 for monolayers obtained at different bulk compositions and with the three different protocols explained above.

The first significant results are associated with the subphase cleaning protocol (SC). In fact, independently from the bulk composition, the recovery values obtained are zero, as also deducible by the curves reported in Figure C.1 to C.5 where for the subphase cleaning protocol (SC) the second collapse occurs at the trough area corresponding to the area of maximum compression ($A_{C2} = A_{MC}$) and thus $N_R = 0$. This observation suggests, first, that resorption can occur only when a bulk NP reservoir is present, and second, that nanoparticles expelled from the monolayer after its collapse disperse back into the bulk rather than accumulating in the subsurface region. As discussed in the previous chapter, the GISAXS patterns recorded after collapse (Figure B.2–B.4) indicate that the collapse proceeds without loss of the bidimensionality of the monolayers. This behavior can be justified by considering that a first step of adsorption is controlled by the diffusion of nanoparticles from the bulk to the surface (Hua et al., 2018). In fact, while the diffusion coefficient of the particles is an intrinsic property and depends only on the composition of the medium surrounding the nanoparticle, the diffusion adsorption rate is proportional to the concentration of the species (Ward et al., 1946). Therefore, since a very small number of nanoparticles desorb into a significantly large bulk volume, the resulting concentration tends toward zero, and consequently, the adsorption rate will also approach zero.

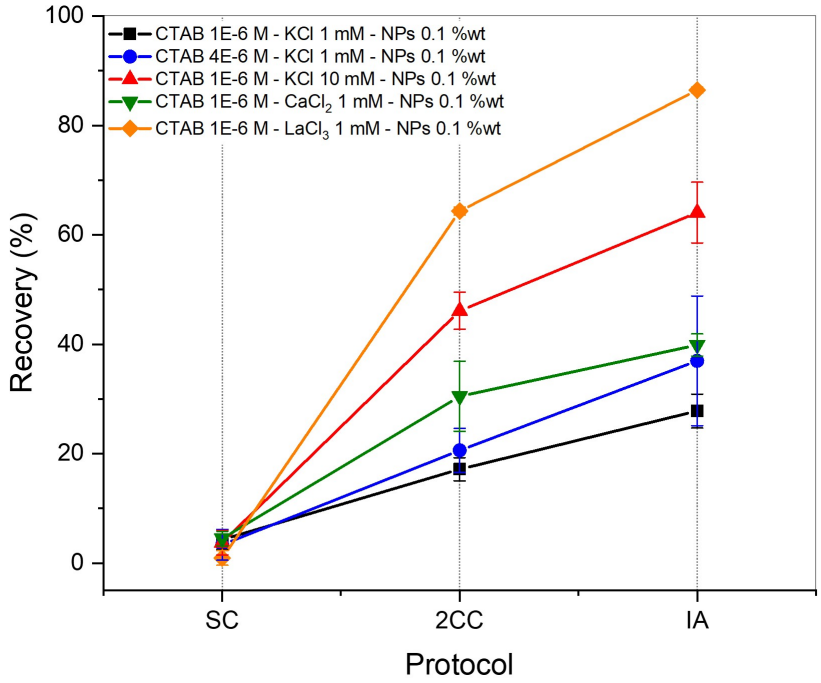

Figure 4.6: *Recovery % values calculated with Equation 4.4 for monolayer with different bulk composition and adopting the three different protocols. SC stands for subphase cleaning, 2CC for two consecutive compression, and IA for intermediate adsorption.*

The recovery obtained for the 2CC and IA protocols, with the first always lower than the second and both greater than zero, shows a clear bulk composition and time dependency.

Importantly, the higher the initial monolayer density, the greater the number of particles that desorb during the first compression. Since we have shown that the interparticle distance at the collapse point is independent of composition, the area at the first collapse (A_{C1}) increases with monolayer density, meaning that denser films collapse "earlier" in terms of area. Given that the area at maximum compression (C_{MC}) is constant across all samples, a larger A_{C1} naturally implies a higher number of desorbed particles, N_D, as described by Equation 4.2. Therefore, despite more particles being desorbed in denser packed monolayers, recovery still increases. Moreover, although denser monolayers lead to a greater number of desorbed nanoparticles, the observed trend of higher recovery for denser films cannot be attributed to this increased desorption, as confirmed by the SC results, where the recovery is zero, independently of the amount of desorbed nanoparticles. Finally, any re-adsorption occurs with the same number of nanoparticles remaining at the interface after the end of the first compression. In fact, although the initial monolayer density varies with composition, the number of particles at the end of the first compression cycle is, aside from possible effects due to partial monolayer amorphization, approximately the same for all samples. Since the macroscopic area at maximum compression (C_{MC}) is constant, and the area per particle at collapse ($a_{collapse}$) is also constant, then the total number of particles at C_{MC} (N_{MC}) must be equal. This implies that the differences in recovery cannot

be attributed to differences in the average monolayer density, but rather to different relaxation mechanisms, which ultimately affect the local microscopic density during re-adsorption.

When discussing the effect of bulk composition on the recovery capacity, it becomes immediately clear that recovery correlates with both the interfacial excess and the relaxation mechanisms observed via GISAXS data. Specifically, increasing the ionic strength, the cation charge, and the CTAB concentration, all of which enhance packing density, also leads to a more efficient recovery process.

However, one notable exception is the sample at 4×10^{-6} M CTAB, which deviates from the overall trend because, despite the higher CTAB concentration favoring the formation of progressively denser monolayers, the recovery between 1×10^{-6} and 4×10^{-6} M CTAB remains essentially the same within experimental error. This suggests that recovery is primarily governed by the underlying mechanism, largely dictated by the ionic strength and the counter-ion charges. Consequently, the bulk electrolyte composition once again emerges as the key parameter controlling interfacial interactions between nanoparticles.

In fact, we observed that for the samples with 1×10^{-6} and 4×10^{-6} M CTAB with 1 mM KCl, expansion results in a gradual and homogeneous increase in interparticle spacing. In contrast, for samples with KCl 10 mM, and $CaCl_2$ or $LaCl_3$ 1 mM, the particles form isolated clusters that remain densely packed even during expansion. In these systems, where particles spread uniformly upon expansion, the adsorption of additional nanoparticles requires cooperative rearrangement of the adsorbed monolayer to create available surface sites (Deshmukh et al., 2015). This process is typically kinetically limited, with the activation energy depending on the probability that a new particle encounters a free adsorption site, effectively controlled by how fast the existing particles can relax within the monolayer (Guzmán et al., 2022b).

On the contrary, when expansion leads to cluster formation, additional adsorption is facilitated by the presence of unoccupied surface regions. In this case, the activation energy for adsorption is mainly associated with the approach of an individual particle to the interface, rather than a collective rearrangement of the existing monolayer. Since the air-water interface is generally considered negatively charged, with the exact potential value still under debate (Gragson et al., 1997; Jungwirth et al., 2006), the adsorption barrier originates from the repulsion between negatively charged nanoparticles at the interface itself (Kettlewell et al., 2007) and it is also correlated to the formation of the image charge (Hatlo et al., 2008). Thus, the higher recovery observed for monolayers in the presence of KCl 10 mM, $CaCl_2$ or $LaCl_3$ 1 mM can be justified by the increased charge screening effect due to the higher ionic strength and cation charge and by the existence of the net attractive force above mentioned. See Figure 4.8 for a schematic illustration of the above proposed recovery mechanisms.

Noteworthy, by qualitatively comparing the trend in the electrophoretic mobility reported in Figure 3.3, we should expect the sample in the presence of $CaCl_2$ to be characterized by values of recovery in between the KCl 10 mM and $LaCl_3$ 1 mM. However,

it represents a clear deviation from the general trend, most likely because its recovery mechanism is intermediate between mechanisms *i*) and *ii*) described above. This interpretation is supported by the GISAXS patterns, which reveal the presence of two uncorrelated peaks (see Figure 4.7), a feature not observed in any of the other samples, which consistently display a single peak, sometimes very broad, but still unique (Figure C.11 to Figure C.14). Therefore, the interparticle distances reported in Figure 4.4 *G*, *H* represent an average of these two structural contributions. In particular, the peak appearing at lower q values is too weak to be reliably fitted and is largely overshadowed by the more intense peak at higher q. As a result, the averaged distance values do not capture the coexistence of two distinct structural organizations within the monolayer, which in turn explains why the recovery for $CaCl_2$ does not follow the expected trend. Consistently, the second compression cycle revealed the presence of isolated clusters within the monolayer, further supporting the hypothesis of a borderline recovery mechanism in this system.

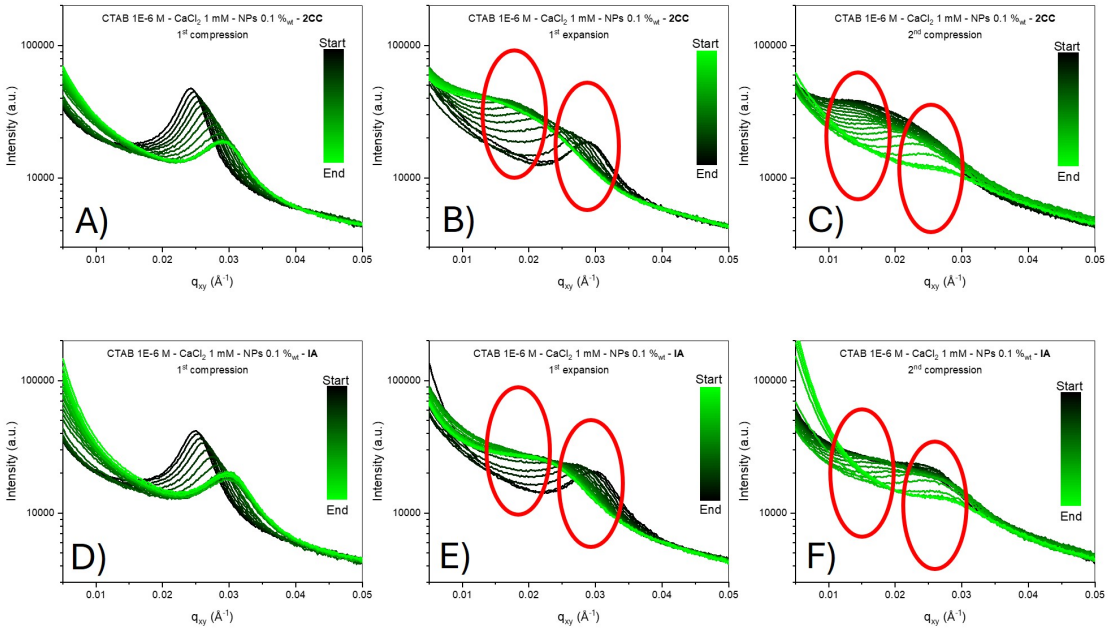

Figure 4.7: *Evolution of the horizontal cuts of the GISAXS pattern for sample CTAB* 1×10^{-6} *M - CaCl*$_2$ *- NPs 0.1* $\%_{wt}$ *during the first compression* (*A*, *D*)*, the expansion* (*B*, *E*) *and the second compression* (*C*, *F*) *by employing two consecutive compression* (2CC) *in* (*A*, *B*, *C*) *and intermediate adsorption* (*IA*) *in* (*D*, *E*, *F*) *protocols. The red circles mark the positions of the two independently evolving GISAXS peaks.*

As for the time dependency, the differences between the 2CC and IA protocols can be explained by taking into account the finite kinetics of adsorption. In fact, longer resting times promote a higher number of nanoparticles to adsorb. However, it must be pointed out that even when a resting time equal to that required for the complete formation of a homogeneous monolayer, *i.e.* 30 minutes, is provided, none of the tested conditions led to a 100% recovery, with the highest values obtained with $LaCl_3$ in the intermediate adsorption protocol of $\sim$ 90%. This incomplete recovery can be rationalized by considering that part of the interfacial configuration is established during the sample preparation step, when the pouring of the suspension into the Langmuir trough

generates bulk convective flows and local surface tension gradients. These gradients, in turn, induce Marangoni stresses that couple interfacial and bulk flows, providing additional mechanical energy to the system and transiently accelerating particle adsorption beyond the rate achievable under purely diffusion-limited conditions (Guzmán et al., 2022b; Duan et al., 2004). In the absence of such externally driven flows, as in the recovery stage, adsorption proceeds solely via Fickian diffusion, leading to slower kinetics and preventing full structural restoration within the accessible timescale.

4.2 Conclusion

In this chapter, we systematically investigated the ability of CTAB-functionalized silica nanoparticle monolayers to dynamically reorganize at the air–water interface following large deformation induced by monolayer mechanical collapse. By applying three complementary compression–expansion protocols and varying the bulk composition through changes in surfactant concentration, ionic strength, and cation valence, we were able to quantify the structural recovery of the monolayers in terms of a well-defined recovery percentage.

Our results reveal that re-adsorption of nanoparticles and subsequent monolayer reconfiguration is only possible in the presence of a bulk nanoparticle reservoir, and that the extent of recovery is significantly modulated by the physicochemical properties of the subphase and the time. Specifically, systems with higher ionic strength and multivalent counterions exhibit more efficient recovery, likely due to enhanced electrostatic screening and reduced interparticle repulsion. Two distinct relaxation mechanisms were identified: a homogeneous spreading of the monolayer during the expansion with a kinetically controlled re-adsorption, and a cluster-mediated rearrangement in which the resorption is likely guided by the single-particle activation energy (Figure 4.8). Moreover, we observed that the second reconfiguration mechanism leads to the highest recovery values. Importantly, these two mechanisms are governed by the nature of interparticle interactions within the monolayer. In particular, the second mechanism is only possible when the bulk composition, namely, high ionic strength or the presence of multivalent cations, favors the establishment of attractive forces between nanoparticles that promote and stabilize the existence of densely packed clusters. The case of $CaCl_2$ further suggests that the two mechanisms are not mutually exclusive: a mixed relaxation pathway is possible when the balance between attractive interparticle forces and those promoting spreading at the interface does not strongly favor either extreme.

However, while these findings provide important insights, they also highlight the complexity of the interfacial dynamics involved. Further investigations are necessary to clarify the microscopic mechanisms underpinning these relaxation modes and to correlate them more directly with specific nanoparticle properties induced by the bulk composition, such as surface charge distribution, aggregation behavior, or the role of the surfactant concentration in the monolayer relaxation and reconfiguration mecha-

nism. A deeper understanding of how these parameters control recovery kinetics and energetics would allow a more predictive design of responsive interfacial materials.

The relevance of these results extends beyond fundamental colloidal science. They provide a valuable framework for developing reconfigurable soft interfaces in a variety of technologies, including Pickering emulsions for drug delivery, adaptive liquid membranes for separation processes, and responsive all-liquid devices in soft robotics and sensing. In these applications, the ability of nanoparticle films to withstand mechanical stress and recover structural integrity is critical to performance and reusability. This work thus contributes not only to our understanding of interfacial nanoparticle assembly but also offers guiding principles for the design of resilient, functional soft interfaces.

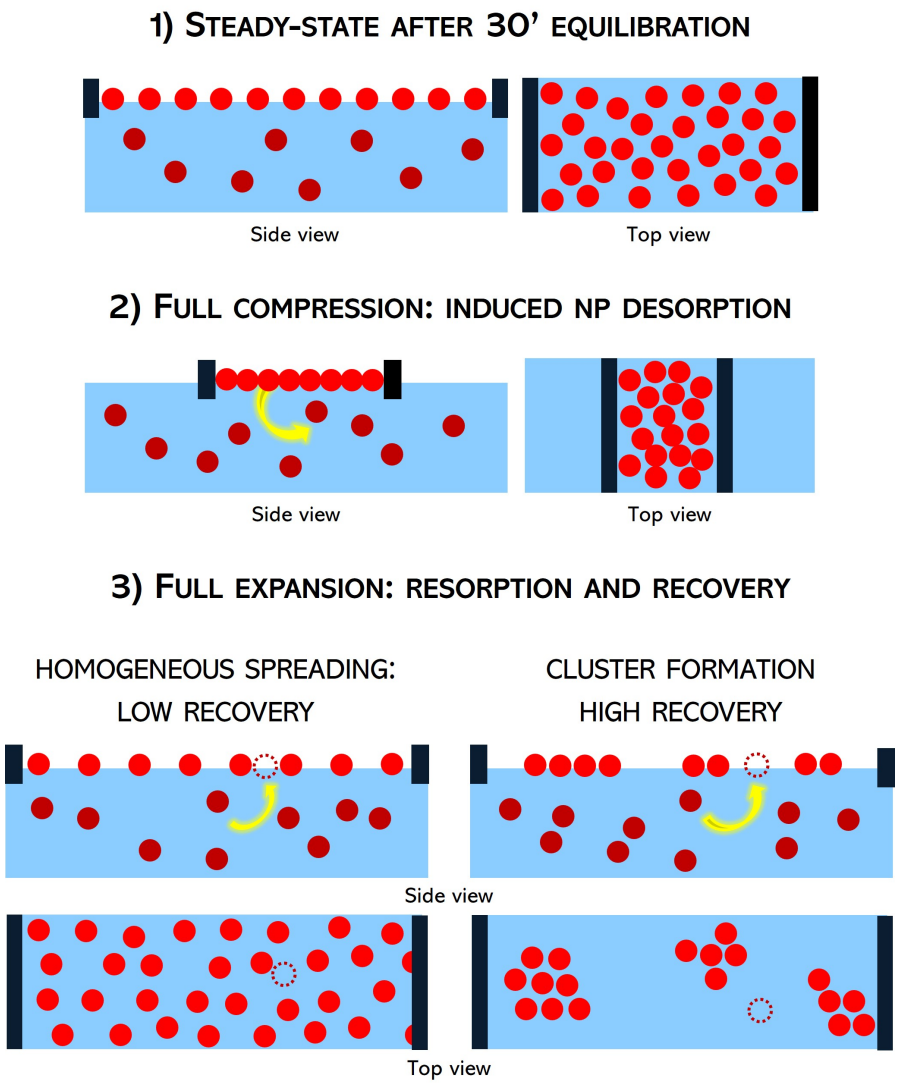

Figure 4.8: *Illustrative sketch of the recovery mechanisms discussed in the main text.*

This page intentionally left blank.

Section 2

This page intentionally left blank.

5

Protein-mediated assembly of silica nanoparticles at the air–water interface: steady-state regime

Proteins are among the most important natural amphiphiles found in biological and technological systems. Their ability to adsorb at fluid interfaces and reduce surface tension is central to a wide range of processes, including foam stabilization in food products, pulmonary surfactant function in the lungs, and the design of biocompatible formulations in pharmaceuticals and cosmetics (Zhang et al., 2022; Han et al., 2023; Schvartz et al., 2023). This interfacial activity arises from the distribution of hydrophobic and hydrophilic residues in their amino acid sequence and three-dimensional structure, which confers an intrinsic amphiphilic character allowing them to anchor simultaneously in both aqueous and air (or oil) environments (Hailing et al., 1981; G. G. Gochev et al., 2024).

The efficiency with which a protein stabilizes an interface, however, is far from universal. Globular proteins, stabilized by compact tertiary structures, may require partial unfolding before effectively lowering surface tension (Foster, 1977; Enders et al., 2023), whereas intrinsically disordered proteins (IDPs) can readily adapt to the interface due to their conformational flexibility (Marinova et al., 2013). Furthermore, the relative content of α-helices, β-sheets, and unstructured regions strongly influences how a protein organizes and reorients upon adsorption. Understanding the role of protein architecture in dictating interfacial properties is therefore of both fundamental and practical importance.

In recent years, there has been growing interest in combining proteins with inorganic nanoparticles (Kopp et al., 2017; Baimanov et al., 2019). Nanoparticles can modulate interfacial properties in several ways: they can compete with proteins for adsorption sites, act as anchoring points that reorganize protein conformations (Shourni et al., 2022), or similarly to classical surfactants promote the formation of densely packed

films with unique mechanical, optical, and rheological properties. Such protein–NP composites have potential applications in areas as diverse as food colloids, biosensors, nanomedicine, and functional coatings. Despite this, the molecular mechanisms governing how proteins and nanoparticles co-assemble at fluid interfaces remain incompletely understood, particularly under steady-state conditions where out-of-equilibrium structures dominate functionality.

In this chapter, we focus on the protein-mediated assembly of silica nanoparticles at the air–water interface. Silica nanoparticles were chosen as a model colloidal system due to their well-known surface chemistry (Kurtz-Chalot et al., 2017), chemical stability (Yang et al., 2018; Cruz Schneid et al., 2022) and well-characterized interaction with proteins in bulk (Galdino et al., 2020; Nairi et al., 2018; Bharti et al., 2014) and at the air-water interface with surfactants and polymers. To explore the influence of protein nature, we selected three representative proteins, namely Bovine Serum Albumin (BSA), β-Casein (BCN), and β-Lactoglobulin (BLG). Their three-dimensional structures, generated using PyMOL from the corresponding PDB entries, are shown in Figure 5.1.

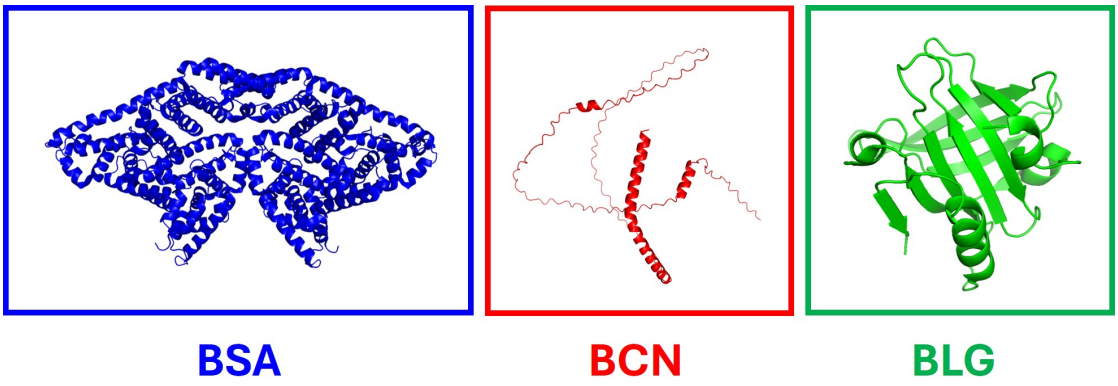

Figure 5.1: *Molecular structures of the proteins investigated in this work: (A) bovine serum albumin (BSA), (B) β-casein (BCN), and (C) β-lactoglobulin (BLG). The structural models were visualized using PyMOL from the corresponding Protein Data Bank (PDB) and AlphaFold Database entries: BSA (PDB ID: 3V03), β-casein (AlphaFold DB ID: AF-P28550-F1), and BLG (PDB ID: 1CJ5). The representations highlight the differences in molecular compactness and secondary-structure organization that underlie their distinct interfacial behaviors.*

BSA is a large, globular protein composed of 583 amino acid residues with a molecular weight of approximately 66.5 kDa. It belongs to the albumin family, which plays a central role in transport and osmotic regulation in blood plasma. Structurally, BSA consists of three homologous domains (I–III), each further divided into subdomains A and B, resulting in an overall prolate ellipsoidal shape (Foster, 1977). Its secondary structure is dominated by α-helices (~55–65%), with a smaller fraction of β-sheets and turns. The protein is stabilized by 17 intramolecular disulfide bonds, which confer high rigidity and resistance to unfolding (Varga et al., 2016). From the perspective of interfacial behavior, BSA is moderately amphiphilic: while its hydrophobic patches enable adsorption at the air–water interface, the compact tertiary structure means that partial

unfolding or reorientation is often necessary to achieve strong surface activity (Cho et al., 1996). BSA has an isoelectric point around pH 4.7, and at neutral pH it carries a net negative charge (Foster, 1977). Its robustness and well-documented interfacial properties make BSA a classical model protein for studying adsorption, protein–particle interactions, and conformational changes at fluid interfaces.

BCN is an intrinsically disordered protein (IDP) with a molecular weight of about 24 kDa. Unlike globular proteins, BCN lacks a well-defined tertiary structure due to the absence of disulfide bonds and the presence of a flexible amino acid sequence rich in proline and charged residues. Its architecture is highly amphiphilic: the N-terminal region is strongly hydrophilic, while the C-terminal domain is predominantly hydrophobic (Huppertz et al., 2018). This block-like arrangement allows BCN to behave similarly to synthetic surfactants, orienting its hydrophobic domain toward the air phase and keeping its hydrophilic domain solvated in water (J. R. Hunter et al., 1991). Such structural flexibility makes BCN an extremely efficient stabilizer of foams and emulsions, as it can rapidly adsorb and rearrange at interfaces without the energetic penalty of unfolding (Atkinson et al., 2007). Its isoelectric point is near pH 5.1, and at neutral pH the protein carries a net negative charge (Huppertz et al., 2018), facilitating electrostatic interactions with cationic or polar surfaces but leading to repulsion from negative ones unless cooperative effects are present. The disordered nature of BCN, combined with its strong amphiphilic character, provides an interesting contrast to globular proteins, making it a model system to study how conformational flexibility influences NP-mediated assembly.

BLG is a globular whey protein with 162 amino acids and a molecular weight of approximately 18.4 kDa. It is the major whey protein in bovine milk and belongs to the lipocalin family, known for their ability to bind and transport hydrophobic ligands. Its tertiary structure is characterized by a β-barrel, commonly referred to as a "calyx," which serves as a binding pocket for fatty acids, retinol, and other small hydrophobic molecules (Kuwata et al., 1999). The protein also contains a short α-helix and several turn regions, but its secondary structure is predominantly β-sheet (~50%) (Creamer et al., 1983).BLG exhibits a pH-dependent structural behavior, where at neutral pH (near its isoelectric point, ~5.2) it is dimeric, while at acidic or alkaline pH it exists primarily in monomeric form (Hector L Casal et al., 1988). This pH sensitivity influences its interfacial activity (Beierlein et al., 2015; Engelhardt et al., 2013). Compared to BSA or BCN, BLG is less flexible and tends to retain its β-barrel architecture upon adsorption at the air–water interface. Its amphiphilicity is therefore weaker and more constrained by the β-barrel fold, making it a less efficient surfactant (Suttiprasit et al., 1992).

Although all three proteins carry a net negative charge at neutral pH (being above their isoelectric point), their surface charge distribution is far from homogeneous. Proteins typically display heterogeneous electrostatic landscapes, with localized "patches" of positive charge arising from lysine, arginine, and histidine residues exposed at the surface. These positively charged domains can mediate attractive interactions with negatively charged substrates such as silica, effectively overriding the repulsion ex-

pected from the overall net charge (Gonzalez-Posada et al., 2024; Uttinger et al., 2022; Pérez-Fuentes et al., 2017). In addition, hydrophobic patches may contribute to adsorption by promoting local dehydration of the solid surface, a phenomenon that has been observed in silica–protein systems through contact angle measurements and foam studies (Giefer et al., 2023; Wahlgren et al., 1990; M. Chen et al., 2018). As a result, protein adsorption at negatively charged interfaces cannot be understood solely in terms of net charge considerations, but must be viewed as the outcome of a balance between electrostatics, hydrophobic interactions, and conformational adaptability.

By systematically varying the protein-nanoparticle bulk ratio and the ionic strength, we aim to unravel how protein type and environmental conditions dictate the structure, density, and stability of protein–NP films. To achieve this, a multi-scale experimental approach was employed: dynamic surface tension (DST) measurements provided macroscopic insights into adsorption kinetics and steady-state interfacial activity; Grazing-incidence small-angle X-ray scattering (GISAXS) probed the lateral organization of nanoparticles within interfacial monolayers; Neutron reflectometry (NR) delivered depth-resolved structural information, with particular attention to protein partitioning across the NP monolayer, and finally, vibrational sum-frequency generation (SFG) spectroscopy revealed molecular-level details of protein secondary structure, side-chain orientation, and interfacial hydration.

Together, these techniques enable us to connect molecular-scale conformational changes with mesoscopic organization and macroscopic functionality. The comparative analysis of BSA, BCN, and BLG provides not only a mechanistic understanding of protein-specific effects but also broader design principles for the rational engineering of bio-nano hybrid interfaces with tailored properties.

5.1 Results and Discussion

5.1.1 Surface Tension

To relate the macroscopic interfacial properties of protein and protein–NP films to their microscopic organization, we first characterized surface tension. Measurements were carried out over 1 h for samples prepared following two experimental protocols (see Section D.1). In protocol *i*), the NP concentration was fixed at 0.1%$_{wt}$ (10 mM NaCl), while protein concentration was varied between 0.0625 and 1 μM, yielding protein:NP bulk ratios from 0.5:1 to 8:1. In protocol *ii*), the protein concentration was fixed at 1 μM and the NP content varied between 0.1 and 1.6%$_{wt}$, thus covering the same range of bulk ratios.

After 1 h of adsorption, all proteins displayed the same trend in protocol *i*): increasing protein concentration systematically decreased surface tension (Figure 5.2), consistent with a quasi-equilibrium adsorption mechanism in which higher bulk concentration promotes more interfacial adsorption. At equal concentration, the surface activity followed the order BCN > BSA ≈ BLG, which well correlates with the relative

surface activity and amphiphilicity of the three proteins (Pérez-Fuentes et al., 2017). However, in all cases, the presence of silica NPs ($0.1\%_{wt}$) led to higher steady-state surface tension compared to the protein-only samples. A similar increase was observed in protocol *ii*), where raising NP concentration at fixed protein content progressively increased surface tension.

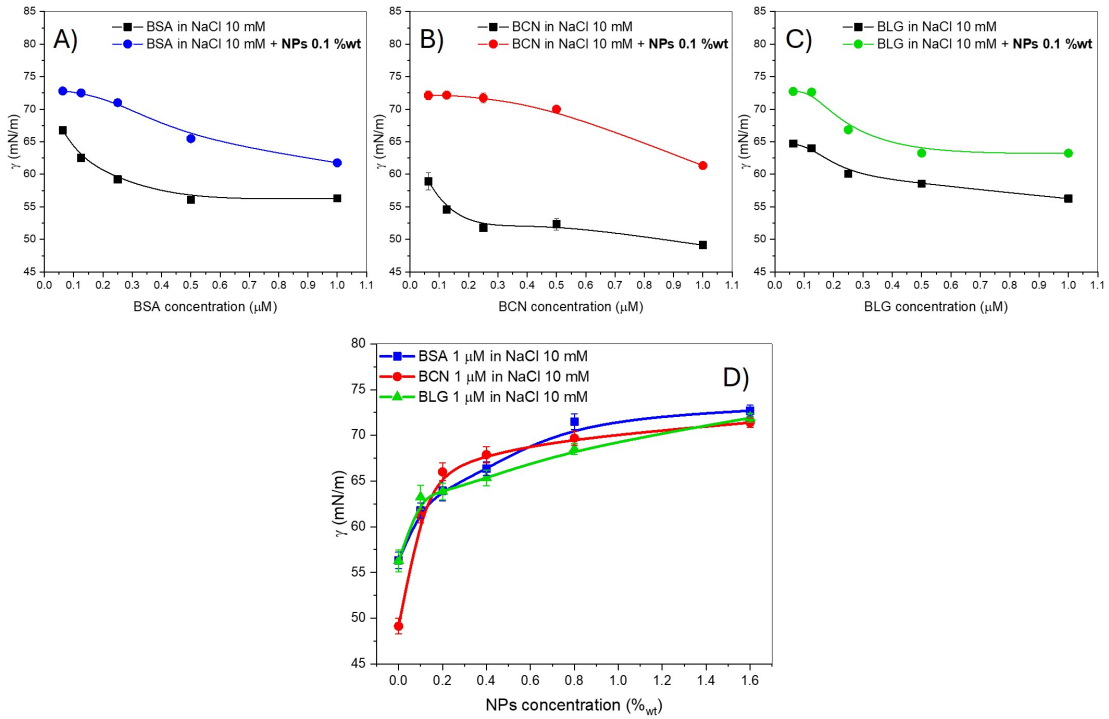

Figure 5.2: *Evolution of the steady-state surface tension (γ) after 1 h of adsorption for sample prepared at variable protein concentration (A, B, and C) and variable NPs concentration (C). The sample was prepared by fixing the ionic strength at 10 mM in the absence (black squares) and in the presence (colored points) of NPs 0.1 $\%_{wt}$ and modulating the concentration of (A) BSA, (B) BCN. and (C) BLG in the range 0.0625-1 μM. The sample in (D) was prepared by fixing the protein concentration at 1 μM and varying the NP concentration from 0 to 1.6 $\%_{wt}$ at the ionic strength of 10 mM. Solid lines are guides for the eyes.*

Adsorption isotherms (γ vs concentration) further revealed protein-specific effects. For BSA and BCN, the presence of NPs markedly altered the isotherm shape, indicating that NP–protein interactions modify both the adsorption mechanism and interfacial structuring. In contrast, BLG displayed nearly identical isotherm profiles with or without NPs, although the absolute γ values were higher in the NP-containing samples. This suggests that BLG–NP complexes are less efficient in lowering surface tension but follow the same adsorption mode.

Dynamic surface tension (DST) curves, reported in Figure D.1 corroborated this picture. For BSA and BCN without NPs, the curves exhibited the typical two-step profile: a slow diffusion-limited regime followed by a faster kinetic adsorption stage, which is a well-established behavior for protein adsorption kinetics at fluid interfaces (Miller et al., 2000; Bos et al., 2001; Lucassen et al., 1972). However, in the presence of NPs this behavior disappeared, with adsorption reduced to a single rapid drop fol-

lowed by arrest at the steady-state. The modification of the adsorption dynamics in the presence of nanoparticles suggests a strong protein–NP interaction, sufficient to alter the kinetic pathway of interfacial adsorption (Shourni et al., 2022). By contrast, BLG maintained the two-step profile in both conditions, though adsorption kinetics were slowed in the presence of NPs, indicating that NP interactions reduce adsorption efficiency without altering its fundamental pathway.

Finally, the effect of the ionic strength in the range 1-50 mM was investigated on BSA-NP sample at the bulk BSA:NP ratio 1:1 with samples prepared both with protocol *i*) and *ii*) (Figure 5.3). In both cases, the increase in the ionic strength has negligible influence on the equilibrium surface tension. In both protocols, the equilibrium values were primarily determined by protein adsorption, being higher for BSA 0.1251 μM than 1 μM as expected, but with the same value independently of the ionic strength. However, in the presence of NPs, surface tension remained close to that of pure water for all the tested compositions, suggesting a dominant effect of nanoparticles in suppressing the interfacial activity of proteins. The only substantial difference observed was that increasing ionic strength promoted faster adsorption kinetics, as evidenced by the DST data in Figure D.2, in agreement with previous reports that electrostatic screening accelerates protein adsorption at fluid interfaces (Yan et al., 2000) and with the results reported in Chapter 4.

These results suggest that the systematic increase in equilibrium surface tension in the presence of NPs may originate from two, not mutually exclusive, mechanisms: (*i*) protein–NP interactions reduce the amount of free protein available for interfacial adsorption, thereby lowering surface coverage; or (*ii*) adsorption of protein–NP complexes leads to conformations that are less surface-active than those adopted by free proteins.

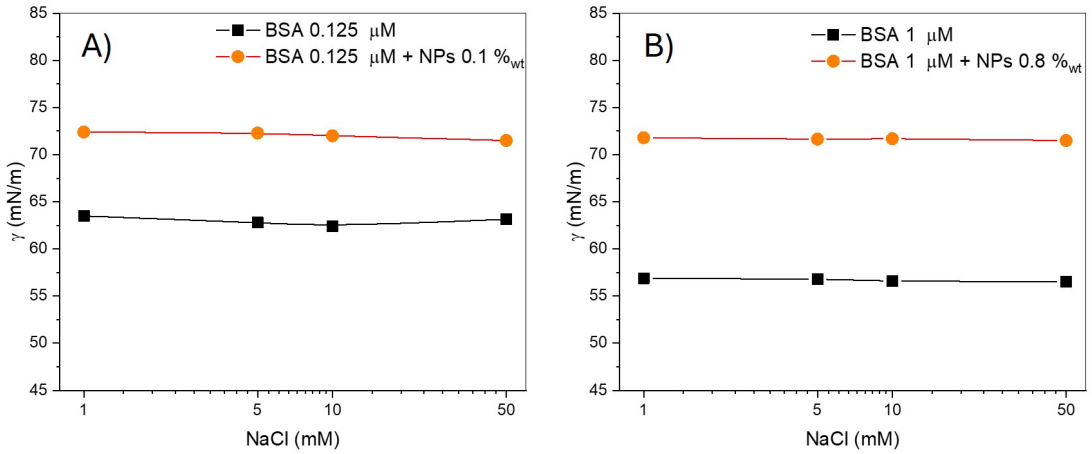

Figure 5.3: *Evolution of the steady-state surface tension γ after 1 h of adsorption as a function of the ionic strength for NaCl. The BSA:Np bulk ratio was fixed to 1:1 and the ionic strength investigated in the range 1-50 mM. In A) BSA 0.125 µM - NPs 0.1 $\%_{wt}$ and B) BSA 1 µM - NPs 0.8 $\%_{wt}$.*

5.1.2 GISAXS

Grazing-incidence small-angle X-ray scattering (GISAXS) was employed to probe the interfacial organization of silica nanoparticles in the presence of different proteins. The scattering patterns reported in Figure D.3, D.4 and D.6, consistently revealed the presence of a single nanoparticle monolayer at the air–water interface: a characteristic Bragg peak was detected along q_{xy}, while no distinct features appeared along q_z. This confirms that the particles arrange predominantly in a two-dimensional configuration without multilayer stacking. Moreover, comparing the GISAXS patterns of protein–NP monolayers with those of CTAB–NP monolayers (Appendix B and Ruffino et al., 2022) reveals that the former are significantly broader and lack higher-order scattering peaks. This indicates that the presence of proteins leads to the formation of more disordered monolayers, characterized by reduced short-range order.

From the position of the in-plane Bragg peak, the interparticle distance was extracted under two experimental protocols: (i) varying the protein concentration at a fixed NP concentration of 0.1% w/w, and (ii) fixing the protein concentration at 1 μM while progressively increasing NP concentration (see Section D.1 for further details). The behavior observed was strongly protein-dependent, as reported in Figure 5.4.

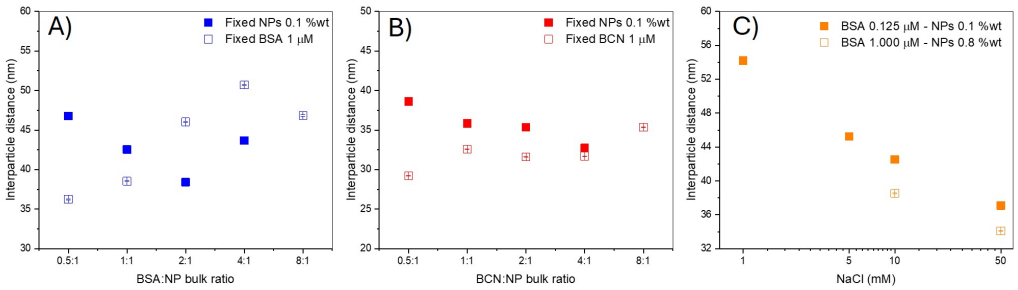

Figure 5.4: *Monolayer interparticle distance for A) different BSA:NP bulk ratio obtained by fixing the NPs concentration to 0.1 $\%_{wt}$ and varying the BSA concentration in the range 0.0625-1 μM (blue filled squares) and fixing the the BSA concentration to 1 μM and varying the NPs concentration from 0.1 to 1.6 $\%_{wt}$ (blue open squares); B) different BCN:NP bulk ratio obtained by fixing the NPs concentration to 0.1 $\%_{wt}$ and varying the BCN concentration in the range 0.0625-1 μM (red filled squares) and fixing the the BCN concentration to 1 μM and varying the NPs concentration from 0.1 to 1.6 $\%_{wt}$ (red open squares); C) fixed BSA:NP bulk ratio to 1:1 with BSA 0.125 μM - NPs 0.1 $\%_{wt}$ (orange filled squares) and BSA 1 μM - NPs 0.8 $\%_{wt}$ (orange open squares). in A) and B) the ionic strength was 10 mM in NaCl. In C) the ionic strength was varied in the range 1-50 mM NaCl.*

For bovine serum albumin (BSA), the interparticle distance as a function of protein concentration displayed a non-monotonic trend with a pronounced minimum (filled blue squares in Figure 5.4*A*). At low BSA concentrations, increasing protein content reduced the interparticle distance, consistent with a cooperative effect in which the presence of protein promotes the adsorption of a larger number of nanoparticles at the interface. At higher BSA concentrations (above a bulk protein:NP ratio of ~2:1), the opposite effect was observed: further increases in BSA concentration led to an increase in interparticle spacing, indicative of a decrease in NP surface coverage. Several mech-

anisms may account for this behavior: (i) increasing BSA concentration may lead to the formation of protein–NP complexes with a more hydrophilic character, thereby reducing their surface activity; (ii) the thickness of the protein shell adsorbed onto the nanoparticles may increase, enforcing larger separations between neighboring particles; (iii) free BSA molecules may adsorb directly at the air–water interface, competitively displacing nanoparticles.

When instead the protein concentration was kept constant at 1 μM and the NP concentration was progressively increased, and thus the BSA:NP bulk ratio decreased, the interparticle distance decreased in an overall monotonic manner, indicating that a higher surface density of nanoparticles is obtained (open blue squares in Figure 5.4*A*). Overall, BSA yielded monolayers with interparticle distances ranging from ~47 to 37 nm in the first protocol and from ~35 to 53 nm in the second. These results highlight that controlling NP concentration at constant BSA allows finer tuning of the monolayer density.

For β-casein (BCN), a similar cooperative-to-competitive behavior was observed, though significantly less pronounced (filled red squares in Figure 5.4*B*). The competitive regime emerged only at much higher bulk ratios, i.e. BCN:NP > 4:1. Conversely, increasing NP concentration at fixed 1 μM protein again produced a progressive reduction in interparticle spacing (open red squares in Figure 5.4*B*). Overall, BCN led to denser monolayers than BSA, with interparticle distances between 28 and 38 nm. This indicates a higher efficiency of BCN in promoting NP adsorption, which can be attributed to its stronger amphiphilic character and smaller molecular size compared to BSA, allowing nanoparticles to approach each other more closely at the interface.

A strikingly different behavior was observed for β-lactoglobulin (BLG). GISAXS patterns consistent with the formation of a nanoparticle monolayer were detected only at one specific condition, namely BLG 1 μM with NP concentration of 0.8%$_{wt}$ and NaCl 10 mM (bulk ratio 1:1). In all other cases, no Bragg peaks were observed, indicating the absence of correlation and ordering of nanoparticles at the interface. The monolayer obtained at this condition exhibited an interparticle distance of ~42.5 nm, which is considerably larger than the distances obtained at the same concentrations with BSA (38 nm) and BCN (32.5 nm). When considered together with the DST results, these findings suggest that BLG–NP interactions hinder the formation of compact, densely packed monolayers. While BLG still adsorbs at the interface and reduces surface tension, its adsorption mechanism remains largely unaltered by the presence of NPs, as indicated by the preserved two-step kinetic profile in the DST curves. The higher equilibrium surface tension values and the larger interparticle distances observed in GISAXS both point to weaker interfacial activity of BLG–NP complexes and a reduced ability of BLG to promote dense nanoparticle packing compared to BSA and BCN.

The influence of ionic strength on the organization of BSA–NP monolayers was investigated in the presence of BSA by varying the NaCl concentration between 1 and 50 mM, for bulk protein:NP ratios of 1:1 (orange squares in Figure 5.4*C*). Two conditions were explored: (i) fixed NP concentration (0.1% w/w) with varying BSA, and

(ii) fixed BSA concentration (1 μM) with varying NP content. In both cases, increasing ionic strength led to a progressive decrease in interparticle distance, following an approximately linear dependence on the logarithm of ionic strength. The interparticle spacing decreased from about 55 nm at 1 mM NaCl to about 37 nm at 50 mM NaCl.

Interestingly, for the samples at 0.8% NP with 1 μM BSA, the interparticle distance was consistently smaller compared to the 0.1% NP with 0.125 μM BSA case, even though both correspond to a 1:1 bulk ratio. This difference indicates that the absolute concentrations of protein and nanoparticles, and thus the local packing and interfacial crowding, influence the final arrangement of the monolayer in addition to the bulk ratio itself.

The linear dependence of interparticle spacing on $\log(I)$, where I is the ionic strength, clearly points to an electrostatic origin of the effect: increased ionic strength screens the repulsive electrostatic interactions between negatively charged nanoparticles and protein–NP complexes, thereby allowing denser packing at the interface. This interpretation is consistent with the discussion presented in Chapter 2, 3 and 4.

5.1.3 Neutron reflectometry (NR)

Before discussing the neutron reflectivity (NR) results, preliminary small-angle neutron scattering (SANS) experiments were performed on both the bare nanoparticles and BSA in bulk solution at the ionic strength of 10 mM (NaCl). This pre-characterization was necessary in order to (i) correlate the bulk structure with the interfacial organization and (ii) determine the size distribution of nanoparticles to be used as fixed input parameters in the physical model described in Appendix H.

SANS measurements on silica nanoparticles reported in Figure 5.5*A* were performed in two solvent contrasts (D_2O/H_2O = 93:7 and 100% H_2O). The scattering data for the two contrasts were co-fitted with a polydisperse hard-sphere model assuming a Gaussian distribution of particle radii (Royall et al., 2013). The results yielded a mean radius of $r = 116.2$ Å with a polydispersity index (PDI) of 0.213 , corresponding to a Gaussian standard deviation $\sigma = 24.8$ Å(with PDI = σ/r). Moreover, the absence of any structure factor demonstrated the homogeneity of the dispersion without any appreciable aggregation.

The scattering profile of BSA in 100% D_2O (Figure 5.5 *B*) was fitted using a tri-axial ellipsoid model (Pedersen, 1997). The extracted semi-axes were $R_a = 74.4 \pm 2.1$ Å, $R_b = 33.9 \pm 1.06$ Å, and $R_c = 14.2 \pm 0.3$ Å. These values are in excellent agreement with the dimensions typically reported in the literature for BSA (Wu et al., 2020; T. Wang et al., 2023).

Neutron reflectometry characterization was performed at the INTER reflectometer of the ISIS pulsed neutron source as detailed explained in Section D.1.5. We firstly investigated the bare air-water interface by co-fitting the reflectivity curves of the three contrast solvents, namely D_2O, SiO_2MW and BSAMW (Figure D.6), using an error function to account for the Gaussian roughness of the surface ($\sigma_{a/w}$) induced by the

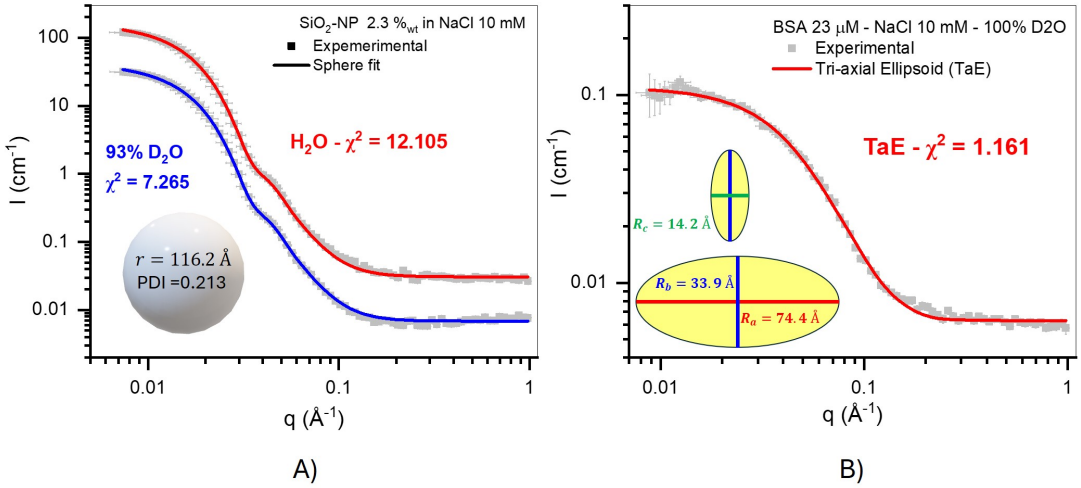

Figure 5.5: *Small Angle Neutron Scattering (SANS) curves (square) and corresponding fit (lines) for: A) NPs 2.3 $\%_{wt}$ in NaCl 10 mM at the solvent contrast $D_2O/H_2O = 93{:}7$ (blue curves) and 100% H_2O (red curves); B) BSA 23 μM in NaCl 10 mM in 100% D_2O.*

capillary-waves thermal motion. Further details on the fitting model can be found in Appendix H. The obtained roughness $\sigma_{a/w} = 2.6$ Åis in good agreement with the predicted capillary-wave amplitude of 2.3 Åfor an interface with $\gamma = 72.5$ mN/m at 25 °C and an instrument resolution of $\sim 3\%$ (Fukuto et al., 2016).

We then performed NR characterization of BSA layers adsorbed at the air–water interface at two concentrations: 0.125 μM and 1 μM, in 10 mM NaCl. The data, reported in Figure 5.6 were analyzed using a multilayer slab model, as described in Appendix H.

From the fits, three structural parameters were obtained for each slab: thickness (d), roughness (σ), and hydration fraction $(h\%)$ which are reported in Table 6.1. From these, the interfacial excess and the molecular area per molecule (APM) could be calculated (values reported in Table 5.1). The surface excess Γ corresponds to the mass of adsorbed protein per unit interfacial area and can be expressed as:

$$\Gamma = \rho_{BSA} \cdot d \cdot (1 - h\%) = [g/cm^2], \tag{5.1}$$

where ρ_{BSA} is the mass density of BSA that was taken equal to 1.35 ± 0.1 g/cm^3 (Fischer et al., 2004), d the thickness of the adsorbed layer, and $(1 - \%h)$ is the dry fraction of protein in the layer. The last two terms are obtained with the reflectivity curves fitting.

From the surface excess, the occupied area per molecule APM can be calculated as the reciprocal of the number of molecules per unit area:

$$APM = \frac{MW_{BSA}}{N_A \cdot \Gamma \cdot (1 - \frac{\sigma}{d})} = [nm^2/molecule] \tag{5.2}$$

where $MW_{BSA} = 66496 g/mol$ is the BSA molecular weight, N_A is the Avogadro number, and σ is the layer roughness. The values of surface excess and APM are reported in Table 5.1

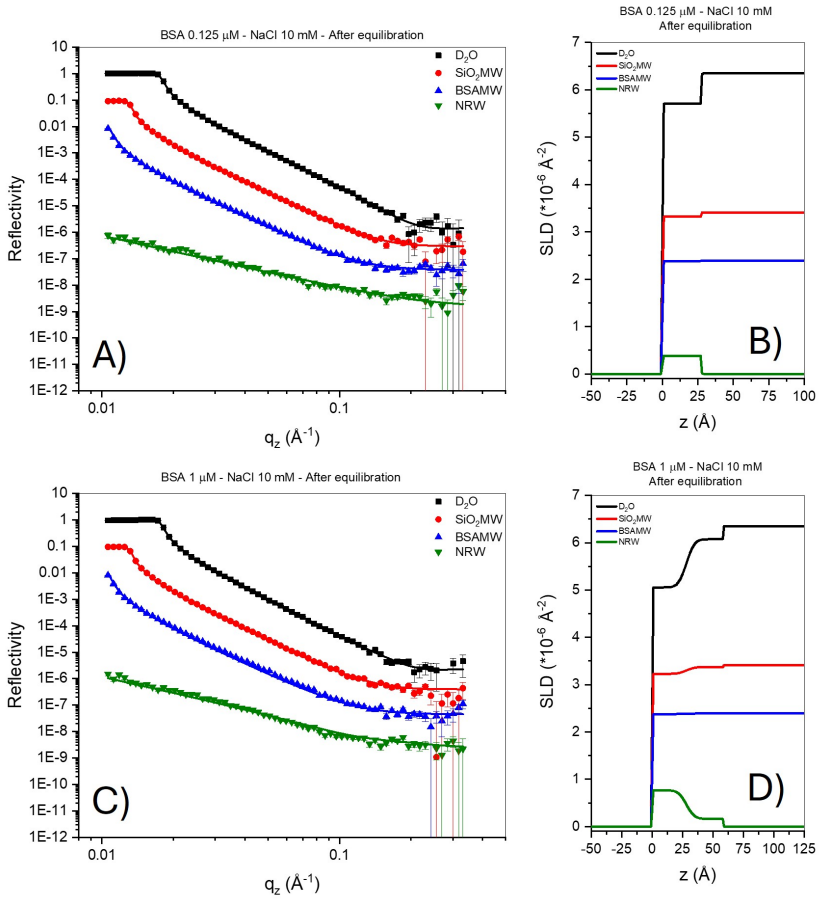

Figure 5.6: *Experimental Reflectivity curves (colored point) with the corresponding fit (solid lines) (A,C) and the corresponding SLD profile (B,D) for systems prepared at the bulk composition (A,B) BSA 0.125 µM - NaCl 10 mM and (C,D) BSA 0.125 µM - NaCl 10 mM. The different contrast solvents used are highlighted by the color curves. Specifically black curves refers to reflectivity acquired in 100 % D_2O ($SLD = 6.356 \times 10^{-6}$ Å^{-2}), red in SiO_2 match-water (SiO_2MW, 57.45% D_2O 42.55% H_2O, $SLD = 3.41 \times 10^{-6}$ Å^{-2}), blue in BSA match water (BSAMW, 42.55% D_2O 57.45% H_2O, $SLD = 2.395 \times 10^{-6}$ Å^{-2}), and green in null-reflecting water (NRW, 8.1% D_2O 91.9% H_2O, $SLD = 0$ Å^{-2}).*

Table 5.1: *Surface excess (Γ) and area per molecule (APM) of the BSA layers at the air-water interface. The numbers in parentheses indicate the uncertainty in the value.*

Sample	1st layer		2nd layer	
	Γ (ng/cm^2)	AMP (nm^2/molecule)	Γ (ng/cm^2)	AMP (nm^2/molecule)
BSA 0.125 uM - NaCl 10 mM	73.38(10.9)	150.4(22.3)	-	-
BSA 1 uM - NaCl 10 mM	149.20(27.1)	74.0(13.4)	34.36(5.6)	311.4(51.1)

At the lower concentration of 0.125 μM, the protein forms a single compact monolayer of thickness d~27.6 Å. This thickness is consistent with the major and medium axis (a and b) lying parallel to the interface and the minor axis (c) oriented perpendicularly. The interfacial excess was found to be 73.8 ng/cm^2, corresponding to an APM of 150.4 nm^2/molecule.

At the higher concentration of 1 μM, together with a first layer of a thickness d~28.1 Å a second diffuse layer (d~30.3 Å) developed beneath the first, consistent with saturation of the primary layer. The first layer showed an interfacial excess of ~149 ng/cm^2 (APM $\approx$ 74 nm^2/molecule), while the second layer contributed an additional inter-

facial excess of ~34 ng/cm^2 (APM ≈ 311 nm^2/molecule). This stratification and the corresponding structural parameters are consistent with previously reported studies on BSA adsorption at the air–water interface (Lu et al., 1999b).

Importantly, these results indicate that BSA does not undergo major structural rearrangements upon interfacial adsorption. This conclusion is supported by the SANS-derived ellipsoidal dimensions: if the minor axis c is oriented perpendicularly to the interface, the projected area per molecule given by the ellipse defined by semi-axes a and b is 79.4 ± 4.7 nm^2/molecule. This value is in very good agreement with the APM obtained from NR of the 1 μM BSA sample, which shows that the second diffused layer is formed when the AMP of the first layer reaches a value of ≈ 74 nm^2/molecule, thus when BSA molecules in the first layer are in contact with one another. This suggests that the protein retains its globular architecture upon adsorption and is consistent with literature evidence that BSA maintains its structural rigidity at interfaces due to the stabilizing effect of intramolecular disulfide bonds (Noskov et al., 2010; Lu et al., 1999a).

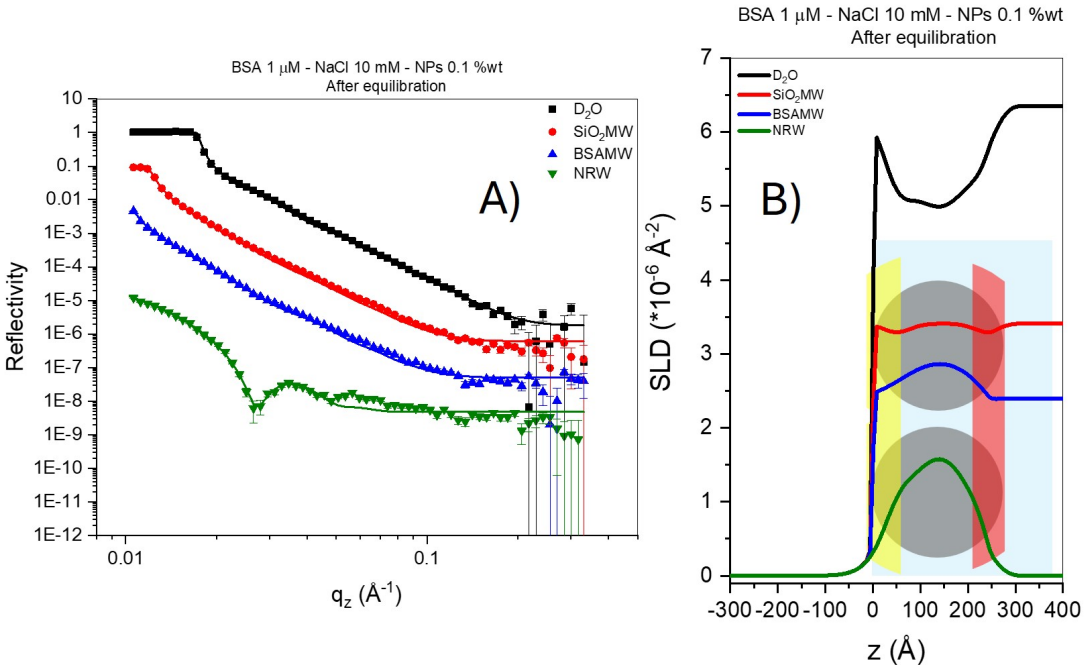

Figure 5.7: *A) Representative reflectivity curves of BSA-NP monolayer obtained with bulk concentration BSA 1 µM - NaCl 10 mM and NPs 0.1 %$_{wt}$, together with the corresponding SLD profile obtained by the fitting of the experimental reflectivity curves (B). The different contrast solvents used are highlighted by the color curves. Specifically black curves refers to reflectivity acquired in 100 % D_2O ($SLD = 6.356 \times 10^{-6}$ Å^{-2}), red in SiO_2 match-water (SiO_2MW, 57.45% D_2O 42.55% H_2O, $SLD = 3.41 \times 10^{-6}$ Å^{-2}), blue in BSA match water (BSAMW, 42.55% D_2O 57.45% H_2O, $SLD = 2.395 \times 10^{-6}$ Å^{-2}), and green in null-reflecting water (NRW, 8.1% D_2O 91.9% H_2O, $SLD = 0$ Å^{-2}). In B) is represented a sketched cartoon of the NP and BSA distribution at the interface.*

Further, we investigated the mixed BSA–NP layers of the samples with bulk composition BSA 0.125, 0.25, and 1 μM, NPs 0.1 %$_{wt}$ and NaCl 10 mM. The obtained reflectivity curves, together with their corresponding SLD profiles are reported in Figure D.9, D.10, and D.11, while in Figure 5.7 is reported a representative sample to help with the

results discussion. In the presence of nanoparticles, the reflectivity curves (Figure 5.7) acquired in null-reflecting water (NRW) contrast show a marked feature at $q_z \sim 0.028$ Å^{-1}, corresponding to a layer thickness $d = 2\pi/q_z \sim 224.4$ Å. This confirms what was already observed by GISAXS, namely that NP assembly at the interface results in the formation of a single NP monolayer rather than a multilayered structure. Detailed information on the structure and composition of the mixed protein–NP monolayers was obtained by fitting the reflectivity curves with the physical model explained in Appendix H. The fitting results are reported in Table D.1, D.2, and D.3.

From these fits it was possible to accurately determine the immersion depth (h) of the nanoparticles within the interfacial monolayer. Independently of the bulk composition, the immersion depth was found to be about 24–25 nm, showing that the nanoparticles are fully immersed in the aqueous phase and do not protrude from the air–water interface. In addition, the NP volume fraction, ϕ_{np}, relative to the theoretical value for a perfectly hexagonally packed monolayer ($\phi_{np} = 1$), is ~0.5 at the lowest BSA concentration and increases to ~0.7 for the two higher concentrations. This is consistent with the GISAXS patterns, which exhibit a very broad Bragg peak and no higher-order scattering peaks, confirming the absence of long-range order in the monolayer.

Turning to the protein structure, the only way to satisfactorily reproduce the NR data was to model the protein-NP complex as a core–shell object, with two distinct shells: one facing air and one facing water. Each shell extends along the z profile in the region $z_i - w_i/2 < z < z_i + w_i/2$, where z_i is the position of the shell with respect to the NP center and w_i its thickness in the z direction (see Appendix H for a detailed description). The shell facing air is located ~8–9 nm above the NP center (z_{air}), while the shell facing water lies ~11–13 nm below it (z_{water}). This suggests two important points: (i) the contact with the air–water interface occurs through the protein shell facing air; and (ii) in the interparticle region the protein concentration is negligible.

The shell thicknesses along z (w_i) are consistently in the range of 3.5–5.5 nm, whereas the radial thickness t_i depends strongly on protein concentration. In particular, t_{air} increases with BSA concentration, being 7.39±0.32, 8.94±0.3, and 10.74±0.59 nm for 0.125, 0.25, and 1 μM, respectively, while t_{water} remains almost constant with values of 7.78±0.08, 8.13±0.89, and 7.18±0.85 nm. This indicates that the increase in protein content leads to an asymmetric growth of the protein shell, mainly towards the air side, which is consistent with the tendency of BSA to adsorb preferentially at the air side to reduce the surface tension. However, despite the progressive increase in t_{air}, this alone does not account for the larger interparticle distance observed in the GISAXS data for the BSA-rich sample (BSA:NP > 2:1). As clearly illustrated in Figure 5.8, there remains a considerable amount of free space that could, in principle, be occupied by additional BSA–NP complexes.

Besides providing structural insights, the model also allowed us to estimate both the BSA:NP ratio at the interface and the surface excess of protein for the different compositions investigated. The BSA:NP ratio was calculated as the ratio between the volumes of the protein shells (V_{air} and V_{water}) and the molecular volume of BSA, ob-

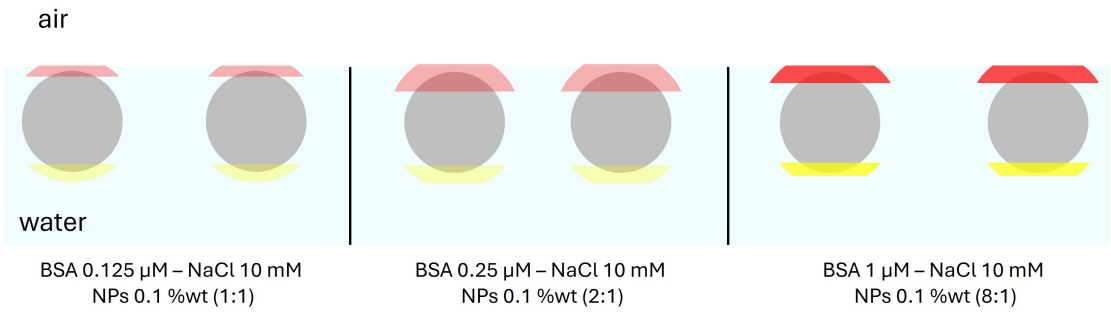

Figure 5.8: *In scale illustration of the geometrical distribution of the BSA-NP complexes adsorbed at the air-water interface as obtained by NR fitting with the physical model described in Section H.5. In gray are represented the silica nanoparticles, in red the air-facing BSA shell, and in yellow the water-facing one. The different BSA shell composition in terms of protein dry fraction $\phi_{BSA,i}$ are reported as differences in the color transparency. The illustration helps to visualize the empty space between BSA-NP complexes.*

tained from SANS data. For a triaxial ellipsoid, the BSA volume is $V_{\mathrm{BSA}} = \frac{4}{3}\pi abc = 150.65(6.89)\ \mathrm{nm}^3$. The shell volumes were calculated by integrating the profile described in Equation H.22 within the limits $z_i - w_i/2 < z < z_i + w_i/2$ as follows:

$$V_i = \phi_{\mathrm{BSA},i} \int_{z_i - w_i/2}^{z_i + w_i/2} \int_{(h)} \int_{(r)} (r_{out} - r_{in})^2 \cdot G(r)\, G(h)\, dr\, dh\, dz, \tag{5.3}$$

where $r_{out} = ((r + t_i)^2 - (z - (r + h))^2)^{1/2}$ and $r_{in} = (r^2 - (z - (r + h))^2)^{1/2}$ are respectively the outer and the inner radii of the core-shell system and $\phi_{BSA,i}$ is the dry fraction of BSA in the shell. Thus, we obtained that:

$$BSA : NP_i = \frac{V_i}{V_{BSA}} \tag{5.4}$$

where i can be equal to air and water. The results of these calculations are reported in Table 5.2.

Table 5.2: *Calculated BSA molecules per NP at the air-water interface. The concentration of NP was 0.1 $\%_{wt}$ and the ionic strength was 10 mM far all samples. V_{air} and V_{water} are the protein shell volume per each NP respectively at the air and water side. BSA:NP$_{air}$ and BSA:NP$_{water}$ are the average number of BSA molecule per nanoparticle respectively in V_{air} and V_{water}, BSA:NP$_{TOT}$ is the sum of BSA:NP$_{air}$ and BSA:NP$_{water}$, and BSA:NP$_{bulk}$ is the nominal molecular ratio in bulk. Numbers in parentheses indicate uncertainties in the value.*

Sample	V_{air} (nm^3)	BSA:NP$_{air}$	V_{water} (nm^3)	BSA:NP$_{water}$	BSA:NP$_{TOT}$	BSA:NP$_{bulk}$
BSA 0.125 μM	950.09 (87.24)	6.31 (0.58)	1045 (62.23)	6.94 (0.41)	13.25 (0.99)	1
BSA 0.25 μM	1667.50 (288.43)	11.07 (1.92)	1064.55 (67.52)	7.07 (0.45)	18.14 (2.37)	2
BSA 1 μM	2665.93 (82.17)	17.70 (0.55)	1010.15 (29.14)	6.71 (0.20)	24.40 (0.75)	8

Further, we also estimated the protein surface excess. To do this, we calculated the volume of the shell normalized by the nanoparticle surface excess as follows:

$$d_i = \int_{z_i - w_i/2}^{z_i + w_i/2} \int_{(h)} \int_{(r)} \frac{2\pi (r_{out} - r_{in})^2}{\phi_{\mathrm{NP}} \cdot \sqrt{3}(2r + s + t_i)^2} \cdot G(r)\, G(h)\, dr\, dh\, dz, \tag{5.5}$$

where d_i is analogous to the layer thickness (d) that is usually obtained with the slab model. Thus, we used d_i to estimate the protein surface excess by using Equation 5.1, where the term $(1 - h\%)$ was substituted by $\phi_{\mathrm{BSA},i}$. The results of this calculation are reported in Table 5.3

Table 5.3: *Surface excess values for layer obtained in the presence of NPs 0.1 $\%_{wt}$ and NaCl 10 mM at variable BSA concentration.*

Sample	Γ (ng/cm^2)		
	Shell in air	Shell in water	TOT
BSA 0.125 μM - NaCl 10 mM - NPs 0.1 %wt	30.13(3.12)	30.92(2.53)	61.05(5.65)
BSA 0.25 μM - NaCl 10 mM - NPs 0.1 %wt	87.31(1.32)	56.07(0.89)	143.38(2.21)
BSA 1 μM - NaCl 10 mM - NPs 0.1 %wt	128.52(0.64)	39.35(0.52)	167.87(1.16)

The obtained results reveal a very interesting behavior. Firstly, the BSA:NP ratio at the interface is consistently higher than the corresponding bulk BSA:NP ratio. Secondly, the results confirm the asymmetric composition of the two protein shells, with the air-facing shell becoming progressively enriched in protein content as the bulk protein concentration increases, as already discussed above. The higher interfacial ratio can be rationalized by two non–mutually exclusive phenomena: (i) the species that preferentially adsorb at the interface are those characterized by a higher bulk BSA:NP ratio, although the sample preparation procedure was optimized to minimize the formation of inhomogeneously BSA-covered NPs, a certain distribution is inevitably present, and (ii) protein accumulates on the air-facing side to minimize surface tension, leading to an interfacial BSA:NP ratio larger than the one expected from the bulk composition.

This asymmetric distribution of protein at the NP monolayer has also been reported previously. Ang et al., 2010 performed combined neutron and X-ray reflectivity measurements on monolayers obtained with BCN and silica nanoparticles of ~4 nm diameter. In their study, the protein was also found to distribute asymmetrically into two layers located above and below the nanoparticle monolayer, with negligible protein density in the interparticle region. Importantly, the air-facing shell exhibited a higher protein concentration compared to the water-facing one. Despite working under conditions of a very large nanoparticle excess with respect to protein (bulk BCN:NP ~0.18), they reported an interfacial molar ratio of ~2.5, i.e. about 14 times larger than in bulk. A very similar proportion is observed in our case: for the sample BSA 0.125 μM – NPs 0.1$\%_{wt}$, the interfacial BSA:NP$_{\mathrm{TOT}}$ ratio is ~13 times larger than in bulk, while it decreases to ~9 and ~3 for the 0.25 and 1 μM BSA samples, respectively.

Furthermore, the calculated surface excess helps to interpret the surface tension results. At a fixed protein concentration, in the presence of NPs the BSA surface excess at the air side is always lower than in bare-BSA systems, while the overall surface excess remains comparable. This suggests that the macroscopic surface tension of the BSA–NP system is primarily governed by the amount of protein at the air side. Since the thickness of the BSA–NP layer extends over ~25 nm, it is reasonable to assume that

the protein localized on the water side has a minor or even negligible effect on the measured surface tension.

It is also worth noting that, for the lowest concentration (BSA 0.125 μM – NPs 0.1%$_{wt}$), the protein surface excess at the air side is ~30 ng/cm^2, yet the measured surface tension is essentially that of the bare air–water interface (~72.5 mN/m). This indicates that upon interaction with NPs, BSA adopts a less surface-active conformation, resulting in negligible changes in surface tension despite a nonzero surface excess.

This hypothesis is further supported by comparing the surface tension of the BSA 1 μM – NPs 0.1%$_{wt}$ sample with that of the bare BSA system at 0.125 μM. In both cases, a steady-state surface tension of ~62.5 mN/m is reached after 1 h of adsorption, even though the protein surface excess at the air side is significantly larger in the presence of NPs (~128 ng/cm^2) than in the bare BSA case (~73.4 ng/cm^2).

Neutron reflectometry could be acquired only for the BSA series at fixed NP loading (0.1%$_{wt}$). Nevertheless, two independent lines of evidence indicate that the structural picture inferred from BSA could be representative of the broader set of samples investigated, at least for BSA and BCN. First, the surface-tension responses display highly similar trends across the two proteins and bulk compositions, suggesting a common interfacial mechanism governing adsorption and protein location. Second, analogous asymmetric protein partitioning has been reported for BCN–silica monolayers, despite different protein/NP chemistries, reinforcing the generality of the mechanism. On this basis, we adopt the BSA-derived NR model as a physically constrained template to interpret the other protein–NP systems. We emphasize that this constitutes a model-based generalization: while the qualitative features (NP immersion, asymmetric partitioning, negligible interparticle protein density) are expected to be robust, protein-specific parameters (e.g., shell thickness and dry fraction) may differ substantially.

5.1.4 SFG Spectroscopy

Sum Frequency Generation (SFG) spectroscopy is a second-order non-linear spectroscopic technique that selectively probes vibrational modes with inherent interfacial specificity (see Appendix I for a detailed description of the theory beyond).

The motivation for performing SFG measurements arises from the fact that, although structural characterization by GISAXS and NR provided valuable insights into the architecture and composition of the protein–NP monolayers, these techniques do not directly address the molecular-level effect of nanoparticles on protein conformation once adsorbed at the interface. As discussed above, the NR data offered a possible interpretation of the surface tension results, but several important questions remain open.

To address these questions, SFG characterization was performed on samples prepared at fixed protein concentration 1 μM, ionic strength 10 mM and NPs concentration spanning from 0.1 to 1.6 %$_{wt}$. For the BSA-NP only the effect of ionic strength was investigated for the samples at bulk BSA:NP ratio 1:1 (BSA 1 μM - NPs 1.6 %$_{wt}$) at the

ionic strength of 1, 5, 10, and 50 mM. Unfortunately, the spectrophotometer detection limit was above the one necessary to investigate sample with protein concentration below 1 μM.

In SFG spectroscopy of proteins at the air-water interface, several distinct vibrational signatures can be observed in unique spectral regions (Figure 5.9), each providing complementary structural and interfacial information.

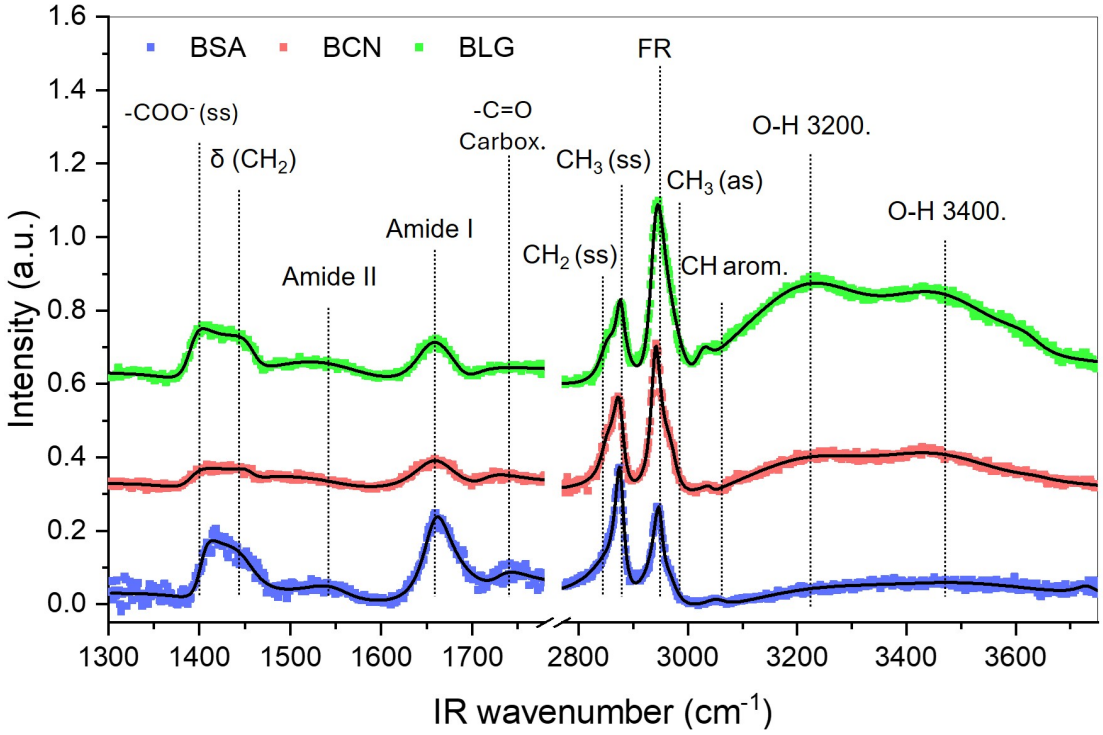

Figure 5.9: *Experimental vibrational SFG spectra of BSA (blue), BCN (red), and BLG (green) layers at the air-water interface and the correspond fitted curved (black lines). The bulk composition was: protein 1 μM - NaCl 10 mM - NPs 0.1 $\%_{wt}$. The vertical dashed black lines indicate the average position of the main vibrational band observed.*

The region comprises between 1300-1800 cm^{-1} is usually known as the Amide region. The strong vibrational band located at 1600-1700 cm^{-1} is known as Amide I. This band arises predominantly from the -C=O stretching vibrations of the protein backbone (J. Wang et al., 2005; Y. Liu et al., 2012). Its frequency depends strongly on the protein secondary structure and thus the relative intensity of this band is widely used to infer conformational rearrangements due to denaturation, unfolding or aggregation both in the bulk and at the interface (Murayama et al., 2004; Engelhardt et al., 2013). Amide II mode (~1550 cm^{-1}) originates from a combination of C-N stretching and N-H bending of the peptide bond (Barth et al., 2002). Due to its low Raman activity and less favorable selection rules, the Amide II band is usually very weak in SFG spectra, although it may still contribute under specific orientations (Socrates, 2004). The symmetric stretching of deprotonated carboxylates (Asp/Glu) is typically observed between 1410-1455 cm^{-1} (Braunschweig et al., 2010). Variations in intensity and frequency are highly sensitive to pH changes, ion binding, and coordination (M. E. Richert et al.,

2019). Protonated carboxylic acid groups (-COOH) give rise to a strong -C=O stretch at 1710-1735 cm^{-1}, often indicative of hydrogen bonding or dehydration of acidic side chains at the interface (Simona Strazdaite et al., 2017; Tyrode et al., 2005; J. Wang et al., 2002). Finally, in this region the characteristic bending mode of the CH_2 is visible in the range 1465–1475 cm^{-1} (Seshadri et al., 1997).

The region in the range 2700-3800 cm^{-1} is known as the CH-OH region where the characteristic vibration bands of the C-H and O-H stretching are present. Aliphatic side chains of the aminoacids produce well-resolved bands, namely CH_2 symmetric stretch at ~2850 cm^{-1}, CH_3 symmetric stretch at ~2875 cm^{-1}, CH_3 Fermi resonance near 2935-2940 cm^{-1}, and CH_3 asymmetric stretch around 2960-2965 cm^{-1}. In addition, aromatic C-H stretches of the aromatic Phe, Tyr, and Trp residues can appear near ~3060 cm^{-1}. The relative intensities of these bands provide information on side-chain orientation and packing at the interface (J. Wang et al., 2003; X. Chen et al., 2010; X. Chen et al., 2007). Finally, in the SFG spectra of interfacial water, two distinct OH stretching bands are typically observed, one centered around ~ 3200 cm^{-1} and the other near ~3400 cm^{-1}. Their precise assignment, however, is still debated. One interpretation attributes the low-frequency band to "ice-like" tetrahedrally coordinated water and the high-frequency band to more weakly hydrogen-bonded, "liquid-like" water molecules. An alternative explanation proposes that the splitting originates from a Fermi resonance between the fundamental OH stretch and the overtone of the bending mode, rather than from structurally distinct water populations. Although the microscopic origin remains non-univocal, in our analysis we adopted a two-band model to fit the experimental spectra, as it provides a consistent and reliable description of the interfacial water response. Richmond, 2002; Yuen Ron Shen et al., 2006.

Overall, the combination of these vibrational fingerprints, which are summarized in Table 5.4, allows one to simultaneously probe the protein secondary structure (Amide I), side-chain chemistry (COOH, COO^-, CH), and interfacial hydration (OH region), thereby providing a comprehensive molecular-level picture of protein organization at the air-water interface.

We now turn to the discussion of the SFG results obtained for BSA-NP layers formed at the air-water interface. The bulk BSA:NP ratio was systematically varied in the range 0.5:1 to 8:1 by changing the NP concentration, while keeping the protein concentration fixed. It is important to note that an increase in the bulk ratio corresponds to a progressive decrease in NP concentration. In particular, the 0.5:1 ratio was achieved at 1.6%$_{wt}$ NPs, whereas the 8:1 ratio corresponds to 0.1%$_{wt}$ NPs. We also investigated the role of ionic strength at the bulk ratio of 1:1.

We begin with the signals associated with the OH stretching region at 3250 and 3400 cm^{-1}. As shown in Figure 5.10*C*, their intensities exhibit a non-monotonic trend, reaching a maximum around a bulk ratio of 2:1. Since these bands are typically associated with water structuring in the presence of charged interfaces, we first characterized the zeta potential of the individual components. BSA alone, under these conditions of pH and ionic strength, exhibits a ζ-potential of about -20 mV. For BSA-NP mixtures,

Table 5.4: *Vibrational modes observed by SFG for proteins at the air-water interface with typical frequency ranges.*

Vibrational mode	Frequency (cm^{-1})	References
COO^- (ss)	1410-1455	M. E. Richert et al., 2019; Braunschweig et al., 2010
CH_2 bending	~2850	Seshadri et al., 1997
Amide II	~1550	Barth et al., 2002
Amide I	1600-1700	J. Wang et al., 2005; Y. Liu et al., 2012
COOH (C=O stretch)	1710-1735	Simona Strazdaite et al., 2017; Tyrode et al., 2005; J. Wang et al., 2002
CH_2 (ss)	~2850	J. Wang et al., 2003; X. Chen et al., 2010; X. Chen et al., 2007
CH_3 (ss)	~2875	J. Wang et al., 2003; X. Chen et al., 2010; X. Chen et al., 2007
CH_3 (FR)	2935-2940	J. Wang et al., 2003; X. Chen et al., 2010; X. Chen et al., 2007
CH_3 (as)	2960-2965	J. Wang et al., 2003; X. Chen et al., 2010; X. Chen et al., 2007
Aromatic C-H	~3060	J. Wang et al., 2003; X. Chen et al., 2010; X. Chen et al., 2007
O-H ("ice-like")	~3200	Richmond, 2002; Yuen Ron Shen et al., 2006
O-H ("liquid-like")	3400-3450	Richmond, 2002; Yuen Ron Shen et al., 2006

(ss) is symmetric stretching, (as) is asymmetric stretching and (FR) is Fermi Resonance.

however, the measured potential was always governed by the nanoparticles, which display a potential of ~ -35 mV, independent of the BSA:NP ratio. This observation indicates that the interpretation of the OH signals must be done in terms of the monolayer structure rather than the surface potential of individual NPs.

The initial increase in OH signal intensity upon decreasing the BSA:NP ratio (i.e., increasing NP concentration) can be rationalized by considering both the immersion depth of the nanoparticles and the protein double-shell structure revealed by NR. Importantly, the SFG signal is directly related to the loss of inversion symmetry. Thus, a higher NP concentration, as confirmed by GISAXS (Figure 5.4*A*) leads to denser interfacial layers and, consequently, a higher density of charged species at the interface. This results in stronger structuring and preferential orientation of interfacial water molecules. This interpretation is also supported by the increase of the amplitude ratio A_{3250}/A_{3400}, which indicates an enhanced fraction of tetrahedral coordinated water with increasing NP density.

At still lower BSA:NP ratios (*i.e.*, below 2:1), the OH signal intensity decreases again. This reduction can be explained by the progressive loss of asymmetry, as also observed in NR. At low BSA:NP ratios, the air- and water-facing protein shells become very similar in composition. Since the NPs are fully immersed in the aqueous phase and thus possess an intrinsic spherical symmetry, the overall inversion asymmetry of the interface decreases and the SFG signal diminishes.

Further, the OH response also shows characteristic trends as a function of ionic strength Figure 5.11*C*. For BSA alone, where the zeta potential changes only modestly from about -22 to -19 mV over the investigated ionic strength range, a progressive and approximately linear decrease in OH signal intensity is observed. This behavior is expected for systems with comparable interfacial compositions (surface tension being essentially unchanged with ionic strength), but exposed to increasingly strong electrostatic screening. Charge screening reduces both the structuring/orientation of water

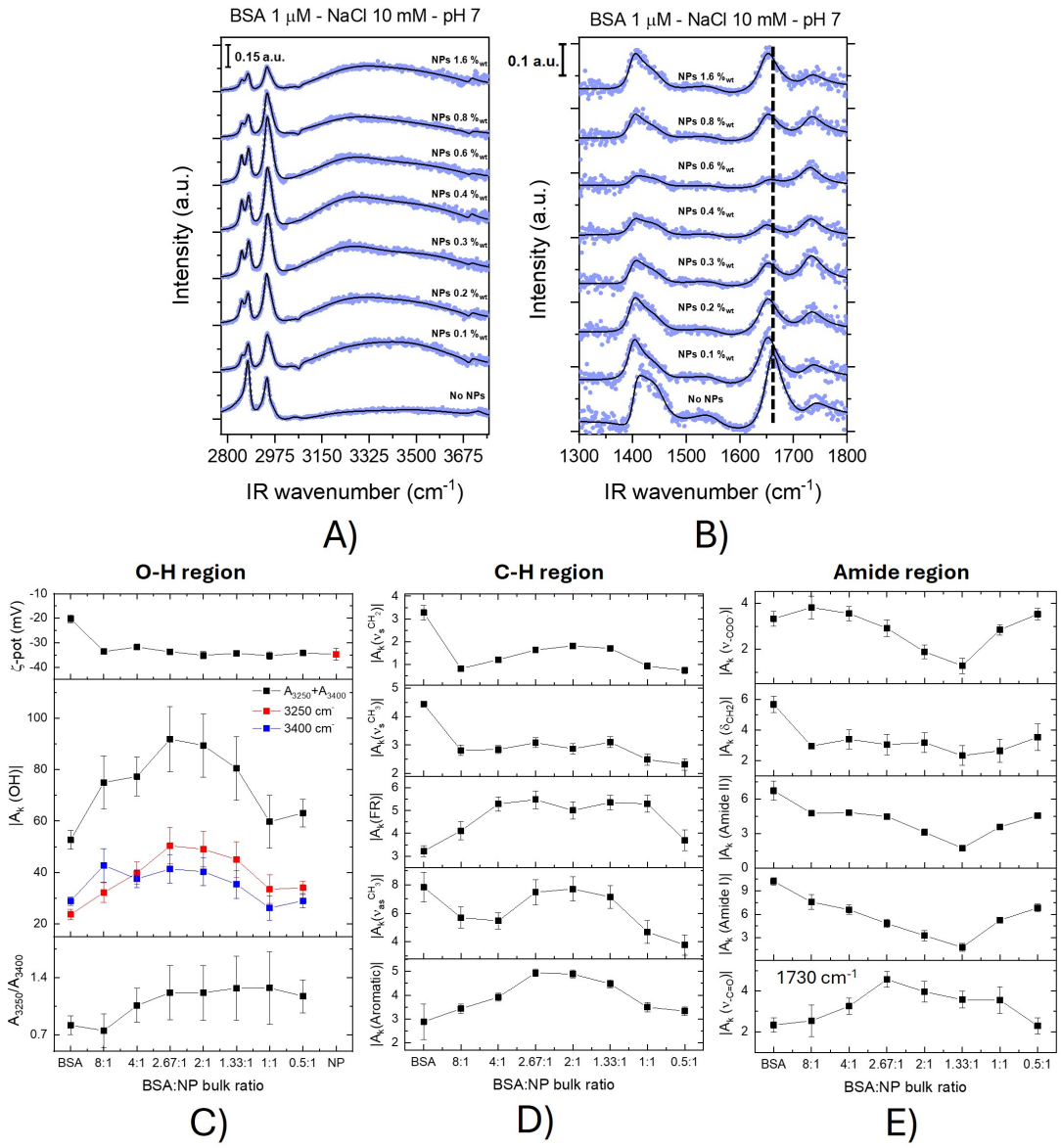

Figure 5.10: *SFG spectra of BSA-NP system in A) the CH-OH region and B) the Amide region, obtained with sample at BSA 1 μM, NaCl 10 mM and NPs in the range 0-1.6 $\%_{wt}$. In C) are reported the ζ-potential and the amplitude of the OH bands. In D) are reported the amplitude of the C-H bands. In D) the amplitude of the signals in the Amide region.*

molecules and the effective contribution from the third-order susceptibility $\chi^{(3)}$, as explained in Appendix I. In contrast, for BSA-NP systems, the decrease in water signals with ionic strength is much less pronounced, despite the significant variation of the NP zeta potential (from about -45 mV at 1 mM NaCl to -25 mV at 50 mM NaCl). This effect can be understood in terms of the different monolayer structures. While higher ionic strength reduces the potential of individual NPs due to charge screening and double-layer contraction, it simultaneously promotes a marked increase in the interfacial NP density, as confirmed by GISAXS. Thus, at high ionic strength, more particles are present at the interface, albeit with a lower individual surface charge density.

The signals associated with the protein itself show particularly intriguing features. Most notably, the Amide I band undergoes a pronounced redshift upon interaction with NPs: from ~1660 cm^{-1} for bare BSA to ~1650 cm^{-1} in the presence of NPs. A redshift in the Amide I region is generally associated with increased compaction of the protein secondary structure. More compact structures are stabilized by stronger hydrogen bonds between the carbonyl and N-H groups of the aminoacidic backbone, which results in a partial charge transfer from the C=O to the N-H bond. This decreases the effective double-bond character of the carbonyl group and thereby lowers the stretching frequency.

In addition, the interaction with NPs significantly modifies the intensities of CH-related signals, which again display a non-monotonic trend. The decrease in CH intensities at high BSA:NP ratios correlates with the higher protein content at the interface, leading to a loss of asymmetry. Concomitant changes are also observed in other vibrational bands. In particular, the symmetric stretching of carboxylates ($–COO^-$) at ~1430 cm^{-1} decreases in intensity, while a new band at ~1730 cm^{-1} progressively emerges. The latter is characteristic of protonated carboxylic groups (Asp/Glu side chains) involved in strong hydrogen bonding. Indeed, the v(C=O) stretching frequency of a free carboxylic acid typically appears in the 1750–1770 cm^{-1} range, and its redshift toward 1730 cm^{-1} is consistent with the formation of highly hydrogen-bonded species at the interface (Strazdaite et al., 2020; Tyrode et al., 2005; J. Wang et al., 2002). This observation is in very good agreement with the redshift of the amide I band, further supporting the hypothesis of a more compact and hydrogen-bonded protein conformation upon interaction with nanoparticles.

An additional aspect concerns the amplitude trends in the amide region (Figure 5.10*E*). In particular, the symmetric stretching of carboxylates ($–COO^-$), Amide II, and Amide I display a pronounced minimum around a bulk BSA:NP ratio of ~1.3:1, whereas both the C=O stretching of protonated carboxylic groups (–COOH) at ~1730 cm^{-1} and the CH-related bands exhibit maxima near 2:1. This behavior can be rationalized by considering the two-shell distribution of BSA revealed by NR. Around 1–1.3:1, the protein composition of the air-facing and water-facing shells is very similar, which increases the overall interfacial symmetry and leads to a partial cancellation of the SFG response of the amide and COO^- modes. Upon moving to ~2:1, the air-facing shell becomes enriched in protein while the water-facing shell remains nearly unchanged, enhancing interfacial asymmetry and the orientational order of apolar side chains; this accounts for the concurrent maximum of the CH bands. In the same regime, the less hydrated environment of the air-facing shell promotes protonation and strong H-bond stabilization of carboxyl groups, thereby boosting the –COOH signal at ~1730 cm^{-1}. At higher bulk ratios, the progressive enrichment of the air-facing shell increases the overall amount of protein at the interface, which explains the recovery of intensity for the amide modes. In contrast, the CH and –COOH bands decrease again due to the compaction of the air-facing layer, which lowers the accessibility and orientational freedom of hydrophobic side chains and protonated carboxyl groups. These trends are consis-

tent with previous SFG studies of BSA at different interfaces (J. Wang et al., 2002), where the absence of C–H signals was attributed to inversion symmetry in hydrophilic environments (e.g., fused silica/BSA solution interface), while strong C–H responses were observed when hydrophobic groups were preferentially oriented toward the air or a hydrophobic medium. In line with these findings, the minimum of the amide and COO^- bands in our system corresponds to a nearly symmetric distribution in the two shells, whereas the maximum of the CH and –COOH bands at 2:1 reflects the point where the air-facing shell is sufficiently enriched to enhance asymmetry and protonation. At higher ratios, the excessive crowding of this shell reduces both accessibility and orientational freedom, leading to the observed decrease in intensity.

Taken together, these observations provide strong evidence that the BSA-NP interaction at the air-water interface induces substantial changes in both protein structure and interfacial orientation. Specifically, BSA adopts a more compact conformation that hinders its ability to achieve the more stable and surface-active arrangement typically observed at the bare air-water interface. This interpretation also rationalizes the surface tension data in combination with the NR results. In fact, at a bulk ratio of 8:1 (NPs 0.1%$_{wt}$, BSA 1 μM), the interfacial protein excess on the air side is even higher than that of bare BSA at 0.125 μM (see NR data), yet the steady-state surface tension values are essentially the same. This behavior can only be explained in terms of the reduced surface activity of BSA upon interaction with nanoparticles.

Finally, it is worth noting that while the BSA spectra in the amide region (1300-1800 cm^{-1}) show only minor differences as a function of ionic strength, the situation changes markedly in the presence of nanoparticles Figure 5.11. In this case, a clear progressive increase in the amide signal intensity is observed. This trend can be rationalized by considering that increasing ionic strength screens the electrostatic repulsion between charged protein molecules, thereby facilitating a higher protein loading at the interface (Galdino et al., 2020). However, the fact that the CH signals remain essentially unaffected provides an important clue regarding the origin of this trend. Since the CH modes are highly sensitive to the loss of inversion symmetry at the air-facing side of the interface, their invariance indicates that the additional protein molecules do not accumulate at the topmost layer in direct contact with air. Instead, the increase of the amide signal must be associated with a progressive enrichment of protein in the water-facing side of the interfacial layer. In this configuration, the additional protein contributes to the overall vibrational response in the amide region, but does not enhance or decrease the interfacial asymmetry required to boost or suppress the CH-related SFG signals.

Having completed the discussion of BSA–NP layers, we now turn our attention to the BCN–NP systems. The SFG spectra together with the fitted amplitudes for these samples are shown in Figure 5.12, which we will analyze in detail below. We first consider the OH stretching region, where BCN–NP samples display a progressive increase of the signal with increasing NP concentration, until a plateau is reached around the 4:1 bulk ratio (NPs 0.2%$_{wt}$). This behavior can be attributed to the stronger ordering of interfacial water molecules induced by the larger surface charge density brought by

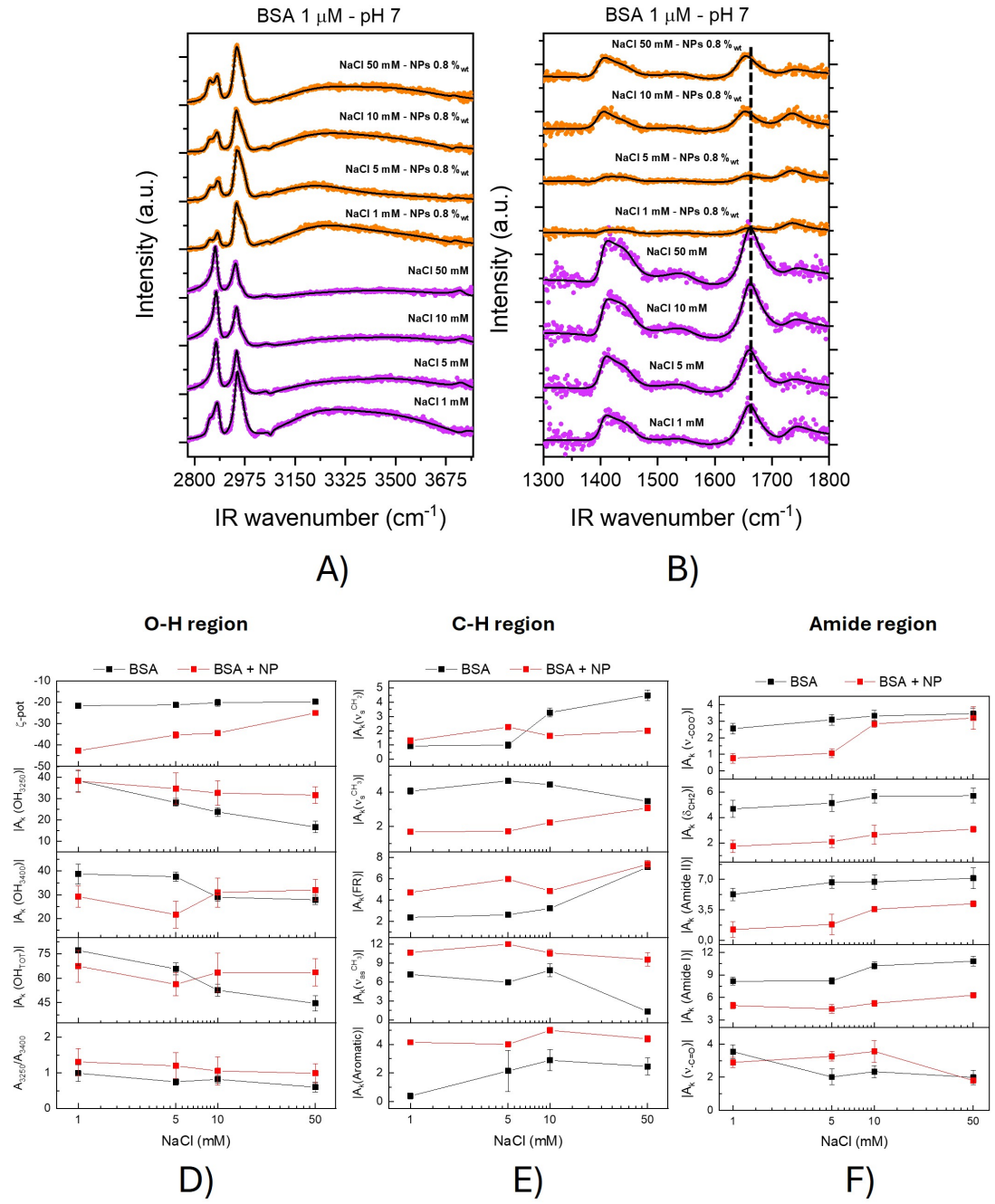

Figure 5.11: *SFG spectra in A) the CH-OH region and B) the Amide region, obtained with sample at BSA 1 μM and NaCl 1-50 mM (purple curves) and BSA 1 μM, NaCl 1-50 mM and NPs 0.8 %$_{wt}$ (orange curves). In C) are reported the ζ-potential and the amplitude of the OH bands. In D) are reported the amplitude of the C-H bands. In D) the amplitude of the signal in the Amide region.*

the nanoparticles. As also observed for BSA, the ζ-potential of the hybrid system is dominated by that of the NPs (~-35 mV, Figure 5.10C), while bare BCN shows a less negative value (~-25 mV, Figure 5.12C). The less pronounced variation compared to the BSA case is consistent with GISAXS data, which show only minor differences in the interparticle distance between the high-NP (ID ≈ 29 nm at 1:1) and low-NP (ID ≈ 35

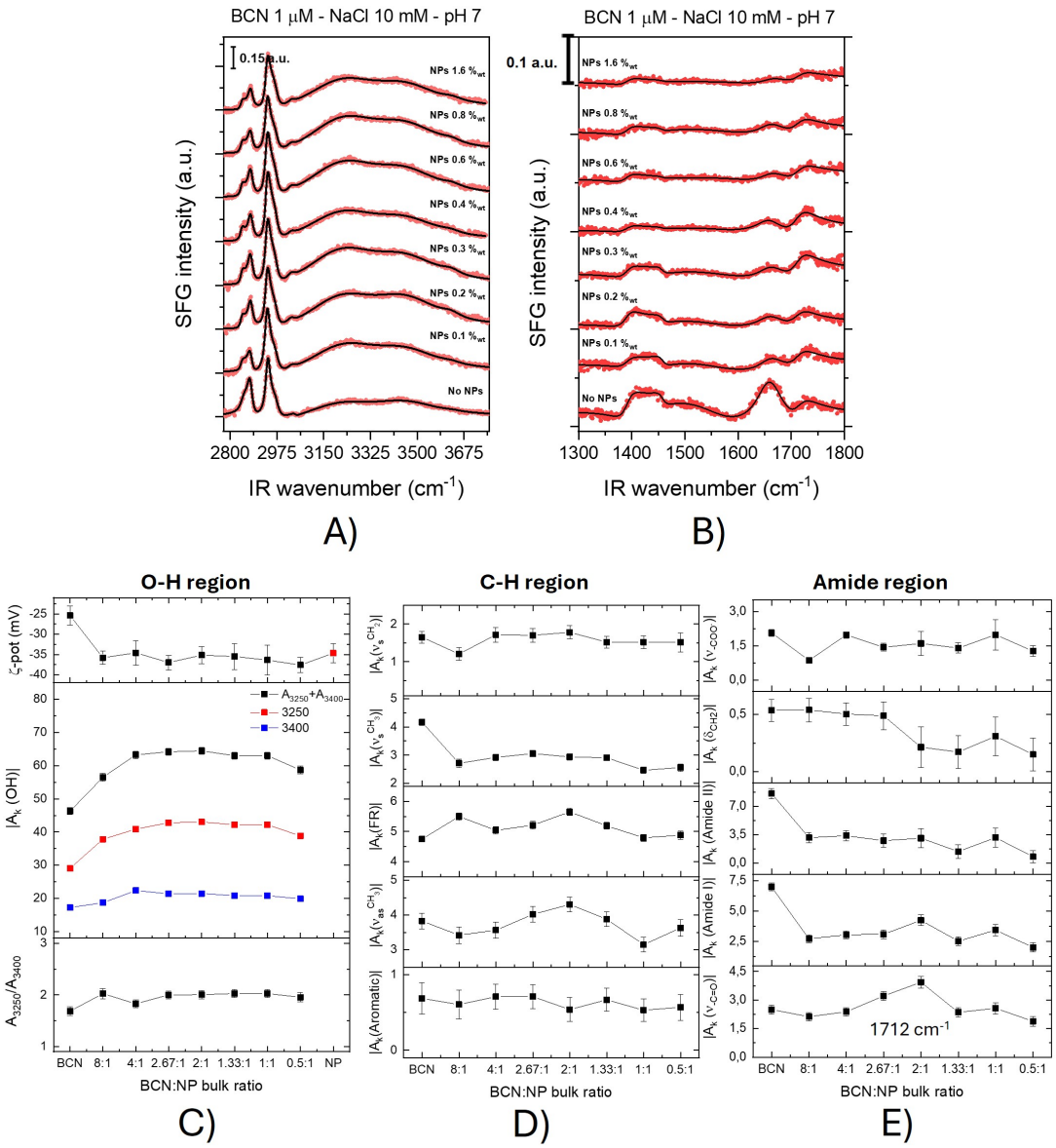

Figure 5.12: *SFG spectra of BCN-NP system in A) the CH-OH region and B) the Amide region, obtained with sample at BCN μM, NaCl 10 mM and NPs in the range 0-1.6 $\%_{wt}$. In C) are reported the ζ-potential and the amplitude of the OH bands. In D) are reported the amplitude of the C-H bands. In D) the amplitude of the signals in the Amide region.*

nm at 8:1) samples, in contrast to the ~15 nm variation observed for BSA.

In the CH region, the spectra remain essentially unaffected by the presence of NPs, with only a small decrease in the symmetric CH_3 stretching band (~2845 cm^{-1}). This indicates that the orientation of hydrophobic side chains exposed to air is largely preserved, consistent with a scenario where BCN, being an intrinsically disordered protein, maintains flexible and heterogeneous conformations at the interface.

A much stronger effect is observed in the amide region (Figure 5.12*B*). Here, all amide-related signals progressively decrease in intensity with increasing NP concentration, except for a band at ~1712 cm^{-1} that remains visible. This feature is assigned to

the C=O stretching of protonated carboxylic side chains (Asp/Glu) and/or C-terminal groups engaged in strong hydrogen bonding. Such an assignment is consistent with SFG and IR studies on amino acids and simple carboxylic acids at the air–water interface (Simona Strazdaite et al., 2017; Moll et al., 2021).

The persistence of this 1712 cm^{-1} band in BCN, contrasted with the higher-frequency carbonyl signal observed for BSA at the air–water interface (~1730 cm^{-1}), highlights the different interfacial organizations of the two proteins. BSA, being globular, tends to expose less hydrated carboxyl groups in a more compact interfacial arrangement, leading to higher-frequency carbonyl stretching. In contrast, BCN behaves more like a macrosurfactant, with a flexible and amphiphilic chain where hydrophobic blocks extend toward the air phase while polar regions remain solvated in contact with water (Harzallah et al., 1998; Mileti et al., 2024). This amphiphilic, intrinsically disordered organization results in a hydrated interfacial film, which is consistent with the red-shifted C=O band at 1712 cm^{-1}.

Taken together, the decrease in amide-related bands with increasing NP concentration is best explained by a reduction of protein coverage at the interface rather than a major structural rearrangement. This interpretation is in line with the surface tension data (steeper decrease for BCN compared to BSA, see Figure 5.2*D*), and with the absence of frequency shifts in the amide bands. Thus, the SFG data show that the interaction between BCN and NPs is dominated by interfacial displacement, while the intrinsic flexibility and amphiphilic character of BCN allow the protein to maintain a similar interfacial conformation even at high NP loadings.

In the case of β-lactoglobulin (BLG) interacting with nanoparticles (NPs), all SFG-active regions (OH stretching, CH, and Amide) exhibit a moderate decrease in signal amplitude as NP concentration increases. This attenuation is mainly appreciable from the spectral fits, while the raw spectra appear nearly identical to the eye, suggesting that the average interfacial conformation of BLG remains largely stable, with only a slight reduction in the density or orientation of vibrationally active groups. The ζ-potential of BLG is around -28 mV, close to that of the NPs. Such similarity implies hindered interaction driving forces, which could explain why at low concentrations the NPs do not efficiently interact with the protein layer at the interface.

An intriguing feature is found in the Amide I region: the main band is centered at $\sim$ 1650 cm^{-1}, a value unexpected for a protein dominated by β-sheets (typically observed at $\sim$ 1630-1640 cm^{-1} for parallel sheets, and $\sim$ 1690-1700 cm^{-1} for antiparallel ones) (Lorenz-Fonfria, 2020). A secondary peak at $\sim$ 1695 cm^{-1} may indeed correspond to antiparallel β-sheets, possibly arising from aggregation or multilayer formation at the interface (H. L. Casal et al., 1988; Ulaganathan et al., 2017; S. Richert et al., 2020). Because SFG is highly sensitive to interfacial order and orientation, the dominance of the 1650 cm^{-1} band may indicate that coil/helix-like structures are preferentially exposed at the surface, whereas the β-sheet components remain buried or less ordered.

GISAXS measurements detect correlated NP domains only at relatively high NP concentration ($\geq$ 0.8 wt%), suggesting that at lower concentrations the NPs remain

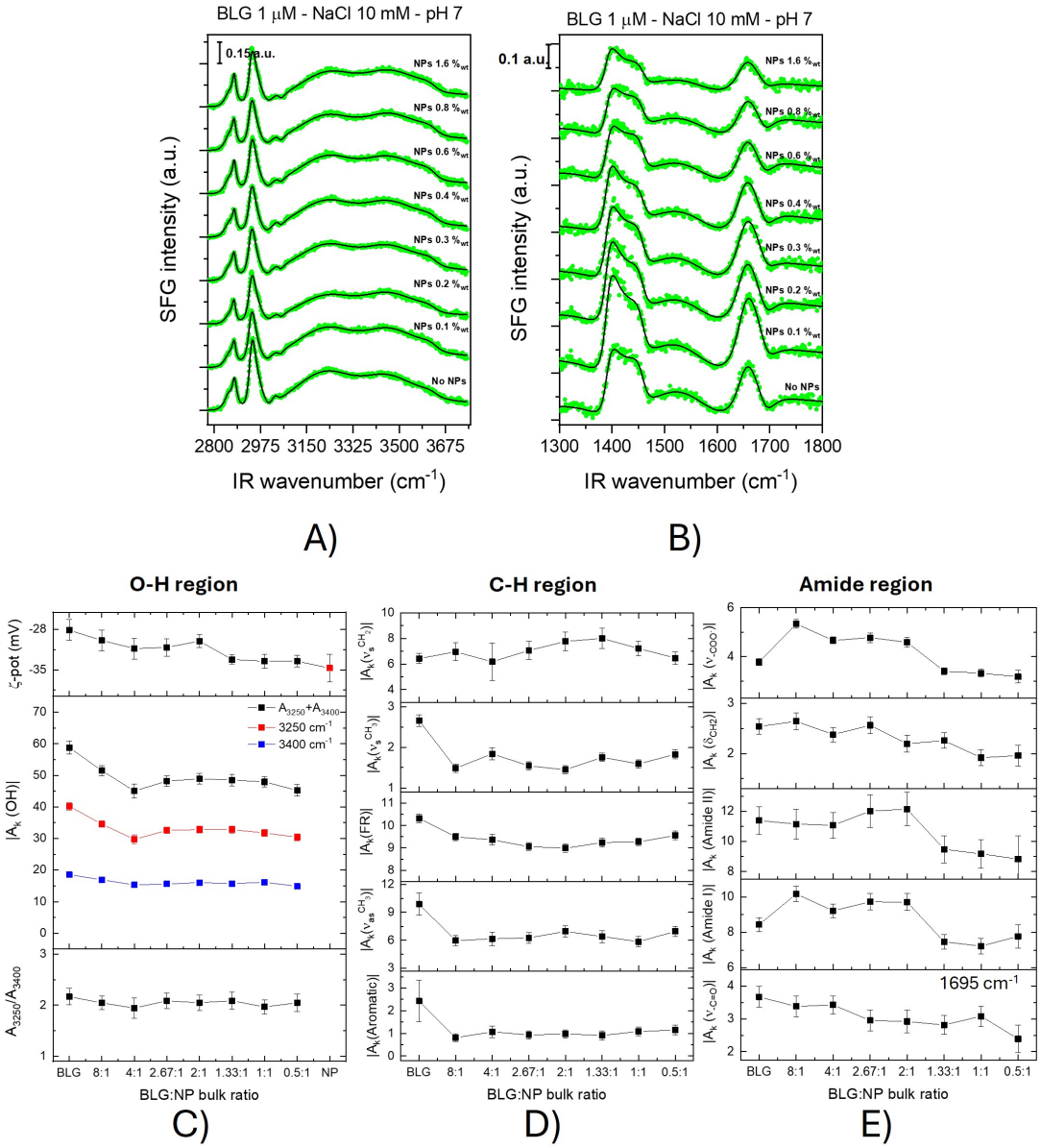

Figure 5.13: *SFG spectra of BLG-NP system in A) the CH-OH region and B) the Amide region, obtained with sample at BLG 1 μM, NaCl 10 mM and NPs in the range 0-1.6 $\%_{wt}$. In C) are reported the ζ-potential and the amplitude of the OH bands. In D) are reported the amplitude of the C-H bands. In D) the amplitude of the signals in the Amide region.*

dispersed and fail to form interfacial aggregates or are even completely absent. At higher concentrations, however, crowding effects overcome the electrostatic barrier, enabling the formation of measurable correlated structures.

In conclusion, when all the observations are combined, they consistently indicate that the interaction between BLG and NPs is very weak. The protein retains a similar interfacial conformation, the nanoparticles only form ordered domains at high concentration, and the surface tension data confirm that the overall interfacial coverage is very low, even though SFG detects strong signals from locally ordered protein domains. The surface tension data further confirm the weak interaction between BLG

and nanoparticles. In contrast to BSA and BCN, the adsorption isotherms of BLG are essentially unaffected by the presence of NPs: the characteristic two-step adsorption kinetics are preserved and the $\gamma(c)$ profiles show the same shape as for the protein alone. However, the absolute equilibrium values remain higher than in the bare-protein case, approaching those of pure water. This behavior indicates that while BLG still adsorbs at the air–water interface, the presence of NPs reduces its adsorption efficiency and prevents the formation of compact, surface-active films. The similarity in ζ-potential between BLG and the NPs likely contributes to this effect, as the lack of a strong electrostatic driving force hinders cooperative adsorption and results in low overall interfacial coverage.

5.2 Conclusion

The multi-scale investigation carried out in this chapter reveals how the interplay between protein architecture and nanoparticle interactions dictates the structure, composition, and macroscopic properties of interfacial films at the air–water interface. By comparing three model proteins, namely BSA, BCN, and BLG, we highlight fundamental mechanistic differences in how proteins organize nanoparticles and how nanoparticles in turn reshape protein adsorption pathways.

For BSA, a large globular protein with a secondary structure mainly composed by α-helices, adsorption in the presence of nanoparticles leads to the formation of asymmetric protein shells around the NP monolayer, with a preferential enrichment on the air-facing side. Neutron reflectometry and SFG spectroscopy show that these interactions drive a partial compaction of the secondary structure, reducing the ability of BSA to lower surface tension despite significant surface excess. This behavior demonstrates that strong protein–NP interactions may stabilize interfacial assemblies but at the cost of lowering macroscopic surface activity.

For BCN, an intrinsically disordered protein, the response is markedly different. Its flexibility and amphiphilic character allow it to act as an efficient macrosurfactant, promoting the formation of dense NP monolayers. SFG spectra indicate that BCN largely retains its disordered conformations at the interface, with only minor changes upon increasing NP concentration. The reduction in amide-related signals is consistent with competitive displacement at the interface rather than structural reorganization. This highlights the unique ability of IDPs to adapt and maintain functionality in hybrid protein–NP systems.

For BLG, a β-sheet-rich globular protein, the interaction with nanoparticles is comparatively weak. Both adsorption kinetics dynamic and surface tension isotherms remain essentially unchanged relative to the protein-only case, while the overall adsorption rate and steady-state surface tension are reduced. Further, GISAXS confirms that detectable NP domains form only at high particle concentrations. The similarity in ζ-potential between BLG and silica nanoparticles reduces electrostatic attraction, hindering cooperative adsorption and leading to loose, weakly surface-active films. SFG

spectra suggest that BLG preserves its interfacial conformation, with β-sheet elements likely buried and less ordered at the air-facing interface.

Taken together, these findings establish a clear structure–function relationship: globular proteins (BSA, BLG) are structurally constrained and their interactions with nanoparticles result either in restricted conformations (BSA) or inefficient packing (BLG). On the contrary, disordered proteins (BCN) adapt their conformation to the hybrid interface and are more effective at driving NP adsorption and dense film formation.

Beyond fundamental insights, these results carry broader implications. They demonstrate that the interfacial performance of protein–NP assemblies cannot be predicted solely from bulk protein:NP ratios or surface charge but is instead governed by the intrinsic conformational flexibility of the protein and its ability to reorganize at interfaces. From an application standpoint, these findings suggest that intrinsically disordered proteins, or engineered variants with tailored amphiphilicity, could be exploited to design efficient bio-nano stabilizers for foams and emulsions, whereas globular proteins might be better suited for applications where the stability and rigidity of the hybrid layer are prioritized over surface activity.

In summary, this chapter shows that protein-mediated nanoparticle assembly at fluid interfaces is a protein-specific and architecture-dependent phenomenon. By bridging macroscopic measurements, mesoscopic organization, and molecular-level spectroscopy, we provide a unified mechanistic framework that not only explains observed interfacial behaviors but also informs the rational design of functional bio-nano hybrid interfaces in food science, colloid engineering, and nanomaterials.

The results discussed in this chapter provide a detailed picture of the structural organization of protein-NP assemblies at the air-water interface under steady-state conditions. However, to fully understand their interfacial behavior, it is essential to explore how these hybrid layers respond to external mechanical perturbations. For this reason, the next chapter focuses on the dynamic regime under lateral compression, where the structural rearrangements and stability of the films can be directly probed.

6

Protein-mediated assembly of silica nanoparticles at the air–water interface: dynamic regime under compression

In the previous chapter, we examined the steady-state organization and interfacial properties of protein–nanoparticle assemblies at the air–water interface. While this static picture is fundamental for understanding the mechanisms of adsorption and hybrid film formation, it only represents one side of the problem. Interfaces in real applications are rarely at equilibrium; they are constantly subjected to external stresses that can drive restructuring, deformation, or even collapse of the monolayer. To gain a more complete view of these systems, it is therefore crucial to investigate their response under mechanical compression.

Lateral compression in a Langmuir trough offers a controlled approach to investigate the dynamic response of interfacial films. By progressively reducing the available surface area, the monolayer is driven to reorganize, thereby exposing its ability to accommodate stress through plastic deformation, reversible rearrangements, or, eventually, collapse, as discussed in the previous section. For protein layers, however, compression isotherms have been less widely applied as a tool to probe packing density and conformational transitions at the air–water interface. Only a few works have been published (Deulgaonkar et al., 2022; Sah et al., 2017), and some of them report the combination with *in situ* scattering techniques, including GISAXS, grazing incidence X-ray off-specular scattering (GIXOS) and grazing incidence X-ray fluorescence (GIXF), to monitor nanoscale rearrangements in real time and to quantify both structural correlations and biomolecular surface density (Abuillan et al., 2012; Singh et al., 2013).

In this chapter, classical surface pressure–area isotherms were combined with *in situ* scattering techniques, specifically Grazing Incidence Small Angle X-ray Scatter-

ing (GISAXS) and Neutron Reflectometry (NR). These methods allow us to follow structural rearrangements at the nanoscale during compression, providing real-time insights into interparticle distances, film thickness, and protein compositional changes.

The goal is to establish direct connections between the molecular nature of the protein, its mode of interaction with the nanoparticles, and the resulting macroscopic mechanical response. By integrating these dynamic results with the steady-state findings presented in Chapter 5, we can build a more comprehensive picture of protein–NP stabilization at liquid interfaces and extract general principles that may guide the design of functional, sustainable interfacial materials.

6.1 Results and Discussion

In this chapter, this section is organized into three subsections, each dedicated to one of the proteins investigated. Unlike Chapter 5, which was structured by experimental technique, here the focus is placed on the specific behavior of each protein, allowing a direct comparison of the corresponding hybrid protein–NP monolayers. In all cases, compression isotherms in a Langmuir trough and *in situ* GISAXS measurements were employed, while neutron reflectometry (NR) could only be performed for the BSA-based systems.

All samples were prepared following the same protocol, which is described in detail in Appendix D. Briefly, after one hour of adsorption at the air–water interface, both pure protein and protein–NP monolayers were compressed in a Langmuir trough at a constant rate of approximately 22 cm^2/min. For the hybrid protein–NP films, GISAXS patterns were recorded continuously during compression, from which the interparticle distance was extracted, as extensively discussed in the previous chapters.

6.1.1 Bovine serum albumin (BSA)

In Figure 6.1 are reported the compression isotherms of BSA and BSA-NP monolayers, measured as surface pressure π versus normalized surface area A/A_0 (where A_0 is the area at full expansion) under different experimental conditions.

The first relevant observation concerns the compression behavior of the bare BSA monolayer (Figure 6.1*A* and *B*). Remarkably, irrespective of the bulk composition—and thus of the interfacial equilibrium conditions—BSA displays a consistently high compressibility, essentially independent of both bulk concentration and ionic strength. At lower concentrations, the surface pressure exhibits a steeper initial rise upon compression ($A/A_0 \leq 0.85$), followed by a regime of nearly constant slope ($d\pi/d(A/A_0) = \text{const}$). Conversely, at higher concentrations, the surface pressure increases almost linearly with compression. Notably, the $\Delta\pi = \pi_{\text{compressed}} - \pi_{\text{expanded}}$, remains in the range of 8–10 mN/m.

This behavior, in good agreement with previous reports (Sah et al., 2017; Singh et al., 2013), strongly supports the view that BSA adsorption at the air–water interface

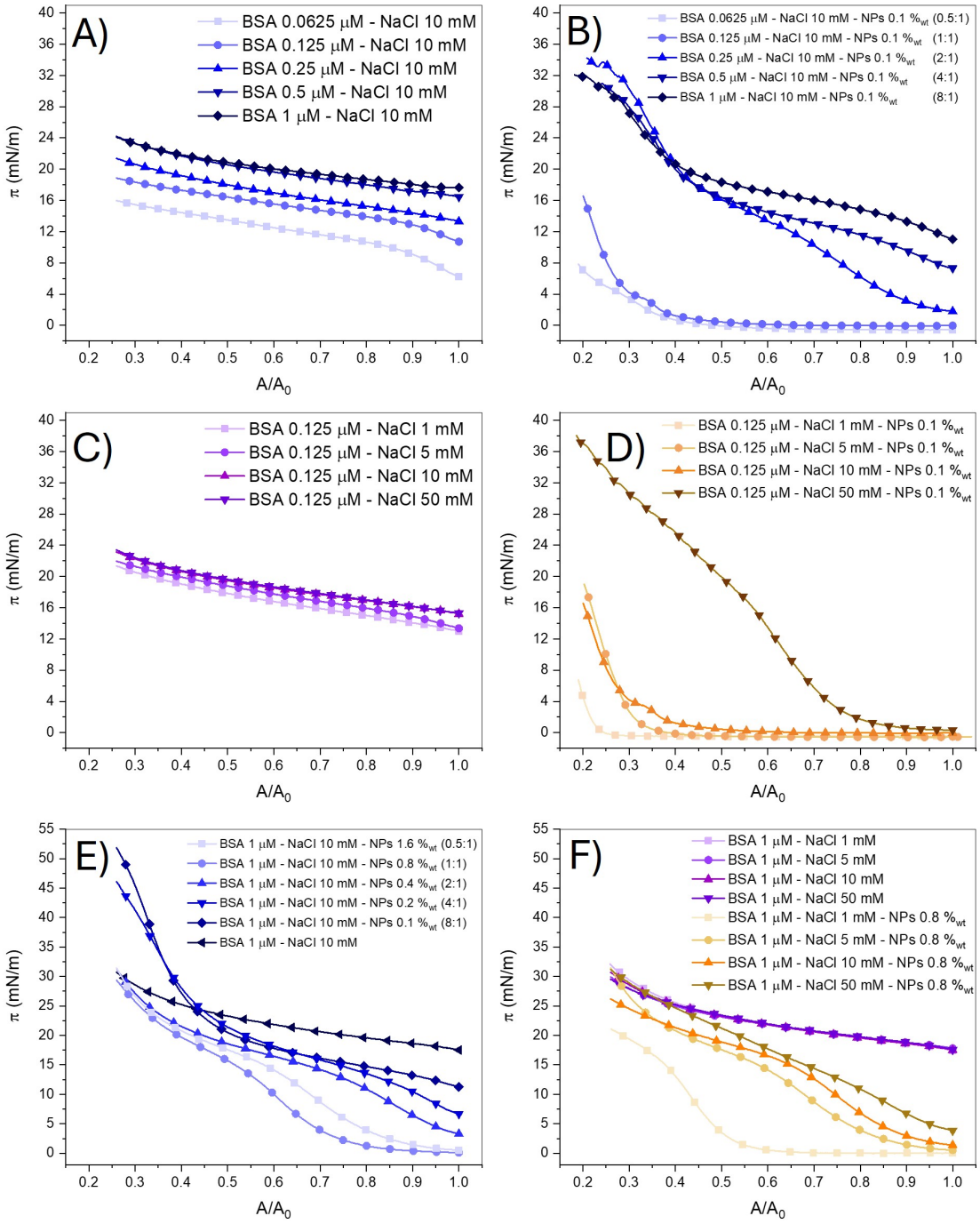

Figure 6.1: *Compression isotherms of surface pressure (π) as a function of the normalized surface area (A/A_0) for adsorbed layers at the air–water interface. (A) BSA in the concentration range 0.0625–1 μM in NaCl 10 mM; (B) BSA in the concentration range 0.0625–1 μM with NPs 0.1 $\%_{wt}$ in NaCl 10 mM; (C) BSA 0.125 μM in NaCl 1–50 mM; (D) BSA 0.125 μM with NPs 0.1 $\%_{wt}$ in NaCl 1–50 mM; (E) BSA 1 μM with NPs in the range 0–1.6 $\%_{wt}$ in NaCl 10 mM; (F) BSA 1 μM with NPs 0.8 $\%_{wt}$ in NaCl 1–50 mM.*

is a quasi-irreversible, far-from-equilibrium process (Liao et al., 2011). In contrast to small amphiphilic molecules, such as surfactants, that are able to maintain equilibrium surface excess by desorbing upon compression, thus exhibiting negligible increase in surface pressure (Ruffino et al., 2022), proteins are much larger entities with signifi-

cantly higher desorption energies. As a result, compression does not induce desorption but instead promotes structural rearrangements within the interfacial film, which may include buckling, folding, and even multilayer formation.

The compression isotherms of the BSA–NP monolayers display a more complex and strongly composition-dependent behavior. At low BSA content (i.e., low BSA:NP bulk ratio), the isotherms closely resemble those of the CTAB–NP monolayers described in Section 1. Specifically, the surface pressure increases slowly at the onset of compression, followed by a sharp rise and eventually a change in slope that is presumably indicative of monolayer collapse. Interestingly, the kink attributed with the collapse shifts to higher A/A_0 values as ionic strength, protein content (below a 2:1 ratio), and nanoparticle concentration increase, as expected for denser monolayers composed of irreversibly adsorbed nanoparticles. The situation becomes more intricate at higher protein contents (bulk ratios of 4:1 and 8:1, Figure 6.1 E and F). In these cases, the compression isotherms are characterized by an initial regime in which the surface pressure evolution mirrors that of pure protein monolayers: a slower but less compressible film at $A/A_0 \lesssim 0.5$. This is followed by a steep increase in surface pressure, consistent with a second regime dominated by nanoparticle packing.

These complex variations in monolayer compressibility, with the 2:1 BSA:NP samples lying in a clear transition regime, are consistent with the trends already observed in static GISAXS and SFG measurements of BSA in Chapter 5. Taken together, the data suggest that at low protein concentration the compressibility of the monolayer is primarily governed by nanoparticle packing, closely resembling the behavior of surfactant–NP systems, whereas at high protein content the initial compression response is dominated by the protein layer, before giving way to a regime once again controlled by nanoparticle packing.

To gain deeper insight into the structural rearrangements induced by compression, we performed *in situ* GISAXS measurements during the compression of the BSA–NP monolayers (see Appendix D for details of the experimental setup). The evolution of the interparticle distance with compression revealed highly interesting and composition-dependent trends, summarized in Figure 6.2. At low BSA:NP ratios, and independently of the ionic strength, the interparticle distance decreased almost linearly with compression, indicating a progressive and continuous packing of the nanoparticles, until a threshold compression at which the interparticle distance remains constant, mirroring the features of the corresponding surface pressure-area isotherms. In contrast, at higher protein contents, the structural response was more intricate: following an initial decrease, the interparticle distance entered a well-defined plateau region extending over a wide A/A_0 range, before decreasing again in a second compression regime followed by a second plateau at lower interparticle distance. Notably, this latter stage coincides with the point at which the compression isotherms exhibit the sharp increase in the surface pressure, previously associated with film collapse. The GISAXS data therefore provide direct structural evidence that the kinks observed in the pressure–area isotherms indeed correspond to the onset of monolayer collapse,

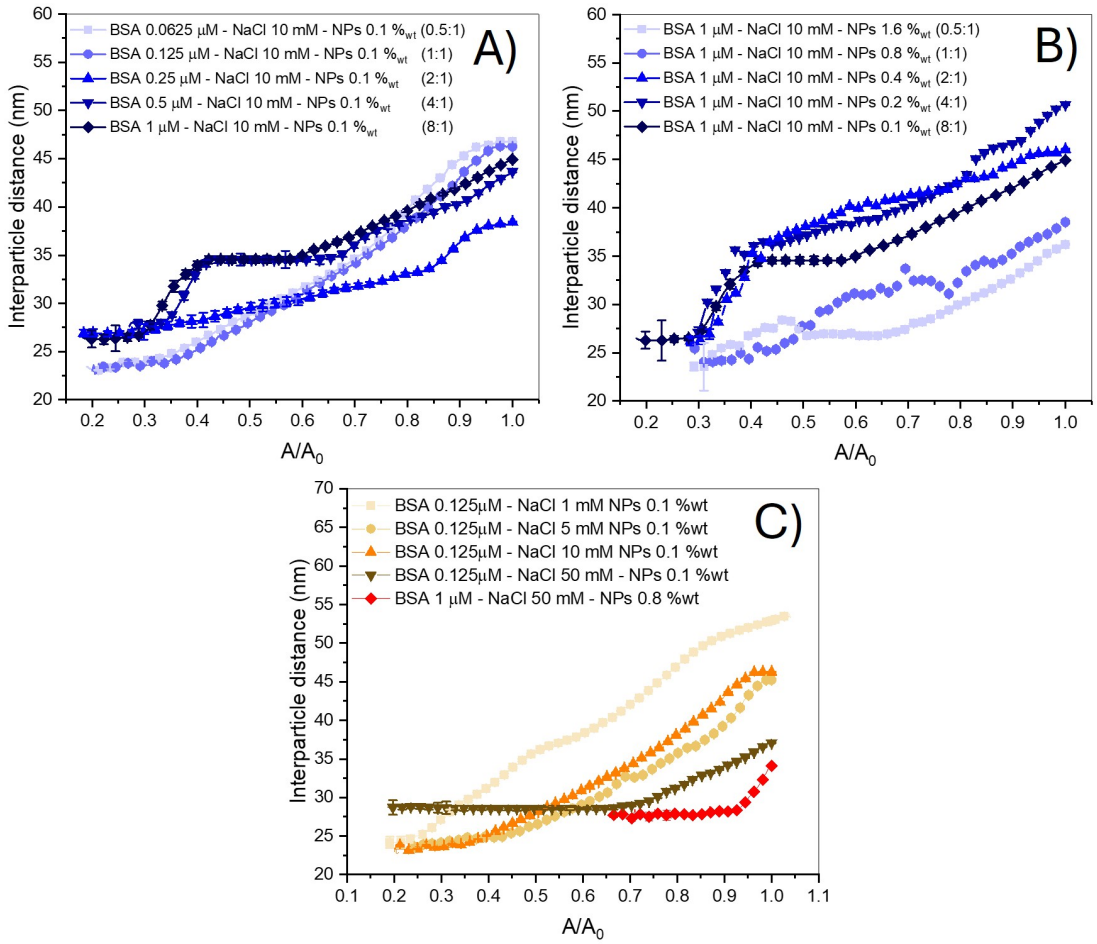

Figure 6.2: *Evolution of the monolayer interparticle distance with compression for BSA-NP hybrid monolayer at the air-water interface.(A) BSA in the concentration range 0.0625–1 µM with NPs 0.1 $\%_{wt}$ in NaCl 10 mM; (B) BSA 1 µM with NPs in the range 0.1–1.6 $\%_{wt}$ in NaCl 10 mM; (C) BSA 0.125 µM with NPs 0.1 $\%_{wt}$ in NaCl 1–50 mM and BSA 1 µM with NPs 0.8 $\%_{wt}$ in NaCl 50 mM (red diamonds).*

confirming the interpretation drawn from the compression isotherm analysis.

It is worth noting that after collapse, the interparticle distances are in the range of 23–25 nm for samples with low protein content or low ionic strength, indicating that the nanoparticles are essentially brought into direct contact. By contrast, for samples with high protein content or ionic strength, the post-collapse distances increase to 27–30 nm. This finding suggests that in these latter conditions the protein remains embedded between the nanoparticles after collapse, preventing direct contact and effectively forcing them apart. Moreover, the persistence of this spacing strongly indicates robust protein–nanoparticle interactions that suppress BSA desorption, even under extreme compression. Importantly, we observe that these trends are preserved whether the BSA:NP ratio is tuned by varying the protein concentration at constant nanoparticle content, or by changing the nanoparticle concentration at fixed protein content. This strongly suggests that the structure and composition of each individual BSA–NP complex at the interface are dictated primarily by the bulk BSA:NP ratio, whereas the absolute bulk composition only controls the overall surface coverage, *i.e.*, the number of

such aggregates that are available to populate the interface.

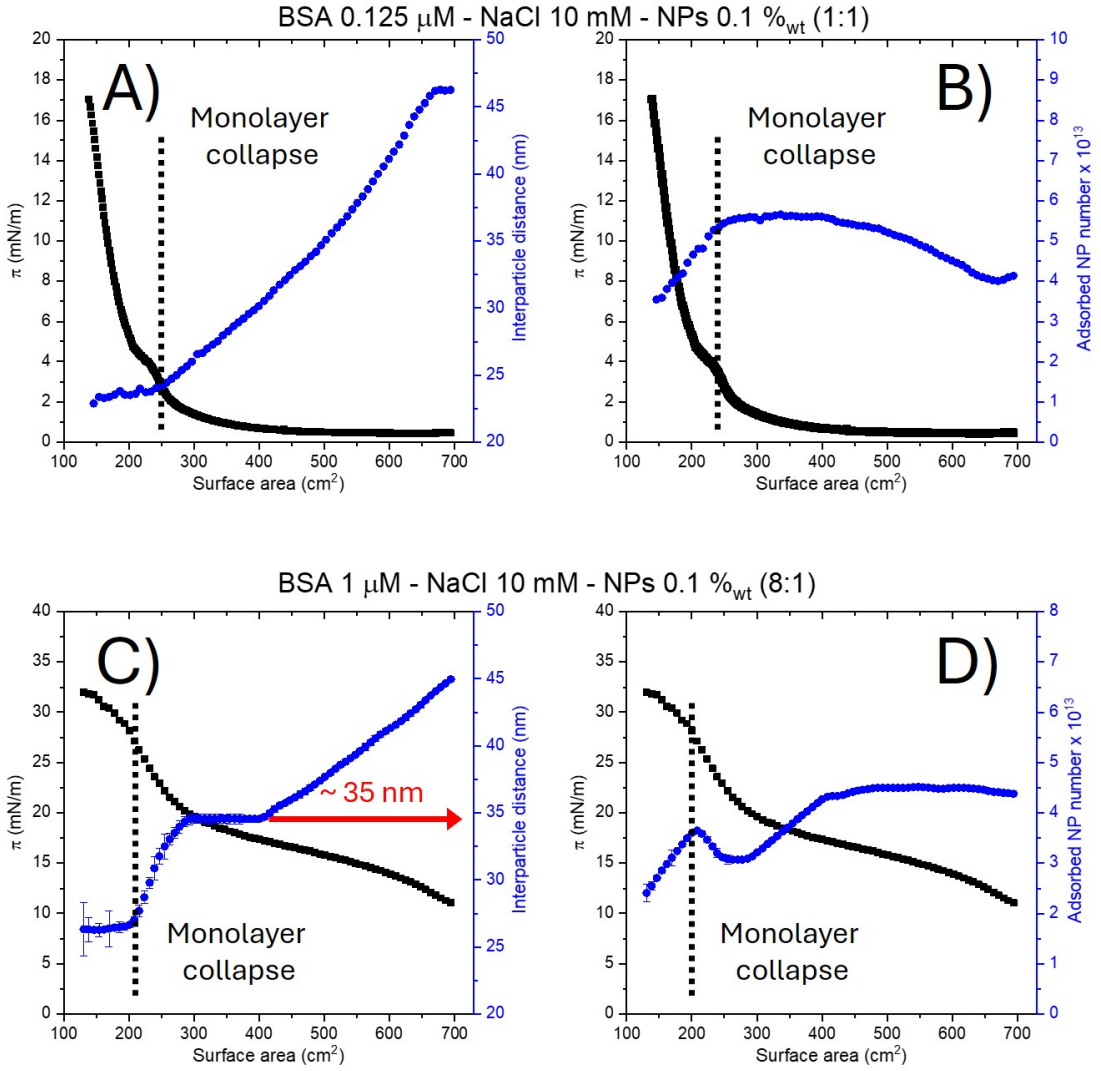

Figure 6.3: *Surface pressure isotherms (black curves, left axes) and interparticle distance from GISAXS analysis (blue curves, right axes in A and C) and the corresponding number of adsorbed nanoparticle for A (blue curves, right axes in B and D), for nanoparticle monolayers obtained with bulk composition (A,B) BSA 0.125 μM - NaCl 10 mM and NPs 0.1 %$_{wt}$, (C) BSA 1 μM - NaCl 10 mM and NPs 0.1 %$_{wt}$. In (A,B) the interparticle distance decreases continuously upon compression with an almost constant number of nanoparticle until the monolayer collapse. This suggest the formation of quasi-homogeneous monolayers. (C,D) At higher BSA concentration (1 μM), the interparticle distance initially decreases at constant NP number, then stabilizes around ~ 35 nm over a broad range of surface areas, and eventually decreases again upon further compression till the monolayer collapse is reached. Vertical dashed lines indicate the collapse point of the monolayer.*

Further insights can be obtained by analyzing the variation of the interparticle distance and particle number during compression in conjunction with the surface pressure. As an illustrative example, Figure 6.3 reports the data for samples containing 0.125 and 1 μM BSA in 10 mM NaCl with 0.1% NPs. The full dataset for all other samples is shown in Figure D.18, Figure D.19, and Figure D.20.

Starting with the sample at 0.125 μM BSA (Figure 6.3 A and B), the compression behavior can be clearly separated into two distinct stages, consistent with what was

already discussed in Chapter 3 (Figure 3.6). In the first stage, the interparticle distance decreases almost linearly while the particle number remains essentially constant and the surface pressure increases only slightly. In the second stage, the interparticle distance plateaus while the particle number decreases, a hallmark of monolayer collapse. This behavior demonstrates that under these conditions BSA is able to promote an effectively irreversible adsorption of the nanoparticles, at least up to the point of collapse. The slight deviation from linearity in the decrease of interparticle distance, along with the fact that the particle number is not perfectly constant, can be attributed to the significant inhomogeneity of the monolayer. This heterogeneity increases further during compression due to amorphization, as evidenced by the progressive broadening of the Bragg peak observed in Figure D.12, Figure D.13, and Figure D.14.

The sample at 1 μM BSA displays a much more complex behavior, as anticipated. Here, a slight initial increase in surface pressure is accompanied by a decrease in interparticle distance. The system enters a plateau regime where, surprisingly, the interparticle distance remains nearly constant at $\sim$ 35 nm across all samples with high BSA content (BSA:NP ratios of 2:1, 4:1, and 8:1). This value corresponds to a surface-to-surface separation distance of approximately 12 nm. Within this plateau, the surface pressure continues to rise slowly until a second regime sets in, characterized by a renewed decrease in interparticle distance and a sharp increase in surface pressure, ultimately culminating in the true monolayer collapse.

The plateau observed in the 1 μM BSA sample can in principle be rationalized by two scenarios. A first possibility is that the monolayer has already undergone a partial collapse. However, this explanation appears unlikely given the relatively large interparticle distance measured in this regime. A second, and more plausible, explanation is that the plateau reflects a structural or compositional transition within the monolayer that takes place at nearly constant interparticle distance.

To gain further insight into this phenomenon, we performed neutron reflectivity (NR) measurements on samples extracted at different stages of compression. Figure 6.4 reports the compression curves for BSA alone (0.125 and 1 μM in 10 mM NaCl, panel A) and for BSA–NP monolayers (0.125, 0.25, and 1 μM BSA in 10 mM NaCl with 0.1 $\%_{wt}$ NPs in panel B, C, and D, respectively), together with the red markers indicating the compression states at which reflectivity was measured.

It is important to note that, for intermediate compressions, the labels "+5 mN/m", "+8 mN/m", etc., refer to the target pressure relative to the steady-state pressure reached after 1 h of adsorption. This procedure was necessary because NR experiments require the acquisition of four contrast conditions, each of which had to be measured on a freshly prepared sample. Inevitably, slight variations in experimental conditions, such as small differences in the immersion of the Wilhelmy plate, led to minor shifts in the absolute steady-state pressure between replicate samples. By defining compression points relative to the equilibrium pressure after 1 h adsorption, we minimized these systematic differences and ensured that all contrasts corresponded to equivalent compression states.

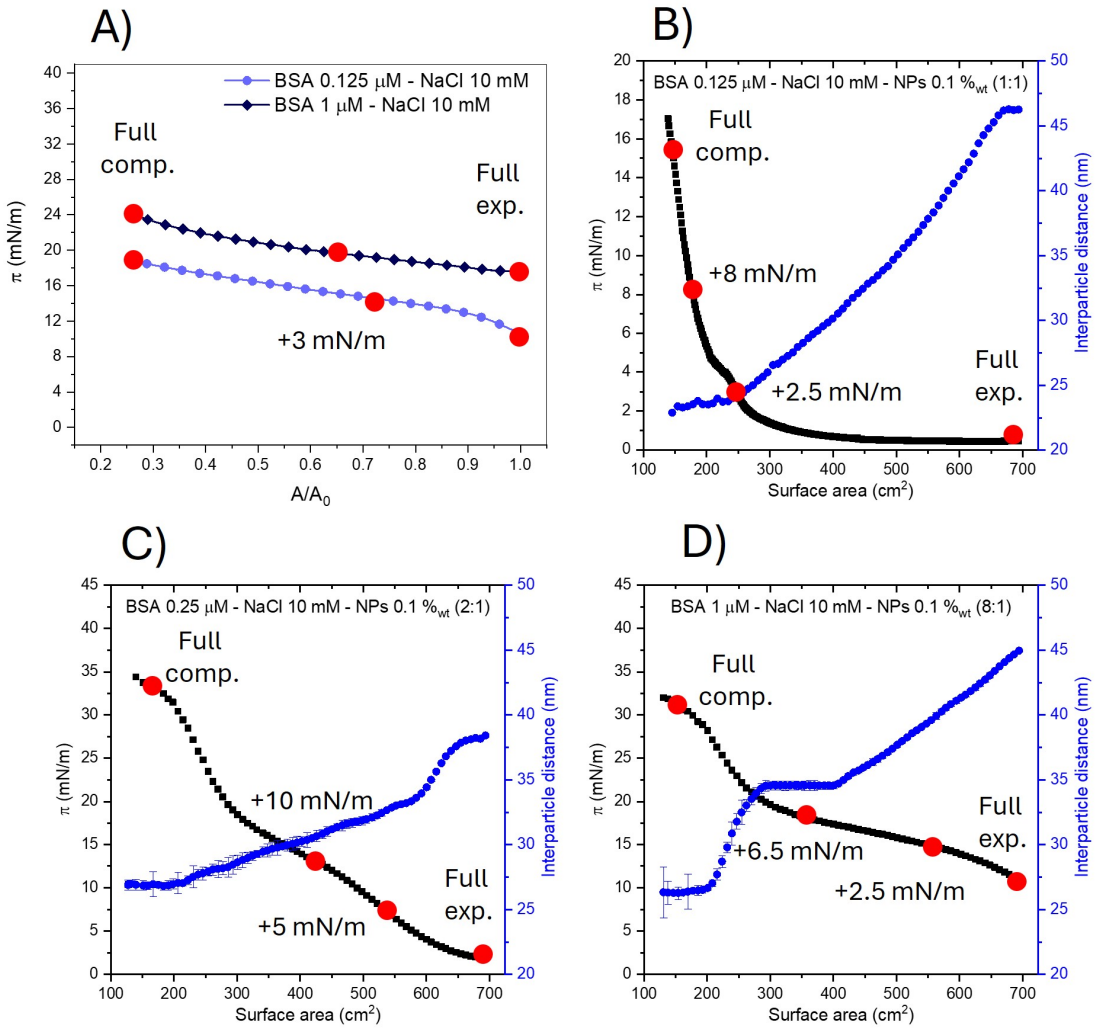

Figure 6.4: *Surface pressure and interparticle distance evolution during compression for BSA-only and BSA–NP layers at the air–water interface. The red markers highlight the surface pressures (and, when applicable, the associated interparticle distances) at which neutron reflectivity curves were recorded. These reference points were selected in order to compare the structural information obtained from GISAXS with the vertical density profiles derived from neutron reflectivity. The annotations (+5 mN/m, +8 mN/m, etc.) indicate the target surface pressures chosen for compression, expressed as increments relative to the equilibrium pressure reached after 1 h of adsorption at the air–water interface. This reference state was taken as the steady-state baseline prior to Langmuir trough compression in order to account for possible variations in the steady-state pressure of sample prepared at different contrast solvent due to experimental factors such as the immersion depth of the Wilhelmy plate.*

For the BSA-only samples, the neutron reflectivity data show an evolution consistent with both the literature and the compression isotherms. As illustrated in Figure D.7 and D.8, and from the fit results summarized in Table 6.1, compression induces a progressive desorption of protein from the interface. However, the desorbed BSA does not disperse into the bulk phase; rather, it accumulates into successive subsurface layers in the aqueous phase. At maximum compression, up to three distinct protein layers are detected, with a total thickness of ~ 90–100 Å. These dimensions are consistent both with a reorientation of the protein axis and the formation of true multi-

Table 6.1: *Neutron reflectometry fitting parameters for BSA layers at different compression stage. d is the layer thickness, σ is the roughness, and h% is the layer hydration. Numbers in parentheses indicate the uncertainty of the value.*

	$\sigma_{a/w}$	Layer 1			Layer 2			Layer 3			χ^2
		d (Å)	σ (Å)	h%	d (Å)	σ (Å)	h%	d (Å)	σ (Å)	h%	
BSA 0.125 μm - NaCl 10 mM											
Full expanded	3.1 (0.2)	27.6 (1.5)	0.1 (0.1)	80.36 (1.6)	-	-	-	-	-	-	57.5450
+3 mN/m	3.4 (0.1)	28.2 (2.1)	0.2 (0.5)	52.92 (1.2)	52.8 (3.4)	8.9 (0.5)	70.76 (3.4)	-	-	-	70.7677
Full compressed	2.8 (0.3)	28.3 (1.3)	0.2 (0.3)	52.08 (7.6)	58.7 (2.1)	11.2 (0.6)	65.18 (5.2)	38.45 (6.2)	34.1 (2.8)	95.88 (6.9)	90.1429
BSA 1 μm - NaCl 10 mM											
Full expanded	2.4 (0.3)	28.1 (1.7)	0.2 (0.3)	60.67 (2.8)	30.3 (0.8)	5.3 (0.8)	91.59 (5.8)	-	-	-	47.7194
+3 mN/m	2.6 (0.2)	29.3 (2.5)	0.4 (0.1)	53.45 (8.9)	55.4 (1.7)	7.6 (1.2)	74.35 (6.7)	-	-	-	50.8481
Full compressed	2.9 (0.1)	28.7 (2.6)	0.7 (0.2)	42.35 (3.2)	61.9 (1.6)	9.5 (3.5)	60.98 (8.9)	42.5 (5.3)	32.8 (4.2)	92.42 (7.4)	66.4573

layers. Comparable thicknesses have indeed been reported by *in situ* GIXOS studies on protein layers at the air-water interface (Singh et al., 2013), as well as in *ex situ* neutron reflectivity experiments where protein layers, transferred from the air–water interface onto solid supports, displayed a similar multilayered organization (Sah et al., 2017).

The most intriguing behavior, however, emerges for the hybrid BSA–NP monolayers. During compression, the nanoparticle layer preserves its monolayer structure, as confirmed by both GISAXS and neutron reflectivity (see reflectivity curves and SLD profile in Figure D.9 to D.11 and the fit values in Table D.1 to D.2), although the monolayers clearly densify (as shown by the decreasing interparticle distance). At the same time, marked changes occur in the protein distribution between the "air-side" and "water-side" shells. To quantify these compositional variations, we calculated the total protein mass at the interface (W_{BSA}) from the interfacial excess (Γ) of the two shells, using the relation

$$W_{BSA} = \Gamma \cdot A \tag{6.1}$$

where A is the macroscopic interfacial area, Γ is the protein surface excess calculated with Equation 5.1 and 5.5. The results, reported in Table 6.2, reveal strikingly different behaviors depending on the BSA:NP ratio.

A feature common to all systems is the redistribution of protein from the air-side to the water-side shell during the early stages of compression (*e.g.*, +2.5 mN/m for 1:1, +5 mN/m for 2:1, and +2.5 mN/m for 8:1). For the 1:1 ratio, this redistribution occurs without significant loss of total protein mass (remaining at ~ 43 – 44 μg). In contrast, for the 2:1 and 8:1 systems, the redistribution is accompanied by a measurable loss of protein to the bulk, with the total interfacial protein mass decreasing from ~100 to ~90 μg and from ~128 to ~94 μg, respectively. It is important to note that for the 1:1 system, the +2.5 mN/m state is already close to the monolayer collapse. The higher compression stages (+8 mN/m and full collapse) were acquired after the monolayer collapse; indeed, the total protein mass decreases significantly due to the compression-induced desorption of the BSA-NP complexes.

For the 2:1 system, the intermediate state at +10 mN/m corresponds to a regime just after the first inflection in the surface pressure isotherm. Here, the total protein mass re-

Table 6.2: *Evolution of the BSA surface mass calculated by the surface excess* (Γ) *and the corresponding macroscopic are* (A) *at different compression target points for BSA-NP monolayers at different BSA:NP bulk ratio. Values are reported as mean*(*error*).

Bulk ratio	Target point for NR	Γ (ng/cm^2)			A (cm^2)	BSA surface mass (μg)		
		Air	Water	TOT		Air	Water	TOT
(1:1)	Full expanded	30.13(3.12)	30.92(2.53)	61.05(5.65)	705.3(0.2)	21.3(2.2)	21.8(1.8)	43.1(4.0)
	+2.5 mN/m	17.38(0.58)	48.14(0.25)	65.52(0.83)	677.5(7.4)	11.8(0.5)	32.6(0.5)	44.4(1.0)
	+8 mN/m	15.80(0.25)	32.89(0.54)	48.69(0.79)	602.8(4.6)	9.5(0.2)	19.8(0.5)	29.3(0.7)
	Full compressed	40.14(1.23)	46.02(2.14)	86.16(3.37)	272.8(62.4)	10.9(2.8)	12.6(3.5)	23.5(6.3)
(2:1)	Full expanded	87.31(1.32)	56.07(0.89)	143.38(2.21)	705.3(0.2)	61.6(0.9)	39.5(0.6)	101.1(1.6)
	+5 mN/m	32.17(0.87)	108.94(0.54)	141.11(1.41)	643.0(4.2)	20.7(0.7)	70.0(0.8)	90.7(1.5)
	+10 mN/m	29.43(1.21)	161.17(0.52)	190.6(1.73)	483.3(47.5)	14.2(2.0)	77.9(7.9)	92.1(9.9)
	Full compressed	127.88(3.48)	107.82(0.74)	235.70(4.22)	178.8(25.2)	22.9(3.8)	19.3(2.8)	42.1(6.7)
(8:1)	Full expanded	128.52(0.64)	39.35(0.52)	167.87(1.16)	705.9(1.8)	87.1(0.6)	41.4(0.6)	128.5(1.2)
	+2.5 mN/m	75.50(0.55)	72.36(0.43)	147.86(0.98)	640.5(13.2)	48.4(1.3)	46.3(1.2)	94.7(2.6)
	+6.5 mN/m	143.61(1.25)	101.12(2.14)	244.73(3.49)	247.0(78.9)	35.5(11.6)	25.0(8.5)	60.4(20.2)
	Full compressed	132.04(2.54)	116.23(0.38)	248.27(2.92)	196.3(22.5)	25.9(3.5)	22.8(2.7)	48.7(6.2)

- (1:1) = BSA 0.125 μM NaCl 10 mM - NPs 0.1 $\%_{wt}$
- (2:1) = BSA 0.25 μM NaCl 10 mM - NPs 0.1 $\%_{wt}$
- (8:1) = BSA 1 μM NaCl 10 mM - NPs 0.1 $\%_{wt}$

mains nearly constant, while the interparticle distance decreases linearly (Figure 6.4*C*). Notably, however, the slope of this decrease is smaller than in the low-protein systems, indicating that part of the applied compression is accommodated by a structural/compositional reorganization of the monolayer rather than by nanoparticle packing alone. This interpretation is consistent with the large uncertainties on the BSA mass observed at +10 mN/m, which point to significant heterogeneity associated with such a rearrangement process.

The most peculiar case is the 8:1 system. Here, progressive compression consistently reduces the protein mass: from ~94 μg at +2.5 mN/m, to ~60 μg at +6.5 mN/m, and finally to ~48 μg at maximum compression. The +6.5 mN/m state coincides with the plateau regime, characterized by significant uncertainty in the interfacial protein mass, which strongly suggests that this plateau corresponds to a structural/compositional transition of the monolayer occurring at nearly constant interparticle distance.

Two main conclusions can be drawn from these results. First, the intermediate compression behavior can be rationalized by a two-layer protein arrangement at the interface. The air-side layer, richer in protein, is composed of a strongly bound protein shell directly associated with the nanoparticles, the so-called hard corona, and an outer, more weakly bound soft corona (Shourni et al., 2022; Halder et al., 2023). This interpretation is fully consistent with SFG results, which reveal an increase in total protein signal (Amide bands) with increasing bulk protein concentration, accompanied by a reduction in CH and COOH bands, reflecting the loss of symmetry at the air-side due to crowding. It also aligns with the NR and compression data. Upon compression, the soft corona desorbs and, similarly to protein-only films, the desorbed material from the air-facing side mainly accumulates in the water-facing shell with minimal desorption toward the bulk. Further compression eventually promotes protein desorption and particle packing, until the nanoparticle monolayer stabilized by the hard corona

collapses due to steric and electrostatic repulsion, leading to the final release of the BSA-NP complexes. Second, a direct correlation emerges between the dynamic GISAXS data and the BSA surface excess at the full-compression stage. Comparing the total interfacial BSA excesses at the points of full compression shows a systematic increase with bulk protein concentration, from $\sim 86\ \mathrm{ng/cm^2}$ for the 1:1 sample to $\sim 235\ \mathrm{ng/cm^2}$ and $\sim 248\ \mathrm{ng/cm^2}$ for the 2:1 and 8:1 systems, respectively. Since full compression corresponds to a state reached after monolayer collapse, where the nanoparticle interfacial excess, and therefore the amount of tightly bound BSA per NP forming the hard corona, remains essentially constant, the increase in protein surface excess accounts for the different threshold interparticle distances, namely ~ 23 nm for the 1:1 samples and ~ 27 nm for the 2:1 and 8:1 systems. At higher protein concentrations, the increased protein density within the hard corona effectively acts as a spacer, preventing direct nanoparticle contact and thereby causing monolayer collapse at larger interparticle separations. This correlation also extends to the high ionic strength sample, where collapse occurs at an interparticle distance of ~ 30 nm.

As a proof of this, we estimated the number of BSA molecules per NP at the full compression stage with Equation 5.4, as explained in Chapter 5. The results, reported in Table 6.3, demonstrate that upon compression of the monolayer beyond collapse, the overall BSA:NP surface ratio decreases to ~14 for the sample at BSA 0.125 μM and to ~16 for the samples at BSA 0.25 and 1 μM, which corresponds to the composition of the hard-corona layer. This calculation allows us to estimate the amount of BSA per NP lost, which corresponds to $\sim$ 0, 2 and 8.5 molecules of BSA per NP for the samples at 0.125, 0.25 and 1 μM BSA, respectively, and accounts for the soft-corona layer composition. Moreover, the slightly higher BSA:NP surface ratios found for the samples at higher protein concentrations are in agreement with the higher collapse interparticle distances.

Table 6.3: *Calculated BSA molecules per NP at the air-water interface at full compression. The concentration of NP was 0.1 $\%_{wt}$ and the ionic strength was 10 mM far all samples. V_{air} and V_{water} are the protein shell volume per each NP respectively at the air and water side. BSA:NP_{air} and BSA:NP_{water} are the average number of BSA molecule per nanoparticle respectively in V_{air} and V_{water}, BSA:NP_{TOT} is the sum of BSA:NP_{air} and BSA:NP_{water}. The loss of BSA molecules per NP was calculated as the difference between the BSA:NP_{TOT} at full expansion and at full compression. Numbers in parentheses indicate uncertainties in the value.*

Sample	Full expanded	Full compressed					Loss BSA per NP
	BSA:NP_{TOT}	V_{air} (nm^3)	BSA:NP_{air}	V_{water} (nm^3)	BSA:NP_{water}	BSA:NP_{TOT}	
BSA 0.125 μM	13.25(0.99)	961.66(83.03)	6.38(0.55)	1186.82(109.12)	6.88(0.73)	13.26(1.28)	~ 0
BSA 0.25 μM	18.14(2.37)	1206.60(72.30)	8.01(0.48)	1222.06(123.30)	8.11(0.82)	16.12(1.30)	2.02(3.67)
BSA 1 μM	24.40(0.75)	1204.01(72.19)	7.99(0.48)	1193.45(74.16)	7.92(0.49)	15.91(0.97)	8.49(1.72)

6.1.2 β-casein (BCN)

The compression behavior of β-casein (BCN) and of its hybrid layers with nanoparticles (BCN–NP) is considerably simpler to interpret compared to BSA systems (Figure 6.5). The compression isotherms of pure β-casein are broadly similar to those of BSA, suggesting an analogous adsorption mechanism. At high protein concentration (1

μM), however, the increase in surface pressure upon compression is more pronounced than for BSA. This can be attributed to the higher flexibility and conformational plasticity of caseins, which can form more entangled interfacial structures, and to their stronger amphiphilic character, which makes desorption from the interface less favorable (Horne, 2006; Gennes, 1980; Yampolskaya et al., 2006).

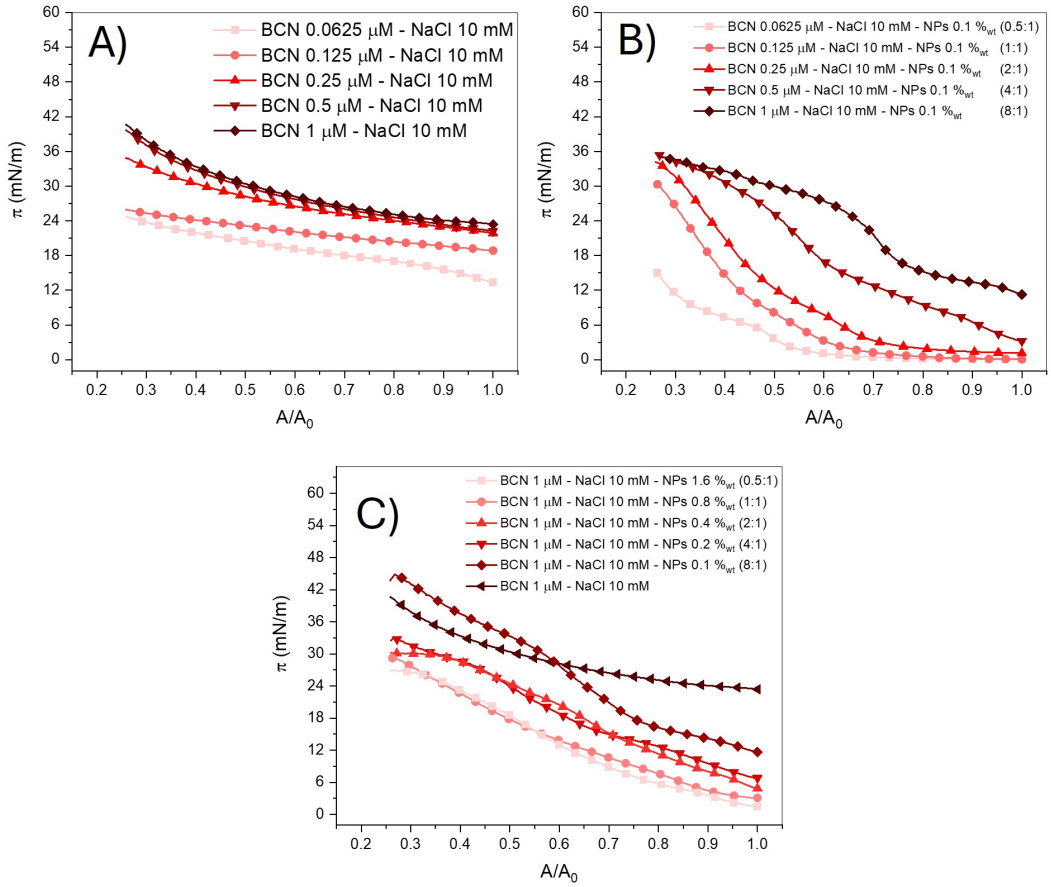

Figure 6.5: *Compression isotherms of surface pressure (π) as a function of the normalized surface area (A/A_0) for adsorbed layers at the air–water interface. (A) BCN in the concentration range 0.0625–1 μM in NaCl 10 mM; (B) BCN in the concentration range 0.0625–1 μM with NPs 0.1 $\%_{wt}$ in NaCl 10 mM; (C) BCN 1 μM with NPs in the range 0.1–1.6 $\%_{wt}$ in NaCl 10 mM.*

In the presence of nanoparticles, the compression isotherms of the BCN–NP systems with constant NP concentration (0.1 $\%_{wt}$) closely resemble those of surfactant–NP monolayers. They exhibit the characteristic three-stage behavior of irreversibly adsorbed NP monolayers: (i) a very slow initial increase in surface pressure, (ii) a sharp rise once electrostatic repulsion between NPs becomes dominant, and (iii) a kink associated with monolayer collapse. By contrast, in systems with constant protein concentration (1 μM), the compression curves are noticeably smoother, with the sharp transitions largely absent and replaced by gradual changes, particularly at higher NP loadings.

These trends are fully consistent with the dynamic GISAXS results (Figure 6.6). In all cases, the interparticle distance decreases linearly with compression until collapse, where it levels off. For the NP-constant systems (0.1 $\%_{wt}$), this transition is abrupt,

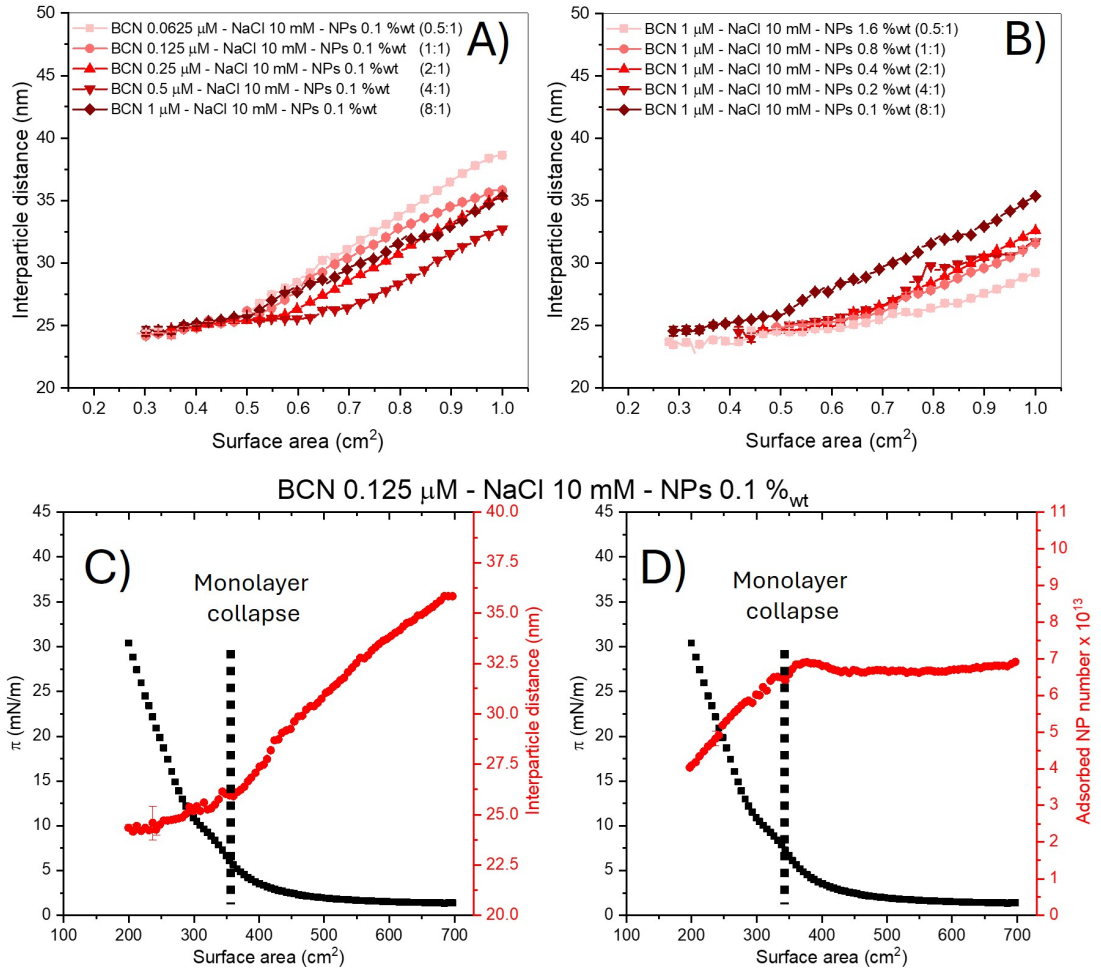

Figure 6.6: *Evolution of the monolayer interparticle distance with compression for BCN-NP hybrid monolayer at the air-water interface.(A) BCN in the concentration range 0.0625–1 µM with NPs 0.1 $\%_{wt}$ in NaCl 10 mM; (B) BCN 1 µM with NPs in the range 0.1–1.6 $\%_{wt}$ in NaCl 10 mM. In (C,D) are reported the evolution of the interparticle distance (red squares, C) and the adsorbed nanoparticle number (red squares, D) with the corresponding surface pressure (black squares, C and D) with compression for one exemplificative composition. Both the interparticle distance and the number of adsorbed nanoparticles follow the two stage compression trend described for CTAB-NP systems in Figure 3.6, suggesting an overall homogeneity of the monolayer.*

whereas for the protein-constant systems the transition is more gradual, extending smoothly from the compression regime into the post-collapse state. This difference is reflected in the GISAXS patterns: samples at constant protein concentration display broader Bragg peaks with lower intensity compared to NP-constant systems, indicating more disordered monolayers with weaker in-plane correlations. Such structural disorder results in a softer compression response, where densification and collapse occur progressively rather than sharply. Importantly, however, even these more disordered BCN–NP monolayers remain significantly more homogeneous than the corresponding BSA–NP systems, as demonstrated by their consistent stage-wise compression behavior (Figure 6.6 C,D) and the irreversible nature of NP adsorption. This improved homogeneity can be ascribed to the reduced degree of protein crowding at the interface

in BCN systems.

A key to understanding these differences lies in the molecular structure of BCN compared to BSA. Caseins are often described as "macro-surfactants" (Horne, 2006; Yampolskaya et al., 2006): the N-terminal region is enriched in highly hydrophilic and phosphorylated residues, while the C-terminal region is predominantly hydrophobic. As a result, BCN carries a more negative net charge, as confirmed by ζ-potential measurements, and exhibits stronger amphiphilic character than BSA. These features confer higher interfacial activity (Pérez-Fuentes et al., 2017), promoting more efficient NP assembly despite a smaller fraction of protein being engaged at the interface, as suggested by the higher steady-state surface tension at equal protein–NP composition and weaker Amide band intensities in SFG spectra.

Moreover, the smaller size and lower abundance of BCN at the interface compared to BSA facilitate tighter nanoparticle packing, as evidenced by consistently lower steady-state interparticle distances under identical protein–NP conditions. The reduced protein content also diminishes attractive interactions (hydrophobic, van der Waals, and dipolar) that otherwise arise from the large polarizable domains of globular proteins such as BSA. These attractions, combined with the presence of local positive and negative patches on the protein surface, even above the isoelectric point (Gonzalez-Posada et al., 2024), induce protein–protein interactions that disrupt lateral order. In contrast, the more amphiphilic, flexible, and surfactant-like BCN promotes higher interfacial activity with less crowding and disorder, thereby yielding more homogeneous hybrid NP monolayers.

6.1.3 β-lactoglobulin (BLG)

In the previous chapter, we showed that BLG–NP systems generally did not exhibit GISAXS patterns consistent with well-correlated NP monolayers, except for the sample with bulk composition BLG 1 μM – NaCl 10 mM – NPs 0.8 $\%_{wt}$ (bulk ratio 1:1). Similarly, SFG spectra indicated that the presence of NPs does not induce significant structural changes in BLG at the interface. This conclusion was further supported by dynamic surface tension (DST) measurements, which, unlike those for BSA and BCN, revealed that NPs only slow down the adsorption kinetics of BLG but do not alter its adsorption mechanism. Consistently, compression isotherms (Figure 6.7) revealed a dynamic behavior that further supports this low BLG-NP interaction.

While pure BLG behaves similarly to BSA and BCN, suggesting again a quasi-irreversible adsorption at the air–water interface, the most informative results were obtained in the presence of NPs. For bulk ratios BLG:NP > 2:1, the compression isotherms are essentially similar to those of pure BLG, reinforcing the idea that adsorption is dominated by free protein with little or no contribution from NPs. Conversely, at lower ratios (0.5:1 and 1:1), the isotherms change significantly, adopting the typical shape of NP monolayers. In the 0.5:1 case, the surface pressure increases only near the end of compression, suggesting the formation of very sparse monolayers. These results remain

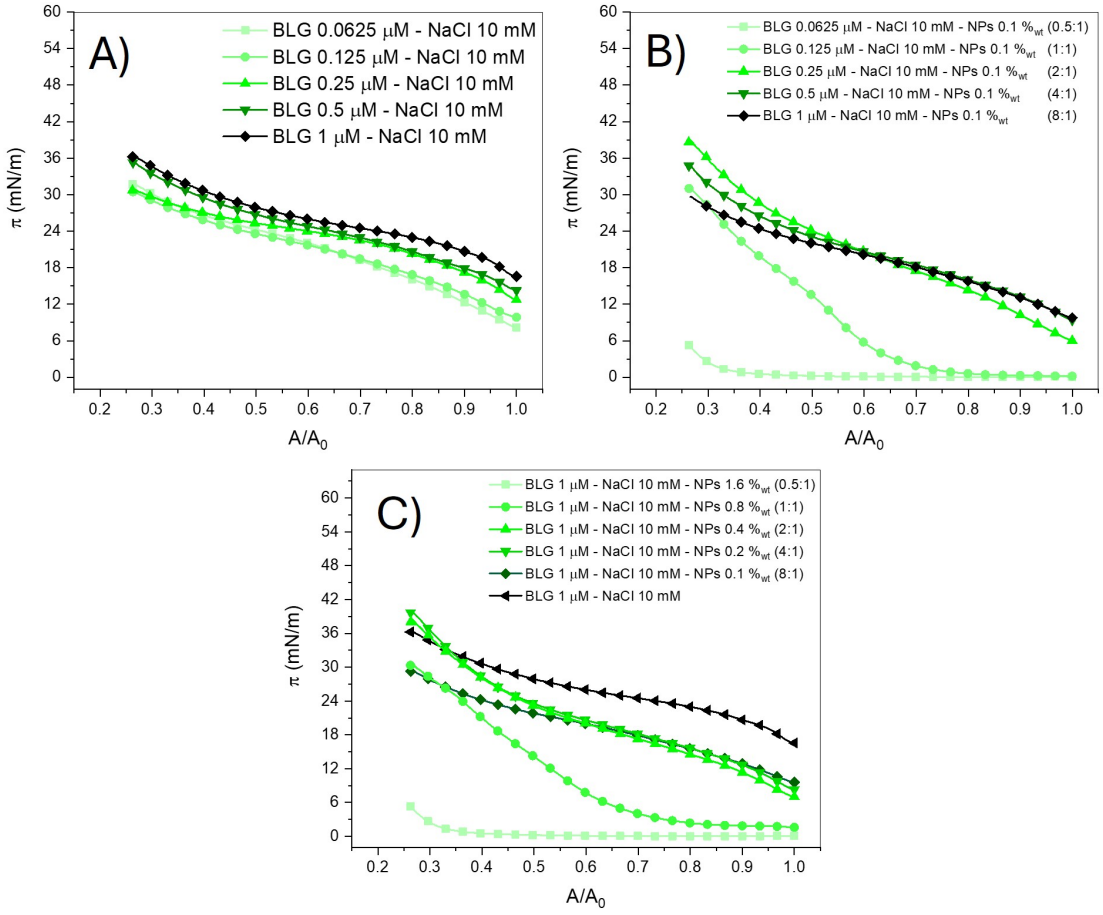

Figure 6.7: *Compression isotherms of surface pressure (π) as a function of the normalized surface area (A/A_0) for adsorbed layers at the air–water interface. (A) BLG in the concentration range 0.0625–1 μM in NaCl 10 mM; (B) BLG in the concentration range 0.0625–1 μM with NPs 0.1 $\%_{wt}$ in NaCl 10 mM; (C) BLG 1 μM with NPs in the range 0.1–1.6 $\%_{wt}$ in NaCl 10 mM.*

puzzling, since despite the similar isotherms observed for 0.5:1 and 1:1 systems (under constant NP or constant protein conditions), GISAXS patterns at the steady-state were observed in only one case.

Dynamic GISAXS experiments helped resolve this apparent inconsistency. For high BLG:NP ratios (see Figure D.11), compression induces a slight but progressive increase in GISAXS intensity, sometimes accompanied by the emergence of a weak peak. Although these signals are too faint to fit quantitatively, they qualitatively demonstrate that even at high protein content a small number of NPs adsorb at the interface, albeit sparsely distributed and poorly correlated, preventing measurable GISAXS features.

By contrast, the monolayer formed at BLG 1 μM – NaCl 10 mM – NPs 0.8 $\%_{wt}$ displays the hallmarks of irreversibly adsorbed NP films. The evolution of GISAXS patterns (Figure 6.8A) shows a progressive shift of the Bragg peak to higher q values, corresponding to a nearly linear decrease in interparticle distance with compression (Figure 6.8B). The number of adsorbed particles remains essentially constant during compression (Figure 6.8C), confirming both the homogeneity of the monolayer and the irreversible adsorption of NPs. For this sample, the interparticle distance was calcu-

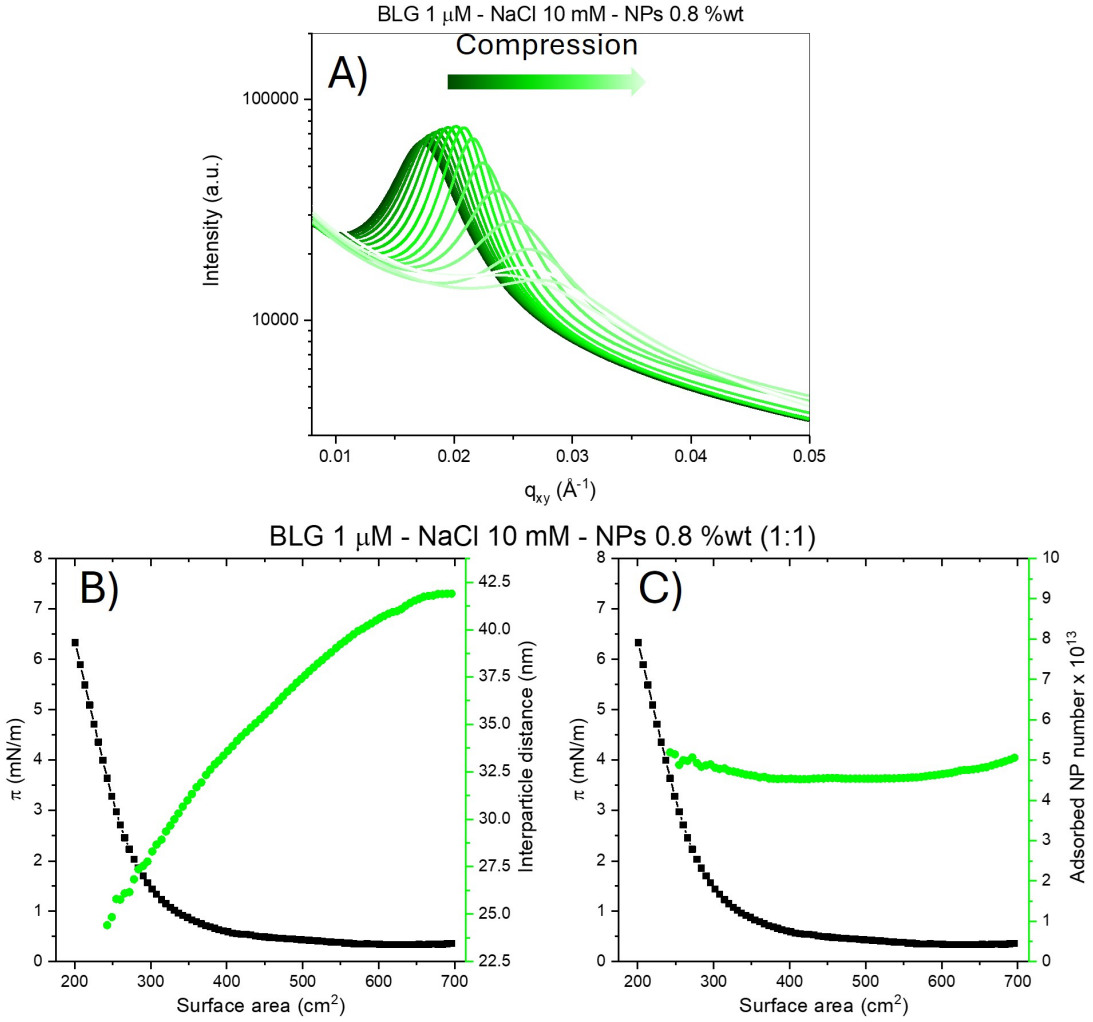

Figure 6.8: *Evolution of (A) 1D GISAXS horizontal cut, (B) interparticle distance (green squares), and (C) the adsorbed nanoparticle number (green squares) and the corresponding surface pressure (black squares, B and C) with compression for sample at the bulk composition BLG 1 μM - NaCl 10 mM - NPs 0.1 %$_{wt}$.*

lated under the assumption of short-range hexagonal packing, *i.e.* $ID = 4\pi/\sqrt{3}q_c$

The most surprising results were obtained for BLG–NP systems at lower BLG concentrations (0.0625 μM and 0.125 μM, corresponding to bulk ratios 0.5:1 and 1:1). Upon compression, well-defined GISAXS patterns emerged in both cases (Figure 6.9*A* and *B*), supporting the formation of NP monolayers. However, the evolution of these patterns differs from what is typically observed. Specifically, two distinct Bragg peaks appear, here denoted as q_{c1} (low q_{xy}) and q_{c2} (high q_{xy}). Strikingly, their evolution is independent: the two peaks do not scale together as expected for different orders of diffraction from the same lattice, as shown in Figure 6.9*C* and *D* (blue squares: q_{c1}; cyan squares: q_{c2}).

To test whether q_{c2} could correspond to a higher-order reflection of q_{c1}, we calculated the theoretical positions of q_{c2} under three packing assumptions: (*i*) square packing, where $q_{c2} = \sqrt{2}q_{c1}$ (red symbols); (*ii*) hexagonal packing, where $q_{c2} = \sqrt{3}q_{c1}$

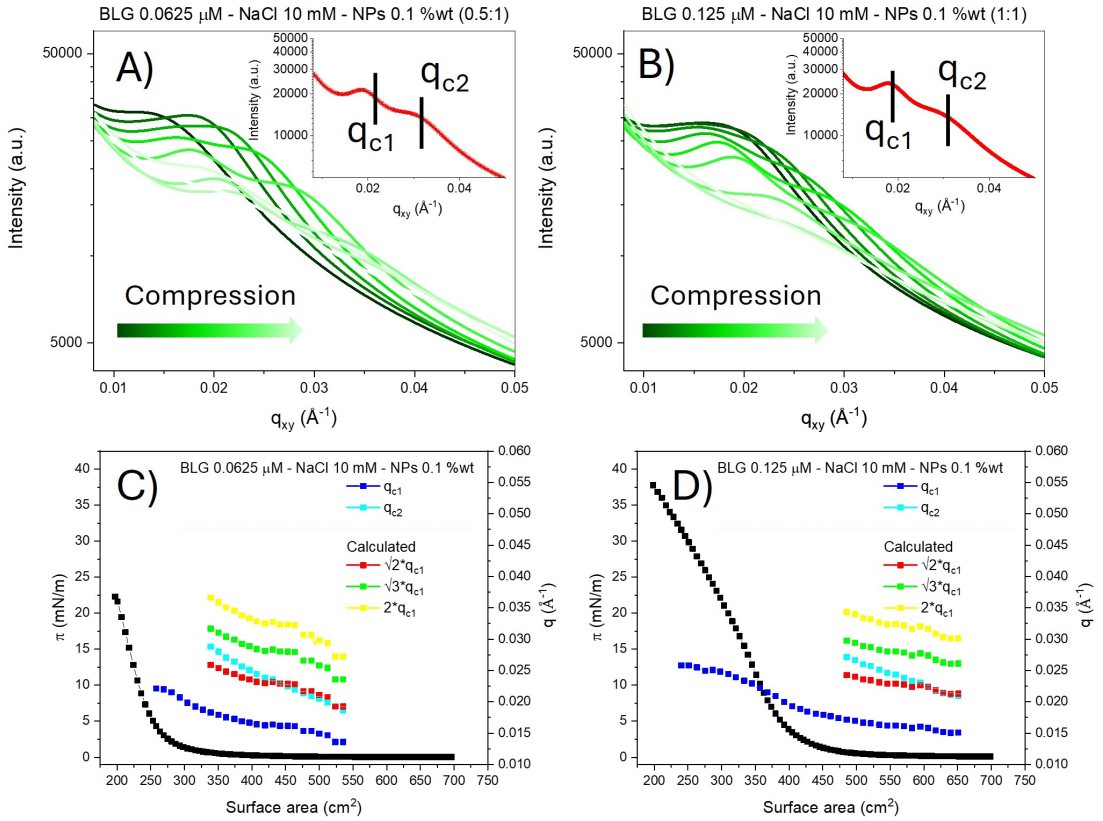

Figure 6.9: *Evolution of (A,B) 1D GISAXS horizontal evolution with monolayer compression. The red curves in the inset show a representative 1D experimental pattern with the two Bragg peaks highlighted. (C,D) Evolution with compression of the two independent maximum position of the two Bragg peaks q_{c1} (blue squares) and q_{c2} (cyan squares) together with the calculated position of the high order Bragg position peaks with respect q_{c1} for the (11) direction in a square lattice ($\sqrt{2}q_{c1}$, red squares), in an hexagonal lattice ($\sqrt{3}q_{c1}$, green squares) and for the (20) direction ($2q_{c1}$, yellow squares). The bulk composition for the two sample was NaCl 10 mM - NPs 0.1 $\%_{wt}$ and (A,C) BLG 0.0625 μM and (B,D) BLG 0.125 μM.*

(green symbols); and (*iii*) a second-order (20) reflection, where $q_{c2} = 2q_{c1}$ (yellow symbols). Experimentally, q_{c2} evolves between the theoretical values expected for square and hexagonal arrangements.

To estimate the real-space interparticle distance (ID) from the first Bragg reflection (q_{c1}), two possible packing geometries were considered, namely, hexagonal ($ID = 4\pi/\sqrt{3}q_{c1}$) and a square ($ID = 2\pi/q_{c1}$) packing of the nanoparticle within the monolayer (Schaefer et al., 1985; Weeks, 2017; Glatter, 2018). The ID values obtained with both assumptions, which are reported in Figure 6.10, are physically reasonable, since they are always larger than $2r_{\mathrm{NP}} = 23.2$ nm which corresponds to the nanoparticle diameter and thus represent the minimum measurable center-to-center distance (silica nanoparticles being rigid and incompressible under these conditions). However, the surface pressure evolution during compression provides a clearer indication. In particular, for the sample at BLG 0.125 μM a sharp increase in surface pressure is observed when the interparticle distance, calculated under the assumption of square packing, approaches $\sim$ 23 nm, *i.e.*, the NP diameter. This behavior is consistent with the mono-

layer collapse, suggesting that, at least in this regime, the square packing assumption gives a more realistic description of the system.

On the other hand, it cannot be excluded that in the final stages of compression the packing becomes progressively more hexagonal. Indeed, in this regime the second Bragg reflection (q_{c2}) shifts towards the theoretical position of the (11) reflection of a hexagonal lattice, indicating a local rearrangement into this symmetry. Further support for this interpretation comes from analogous systems (e.g. BSA adsorbed on nanoparticles), where monolayer collapse was also observed at interparticle distances of about ~ 30 nm at high BSA:NP ratio. However, this would suggest the presence of a significant amount of protein strongly attached to the nanoparticle surface leads to the effectively increasing of the critical collapse distance.

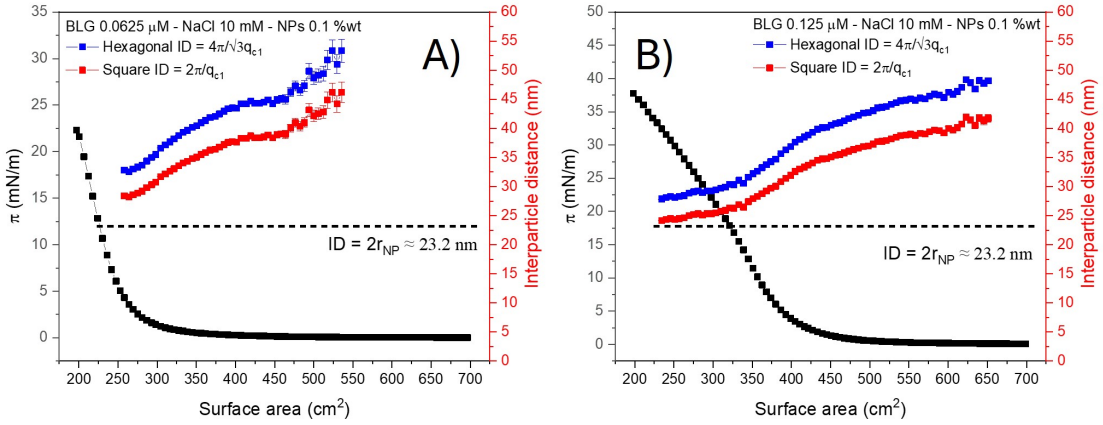

Figure 6.10: *Evolution of the monolayer interparticle distance (right axis) and surface pressure (left axis) with compression calculated from the value of q_{c1} by considering a hexagonal packing with $ID = 4\pi/\sqrt{3}q_{c1}$ (blue squares) and a square packing with $ID = 2\pi/q_{c1}$ (red squares). The bulk composition for the two sample was NaCl 10 mM - NPs 0.1 $\%_{wt}$ and (A) BLG 0.0625 μM and (B) BLG 0.125 μM.*

To further characterize the structural re-organization during compression, we also analyzed the relative evolution of the two peaks q_{c1} and q_{c2}. Assuming that q_{c2} corresponds to the (11) reflection of the same lattice giving rise to q_{c1}, the ratio $r = q_{c2}/q_{c1}$ can be directly related to the lattice angle γ of an oblique two-dimensional unit. In general, for an oblique lattice, the scattering vector is given by (Glatter, 2018):

$$q_{hk} \propto \sqrt{h^2 + k^2 + 2hk\cos\gamma}, \tag{6.2}$$

so that the ratio between the (11), with $h = 1$ and $k = 1$, and (10), with $h = 1$ and $k = 0$, reflections depends explicitly on the lattice angle according to:

$$r = \sqrt{2 + 2\cos\gamma} \quad \Rightarrow \quad \gamma = \arccos\left(\frac{r^2}{2} - 1\right). \tag{6.3}$$

This approach allows following the in-plane symmetry of the ordered domains during compression. For ideal square packing $\gamma = 90°$, while hexagonal packing corresponds to $\gamma = 60°$. Values between these limits indicate distorted or oblique lattices. As shown in Figure 6.11, γ progressively decreases from nearly $90°$ towards $\sim 75°$, con-

firming the transition from square-like to oblique/distorted-hexagonal configurations.

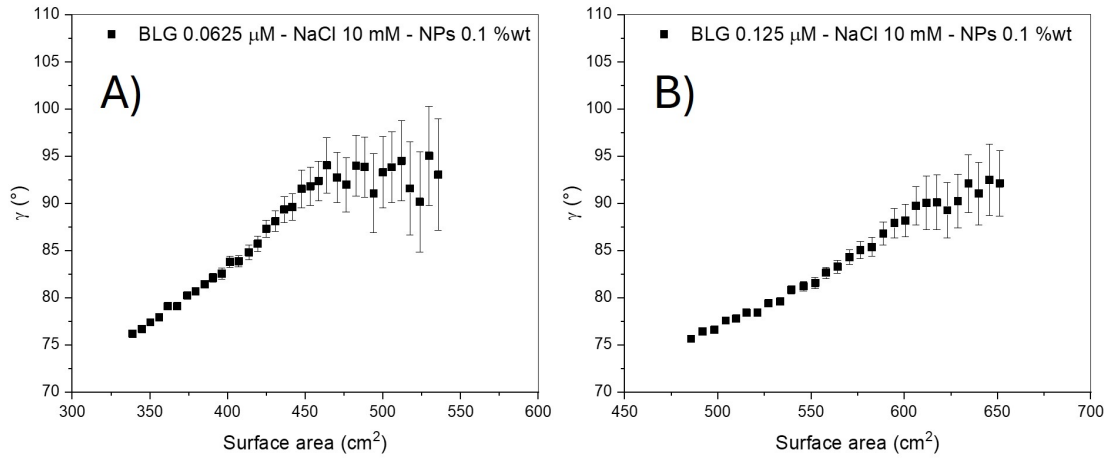

Figure 6.11: *Evolution of the lattice angle γ as a function of the macroscopic surface area during monolayer trough compression. The data reveal a structural transition of the ordered nanoparticle domains: from square-like ($\gamma \approx 90°$) to oblique/distorted-hexagonal geometries ($\gamma > 75°$). The coexistence with a liquid-like correlation peak indicates that both disordered and ordered phases contribute to the scattering signal of q_{c1}.*

Interestingly, the correlated domains observed upon compression do not directly evolve towards a hexagonal packing, but instead first display nearly square symmetry ($\gamma \approx 90°$). This intriguing behavior, never observed for BSA and BCN, can be rationalized by considering that BLG adsorption introduces heterogeneities and directional constraints at the air–water interface, which hinder the formation of isotropic hexagonal order and transiently stabilize square-like configurations. Similar square-to-hexagonal transitions have been reported in 2D colloidal systems under confinement or anisotropic interactions (Rey et al., 2018; Schmidt et al., 1997; Glotzer et al., 2007; Aoyama et al., 2025; Harland et al., 1997). With further compression, these square-like domains distort progressively towards oblique and eventually hexagonal geometries, consistent with a constrained 2D packing scenario in which proteins mediate the structural transition of the NP monolayer. Noteworthy, at the 1:1 bulk ratio with high NP content (*i.e.*, BLG 1 μM - NPs 0.8%$_{wt}$), the interfacial behavior differs markedly: the monolayer does not display the square-to-oblique sequence seen at lower NP coverages. A plausible explanation is that, under these conditions, the interface becomes NP-dominated. As a result, protein-induced heterogeneities, responsible for driving the formation of the square lattice at lower NP loadings, are largely suppressed. The effective NP-NP interactions are more isotropic at high surface coverage, and adsorption provides sufficient time for rapid formation of close-packed domains. Consequently, the film evolves directly towards near-hexagonal packing without stabilizing metastable square-like arrangements.

6.2 Conclusion

Compression experiments, combined with *in situ* GISAXS and neutron reflectometry, revealed that the dynamic response of protein–NP hybrid films is governed by the intrinsic molecular nature of the protein and its mode of interaction with silica nanoparticles.

For BSA–NP systems, compression isotherms and scattering data highlighted a strongly composition-dependent behavior. At low protein content, the film compressibility was dictated by nanoparticle packing, whereas at high protein content, the protein layer dominated the initial response, leading to a plateau regime associated with structural or compositional transitions. Neutron reflectivity confirmed a redistribution of protein between air- and water-facing shells, consistent with the desorption of a soft corona and the persistence of a tightly bound hard corona stabilizing the NP monolayer.

In BCN–NP systems, the compression response was more homogeneous and predictable, with interparticle distances decreasing linearly until collapse. The strong amphiphilic character and higher interfacial activity of β-casein promoted efficient NP assembly with reduced crowding and disorder compared to BSA. The resulting hybrid films displayed the hallmarks of irreversible NP adsorption, with compression behavior closely resembling that of surfactant–NP monolayers.

By contrast, BLG–NP systems exhibited the weakest ability to promote NP assembly at the interface. In fact, only under specific stoichiometric conditions, specifically at a low BLG:NP bulk ratio, NP monolayers form. However, BLG was the only protein showing complex and unusual features such as transient square-to-oblique ordering under compression.

This comparative analysis demonstrates that the balance between protein conformational flexibility, amphiphilicity, and interfacial affinity dictates both the structural evolution and the mechanical robustness of hybrid films. By integrating these findings with the steady-state results of Chapter 5, we conclude that protein molecular properties can be leveraged as design parameters to engineer functional, sustainable interfacial materials with tailored dynamic responses to mechanical stress.

7
General conclusions

The present doctoral work provides a comprehensive investigation of the mechanisms governing the adsorption, structure, and stability of silica nanoparticle monolayers at liquid surfaces. By combining advanced scattering and spectroscopic techniques with systematic variations in additives and bulk composition, this research has clarified fundamental aspects of interfacial self-assembly and offered new perspectives for the rational design of functional and sustainable nanomaterials.

The first part of this thesis was devoted to silica nanoparticles assembled at the water–air interface in the presence of ionic additives, with CTAB as a model cationic surfactant. In Chapter 2 a time-resolved GISAXS protocol was established to investigate the adsorption of silica nanoparticles at the air–water interface in the presence of CTAB. By correlating surface pressure with the time evolution of the scattering Bragg peaks, it was possible to follow in real time both the build-up of interfacial order and the associated adsorption kinetics. This methodology not only captured the rapid formation of hexagonally packed domains after a short induction time, but also provided non-equilibrium thermodynamic parameters such as the steady-state interfacial excess. Two distinct processes were identified: first, CTAB desorption, which governs the induction time and is strongly affected by surfactant concentration and ionic strength; second, the characteristic times of nanoparticle adsorption and ordering, which determine the evolution and final structure of the monolayer. Together, these results deliver a direct and quantitative picture of the dynamic pathway of nanoparticle assembly at fluid interfaces. In Chapter 3, the focus was placed on the role of electrolyte composition, with particular attention to valence-dependent specific ion effects. Using GISAXS in combination with compression isotherms, it was shown that both ionic strength and cation valence strongly influence the adsorption and structural organization of CTAB-decorated nanoparticle monolayers. Increasing ionic strength or switching from monovalent to multivalent cations enhanced the steady-state surface excess and promoted denser packing. However, this came at the expense of long-range lateral order: higher-order Bragg peaks weakened or disappeared at high ionic strength or in the presence of $LaCl_3$, revealing a loss of long-range order when electrostatic

repulsion is strongly screened. From the compression data, the effective interaction potential was resolved into two components: a long-range repulsive branch, exponentially decaying and highly sensitive to electrolyte composition, and a short-range steric contribution associated with the CTAB corona, essentially insensitive to the nature of the salt. Chapter 4 addressed the dynamic response of the same systems under non-equilibrium conditions, focusing on their ability to recover their structure after large, non-elastic deformation. By employing compression/expansion protocols and in situ GISAXS, it was shown that re-adsorption of nanoparticles requires a reservoir in the bulk and is strongly favored by higher ionic strength and multivalent cations. Two relaxation/recovery mechanisms were identified, namely homogeneous re-spreading of nanoparticles and cluster-mediated rearrangement. The relative weight of these pathways depended on the cation and ionic strength: KCl at low ionic strength shows only the re-spreading process, $CaCl_2$ promoted mixed behavior, whereas KCl at high ionic strength and $LaCl_3$ proceeded through the cluster-mediated process, yielding the highest recovery, though complete reformation of the original structure was never achieved. The occurrence of cluster-mediated recovery indicates that, beyond purely repulsive interactions, attractive forces emerge between colloids, favoring their re-aggregation upon re-adsorption. These findings highlight how electrolyte identity and concentration not only program the steady-state structure of nanoparticle monolayers, but also dictate their resilience and capacity for reconfiguration after non-elastic deformation.

The second part of this thesis, developed in Chapter 5 and Chapter 6, explored the role of proteins as additives in nanoparticle interfacial assembly, taking bovine serum albumin (BSA), β-casein (BCN), and β-lactoglobulin (BLG) as representatives of different structural classes. For BSA, static GISAXS, NR, and SFG measurements revealed that proteins profoundly reshape the interfacial architecture. Specifically, the data pointed to a two-layer organization, with a hard corona tightly bound to the nanoparticles and a softer, more labile shell, whose asymmetry at the air– and water–sides was reflected in the spectroscopic signatures. Dynamic compression experiments confirmed that the BSA:NP ratio dictates the mechanical response, where at low protein content the film behaves like a nanoparticle-dominated monolayer, while at high content the initial resistance is set by the protein network before giving way to nanoparticle packing and collapse. BCN, owing to its amphiphilic and flexible character, produced more homogeneous interfacial layers. Static measurements showed efficient adsorption and reduced crowding compared to BSA, while compression experiments displayed smooth and surfactant-like isotherms, consistent with a uniform structural organization and enhanced stability under stress. BLG, in contrast, exhibited the weakest interfacial activity. Its static assemblies formed only at specific stoichiometries and exhibited unusual features under compression with a square-to-distorted hexagonal transition. Taken together, Chapter 5 and 6 demonstrate that proteins not only stabilize nanoparticle monolayers but also determine their structural and mechanical regimes in a protein-specific manner, with outcomes directly linked to the molecular properties of each protein.

Beyond specific results, this thesis contributed novel methodological approaches. The development of a time-resolved GISAXS protocol allowed kinetic and thermodynamic analysis of non-equilibrium monolayers, while the combined use of X-ray, neutron, and nonlinear optical spectroscopies enabled complementary insights spanning from nanoscale ordering to molecular-level conformational changes. These techniques, when applied in synergy, constitute a powerful toolkit for future investigations of dynamic interfacial phenomena.

The outcomes of this research are relevant beyond fundamental colloid and interface science. Understanding how surfactants, salts, and biomolecules direct nanoparticle assembly has implications for the rational design of nanostructured coatings, responsive membranes, and smart materials with adaptive functionalities. Furthermore, the demonstration of protein-assisted stabilization opens the way to greener formulations in fields ranging from food science to biomedical engineering, where sustainability and biocompatibility are increasingly critical.

Despite the progress achieved, several questions remain open and provide clear directions for future work. A first challenge concerns the detailed understanding of specific ion effects beyond the valence-dependent framework discussed here. Comparative studies involving ions with the same charge but different hydration and polarizability, such as Na^+, K^+, and Li^+ or Ca^{2+} and Mg^{2+}, would help to isolate chemical specificity from purely electrostatic screening. Similarly, the influence of anions and mixed electrolytes on nanoparticle adsorption remains largely unexplored and could reveal new pathways for tuning interfacial organization. A particularly promising direction would be to probe the structure and asymmetry of the electrical double layer surrounding nanoparticles at liquid interfaces, and to investigate how it both influences and is influenced by the inherent interfacial asymmetry. Advanced scattering and spectroscopic techniques, possibly combined with electrokinetic measurements, could provide new insights into how charge distribution and interfacial curvature jointly control adsorption, stability, and particle-particle interactions. On the methodological side, future developments could focus on coupling in situ GISAXS with Brewster angle microscopy to directly visualize domain heterogeneity, and on performing AFM or cryo-TEM on transferred monolayers to correlate local topography with averaged scattering signatures. Improved time resolution or oscillatory compression protocols could further clarify the interplay between interfacial rheology and structural rearrangements. The introduction of stimuli-responsive surfactants and additives, such as photo-, pH-, or redox-active molecules, represents another powerful avenue for exploration. These systems could enable the design of smart interfaces whose structure, dynamics, and mechanical properties can be externally modulated in real time. In this context, the approaches developed in this work could be extended to quantify how external triggers reshape interfacial energetics and nanoparticle organization, providing a mechanistic framework for the creation of adaptive, stimuli-responsive materials. Extending this approach to multicomponent and biomimetic systems also appears particularly promising. Mixtures of nanoparticles, surfactants, and proteins could serve as model

systems to probe cooperative or competitive adsorption and to investigate how protein unfolding, denaturation, or flexibility modulate nanoparticle assembly. Beyond the air-water interface, translating these principles to oil-water interface would enable the rational design of coatings, emulsifiers, and catalytic films based on controlled non-equilibrium assembly. In this perspective, application-oriented experiments could explore the formulation of foams and emulsions with tailored interfacial properties, exploiting responsive surfactants or proteins with specific catalytic or redox functionalities to develop systems capable of environmental remediation through pollutant degradation, selective capture or sequestration, and the removal of contaminants from water or oil interfaces. Such hybrid interfacial materials could be applied to water purification, oil-spill cleanup, or the recovery of heavy metals and organic pollutants from complex fluids. Finally, a broader theoretical and modeling effort could help link the kinetic data obtained here with mesoscopic simulations or free-energy landscapes, providing predictive tools for guiding experiments and designing functional interfacial materials.

Overall, this thesis demonstrates that the assembly of nanoparticles at liquid interfaces is governed by a subtle interplay between molecular additives, ionic environment, and out-of-equilibrium dynamics. By elucidating these mechanisms and introducing new experimental methodologies, the work advances the fundamental understanding of interfacial phenomena and points toward innovative strategies for engineering sustainable, functional, and reconfigurable nanomaterials. In essence, this work demonstrates that controlling the interplay between interfacial energetics and kinetics provides a unifying framework for understanding and designing nanoparticle-laden interfaces. By quantifying how ionic composition, surfactant adsorption, and protein structure cooperatively shape both the dynamics and stability of these systems, the thesis bridges molecular-scale interactions with macroscopic behavior. The methodological advances introduced here, particularly the integration of time-resolved scattering with complementary spectroscopic techniques, extend the experimental toolbox available for studying dynamic colloidal interfaces. Altogether, these contributions establish a foundation for future investigations into non-equilibrium self-assembly and for the rational design of adaptive and sustainable interfacial materials.

This page intentionally left blank.

Appendices

This page intentionally left blank.

A

Supporting Information: Chapter 2

A.1 Materials and Methods

Negatively charged monodisperse Ludox TMA silica nanoparticles, having a diameter of 24.6 $\pm$3.9 nm as determined by transmission electron microscopy, [23] were purchased from Sigma Aldrich, Milan (Italy) and purified in a dialysis tube (Spectra/Por® 4 Dialysis Membrane with a molecular weight cutoff of 12–14 kDa), also purchased from Sigma Aldrich, Milan (Italy). The dialysis tube filled with LUDOX nanoparticles was dialyzed against ultrapure water (Milli-Q, 18.2 MΩ□ cm) in a 1 L beaker under constant agitation for 48 h, changing the water every 12 h. Before every use, nanoparticle dispersion was sonicated for 30 min in an ultrasonic bath to improve homogenization. NaCl (purity > 99 %), dodecyltrimethylammonium bromide (DTAB) (purity ~99 %) and Cetyltrimethylammonium bromide (CTAB) (purity $\geq$ 99 %) were purchased from Sigma Aldrich, Milan (Italy) and used without further purification. All aqueous solutions and dispersions were prepared with ultrapure water (Milli-Q, 18.2 MΩ · cm).

Silica dispersions were prepared by mixing the desired volumes of the NaCl stock solution and NP dispersion, and then ultrapure water was added to reach the desired concentration. Nanoparticle/surfactant dispersions were obtained by mixing chosen volumes of surfactant and NaCl stock solutions and silica dispersions followed by dilution with ultrapure water to reach the desired concentration. In all the dispersions investigated, the NP concentration was kept at 0.1 %wt, while NaCl concentration varied from 0.1 mM to 10 mM and CTAB concentration varied between 10^{-6} M and 10^{-5} M.

Concentrated surfactant solutions, having a concentration between 1 mM and 10 mM, were prepared by dissolving a weighted amount of surfactant in the appropriate volume of ultrapure water. The concentrations were chosen in order to reach a final surfactant concentration of 1x10^{-6} M, 4x10^{-6} M, and 1x10^{-5} M upon spreading 375

µL of the concentrated solution in the Langmuir trough containing 375 mL of silica dispersion at the speed of 2 mL/min. This allowed us to *i*) use the same spread volume for all samples and *ii*) minimize the volume variation upon CTAB spreading.

A.1.1 Grazing Incidence Small Angle X-ray Scattering (GISAXS)

GISAXS measurements were performed at the ID 10 beamline of the European Synchrotron (ESRF) in Grenoble (France). We employed a 22 keV beam with an incident grazing angle of 0.04°. A Pilatus 300 k 2D detector was placed at 4202 mm from the sample to record the GISAXS pattern. The Digital Object Identifier of the GISAXS data employed in this chapter is `https://doi.org/10.15151/ESRF-ES-1126485822`.

The analyzed dispersions were poured in a Langmuir trough mounted in the beamline allowing us to record the GISAXS data and the surface pressure simultaneously.A total of 375 µL of the concentrated surfactant solution was spread onto the silica dispersions using a remotely controlled syringe. The syringe was placed perpendicularly to the Langmuir trough containing 375 mL of surfactant-free dispersion at a distance of a few millimeters from the dispersion surface. After aligning the air/water interface height with respect to the X-ray beam, the syringe was commanded to dispose 375 µL of the concentrated surfactant solution (A video illustration of the CTAB spreading on the NPs/NaCl solution can be found in Tomasella et al., 2025). This low volume allowed us to avoid any height misalignment and to perform GISAXS immediately after the spreading. The pattern evolution was followed for 1 h by performing 1 s counts every 5 s. Under these conditions, the beam did not damage the sample (see Figure 2.3).

The quantitative analysis of the evolution of the GISAXS patterns with time was performed after cutting and integrating the 2D GISAXS patterns along q_z between 0.014 $Å^{-1}$ and 0.023 $Å^{-1}$, obtaining a 1D pattern where the integrated intensity of the scattered beam was plotted against the scattering vector along the xy direction (q_{xy}). A detailed description of the GISAXS technique can be found in Appendix G. The temporal evolution of the GISAXS patterns is shown in video form in Tomasella et al., 2025.

The 1D curves show up to three distinct peaks at positive and negative values of $q_x y$. These peaks were then fitted independently with the following equation:

$$y = (y_0 + \frac{B}{q}) + \frac{2A}{\pi}\frac{w}{(q-q_c)^2+w^2} + \frac{2A_1}{\pi}\frac{w_1}{(q-\sqrt{3}q_c)^2+w_1^2} + \frac{2A_2}{\pi}\frac{w_2}{(q-2q_c)^2+w_2^2} \quad \text{(A.1)}$$

where the first term accounts for the background consisting of a q-independent term y_0 and a q-dependent term B. The second term accounts for the main Bragg peak centered at q_c and having an amplitude A and a full width at half maximum w. The last two terms account for the eventual higher order peaks centered respectively at $\sqrt{3}q_c$ and $2q_c$ and characterized respectively by an amplitude A_1 and A_2 and by a full width at half maximum w_1 and w_2. An example of curve fitting is reported in the Section A.2, Figure 2.3.

A.1.2 Dynamic Surface Tension (DTS)

Dynamic surface tension (DST) measurements upon surfactant spreading were performed with a KSV Minitrough, Helsinki (Finland), equipped with a paper Wilhelmy plate for the measurement of the surface pressure (Π), that is the difference between the surface tension of the pure air/water interface ($\gamma_0 = 72.8$ mN/m at 20 $\circ$C) and the time-dependent solution/dispersion surface tension (γ), as follows

$$\Pi(t) = \gamma_0 - \gamma(t) \tag{A.2}$$

A.1.3 DLS and ζ-potential

Particle size and electrophoretic mobility measurements were performed using a Zetasizer Nano ZS (Malvern Instruments, UK) equipped with a He–Ne laser. Dynamic Light Scattering (DLS) analyses were conducted in 1 mL disposable polystyrene cuvettes (DTS0012) under optimized acquisition times and laser attenuation settings. Each sample was measured in triplicate to ensure reproducibility. Prior to analysis, Ludox TMA silica NP suspensions were filtered through 0.22 μm syringe filters. The electrophoretic mobility of the samples was determined in triplicate using a DTS1070 folded capillary zeta cell. Zeta-potential (ζ) was calculated from the electrophoretic mobility using the Smoluchowski equation: $\zeta = \eta u \epsilon$ where η is the viscosity of the medium, u is the electrophoretic mobility, and ϵ is the dielectric permittivity of water. A viscosity of 0.887 mPa·s and a refractive index of 1.33 were assumed for the aqueous medium. Zeta potential results are reported as the mean $\pm$ standard deviation.

A.2 Supplementary Materials

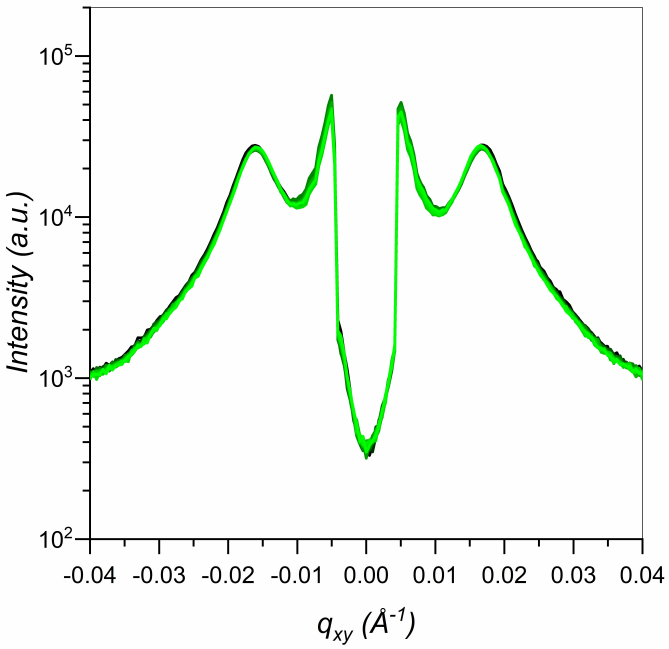

Figure A.1: *Radiation damage test executed with 100 consecutive GISAXS acquisition recorded with 1 sec X-ray irradiation every 5 seconds. These conditions ensured preventing any appreciable monolayer damage.*

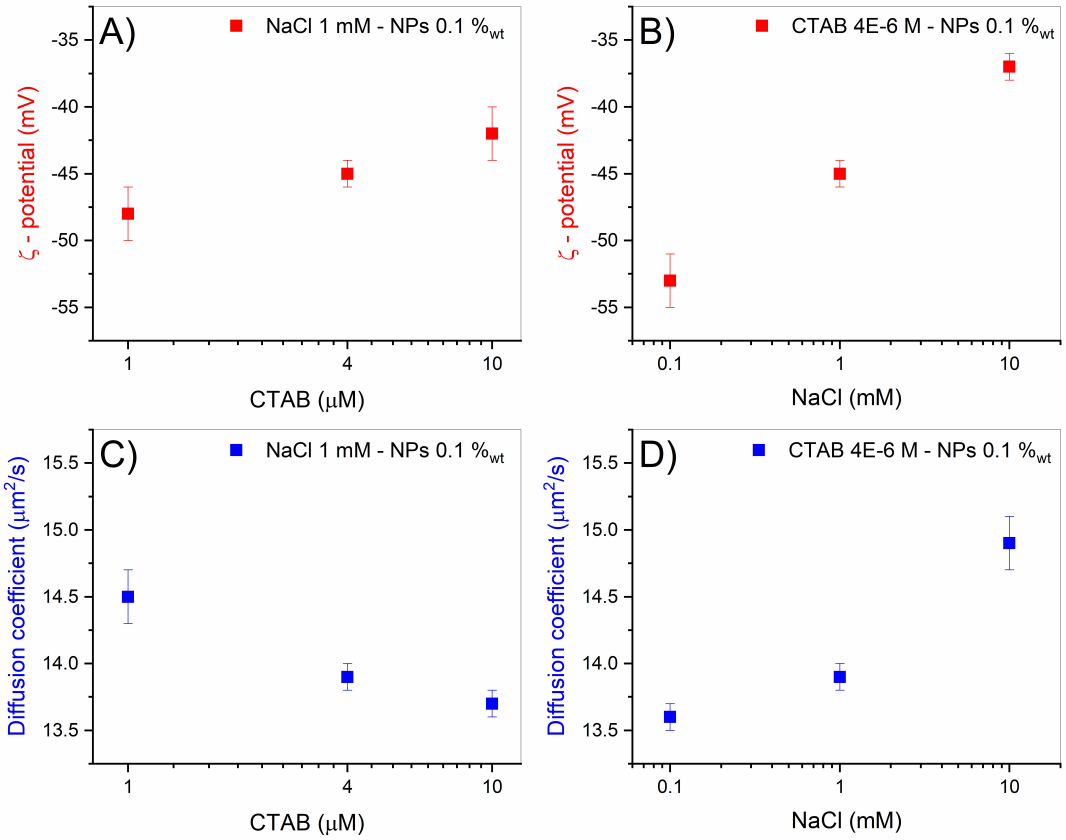

Figure A.2: *Zeta potential of CTAB-decorated silica NPs as a function of the CTAB concentration (A) and of the ionic strength (B). Diffusion coefficient of CTAB-decorated silica NPs as a function of the CTAB concentration (C) and of the ionic strength (D). In A and C all the samples have 1 mM ionic strength, in B and D all the samples have 4x10^{-6} M CTAB concentration.*

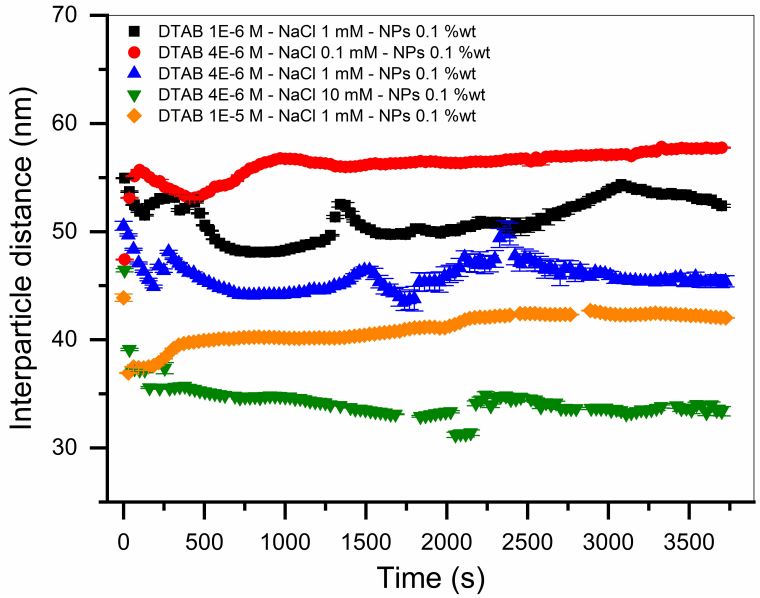

Figure A.3: *Interfacial inter-particle distance evolution recorded with GISAXS upon spreading of DTAB concentrated solutions. The irregular observed trend is ascribed to the inhomogeneous DTAB spreading (K. Lee et al., 2007).*

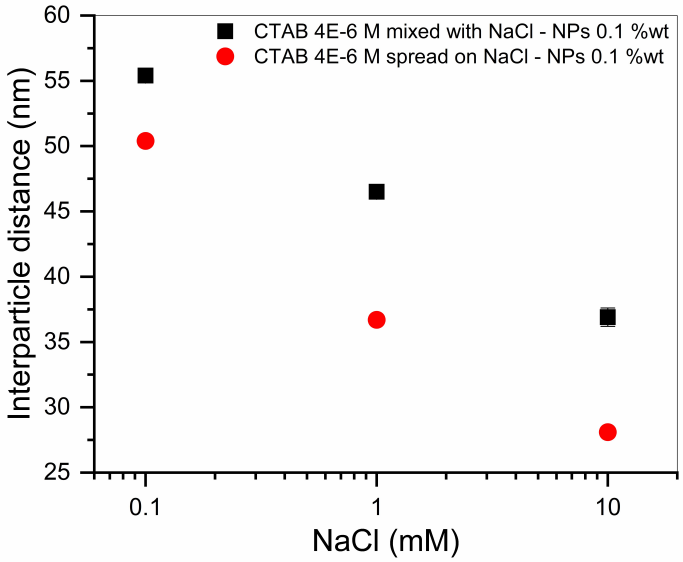

Figure A.4: *Interfacial inter-particle distance recorded with GISAXS after 1 hour equilibration for samples prepared by spreading CTAB on pre-aligned NP dispersions (red circles) and for samples prepared by bulk mixing CTAB and NP (red squares). All the samples have 4x10^{-6} M CTAB concentration.*

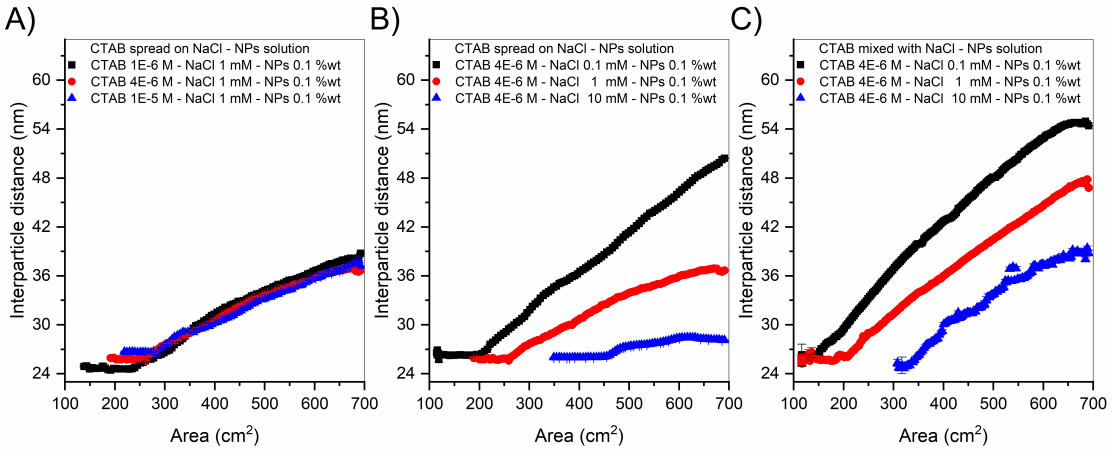

Figure A.5: *Interfacial inter-particle distance evolution with compression for samples prepared by spreading CTAB solutions of different concentrations on pre-aligned NP dispersions (A), by spreading CTAB solutions with the same concentrations on pre-aligned NP dispersions with different ionic strengths (B) and for samples prepared by bulk mixing CTAB and NP (C). In B and C all the samples have 4x10^{-6} M CTAB concentration while the ionic strength is varied between 0.1 and 10 mM. In C, the slope of the curves is the highest and, unlike in A and B, it is independent of composition. This indicates that the samples prepared by mixing (C) form homogeneous monolayers, in which nanoparticles gradually approach each other upon compression. Since the compression rate is constant, being solely determined by the trough size, the rate at which the NPs approach (reflected in the slope of the curves) is also constant and maximal in the case of homogeneous monolayers. Conversely, the lower and composition-dependent slopes observed in (A) and (B) suggest that the NP monolayers obtained by spreading are not homogeneous. Instead, they are likely composed of domains that progressively approach one another during compression. This behavior becomes especially pronounced at higher ionic strengths.*

B

Supporting Information: Chapter 3

B.1 Materials and Methods

Negatively charged monodisperse Ludox TMA silica nanoparticles NPs, having a diameter of 23.2 ± 4.9 nm as determined by Small Angle Neutron Scattering (SANS) (Figure 5.5), were purchased from Sigma Aldrich, Milan (Italy) and purified in a dialysis tube (Spectra/Por® 4 Dialysis Membrane with a molecular weight cutoff of 12–14 kDa), also purchased from Sigma Aldrich, Milan (Italy). The dialysis tube filled with LUDOX nanoparticles was dialyzed against ultrapure water in a 1 L beaker under constant agitation for 48 h, changing the water every 12 h. Before every use, nanoparticle dispersion was sonicated for 30 min in an ultrasonic bath to improve homogenization. Potassium chloride (KCl, purity $>$ 99.999 %, catalog n° 409316), calcium chloride tetrahydrate ($CaCl_2 \cdot 2H_2O$, purity $>$ 99.995 %, catalog n° 1023840100), lanthanum(III) chloride eptahydrate ($LaCl_3 \cdot 3H_2O$, purity $>$ 99.999 %, catalog n° 203521), and Cetyltrimethylammonium bromide (CTAB) (purity $\geq$ 99 %) were purchased from Sigma Aldrich, Milan (Italy) and used without further purifications. All aqueous solutions and dispersions were prepared with ultrapure water (Milli-Q, 18.2 M$\Omega \cdot$ cm).

Solutions containing CTAB, silica nanoparticles (NPs), and salts were prepared by mixing equal volumes of two stock solutions under stirring. One stock solution contained CTAB, while the other contained both NPs and the salt at the desired concentrations. To ensure that the final concentrations matched the target values after mixing, both stock solutions were prepared at twice the desired final concentration. For example, to prepare 500 mL of a solution containing 1 μM CTAB, 1 mM KCl, and 0.1 $\%_{wt}$ NPs, 250 mL of a 2 μM CTAB solution was mixed with 250 mL of a solution containing 2 mM KCl and 0.2 $\%_{wt}$ NPs.

The final solutions were formulated to have ionic strengths of 0.1 mM, 1 mM and 10 mM, 1 μM CTAB and 0.1 $\%_{wt}$ NPs for GISAXS and ζ-potential measurements, while

for the surface tension the CTAB concentration was investigated in the range 1 μM - 1 mM . Since the salts used were of different stoichiometry, KCl (1:1), $CaCl_2$ (1:2), and $LaCl_3$ (1:3), the relationship between the bulk concentration of the salt (C) and the ionic strength (I) is as follows:

$$I_{KCl} = C_{KCl}$$
$$I_{CaCl_2} = 3C_{CaCl_2}$$
$$I_{LaCl_3} = 6C_{LaCl_3}$$

Accordingly, to achieve the desired ionic strengths of 0.1 mM, 1 mM, and 10 mM, the corresponding salt concentrations in the final (bulk) solution were:

- C_{KCl} = 0.1 mM, 1 mM, 10 mM
- C_{CaCl_2} = 0.0333 mM , 0.333 mM, 3.33 mM
- C_{LaCl_3} = 0.0167 mM, 0.167 mM and 1.67 mM

B.1.1 Grazing Incidence Small Angle X-ray Scattering (GISAXS)

GISAXS measurements were performed at the SIRIUS beamline of the SOLEIL French National Synchrotron in Paris (France). We employed an 8 KeV beam (wavelength 1.55 Å) with an incident grazing angle of 0.12° corresponding to 80 % of the water critical angle for total external reflection. A Pilatus 3 model 1M 2D detector was placed at 4490 mm from the sample to record the GISAXS pattern.

The CTAB–NP–salt solution to be analyzed was poured into a custom-made Langmuir trough and allowed to stabilize for 30 minutes. After stabilization, the solution was compressed at a constant rate of approximately 22 cm^2/min, and the evolution of the surface pressure during compression ($\Pi = \gamma_0 - \gamma$, where γ_0 = 72.5 mN/m is the surface tension of the air-water interface at 25 °C and γ is the change in surface tension due to the NP monolayer) was recorded using a paper Wilhelmy plate. Simultaneously, GISAXS patterns were acquired with an exposure time of 1 s, followed by 5 s of no exposure between acquisitions. This exposure/dark configuration was chosen to prevent radiation damage to the sample, as shown in Figure B.1. The obtained GISAXS patterns were analyzed as extensively explained in Appendix G. The fitting function used to extrapolate quantitative information from the reduced 1D GISAXS pattern was the same as Equation A.1.

B.1.2 Surface tension measurements

The dispersion-air surface tension was measured by a Drop Shape tensiometer, PAT-1 by Sinterface, Germany. Details on this technique can be found elsewhere (Loglio et al., 2001). A pendant drop of 12 μL was formed at the end of a flat metal needle, thermostatted at 25 °C, and the drop shape was monitored and analyzed over time

using the Young-Laplace equation, until the steady-state condition was reached. Note that the PAT-1 is equipped with a feedback control system ensuring a constant drop volume during the measurement.

B.1.3 Electrophoretic mobility

Particle electrophoretic mobility measurements were performed using a Zetasizer Nano ZS (Malvern Instruments, UK) equipped with a He–Ne laser. Prior to analysis, CTAB-NP-salt suspensions were filtered through 0.22 μm syringe filters. The electrophoretic mobility of the samples was determined in triplicate using a DTS1070 folded capillary zeta cell. A viscosity of 0.887 mPa·s and a refractive index of 1.33 were assumed for the aqueous medium. Electrophoretic mobility results are reported as the mean ± standard deviation.

B.1.4 Compression isotherms

Compression isotherms were performed with a KSV Minitrough, Helsinki (Finland), equipped with a paper Wilhelmy plate for the measurement of the surface pressure (Π). After 30 minutes for equilibration, the obtained monolayers were compressed at the constant barrier speed of 15 mm/min, corresponding to a macroscopic surface area reduction of $\sim 22 cm^2/min$.

B.2 Supplementary Materials

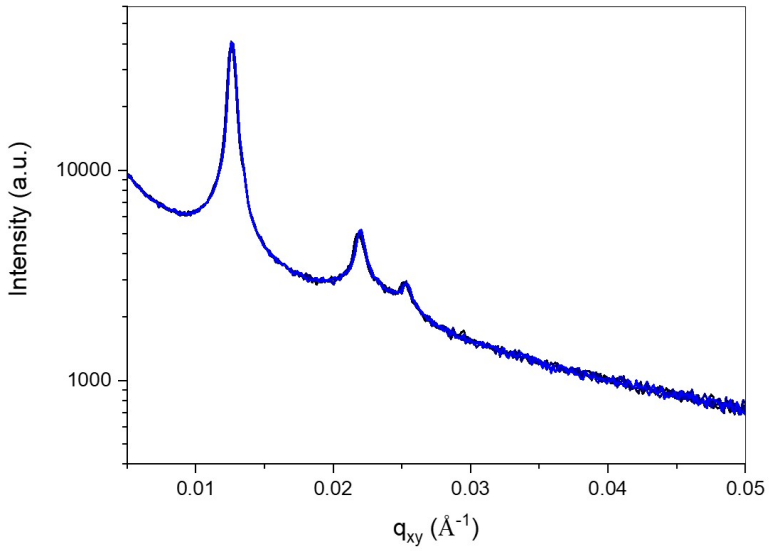

Figure B.1: *Radiation damage test executed with 20 consecutive GISAXS acquisition recorded with 1 sec X-ray irradiation every 5 seconds. These conditions ensured preventing any appreciable monolayer damage.*

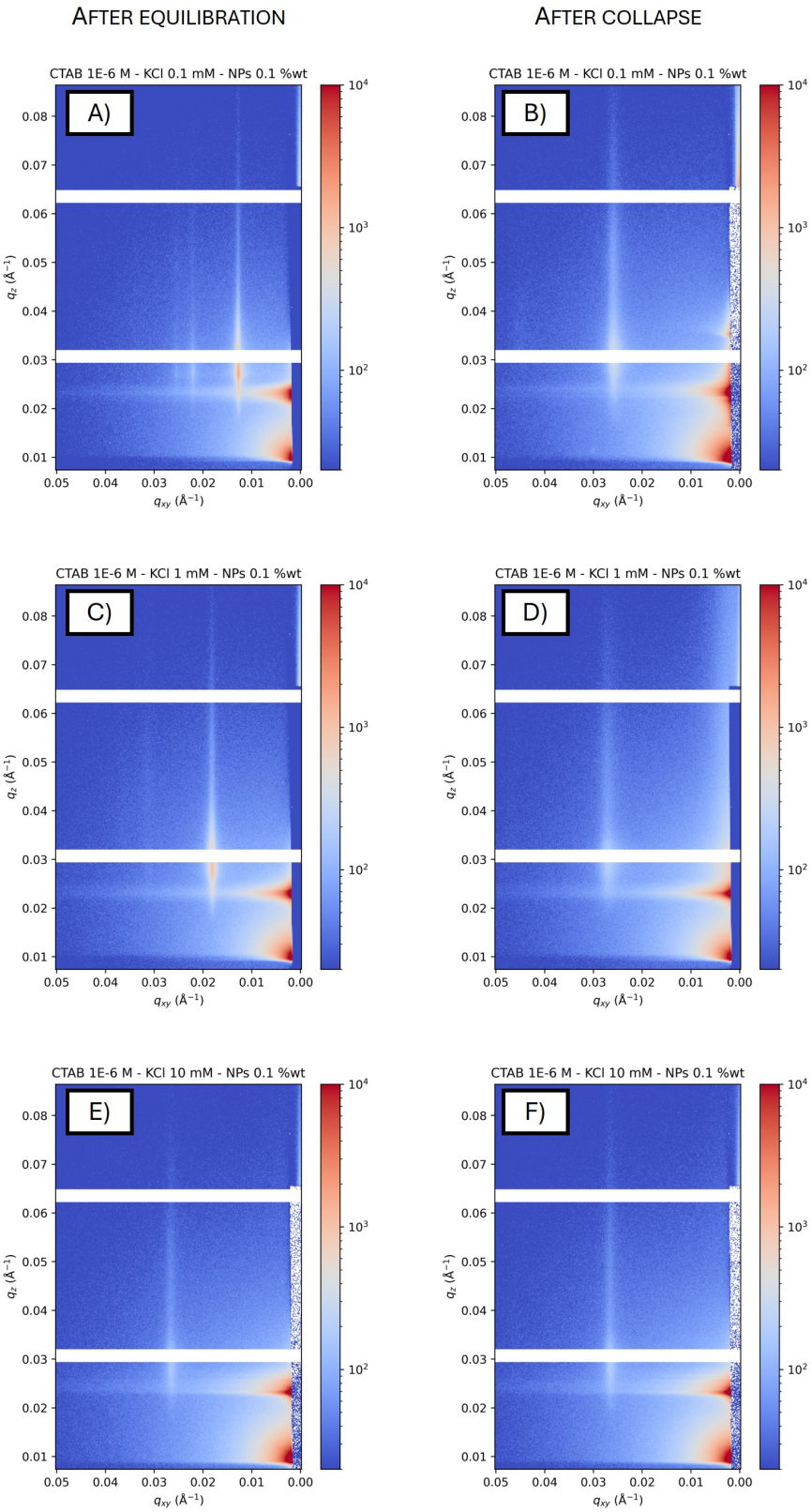

Figure B.2: *GISAXS patterns acquired after 30 minutes of equilibration (A, C, E) and after the monolayer collapse (B, D, F) for suspension of CTAB 1 μM, NPs 0.1 $\%_{wt}$ and KCl ionic strength of (A,B) 0.1 mM, (C,D) 1 mM and (E, F) 10 mM.*

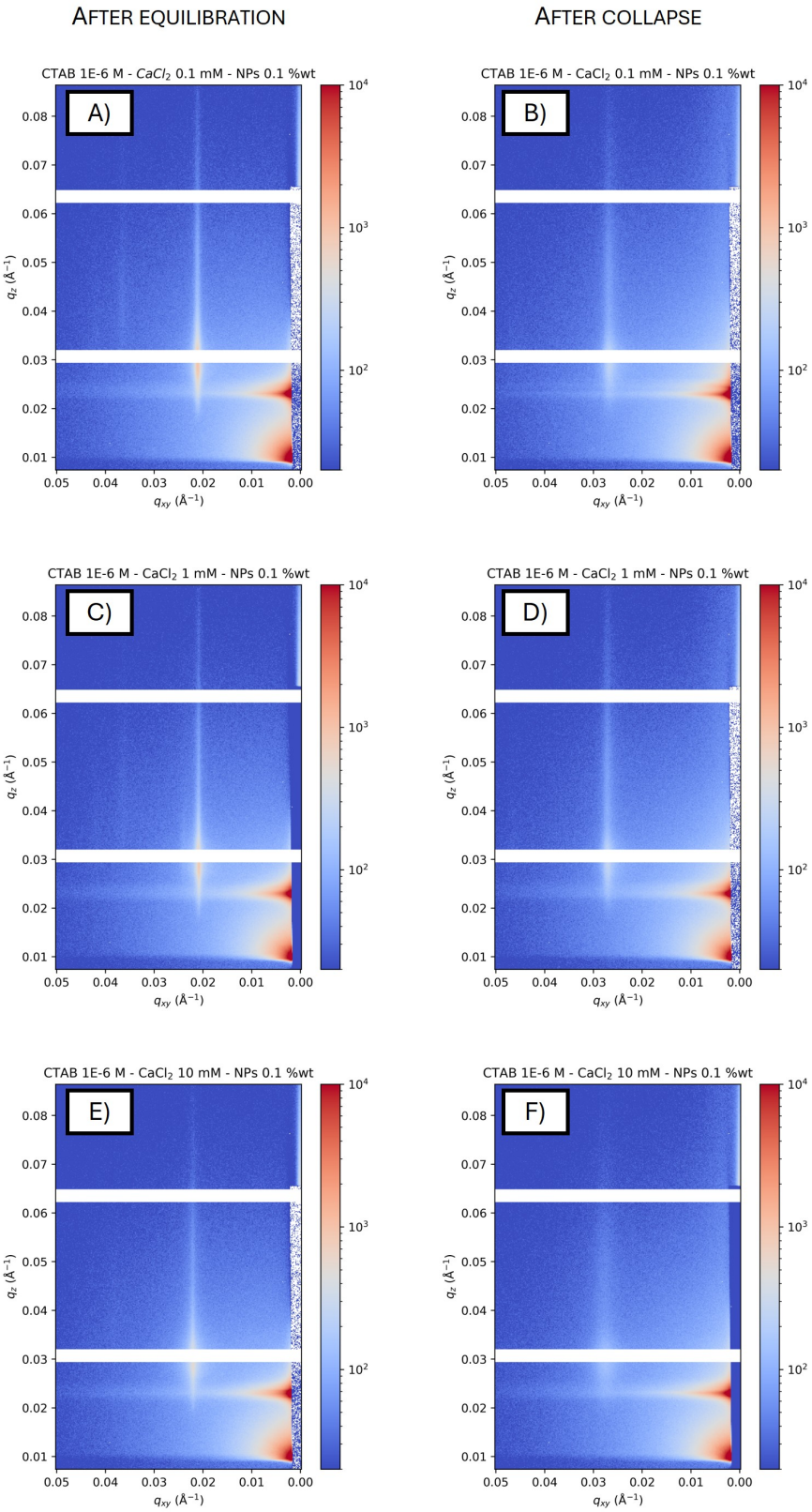

Figure B.3: *GISAXS patterns acquired after 30 minutes of equilibration (A, C, E) and after the monolayer collapse (B, D, F) for suspension of CTAB 1 µM, NPs 0.1 $\%_{wt}$ and $Cacl_2$ at the ionic strength of (A,B) 0.1 mM, (C,D) 1 mM and (E, F) 10 mM.*

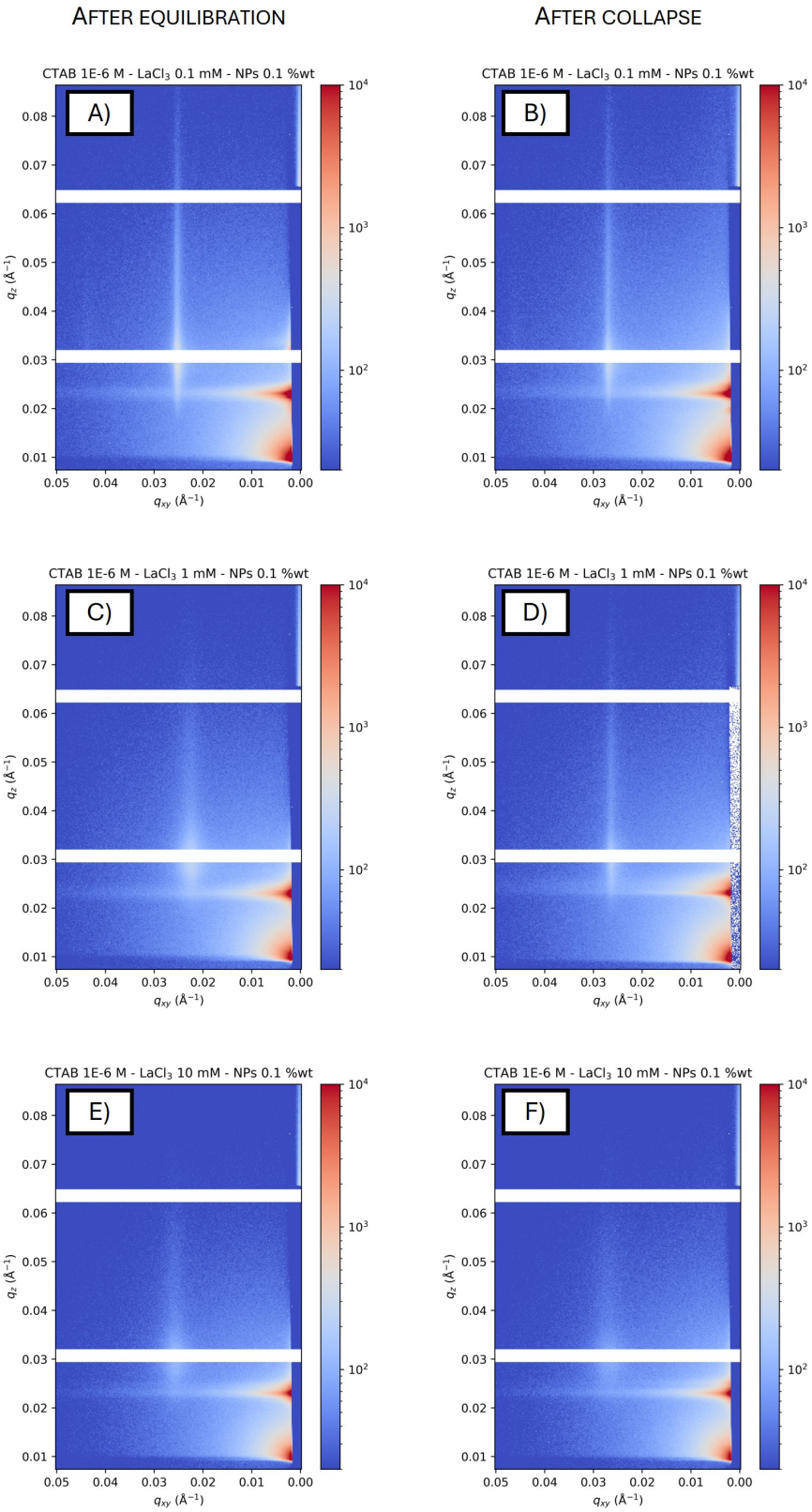

Figure B.4: *GISAXS patterns acquired after 30 minutes of equilibration (A, C, E) and after the monolayer collapse (B, D, F) for suspension of CTAB 1 μM, NPs 0.1 $\%_{wt}$ and $laCl_3$ at the ionic strength of (A,B) 0.1 mM, (C,D) 1 mM and (E, F) 10 mM.*

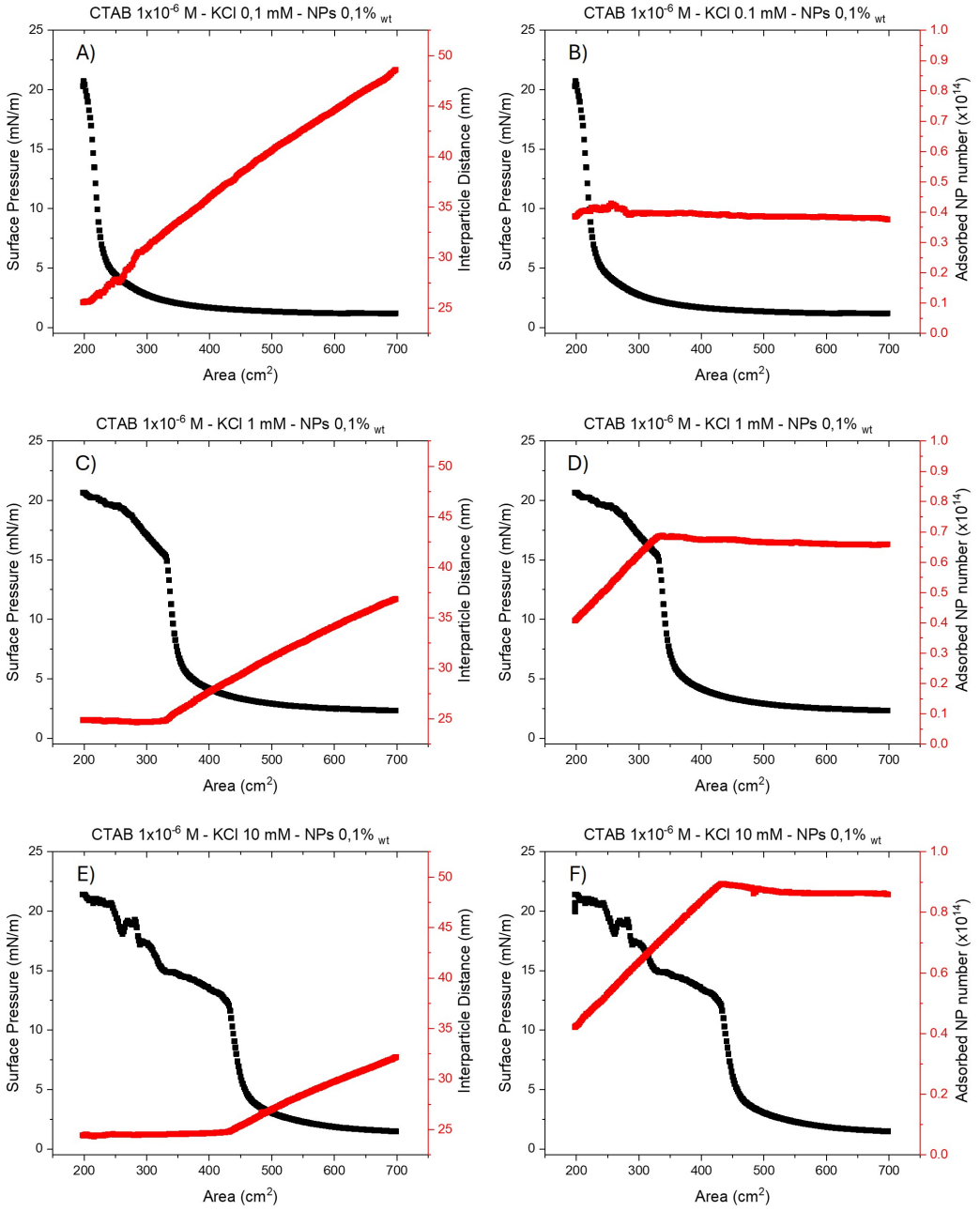

Figure B.5: *Monolayer interparticle distance (red squares in A, C, E) and adsorbed NP number (red squares B, D, F) evolution during compression together with the corresponding surface pressure variation (black line) for suspension of CTAB 1 µM, NPs 0.1 $\%_{wt}$ and KCl at the ionic strength of (A,B) 0.1 mM, (C,D) 1 mM and (E, F) 10 mM.*

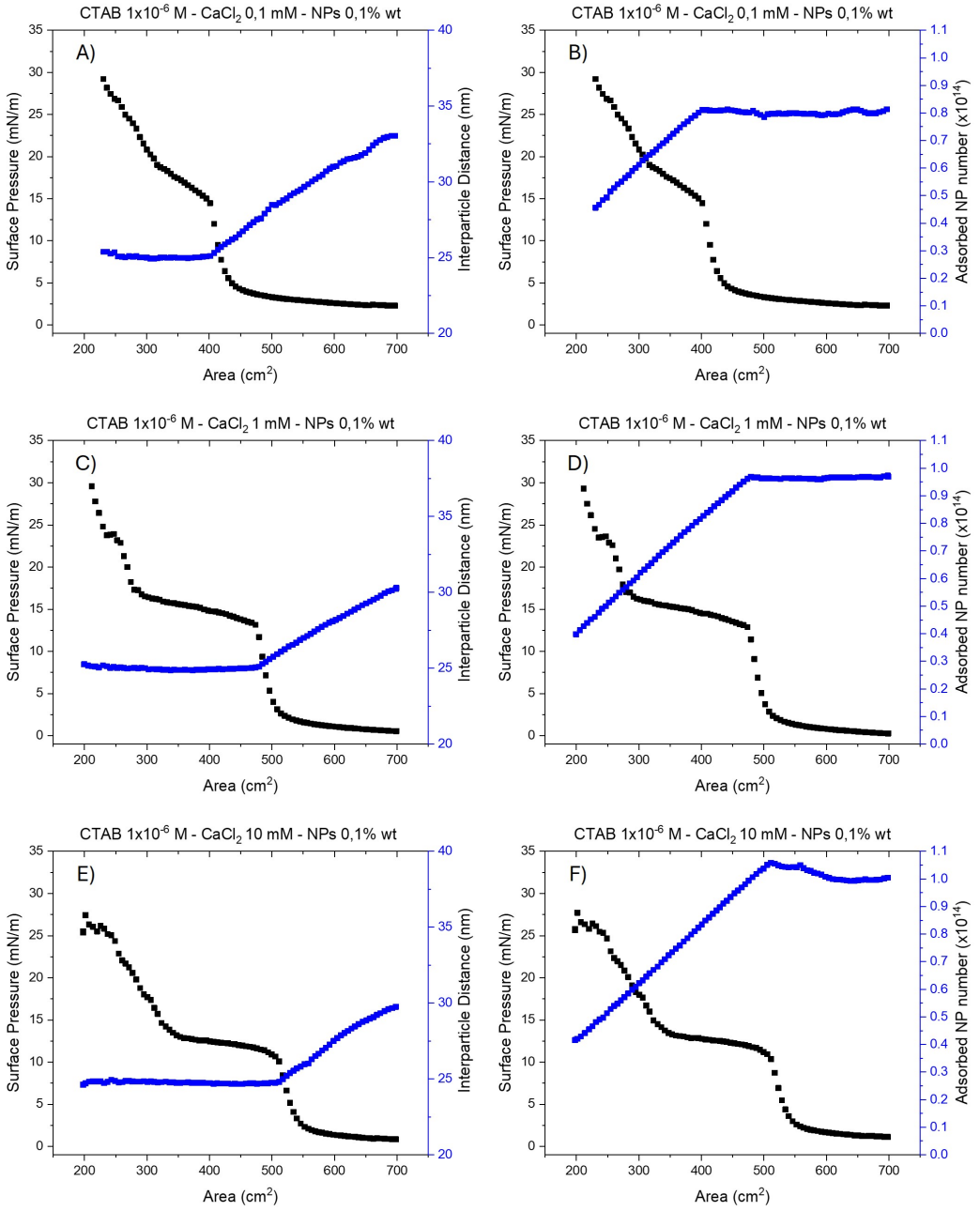

Figure B.6: *Monolayer interparticle distance (blue squares in A, C, E) and adsorbed NP number (blue squares B, D, F) evolution during compression together with the corresponding surface pressure variation (black line) for suspension of CTAB 1 μM, NPs 0.1 $\%_{wt}$ and $CaCl_2$ at the ionic strength of (A,B) 0.1 mM, (C,D) 1 mM and (E, F) 10 mM.*

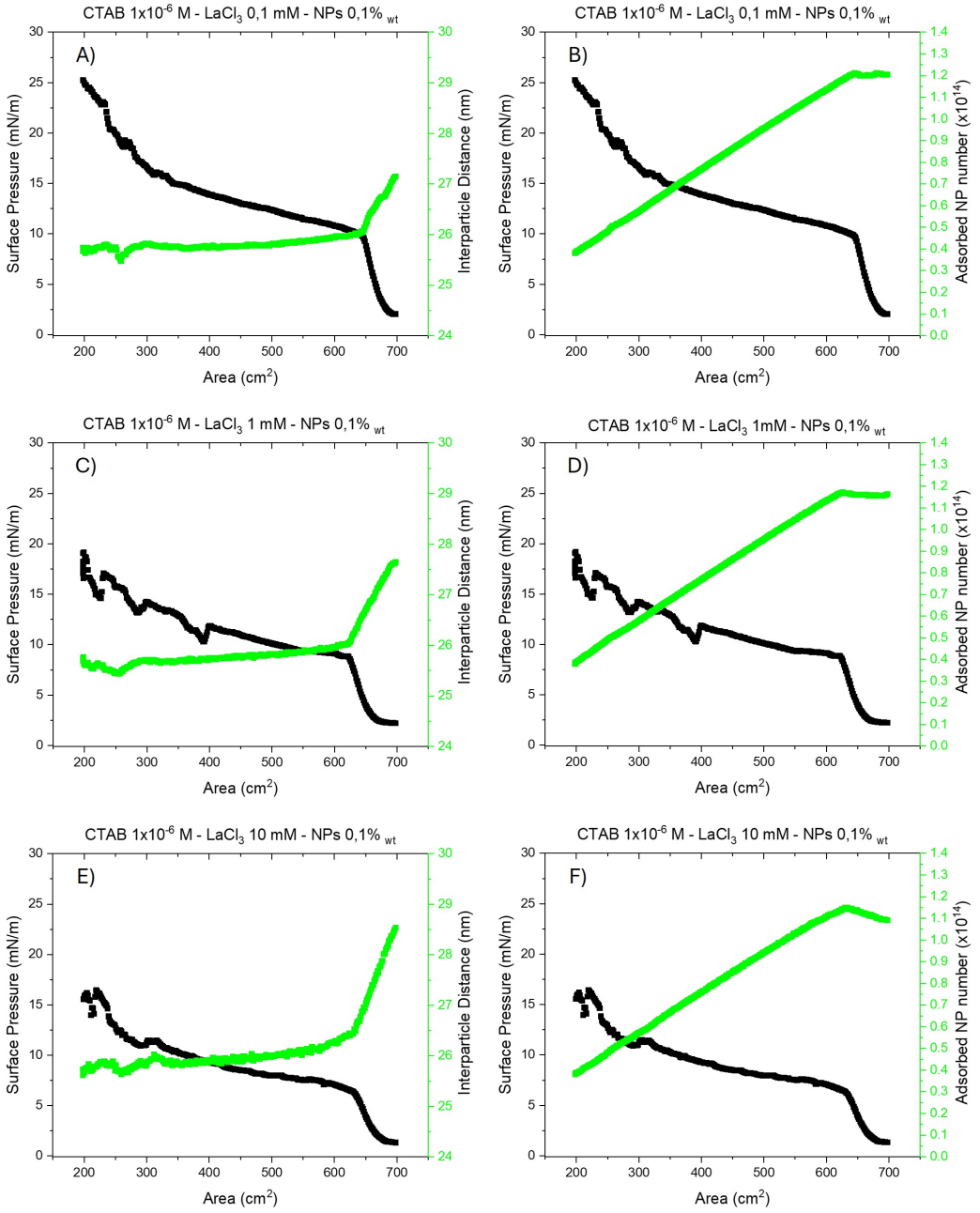

Figure B.7: *Monolayer interparticle distance (green squares in A, C, E) and adsorbed NP number (green squares B, D, F) evolution during compression together with the corresponding surface pressure variation (black line) for suspension of CTAB 1 μM, NPs 0.1 $\%_{wt}$ and $LaCl_3$ at the ionic strength of (A,B) 0.1 mM, (C,D) 1 mM and (E, F) 10 mM.*

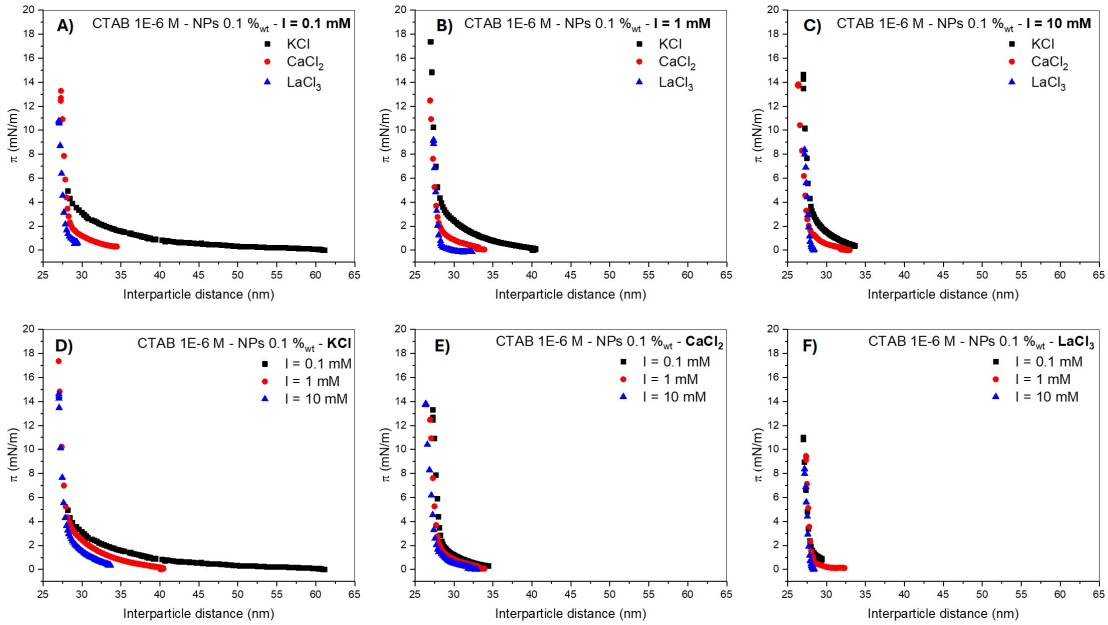

Figure B.8: *Monolayers surface pressure evolution with respect to the reduction in the interparticle distance during compression as a function of the bulk ionic strength (I) equal to A) 0.1 mM, B) 1 mM and C) 10 mM inKCl (black squares), $CaCl_2$ (red circles) and $LaCl_3$ (blue triangles) and as function of the salt used, namely KCl in D), $CaCl_2$ in E), and $LaCl_3$ in F) at the bulk ionic strength of 0.1 mM (black squares), 1 mM (red circles), and 10 mM (blue triangles). All the tested monolayers were obtained in the presence of CTAB 1 μM and NPs 0.1 $\%_{wt}$.*

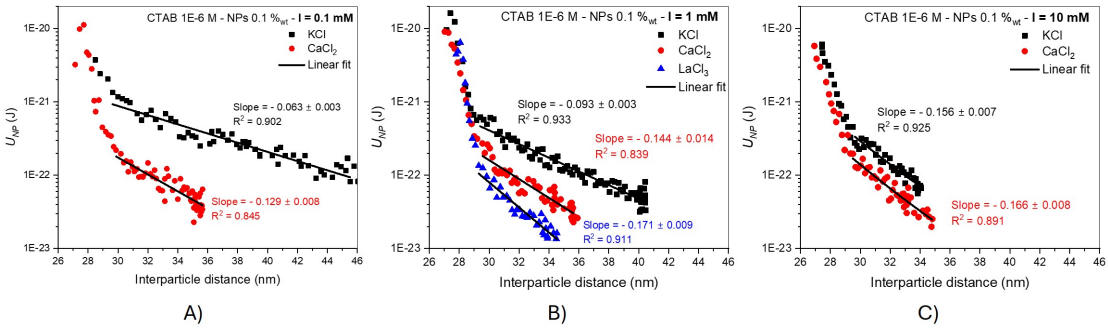

Figure B.9: *Linear fit of the potential vs interparticle distance curves in the long-range regime for bulk ionic strength of A) 0.1 mM, B) 1 mM, and C) 10 mM in KCl (black squares), $CaCl_2$ (red circles) and $LaCl_3$ (blue triangle). The bulk concentration was 1×10^6 M in CTAB and $0.1\%_{wt}$ in NPs.*

C

Supporting Information: Chapter 4

C.1 Materials and Methods

Information on the materials used and methods (GISAXS and compression isotherms) adopted in this chapter can be found in Section B.1. The description of the protocols used for the compression/expansion cycles is reported in Section 4.1.

C.2 Supplementary Materials

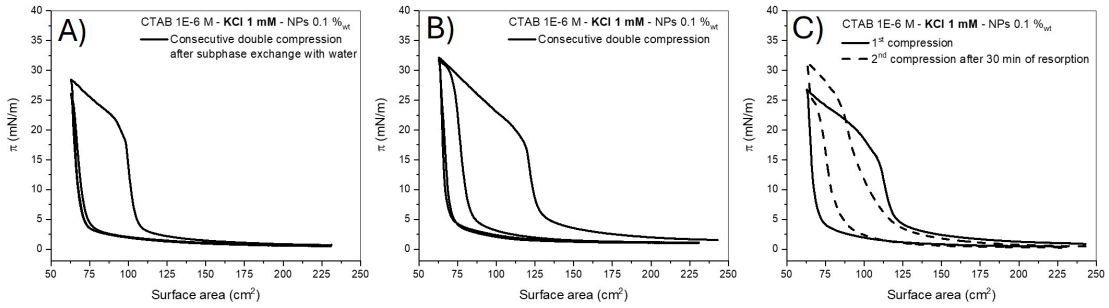

Figure C.1: *Compression/expansion isotherms for CTAB* $1 \times 10^{-6} M$ *- KCl 1 mM and NPs 0.1* $\%_{wt}$ *obtained with protocol A) subphase cleaning (SC), B) two consecutive compression (2CC), and C) Intermediate adsorption (IA).*

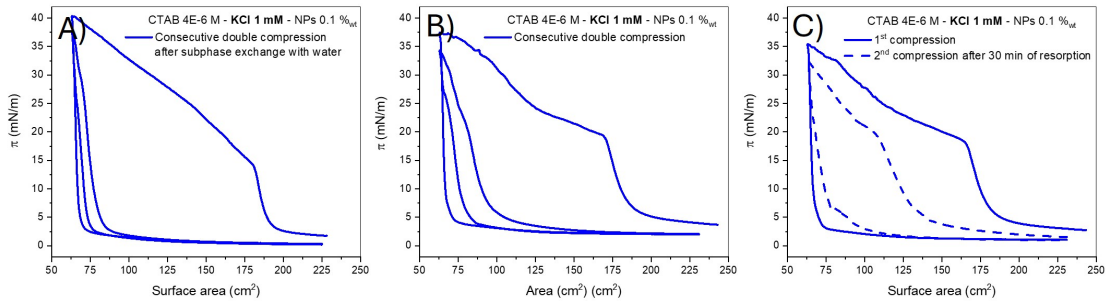

Figure C.2: *Compression/expansion isotherms for CTAB* $4 \times 10^{-6} M$ *- KCl 1 mM and NPs 0.1* $\%_{wt}$ *obtained with protocol A) subphase cleaning (SC), B) two consecutive compression (2CC), and C) Intermediate adsorption (IA).*

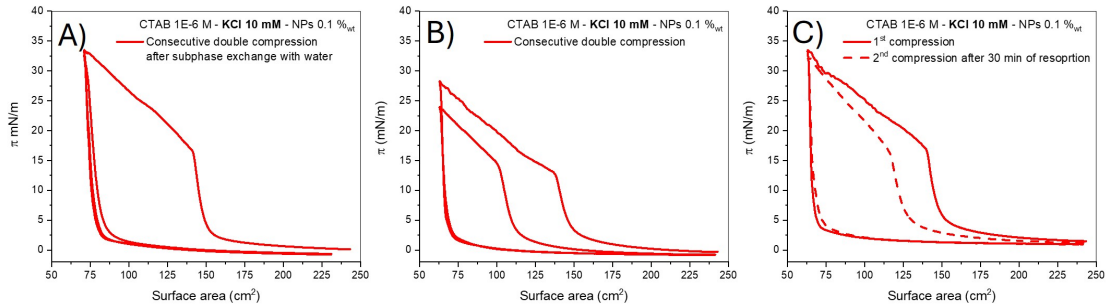

Figure C.3: *Compression/expansion isotherms for CTAB* $1 \times 10^{-6} M$ *- KCl 10 mM and NPs 0.1* $\%_{wt}$ *obtained with protocol A) subphase cleaning (SC), B) two consecutive compression (2CC), and C) Intermediate adsorption (IA).*

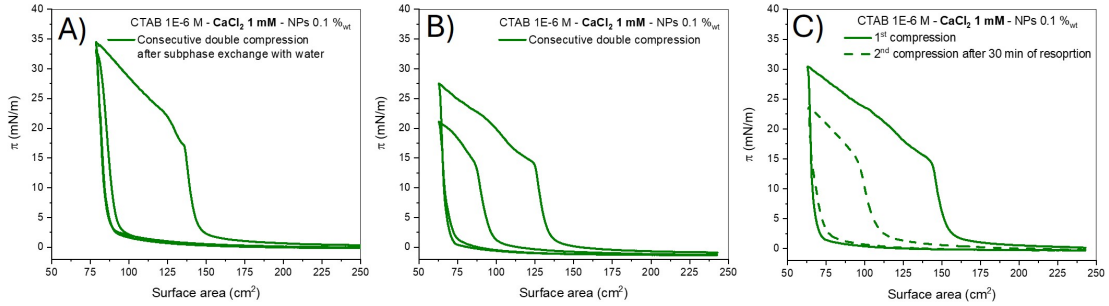

Figure C.4: *Compression/expansion isotherms for CTAB* $1 \times 10^{-6} M$ *- $CaCl_2$ 1 mM and NPs 0.1* $\%_{wt}$ *obtained with protocol A) subphase cleaning (SC), B) two consecutive compression (2CC), and C) Intermediate adsorption (IA).*

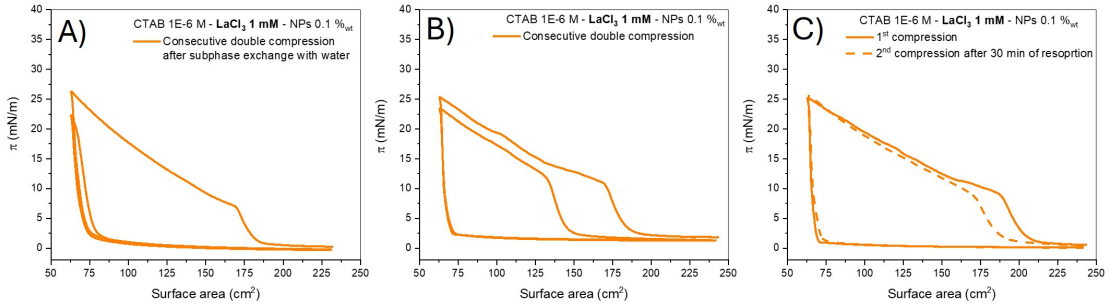

Figure C.5: *Compression/expansion isotherms for CTAB* $1 \times 10^{-6} M$ *- $LaCl_3$ 1 mM and NPs 0.1* $\%_{wt}$ *obtained with protocol A) subphase cleaning (SC), B) two consecutive compression (2CC), and C) Intermediate adsorption (IA).*

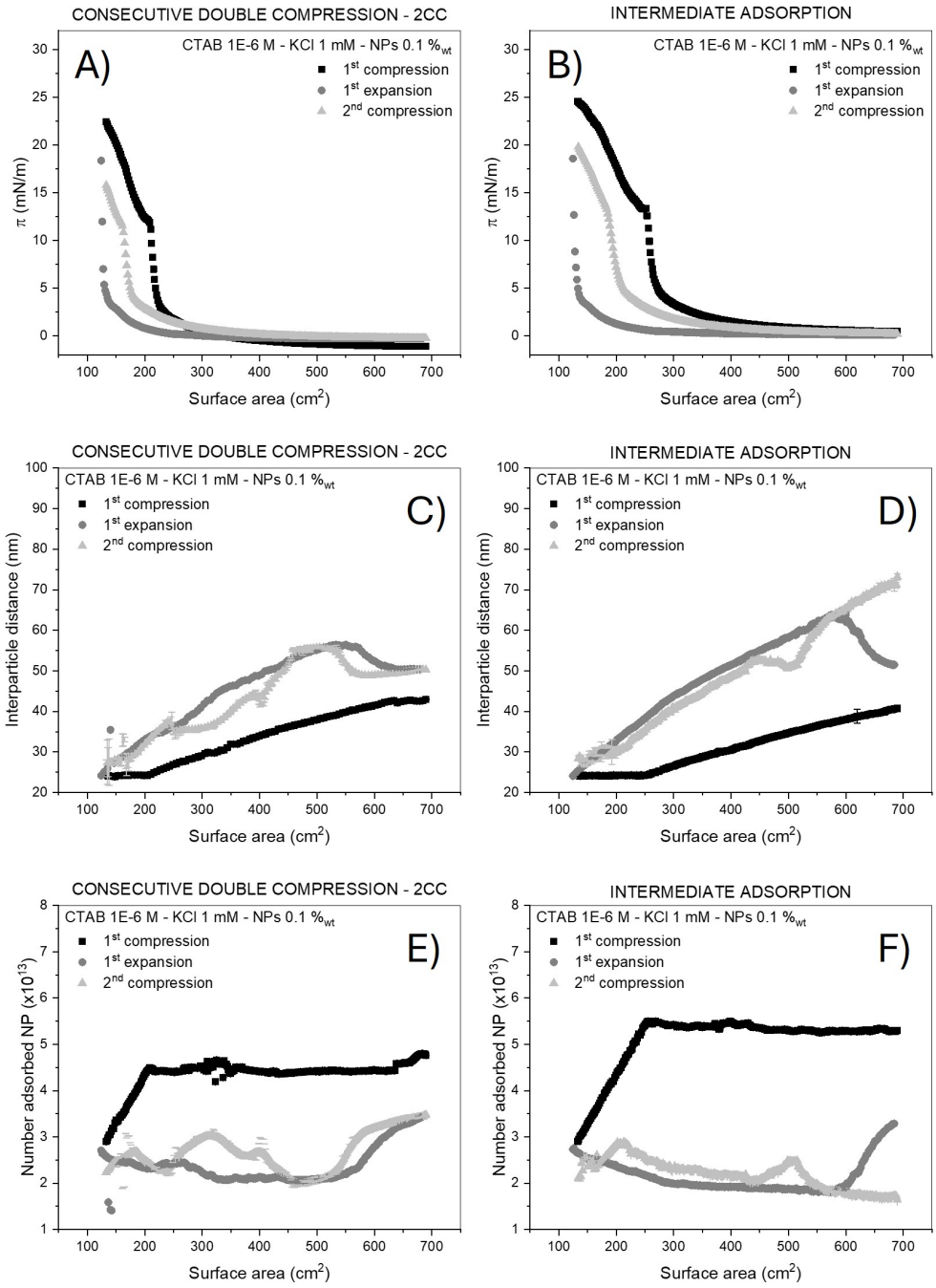

Figure C.6: *Surface pressure (A,B), interparticle distance (C,D) and adsorbed nanoparticle number (E,F) evolution during compression/expansion cycles obtained with (A,C,E) two consecutive compression - 2CC, and (B,D,F) intermediate adsorption - IA protocols. The bulk composition was CTAB* $1 \times 10^{-6} M$ *- KCl 1 mM and NPs 0.1* $\%_{wt}$.

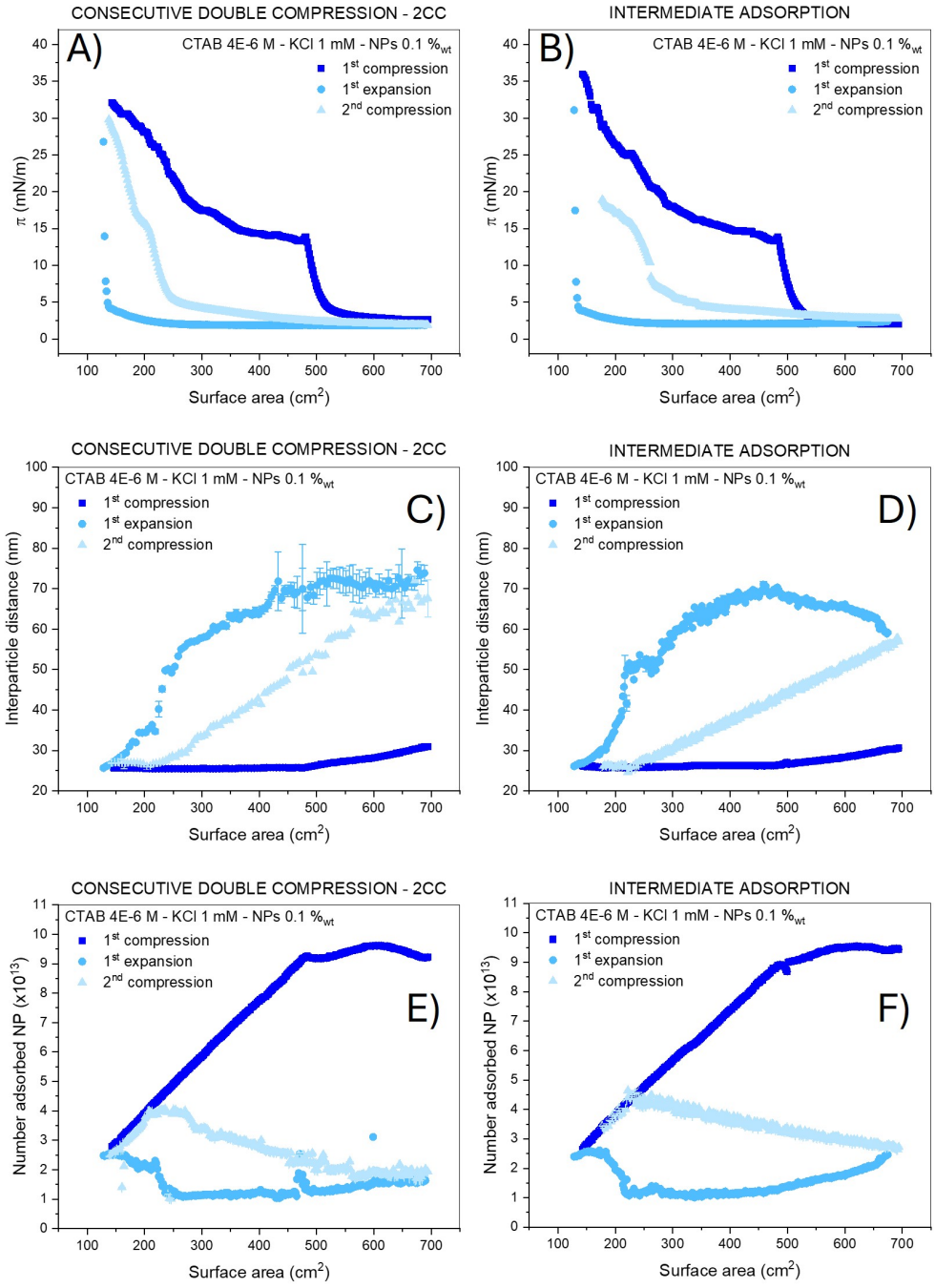

Figure C.7: *Surface pressure (A,B), interparticle distance (C,D) and adsorbed nanoparticle number (E,F) evolution during compression/expansion cycles obtained with (A,C,E) two consecutive compression - 2CC, and (B,D,F) intermediate adsorption - IA protocols. The bulk composition was CTAB* $4 \times 10^{-6} M$ *- KCl 1 mM and NPs 0.1* $\%_{wt}$.

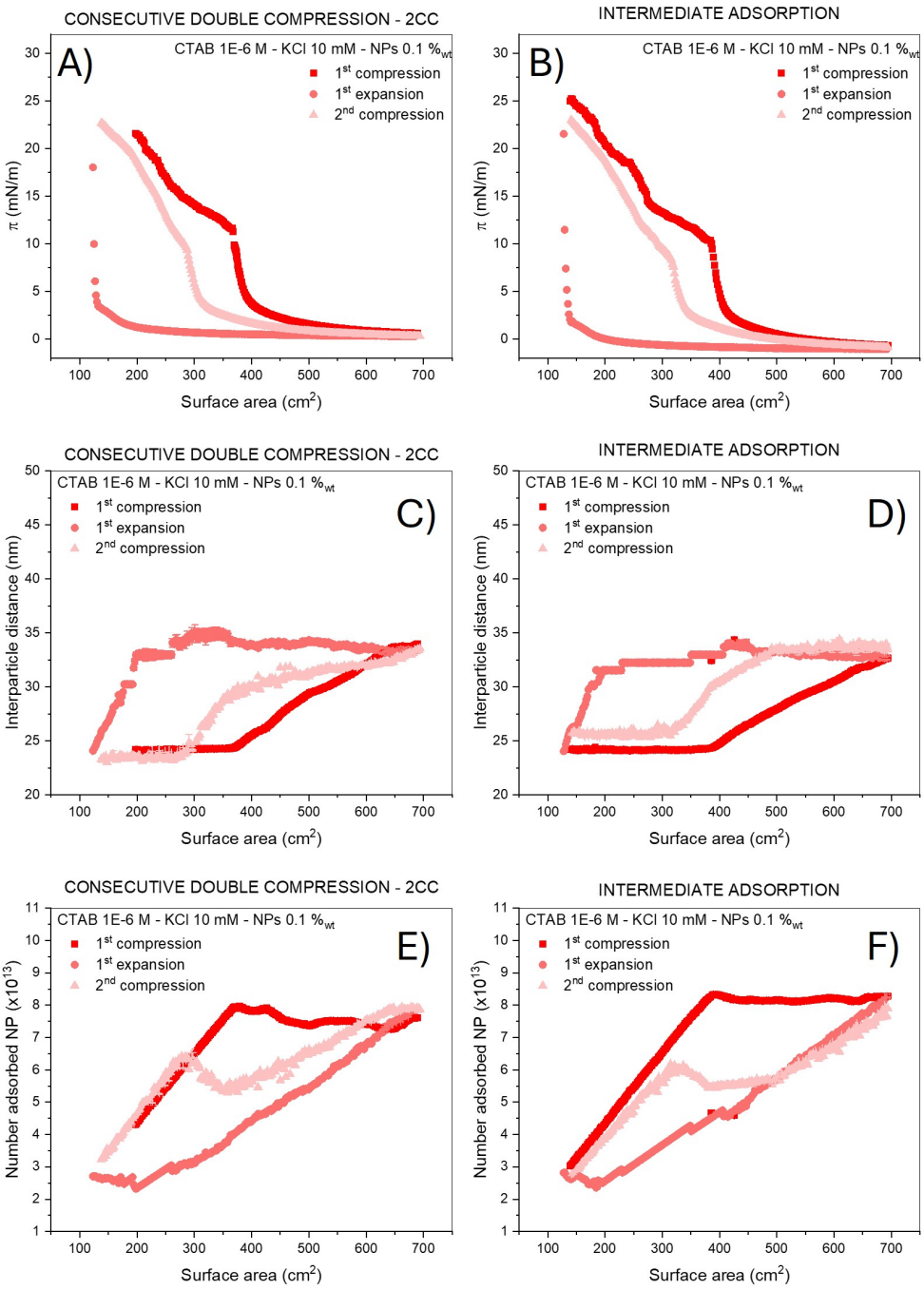

Figure C.8: *Surface pressure (A,B), interparticle distance (C,D) and adsorbed nanoparticle number (E,F) evolution during compression/expansion cycles obtained with (A,C,E) two consecutive compression - 2CC, and (B,D,F) intermediate adsorption - IA protocols. The bulk composition was CTAB* $1 \times 10^{-6} M$ *- KCl 10 mM and NPs 0.1* $\%_{wt}$.

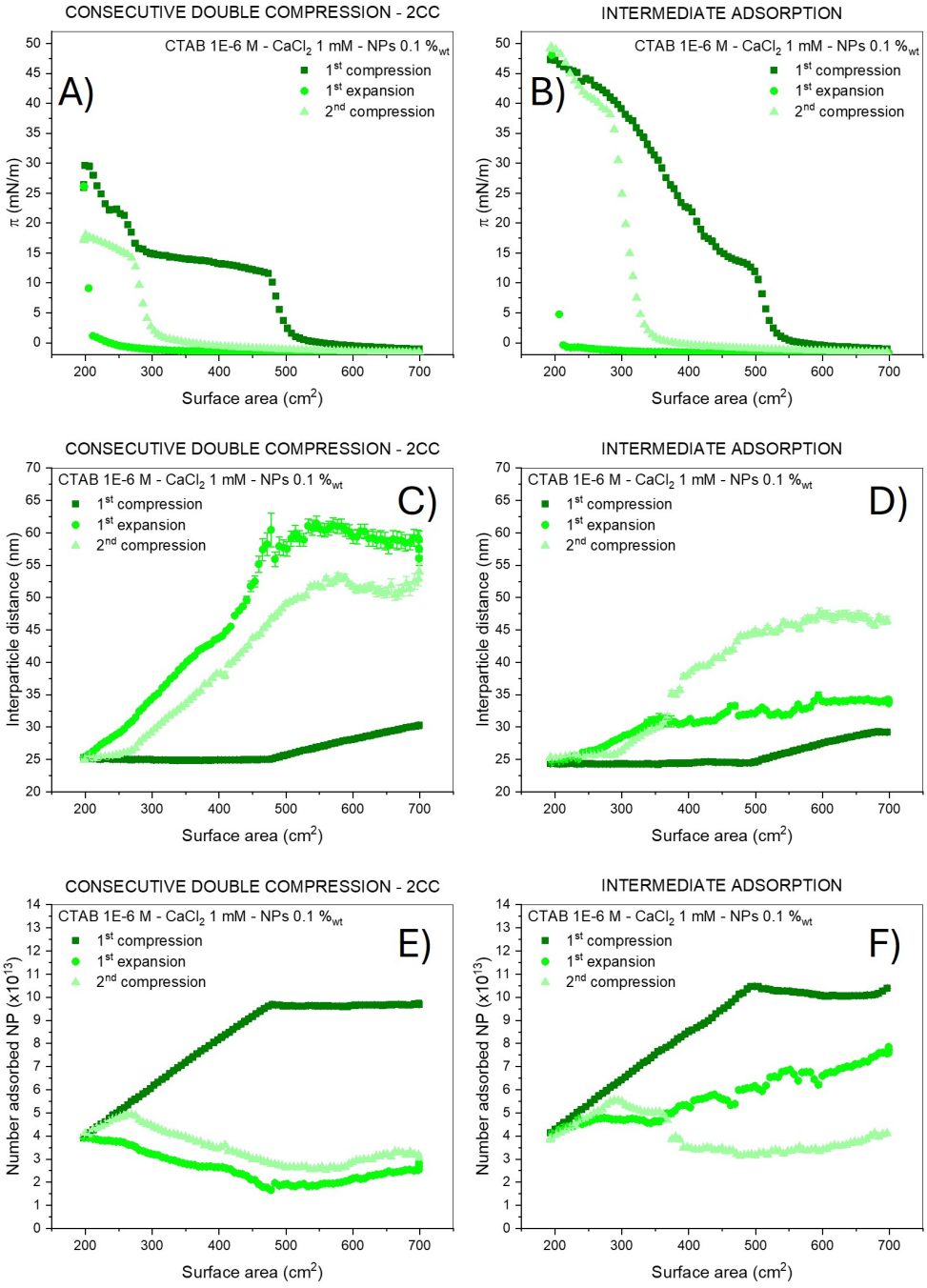

Figure C.9: *Surface pressure (A,B), interparticle distance (C,D) and adsorbed nanoparticle number (E,F) evolution during compression/expansion cycles obtained with (A,C,E) two consecutive compression - 2CC, and (B,D,F) intermediate adsorption - IA protocols. The bulk composition was CTAB* $1 \times 10^{-6} M$ *- CaCl*$_2$ *1 mM and NPs 0.1* $\%_{wt}$.

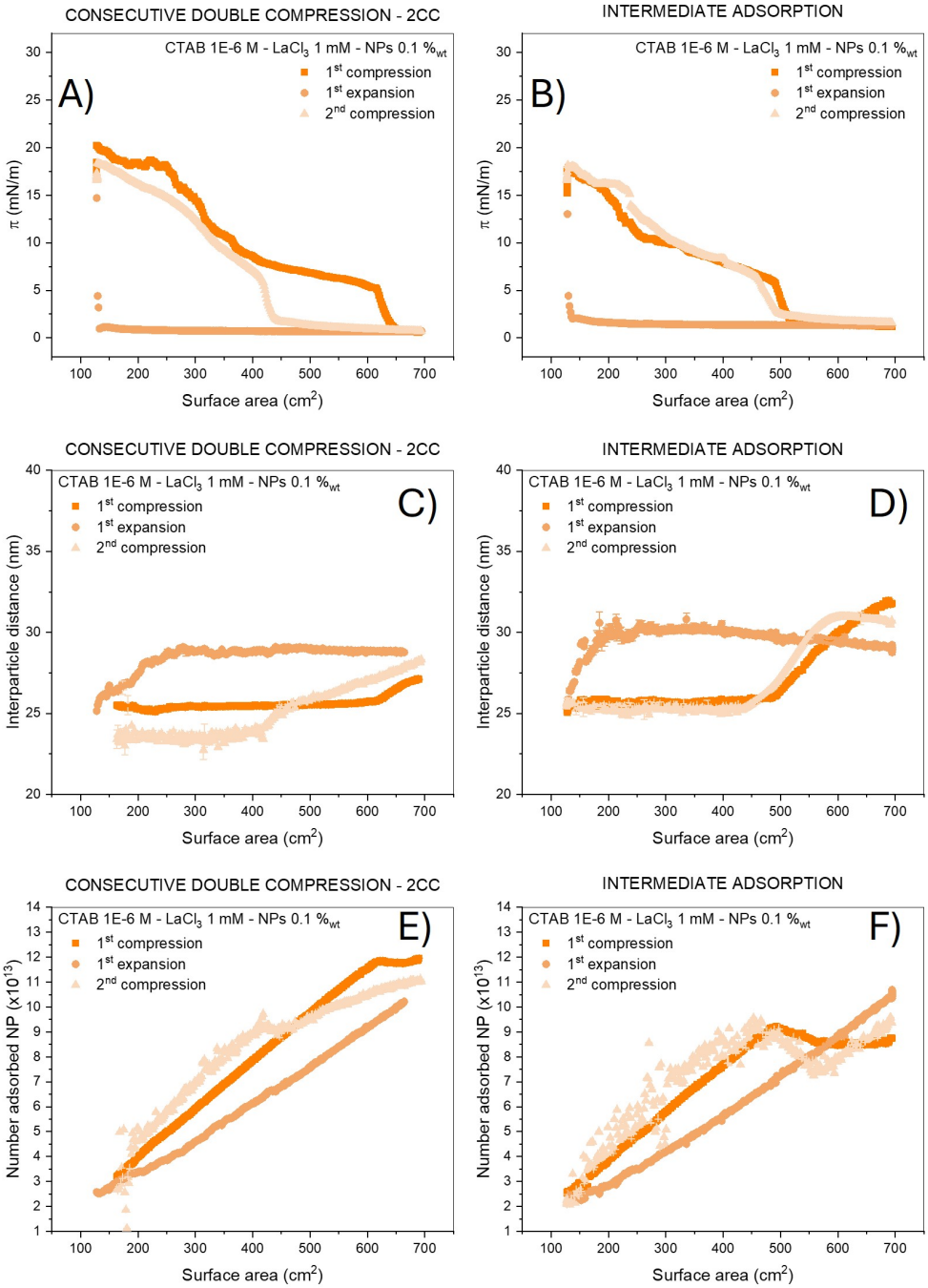

Figure C.10: *Surface pressure (A,B), interparticle distance (C,D) and adsorbed nanoparticle number (E,F) evolution during compression/expansion cycles obtained with (A,C,E) two consecutive compression - 2CC, and (B,D,F) intermediate adsorption - IA protocols. The bulk composition was CTAB* $1 \times 10^{-6} M$ *- LaCl*$_3$ *1 mM and NPs 0.1* $\%_{wt}$.

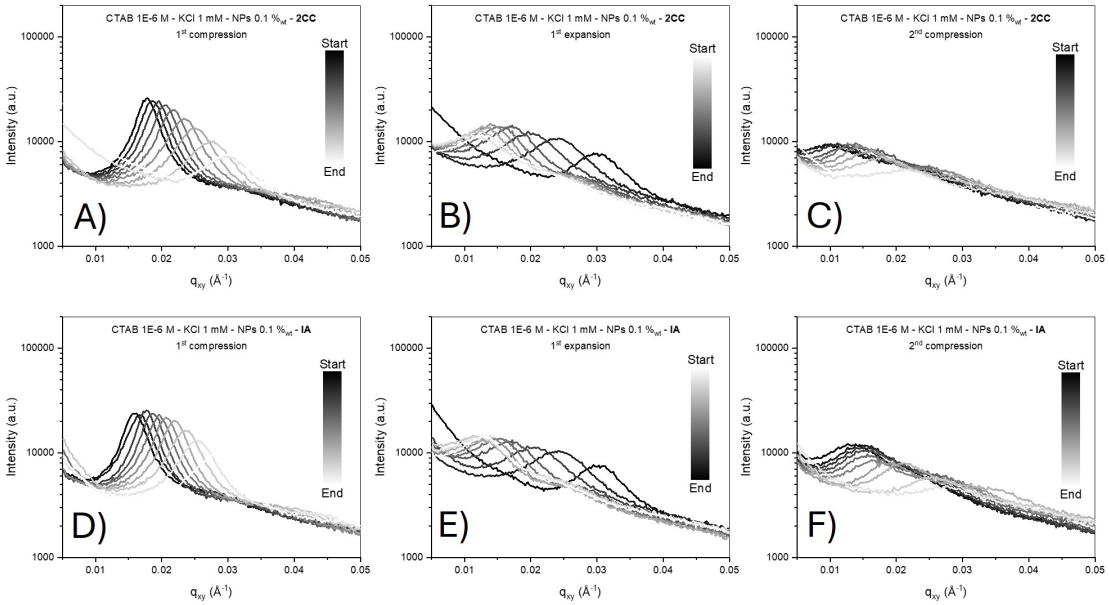

Figure C.11: *Evolution of the horizontal cuts of the GISAXS pattern for sample CTAB* 1×10^{-6} *M - KCl 1 mM - NPs 0.1* $\%_{wt}$ *during the first compression* (A, D)*, the expansion* (B, E) *and the second compression* (C, F) *by employing two consecutive compression* $(2CC)$ *in* (A, B, C) *and intermediate adsorption* (IA) *in* (D, E, F) *protocols. The red circles mark the positions of the two independently evolving GISAXS peaks.*

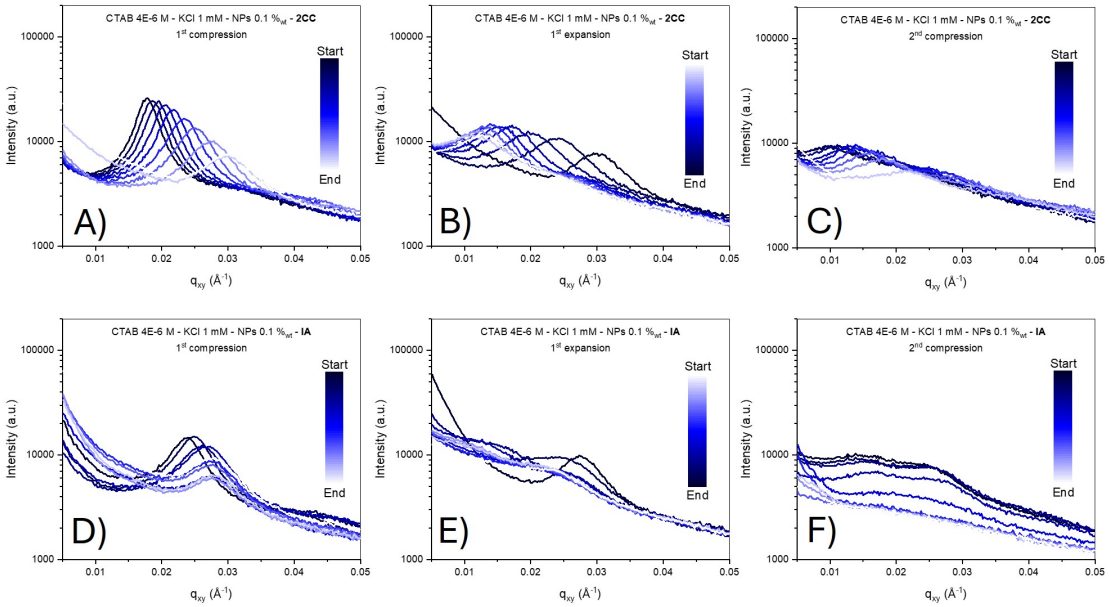

Figure C.12: *Evolution of the horizontal cuts of the GISAXS pattern for sample CTAB* 4×10^{-6} *M - KCl 1 mM - NPs 0.1* $\%_{wt}$ *during the first compression* (A, D)*, the expansion* (B, E) *and the second compression* (C, F) *by employing two consecutive compression* $(2CC)$ *in* (A, B, C) *and intermediate adsorption* (IA) *in* (D, E, F) *protocols. The red circles mark the positions of the two independently evolving GISAXS peaks.*

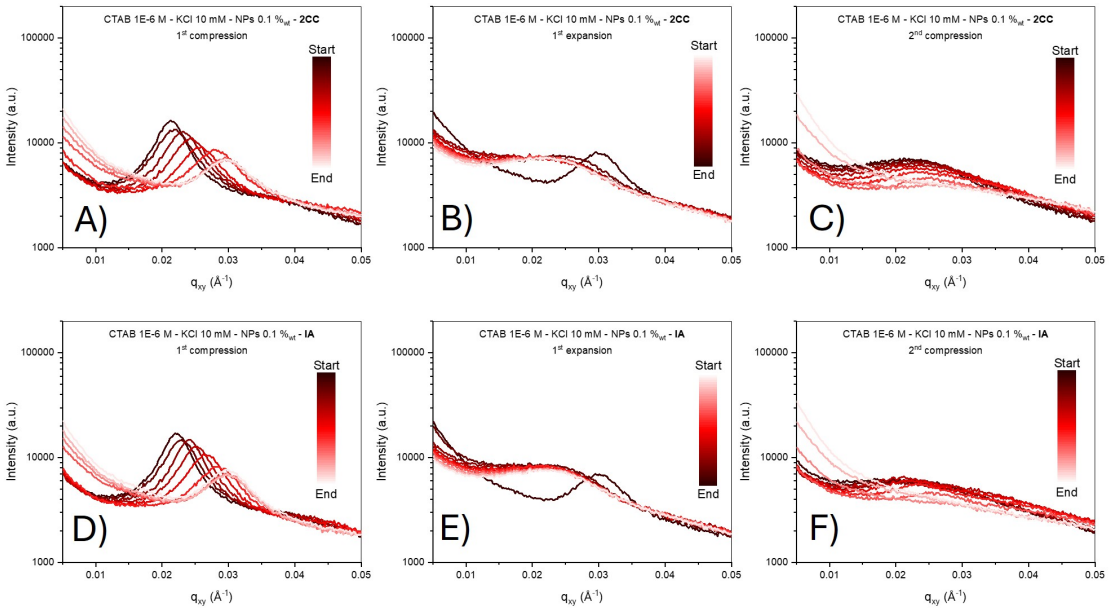

Figure C.13: *Evolution of the horizontal cuts of the GISAXS pattern for sample CTAB* 1×10^{-6} *M - KCl 10 mM - NPs 0.1* $\%_{wt}$ *during the first compression* (A, D)*, the expansion* (B, E) *and the second compression* (C, F) *by employing two consecutive compression* $(2CC)$ *in* (A, B, C) *and intermediate adsorption* (IA) *in* (D, E, F) *protocols. The red circles mark the positions of the two independently evolving GISAXS peaks.*

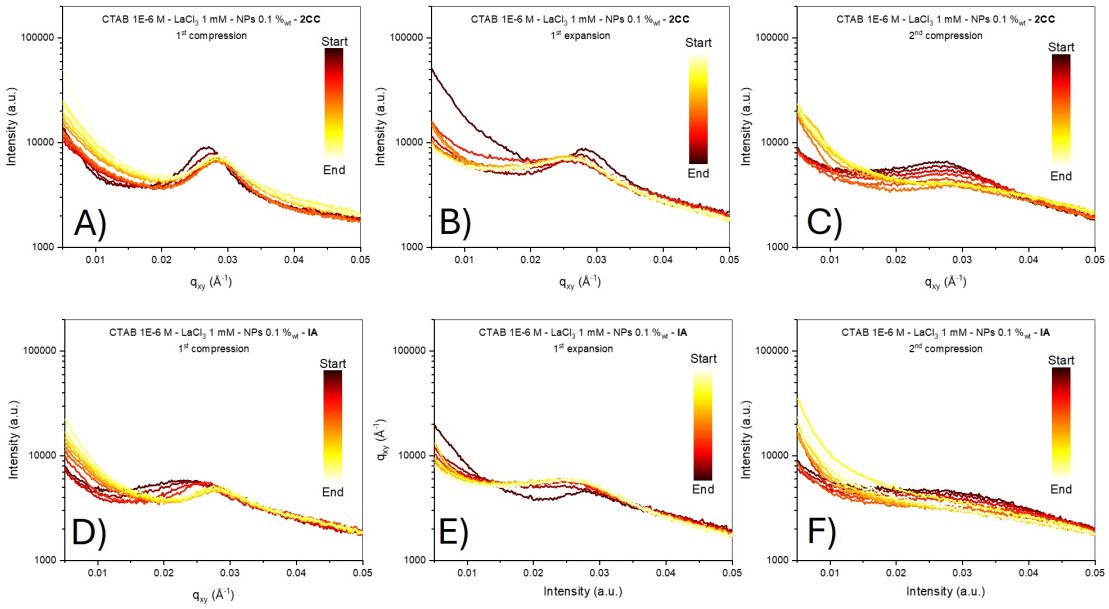

Figure C.14: *Evolution of the horizontal cuts of the GISAXS pattern for sample CTAB* 1×10^{-6} *M - $LaCl_3$ 1 mM - NPs 0.1* $\%_{wt}$ *during the first compression* (A, D)*, the expansion* (B, E) *and the second compression* (C, F) *by employing two consecutive compression* $(2CC)$ *in* (A, B, C) *and intermediate adsorption* (IA) *in* (D, E, F) *protocols. The red circles mark the positions of the two independently evolving GISAXS peaks.*

D

Supporting Information: Chapter 5 and 6

D.1 Materials and Methods

Negatively charged monodisperse Ludox TMA silica nanoparticles NPs, having a diameter of 23.2 $\pm$ 4.9 nm as determined by Small Angle Neutron Scattering (SANS) (Figure 5.5), were purchased from Sigma Aldrich, Milan (Italy) and purified in a dialysis tube (Spectra/Por® 4 Dialysis Membrane with a molecular weight cutoff of 12–14 kDa), also purchased from Sigma Aldrich, Milan (Italy). The dialysis tube filled with LUDOX nanoparticles was dialyzed against ultrapure water in a 1 L beaker under constant agitation for 48 h, changing the water every 12 h. Before every use, nanoparticle dispersion was sonicated for 30 min in an ultrasonic bath to improve homogenization. Sodium chloride (KCl, purity $>$ 99.9 %), heat shock fraction, fatty acid-free Bovine Serum Albumin (BSA, $\geq$ 96%, catalog n° A7030), lyophilized powder β-Casein from bovine milk (BCN, $\geq$ 98%, catalog n° C6905), and lyophilized powder β-Lactoglobulin from bovine milk (BLG, $\geq$ 90%, catalog n° L3908) were purchased from Sigma Aldrich, Milan (Italy) and used without further purification. All aqueous solutions and dispersions were prepared with ultrapure water (Milli-Q, 18.2 M$\Omega \cdot$ cm).

Protein-only dispersions were prepared by first preparing a protein stock solution at a concentration of 1×10^{-4} M, obtained by dissolving the solid protein in ultrapure water. Working solutions were then obtained by diluting the stock in NaCl solutions in order to simultaneously adjust the protein concentration and the desired ionic strength. Unless otherwise stated, all protein samples were studied at an ionic strength of 10 mM (NaCl) at protein concentrations of 0.0625, 0.125, 0.250, 0.500, and 1 μM. For BSA, the effect of ionic strength was also investigated at 0.125 and 1 μM, using NaCl concentrations of 1, 5, 10, and 50 mM.

Protein-nanoparticle (protein+NP) dispersions were prepared in order to investigate the effect of the bulk protein:NP molar ratio on the interfacial properties of protein

monolayers at the air-water interface. Two complementary protocols were followed:

(i) The NP concentration was fixed at 0.1 $\%_{wt}$ (corresponding to a molar concentration of 0.125 μM), while the protein concentration was varied over the same concentration range as for the protein-only samples (0.0625-1 μM). This yielded bulk protein:NP molar ratios of 0.5:1, 1:1, 2:1, 4:1, and 8:1.
(ii) The protein concentration was fixed at 1 μM, while the NP concentration was varied (1.6, 0.8, 0.4, 0.2, 0.1 $\%_{wt}$), corresponding to bulk molar ratios of protein:NP equal to 0.5:1, 1:1, 2:1, 4:1, and 8:1.

In all cases, the ionic strength was fixed at 10 mM NaCl. For BSA, the role of ionic strength was further examined at the 1:1 protein:NP molar ratio, using both protocol (*i*, BSA 0.125 μM and NPs 0.1 $\%_{wt}$) and protocol (*ii*, BSA 1 μM and NPs 0.8 $\%_{wt}$), investigating NaCl concentration of 1, 5, 10 e 50 mM.

For both protocols, dispersions were prepared following a standardized procedure designed to optimize sample homogeneity. Specifically, equal volumes of a protein solution and an NP+NaCl dispersion (both prepared at twice the target final concentration) were mixed under constant stirring. In particular, the BSA solution was added gradually (almost drop-wise) to the NP+NaCl dispersion, which was kept under gentle stirring throughout the process. This approach ensured that, upon mixing under constant stirring, the final concentrations of protein, NP, and NaCl matched the desired values, while avoiding concentration gradients or artifacts arising from local inhomogeneities.

Finally, the pH of all dispersions (protein-only and protein+NP) was adjusted to 7.0 ± 0.5 by the addition of small aliquots of concentrated HCl or NaOH. The resulting ionic strength variation due to pH adjustment was at most 0.1 mM, well within the experimental uncertainty, and therefore negligible with respect to the evaluation of ionic strength effects in BSA+NP samples.

D.1.1 Dynamic surface tension (DST) and compression isotherms

Dynamic surface tension (DST) and compression isotherms were characterized using a KSV Minitrough (KSV Instruments, Helsinki, Finland), equipped with a paper Wilhelmy plate for surface pressure (π) measurements. The dispersion under investigation was gently poured into the trough, and the system was allowed to equilibrate for 1 h, during which the time evolution of the surface pressure was continuously monitored. After equilibration, the adsorbed interfacial film was compressed at a constant barrier speed of 15 mm/min, corresponding to a macroscopic surface area reduction of approximately 22 cm^2/min. All measurements were performed at a controlled temperature of 25 °C. The dynamic surface tension, $\gamma(t)$, was determined according to:

$$\gamma(t) = \gamma_0 - \pi(t),$$

where γ_0 = 72.8mN/m is the surface tension of the bare air-water interface, and $\pi(t)$ is the time-dependent surface pressure.

D.1.2 Grazing Incidence Small Angle X-ray Scattering (GISAXS)

GISAXS measurements were performed both at the ID 10 beamline of the European Synchrotron (ESRF) in Grenoble (France) and at the SIRIUS beamline of the SOLEIL French National Synchrotron in Paris (France). The Digital Object Identifier of the data acquired at the ESRF is (https://doi.esrf.fr/10.15151/ESRF-ES-1578697122).

At ESRF we employed a 22.5 KeV (wavelength 0.55 Å) beam with an incident grazing angle of 0.045° corresponding to the 82.5 % of the water critical angle for total external reflection. A Dectris eiger2 1M 2D detector was placed at 4331 mm from the sample to record the GISAXS pattern. At SOLEIL we employed a 10 KeV beam (wavelength 1.24 Å) with an incident grazing angle of 0.1° corresponding to the 80 % of the water critical angle for total external reflection. A Dectris Pilatus3 1M 2D detector was placed at 4490 mm from the sample to record the GISAXS pattern.

The Protein–NP–NaCl dispersion to be analyzed was poured into a custom-made Langmuir trough and allowed to stabilize for 1 h. After stabilization, the solution was compressed at a constant rate of approximately 22 cm^2/min, and the evolution of the surface pressure during compression ($\Pi = \gamma_0 - \gamma$, where $\gamma_0 = 72.5$ mN/m is the surface tension of the air-water interface at 25 °C and γ is the change in surface tension due to the NP monolayer) was recorded using a paper Wilhelmy plate. Simultaneously, GISAXS patterns were acquired with an exposure time of 1 s, followed by 5 s of no exposure between acquisitions. The 2D GISAXS patterns were cut and integrated along q_z in the range 0.0283-0.0358 $Å^{-1}$ and the so-obtained 1D patterns analyzed as extensively explained in Appendix G. The fitting function used to extrapolate quantitative information from the reduced 1D GISAXS pattern was the same as Equation A.1.

D.1.3 Small Angle Neutron Scattering (SANS)

Small-angle neutron scattering (SANS) measurements were performed on SANS2D at ISIS Pulsed Neutron Source (https://doi.org/10.5286/ISIS.E/ISIS.E.RB2410233). SANS2D is a time-of-flight instrument with two movable detectors. The detector was placed at 4 m distance from the sample giving, a momentum transfer range of 0.004-1.00 $Å4^{-1}$. 2.3 $\%_{wt}$ silica nanoparticle dispersion in 93% D_2O / 7 % H_2O and in 100 % H_2O, and BSA solution in 100 % D_2O at the concentration 23 μM were measured into 2 mm path length, 1 cm wide, quartz Hellma cells. Data were reduced using the routines within Mantid (Arnold et al., 2014). The data were normalized to the sample transmission, and corrected for detector efficiencies, then scattering from the empty cell was subtracted. The output data were the absolute scattered intensity, I(q) in cm^{-1}, versus the momentum transfer, q in $Å^{-1}$. The scattering of the pure solvents were afterwards subtracted accounting for the incoherent contribution. An instrument resolution $q/dq \sim 8\%$ was used.

D.1.4 Neutron Reflectometry (NR)

NR measurements were performed at the INTER reflectometer at the ISIS Neutron Facility, Rutherford Appleton Laboratory, Didcot, U.K. (https://doi.org/10.5286/ISIS.E/ISIS.E.RB2410233). INTER has a wavelength range of 1.5–16 Å(Webster et al., 2011). Using a neutron supermirror to allow the air-water interface to remain horizontal, measurements were taken at three angles of θ = 0.8, 1.2, and 2.3°, giving a momentum transfer range of 0.01–0.33 $Å^{-1}$. A resolution of ~ 3% was used. All measurements were carried out at a controlled room temperature of 25 ± 1 °C. The reflectivity data were analyzed using RasCAL software. Protein films were modeled as a series of layers, each with a thickness (d), a roughness (σ) and a hydration ($h\%$), while the protein-NP monolayers were modeled with a custom SLD profile. A detailed description of the models and SLD values used can be found in Appendix H.

D.1.5 Vibrational Sum Frequency Generation spectroscopy (SFG)

SFG spectra were recorded with the Münster Ultra-fast Spectrometer for Interfacial Chemistry (MUSIC) broadband sum-frequency spectrometer (García Rey et al., 2018). The system consists of a Solstice-Ace Ti:sapphire amplifier (Spectra Physics), seeded by a Ti:sapphire fs-oscillator and pumped by a Q-switched laser (Ascend 60, 520 nm, 1 kHz, 32 W). The oscillator emits at 794 nm with a bandwidth of 22 nm (Spectra Physics MaiTai SP, 84 MHz, 770 mW). The Solstice-Ace regenerative amplifier delivers about 7 W (1 kHz, 796 nm) of average power.

The uncompressed beam is split by an internal 50:50 beam splitter: one beam is sent to the internal compressor, the other to an external compressor. A total of 3.2 W of the amplified and compressed beam (796 nm, 18 nm bandwidth) pumps an optical parametric amplifier (OPA, Light Conversion TOPAS Prime) followed by a non-collinear difference frequency generation (NDFG) unit that combines the OPA idler and signal photons. The NDFG produces broadband femtosecond IR pulses tunable from 2.5 to 20 μm, with a full width at half-maximum bandwidth >300 cm^{-1}.

An air-spaced etalon (SLS Optics LTD, FSR 12.4 nm at 735 nm, $R = 94.5\%$) was inserted into the external compressor to generate a narrow-band VIS pulse centered at 804.1 nm with a bandwidth of 4 cm^{-1}. Etalon sidebands are removed by beam blocks placed inside the external compressor.

For the SFG experiment, the VIS and IR pulses overlap in space and time at 55° and 60° incidence, respectively. The mean circularized focused beam diameters ($1/e^2$) were 530 μm (VIS) and 260 μm (IR), using a VIS lens f' = +500 mm (N-BK7, Thorlabs LA1908-780) and an IR lens f' = +100 mm (ZnSe, AMSTechnologies ZC-PX-25-100 BB-AR coated).

The SFG photons were collected with a collimating lens f' = +200 mm (N-BK7, Thorlabs LA1979-A) and focused with a lens f' = +100 mm (LA1509-A), before being directed into a spectrograph (Kymera-328i-D2-SIL, Andor) with a 1200 g/mm grating imaged onto an EMCCD detector (Andor Newton, Du97P-BVF). A short-pass filter

with a cutoff at 763 nm (AHF, F76-789) was used to block the visible beam.

For the liquid–gas interface, all spectra were recorded in the ssp polarization configuration (s-polarized SF, s-polarized VIS, p-polarized IR). The polarization optics included a half-wave plate for the VIS (Bernhard Halle Nachfl RZQ 2.15.0795), and for the IR, an achromatic half-wave plate (Bernhard Halle Nachfl RAC 4.2.15) combined with a calcite Glan polarizing prism (Bernhard Halle Nachfl, PGL 12). The Glan prism ensured matching to the spectrograph grating, rendering the setup insensitive to the selected SFG polarization.

The IR beam path and the automated sample stage were enclosed in a compressed-air-purged box, maintaining relative humidity below 3%.

SFG spectra were acquired by scanning three IR frequencies from 2800 to 3800 cm^{-1} (C–H and O–H stretching vibrations), and two IR frequencies from 1300–1800 cm^{-1} (amide vibrations). The average IR beam power was set to 15 mW in the 2800-3800 cm^{-1} and 12 mW in the 1300–1800 cm^{-1} range. For each center frequency, two acquisitions of 60 s each for the C–H/O–H region, and four acquisitions of 60 s each for the amide region were integrated. The stitched data were normalized to the SFG signal from a plasma-cleaned gold film reference. For air–liquid measurements, a glass Petri dish containing 2.5 mL of liquid was used. The dish had been cleaned overnight in a sulfuric acid/Nochromix solution, extensively rinsed with Milli-Q water, and dried with N_2.

D.2 Supplementary Materials

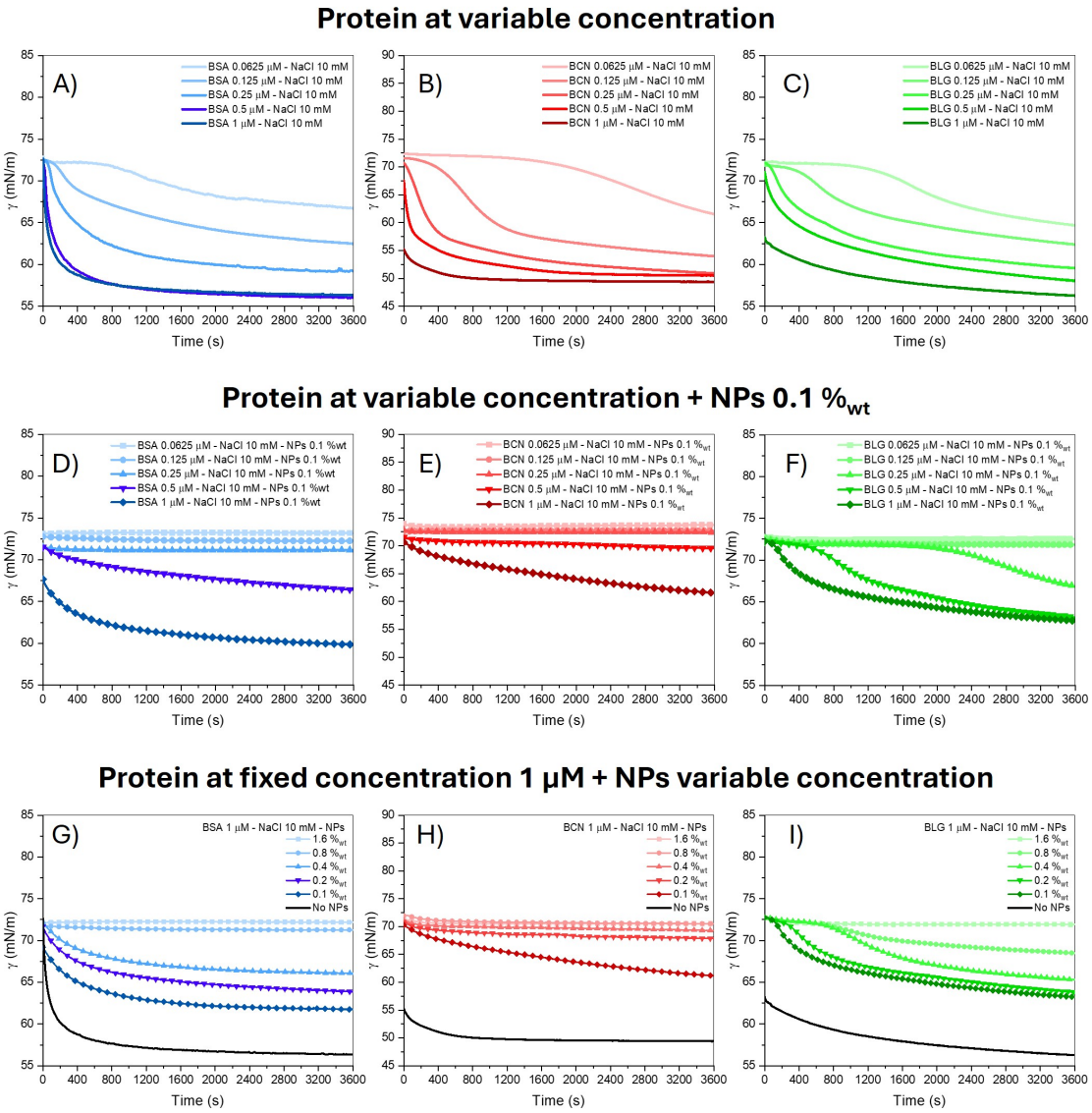

Figure D.1: *Dynamic surface tension γ evolution with time for samples prepared at different BSA:NP bulk ration in (D,G), BCN:NP in (E,H), and BLG:NP in (F,I). Samples in (A,B,C) are prepared with protein concentration from 0.0625 to 1 μM in NaCl 10 mM with (A) BSA, (B) BCN, and (C) BLG. Samples in (D,E,F) are prepared with protein concentration from 0.0625 to 1 μM in NaCl 10 mM and NPs 0.1 $\%_{wt}$ with (D) BSA, (E) BCN, and (F) BLG. Samples in (A,B,C) are prepared with protein concentration 1 μM in NaCl 10 mM and NPs in the range 0-1.6 $\%_{wt}$ with (G) BSA, (H) BCN, and (I) BLG.*

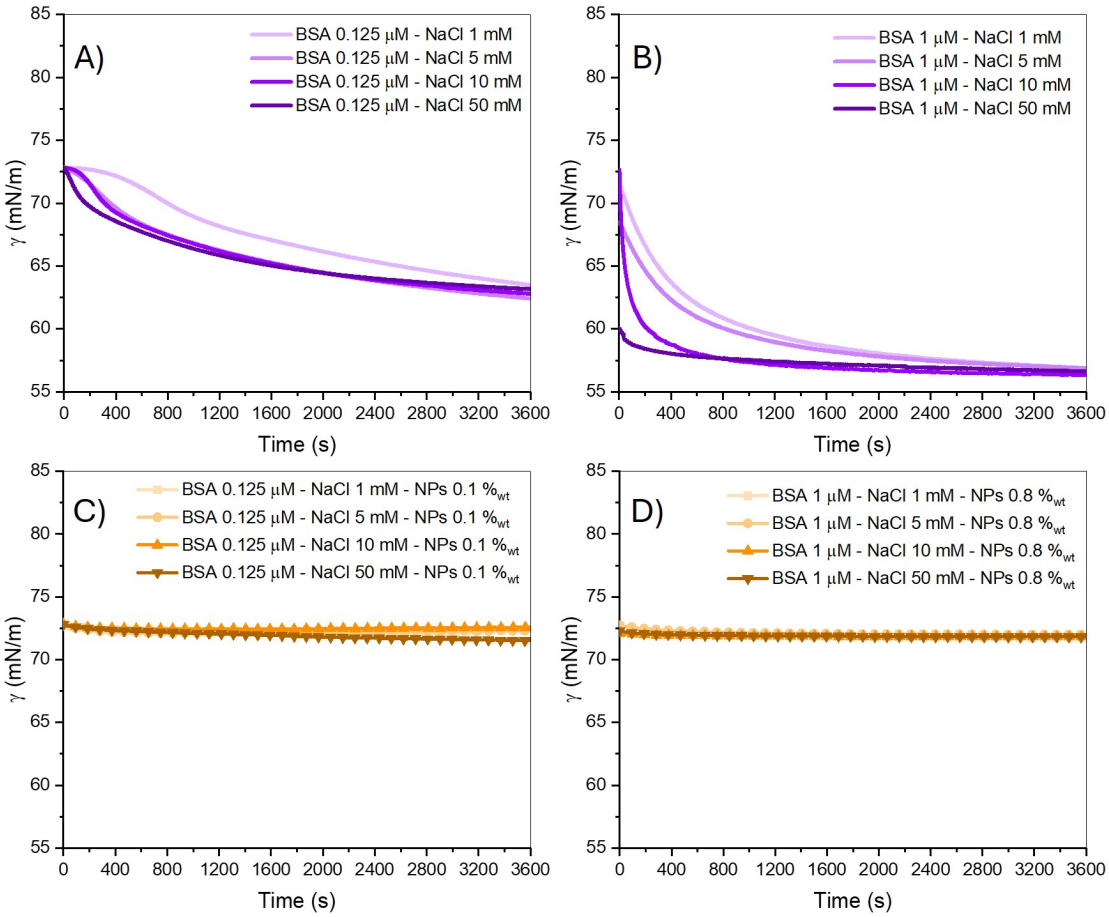

Figure D.2: *Dynamic surface tension γ evolution with time for samples prepared at BSA 0.125 μM (A), BSA 1 μM (A), BSA 0.125 μM - NPs 0.1 $\%_{wt}$ (C), and BSA 1 μM - NPs 0.8 $\%_{wt}$ (D). In all sample the ionic strength was investigated at the concentrations 1, 5, 10, and 50 mM.*

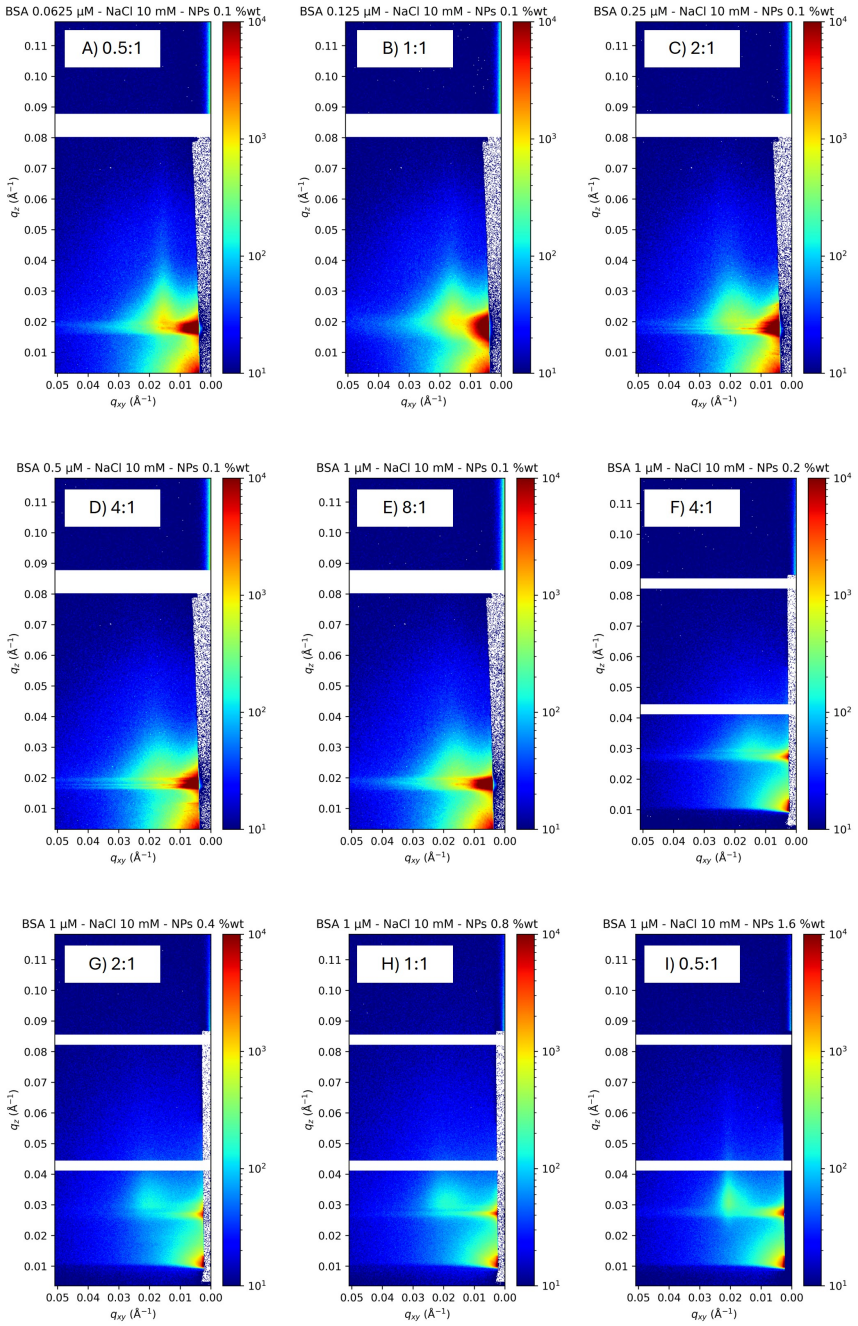

Figure D.3: *2D GISAXS pattern obtained at variable BSA:NP bulk ration in NaCl 10 mM. In (A,B,C,D,E) the NPs concentration was fixed at 0.1 $\%_{wt}$ and the protein concentration varied from 0.0625 to 1 μM. In (E,F,G,H,I) the NPs concentration was varied from 0.1 to 1.6 $\%_{wt}$ and the protein concentration fixed at 1 μM.*

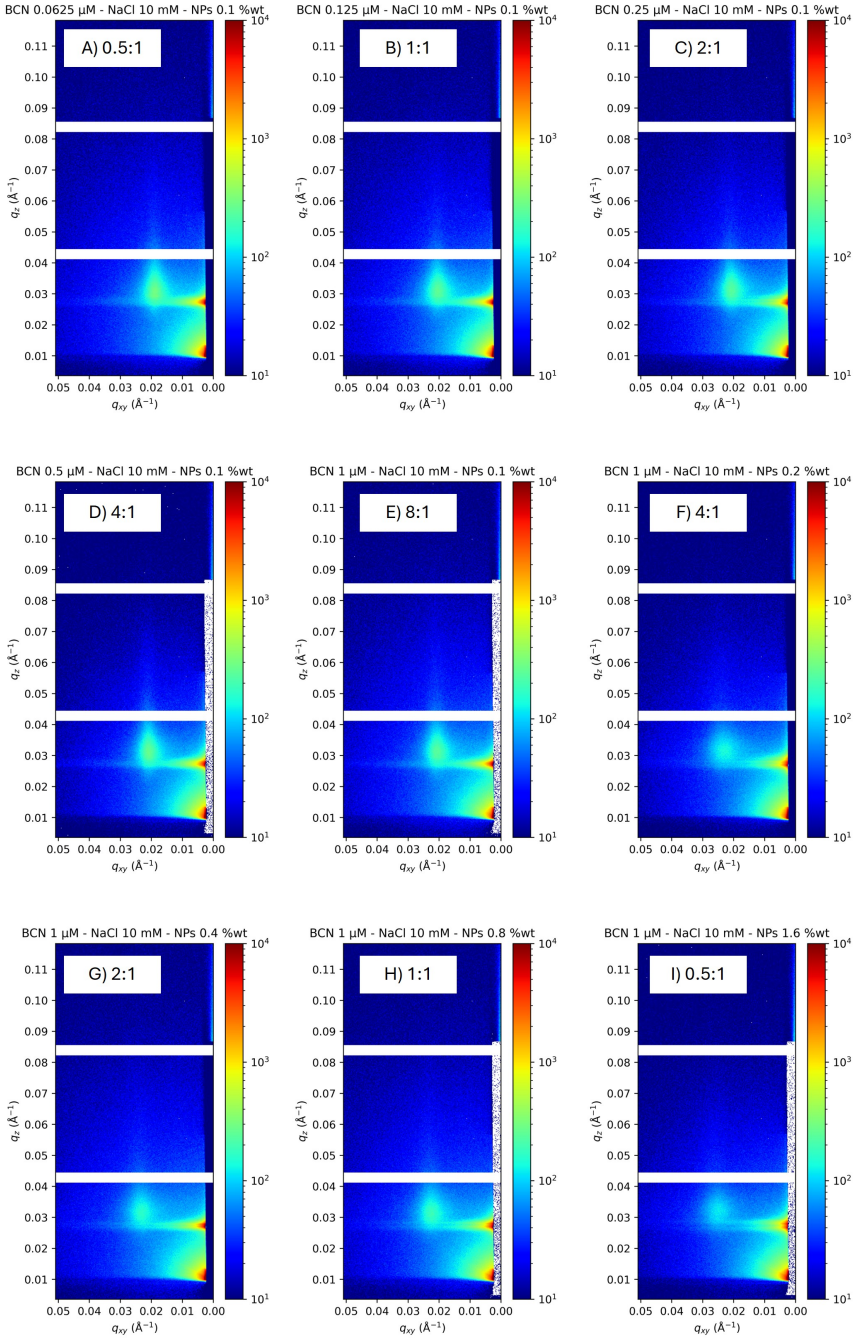

Figure D.4: *2D GISAXS pattern obtained at variable BCN:NP bulk ration in NaCl 10 mM. In (A,B,C,D,E) the NPs concentration was fixed at 0.1 $\%_{wt}$ and the protein concentration varied from 0.0625 to 1 µM. In (E,F,G,H,I) the NPs concentration was varied from 0.1 to 1.6 $\%_{wt}$ and the protein concentration fixed at 1 µM.*

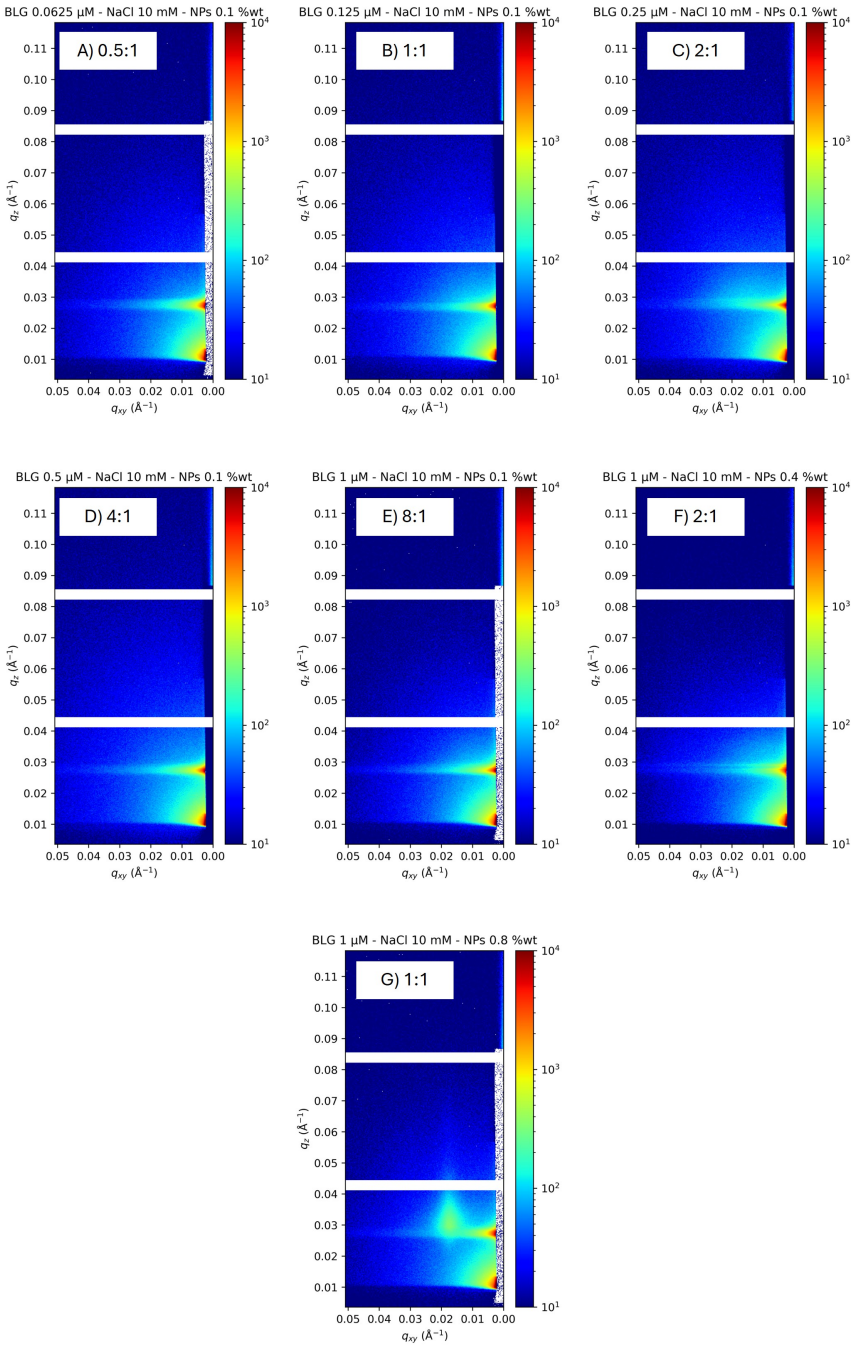

Figure D.5: *2D GISAXS pattern obtained at variable BLG:NP bulk ration in NaCl 10 mM. In (A,B,C,D,E) the NPs concentration was fixed at 0.1 $\%_{wt}$ and the protein concentration varied from 0.0625 to 1 µM. In (E,F,G) the NPs concentration was varied from 0.1 to 1.6 $\%_{wt}$ and the protein concentration fixed at 1 µM.*

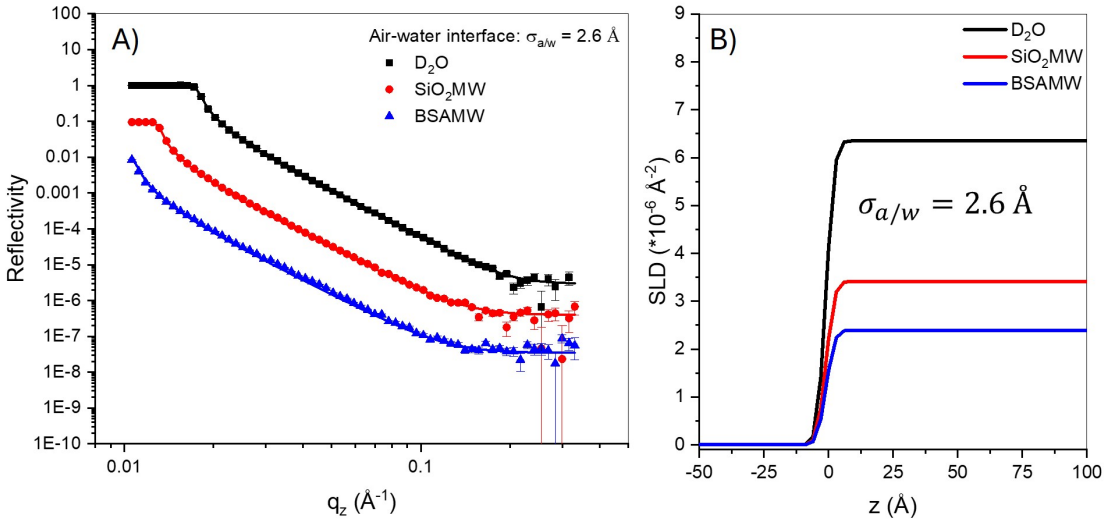

Figure D.6: *Experimental Reflectivity curves (colored point) with the corresponding fit (solid lines) (A) and the corresponding SLD profile (B) for the bare air-water interface. The different contrast solvents used are highlighted by the color curves. Specifically black curves refers to reflectivity acquired in 100 % D_2O ($SLD = 6.356 \times 10^{-6}$ Å^{-2}), red in SiO_2 match-water (SiO_2MW, 57.45% D_2O 42.55% H_2O, $SLD = 3.41 \times 10^{-6}$ Å^{-2}), blue in BSA match water (BSAMW, 42.55% D_2O 57.45% H_2O, $SLD = 2.395 \times 10^{-6}$ Å^{-2}), and green in null-reflecting water (NRW, 8.1% D_2O 91.9% H_2O, $SLD = 0$ Å^{-2}).*

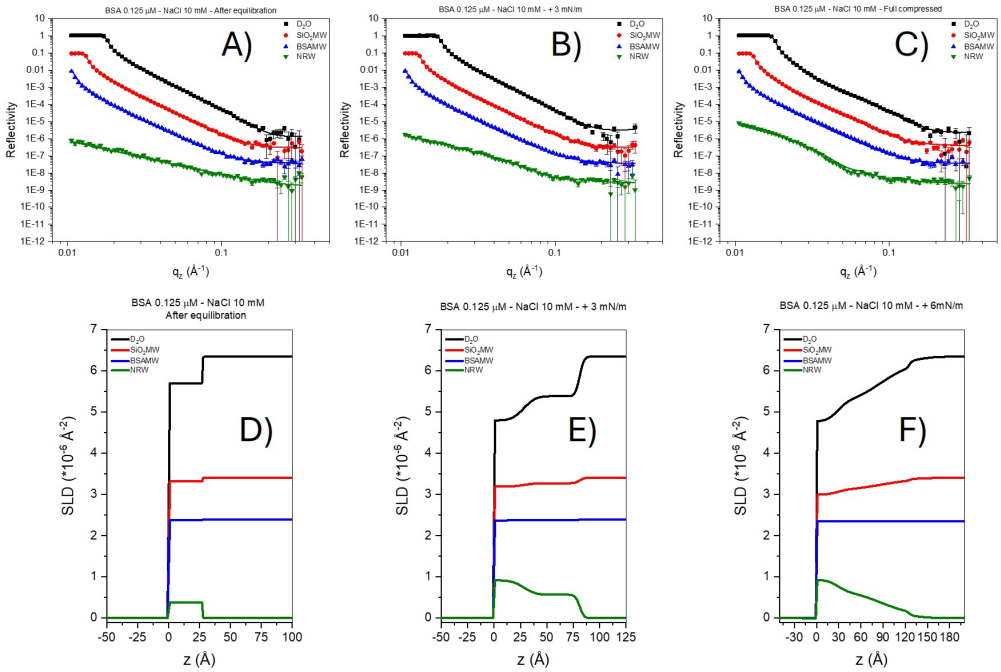

Figure D.7: *Experimental Reflectivity curves (colored point) with the corresponding fit (solid lines) (A,B,C) and the corresponding SLD profile (D,E,F) for system prepared at the bulk composition BSA 0.125 µM - NaCl 10 mM acquired (A,D) at the steady-state, (B,E) by compressing the layer at the target pressure +3 mN/m with respect to the steady-state, and (C,F) for the full compressed monolayer. The different contrast solvents used are highlighted by the color curves. Specifically black curves refers to reflectivity acquired in 100 % D_2O, red in SiO_2 match-water (SiO_2MW), blue in BSA match water (BSAMW), and green in null-reflecting water (NRW).*

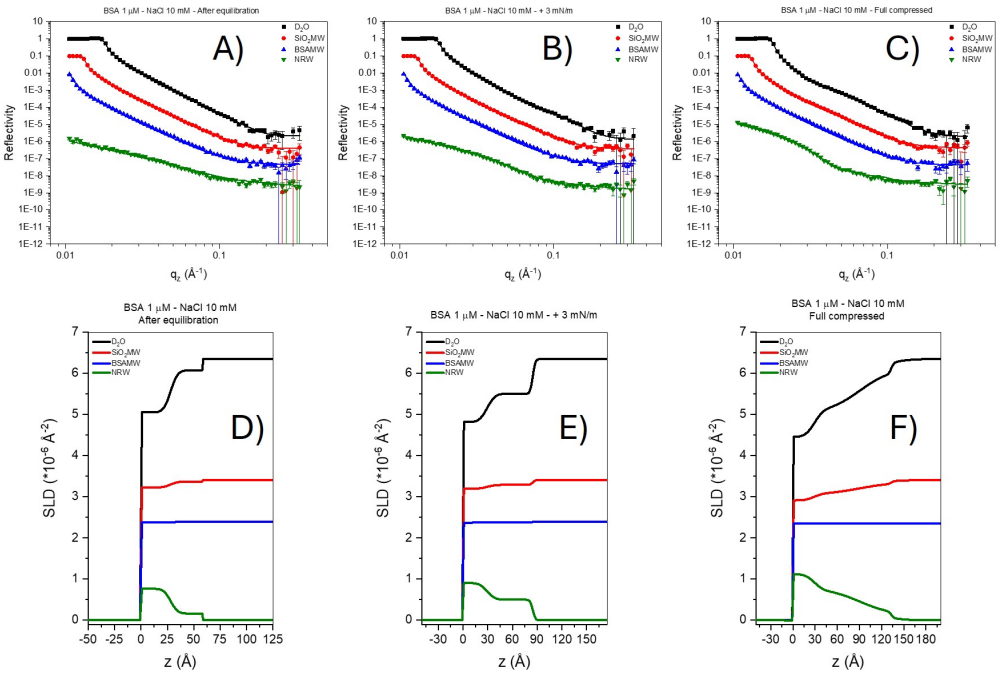

Figure D.8: *Experimental Reflectivity curves (colored point) with the corresponding fit (solid lines) (A,B,C) and the corresponding SLD profile (D,E,F) for system prepared at the bulk composition BSA 1 μM - NaCl 10 mM acquired (A,D) at the steady-state, (B,E) by compressing the layer at the target pressure +3 mN/m with respect to the steady-state, and (C,F) for the full compressed monolayer. The different contrast solvents used are highlighted by the color curves. Specifically black curves refers to reflectivity acquired in 100 % D_2O, red in SiO_2 match-water (SiO_2MW), blue in BSA match water (BSAMW), and green in null-reflecting water (NRW).*

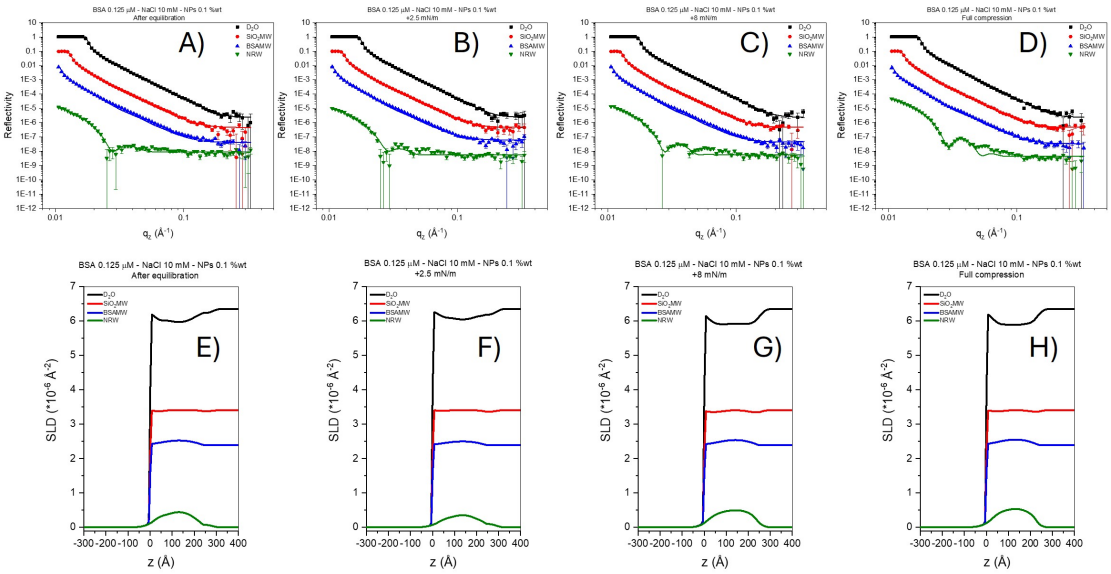

Figure D.9: *Experimental Reflectivity curves (colored point) with the corresponding fit (solid lines) (A,B,C,D) and the corresponding SLD profile (E,F,G,H) for system prepared at the bulk composition BSA 0.125 μM - NaCl 10 mM - NPs 0.1 $\%_{wt}$ acquired (A,E) at the steady-state, (B,F) by compressing the layer at the target pressure +2.5 mN/m with respect to the steady-state, (C,G) by compressing the layer at the target pressure +8 mN/m with respect to the steady-state, and (D,H) for the full compressed monolayer. The different contrast solvents used are highlighted by the color curves. Specifically black curves refers to reflectivity acquired in 100 % D_2O, red in SiO_2 match-water (SiO_2MW), blue in BSA match water (BSAMW), and green in null-reflecting water (NRW).*

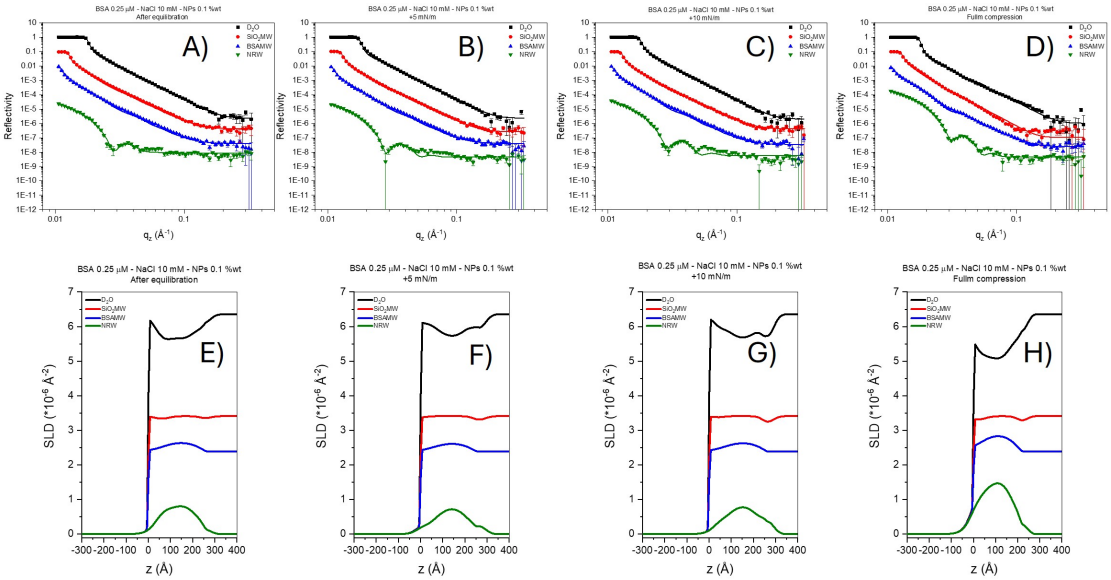

Figure D.10: *Experimental Reflectivity curves (colored point) with the corresponding fit (solid lines) (A,B,C,D) and the corresponding SLD profile (E,F,G,H) for system prepared at the bulk composition BSA 0.25 μM - NaCl 10 mM - NPs 0.1 $\%_{wt}$ acquired (A,E) at the steady-state, (B,F) by compressing the layer at the target pressure +5 mN/m with respect to the steady-state, (C,G) by compressing the layer at the target pressure +10 mN/m with respect to the steady-state, and (D,H) for the full compressed monolayer. The different contrast solvents used are highlighted by the color curves. Specifically black curves refers to reflectivity acquired in 100 % D_2O, red in SiO_2 match-water (SiO_2MW), blue in BSA match water (BSAMW), and green in null-reflecting water (NRW).*

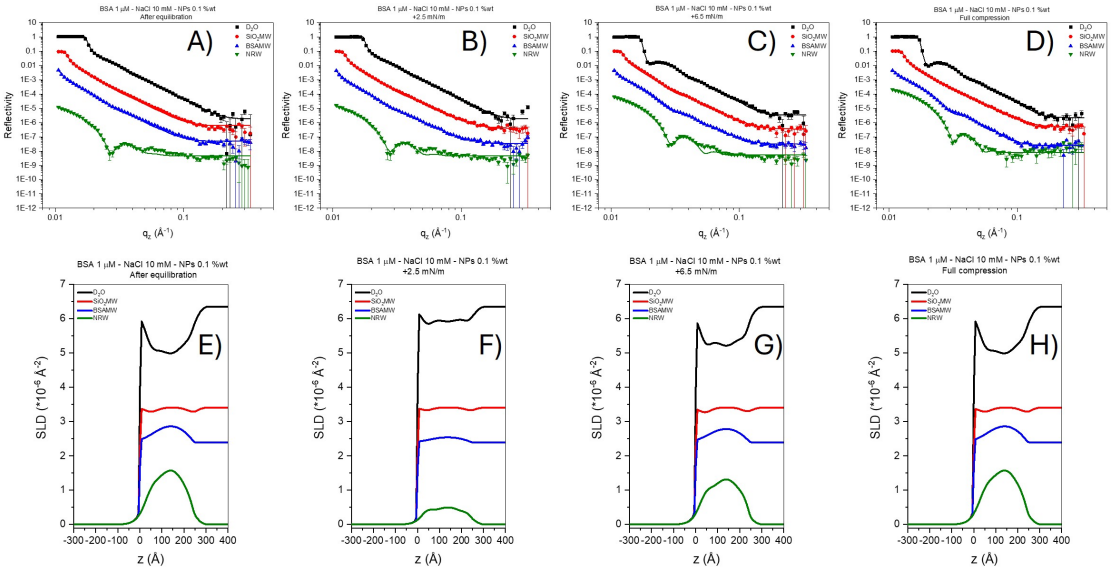

Figure D.11: *Experimental Reflectivity curves (colored point) with the corresponding fit (solid lines) (A,B,C,D) and the corresponding SLD profile (E,F,G,H) for system prepared at the bulk composition BSA 1 μM - NaCl 10 mM - NPs 0.1 $\%_{wt}$ acquired (A,E) at the steady-state, (B,F) by compressing the layer at the target pressure +2.5 mN/m with respect to the steady-state, (C,G) by compressing the layer at the target pressure +6.5 mN/m with respect to the steady-state, and (D,H) for the full compressed monolayer. The different contrast solvents used are highlighted by the color curves. Specifically black curves refers to reflectivity acquired in 100 % D_2O, red in SiO_2 match-water (SiO_2MW), blue in BSA match water (BSAMW), and green in null-reflecting water (NRW).*

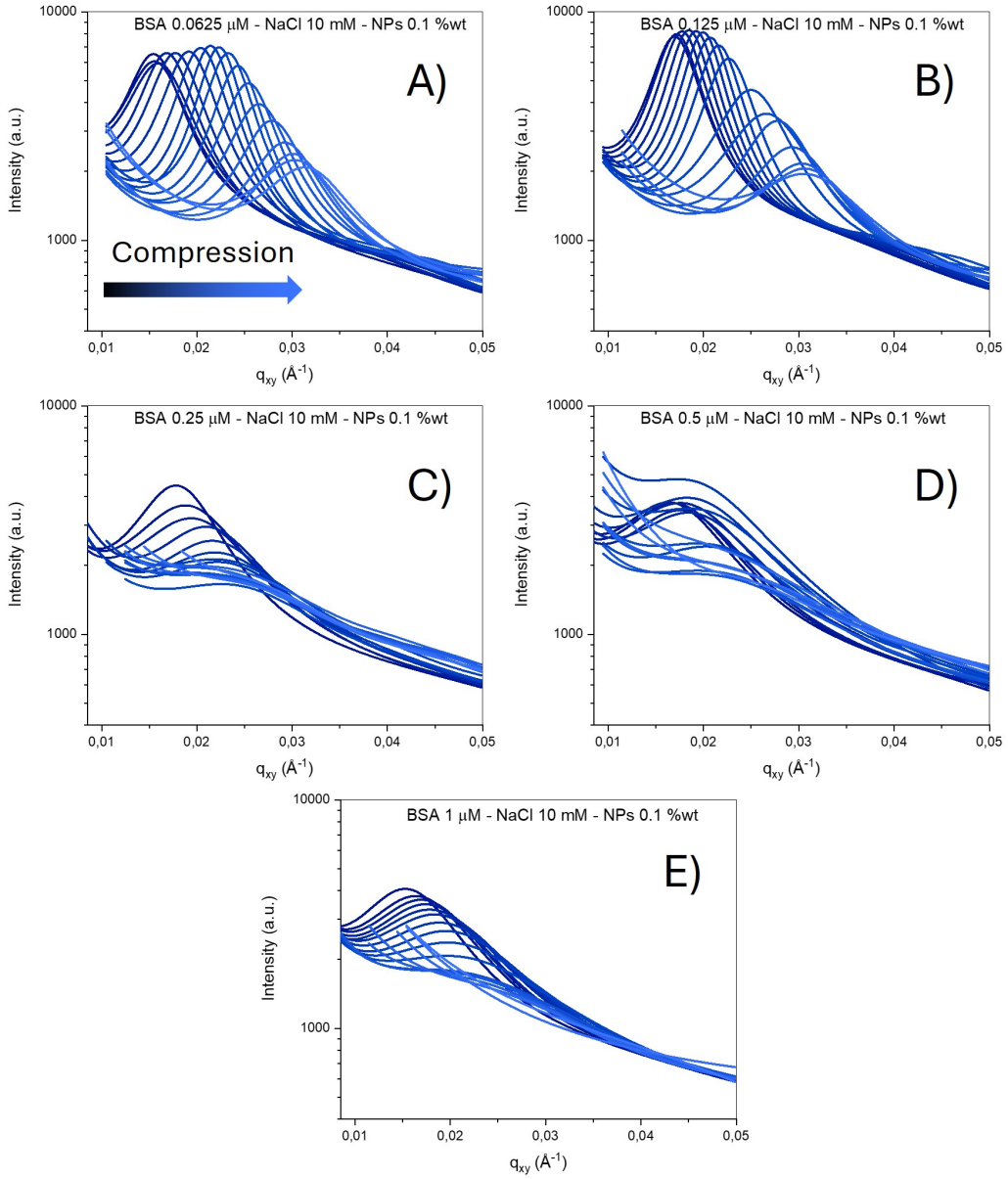

Figure D.12: *Evolution of 1D GISAXS horizontal cuts during lateral compression for hybrid BSA–NP monolayers prepared at fixed NP content* $(0.1\ \%_{wt})$ *in NaCl 10 mM and varying BSA bulk concentration:* (A) *0.0625 µM,* (B) *0.125 µM,* (C) *0.25 µM,* (D) *0.5 µM,* (E) *1 µM. Curves are shown as intensity* $I(q_y)$ *vs in-plane scattering vector* q_{xy}*; peak positions shift to higher* q_{xy} *upon compression, reflecting a decrease of the interparticle distance extracted from* $ID = 2\pi/\sqrt{3}q_{\mathrm{peak}}$.

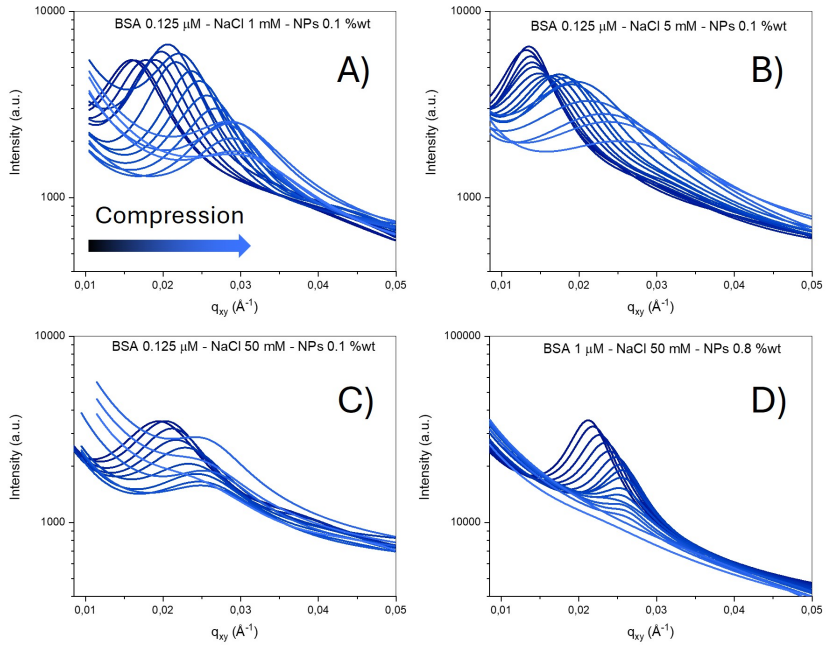

Figure D.13: *Evolution of 1D GISAXS horizontal cuts during lateral compression for hybrid BSA–NP monolayers prepared at (A) BSA 0.125 µM - NaCl 1 mM - NPs 0.1 $\%_{wt}$, (B) BSA 0.125 µM - NaCl 5 mM - NPs 0.1 $\%_{wt}$, (C) BSA 0.125 µM - NaCl 50 mM - NPs 0.1 $\%_{wt}$, (D) BSA 1 µM - NaCl 50 mM - NPs 0.8 $\%_{wt}$. Curves are shown as intensity $I(q_y)$ vs in-plane scattering vector q_{xy}; peak positions shift to higher q_{xy} upon compression, reflecting a decrease of the interparticle distance extracted from $ID = 2\pi/\sqrt{3}q_{\mathrm{peak}}$.*

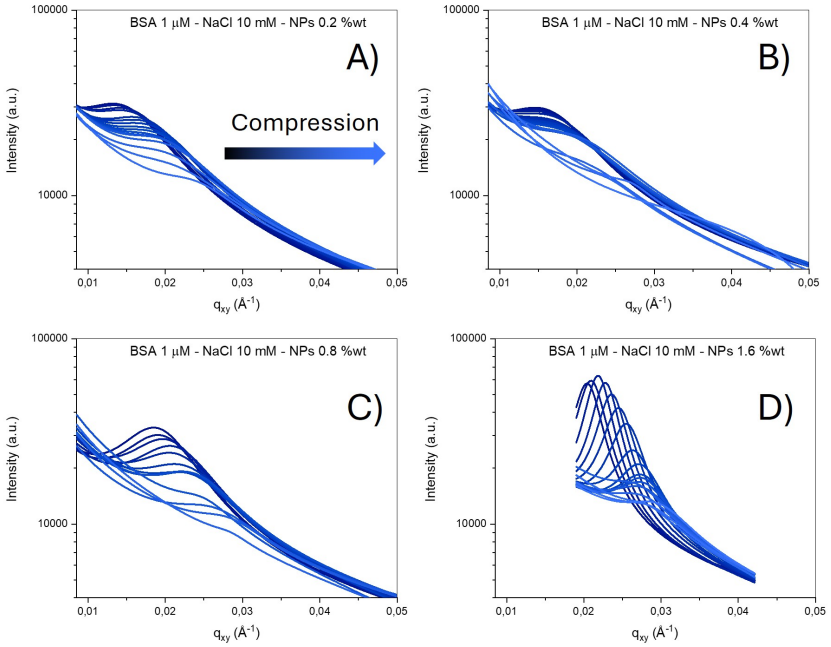

Figure D.14: *Evolution of 1D GISAXS horizontal cuts during lateral compression for hybrid BSA–NP monolayers prepared at fixed BSA content (1 µM) in NaCl 10 mM and varying NPs bulk concentration: (A) 0.2 $\%_{wt}$, (B) 0.4 $\%_{wt}$, (C) 0.8 $\%_{wt}$, (D) 1.6 $\%_{wt}$. Curves are shown as intensity $I(q_y)$ vs in-plane scattering vector q_{xy}; peak positions shift to higher q_{xy} upon compression, reflecting a decrease of the interparticle distance extracted from $ID = 2\pi/\sqrt{3}q_{\mathrm{peak}}$.*

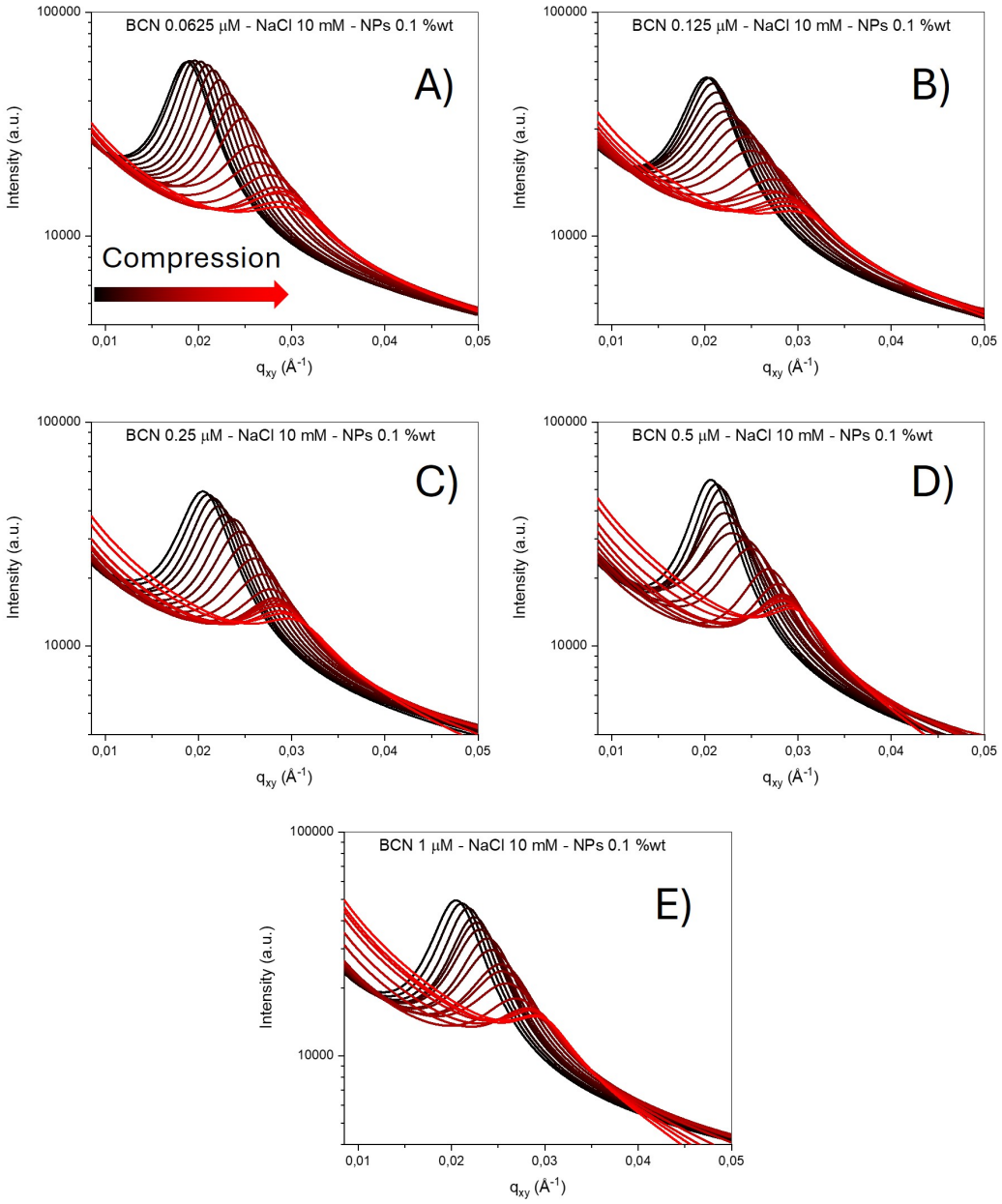

Figure D.15: *Evolution of 1D GISAXS horizontal cuts during lateral compression for hybrid BCN–NP monolayers prepared at fixed NP content* $(0.1\ \%_{wt})$ *in NaCl 10 mM and varying BCN bulk concentration:* (A) *0.0625 µM,* (B) *0.125 µM,* (C) *0.25 µM,* (D) *1 µM. Curves are shown as intensity* $I(q_y)$ *vs in-plane scattering vector* q_{xy}*; peak positions shift to higher* q_{xy} *upon compression, reflecting a decrease of the interparticle distance extracted from* $ID = 2\pi/\sqrt{3}q_{\mathrm{peak}}$.

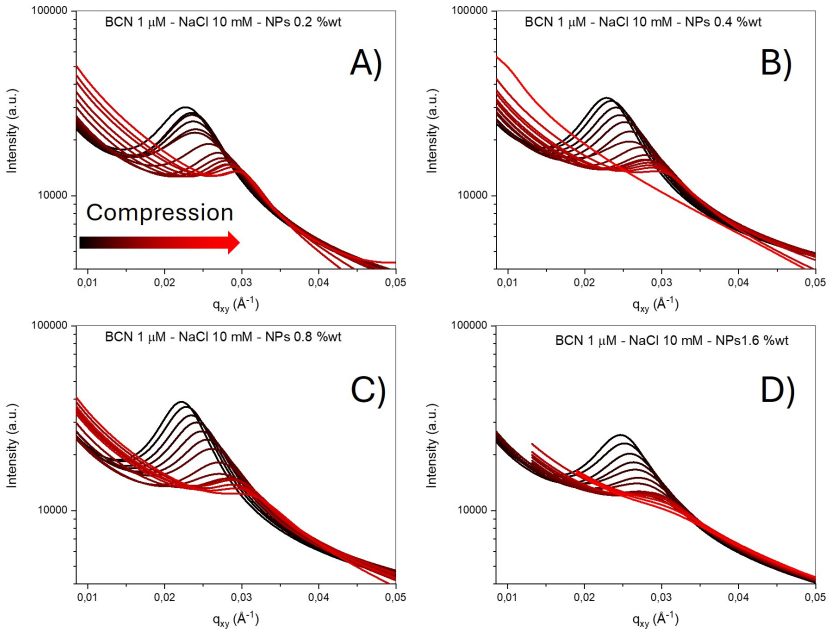

Figure D.16: *Evolution of 1D GISAXS horizontal cuts during lateral compression for hybrid BCN–NP monolayers prepared at fixed BCN content (1 µM) in NaCl 10 mM and varying NPs bulk concentration: (A) 0.2 $\%_{wt}$, (B) 0.4 $\%_{wt}$, (C) 0.8 $\%_{wt}$, (D) 1.6 $\%_{wt}$. Curves are shown as intensity $I(q_y)$ vs in-plane scattering vector q_{xy}; peak positions shift to higher q_{xy} upon compression, reflecting a decrease of the interparticle distance extracted from $ID = 2\pi/\sqrt{3}q_{\mathrm{peak}}$.*

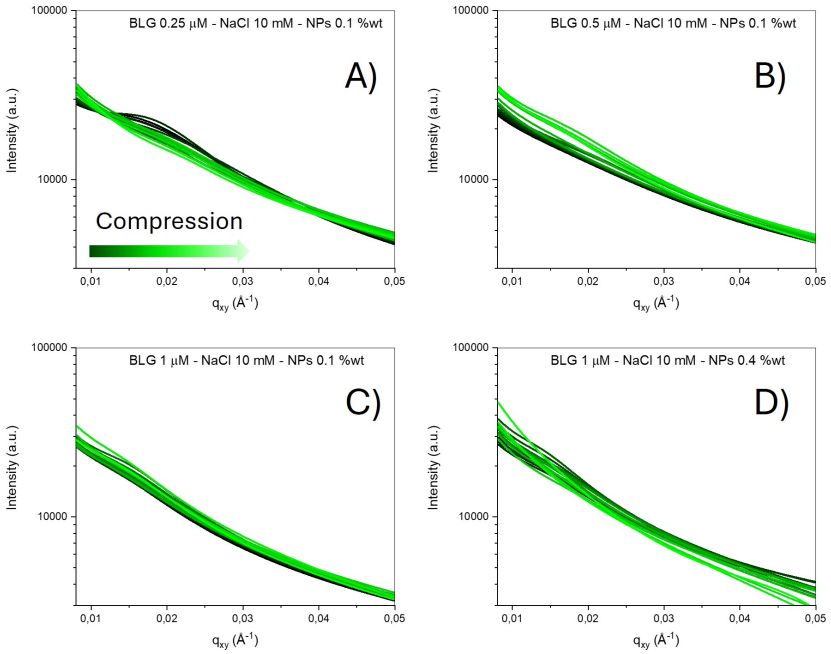

Figure D.17: *Evolution of 1D GISAXS horizontal cuts during lateral compression for hybrid BLG–NP monolayers prepared at bulk concentration: (A) BLG 0.25 µM) - NaCl 10 mM - NPs 0.1 $\%_{wt}$, (B) BLG 0.5 µM) - NaCl 10 mM - NPs 0.1 $\%_{wt}$, (C) BLG 1 µM) - NaCl 10 mM - NPs 0.1 $\%_{wt}$, and (D) BLG 1 µM) - NaCl 10 mM - NPs 0.4 $\%_{wt}$. Curves are shown as intensity $I(q_y)$ vs in-plane scattering vector q_{xy}; The peak intensity was to weak to be fitted properly.*

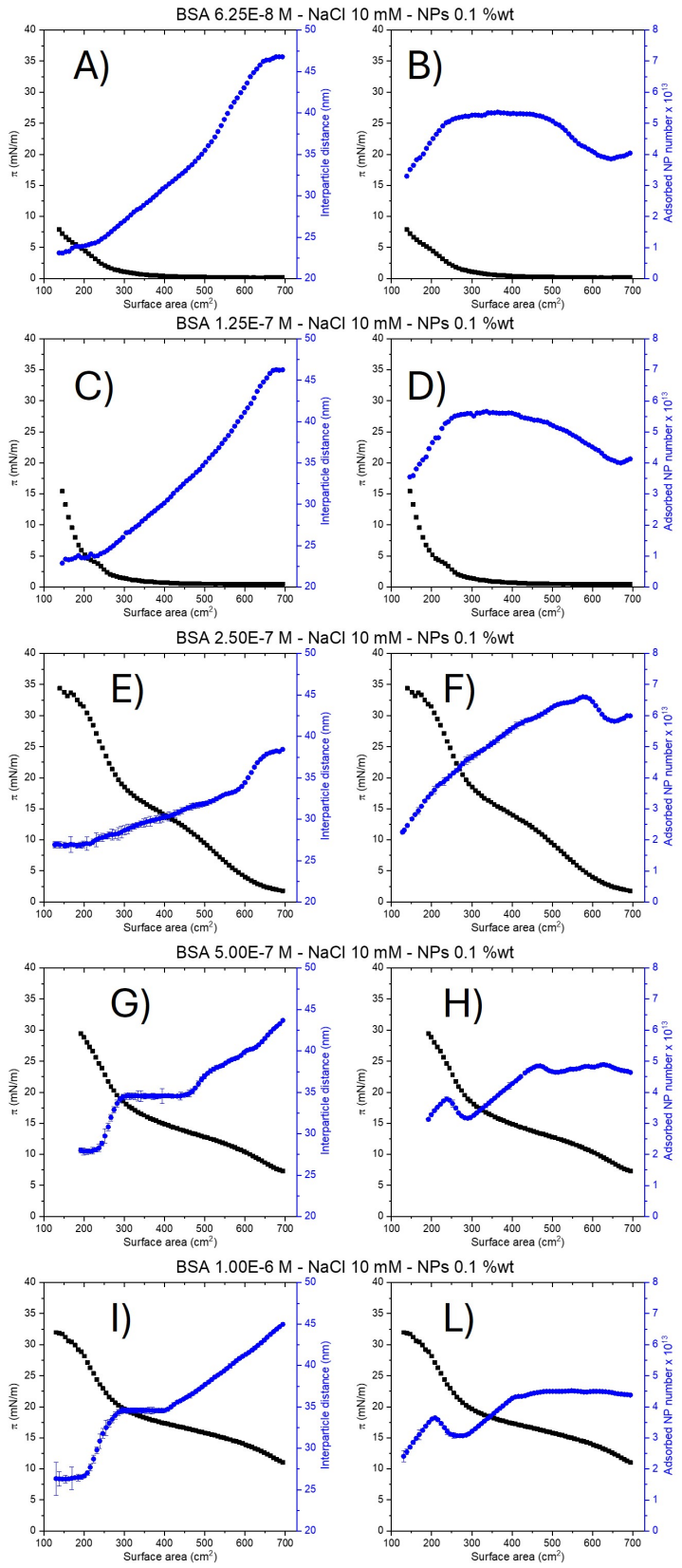

Figure D.18: *Monolayer interparticle distance (blue squares in A, C, E, G, I) and adsorbed NP number (blue squares B, D, F, H, L) evolution during compression together with the corresponding surface pressure variation (black line) for hybrid BSA–NP monolayers prepared at fixed NP content (0.1 $\%_{wt}$) in NaCl 10 mM and varying BSA bulk concentration: (A,B) 0.0625 μM, (C,D) 0.125 μM, (E,F) 0.25 μM, (G,H) 0.5 μM, (I,L) 1 μM.*

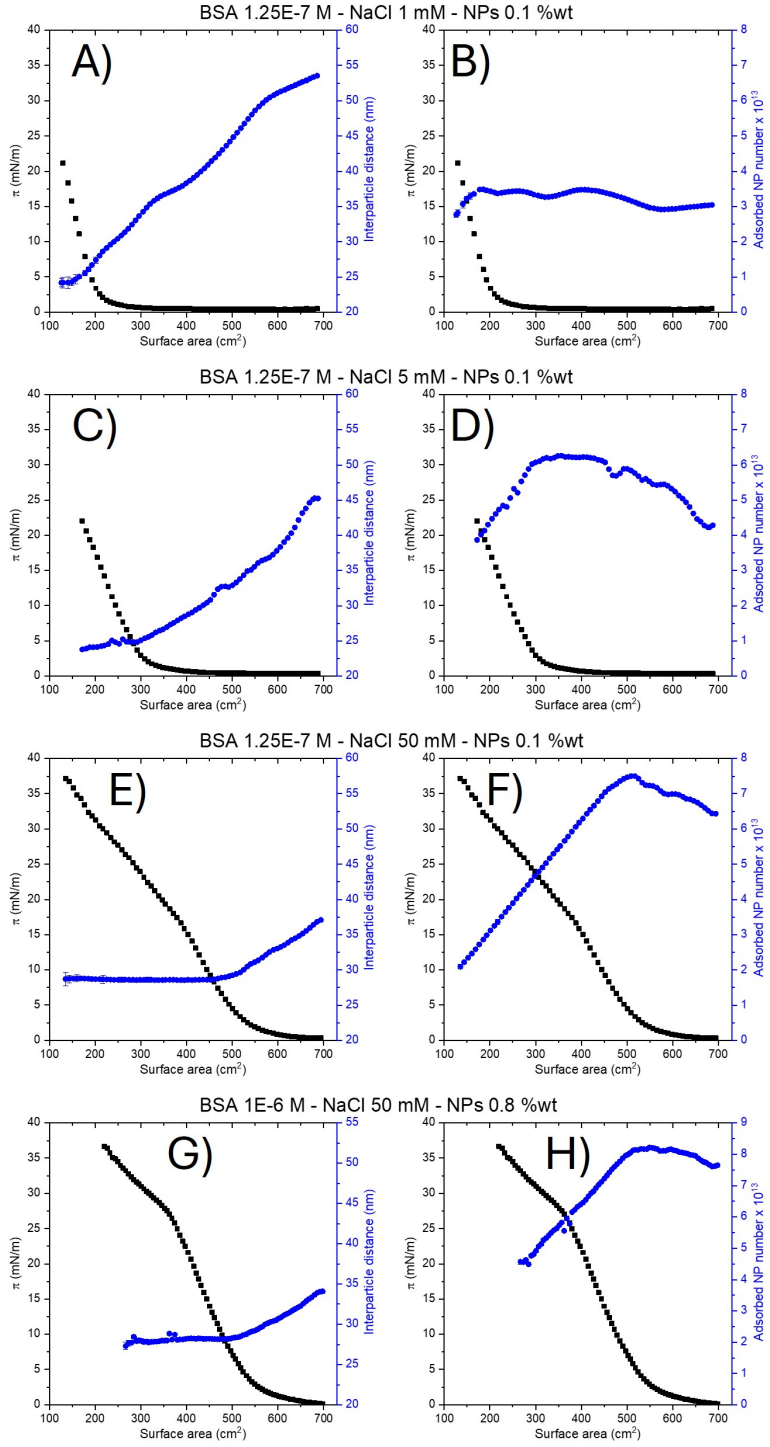

Figure D.19: *Monolayer interparticle distance (blue squares in A, C, E, G) and adsorbed NP number (blue squares B, D, F, H) evolution during compression together with the corresponding surface pressure variation (black line) for hybrid BSA–NP monolayers prepared at (A,B) BSA 0.125 μM - NaCl 1 mM - NPs 0.1 $\%_{wt}$, (C,D) BSA 0.125 μM - NaCl 5 mM - NPs 0.1 $\%_{wt}$, (E,F) BSA 0.125 μM - NaCl 50 mM - NPs 0.1 $\%_{wt}$, (G,H) BSA 1 μM - NaCl 50 mM - NPs 0.8 $\%_{wt}$.*

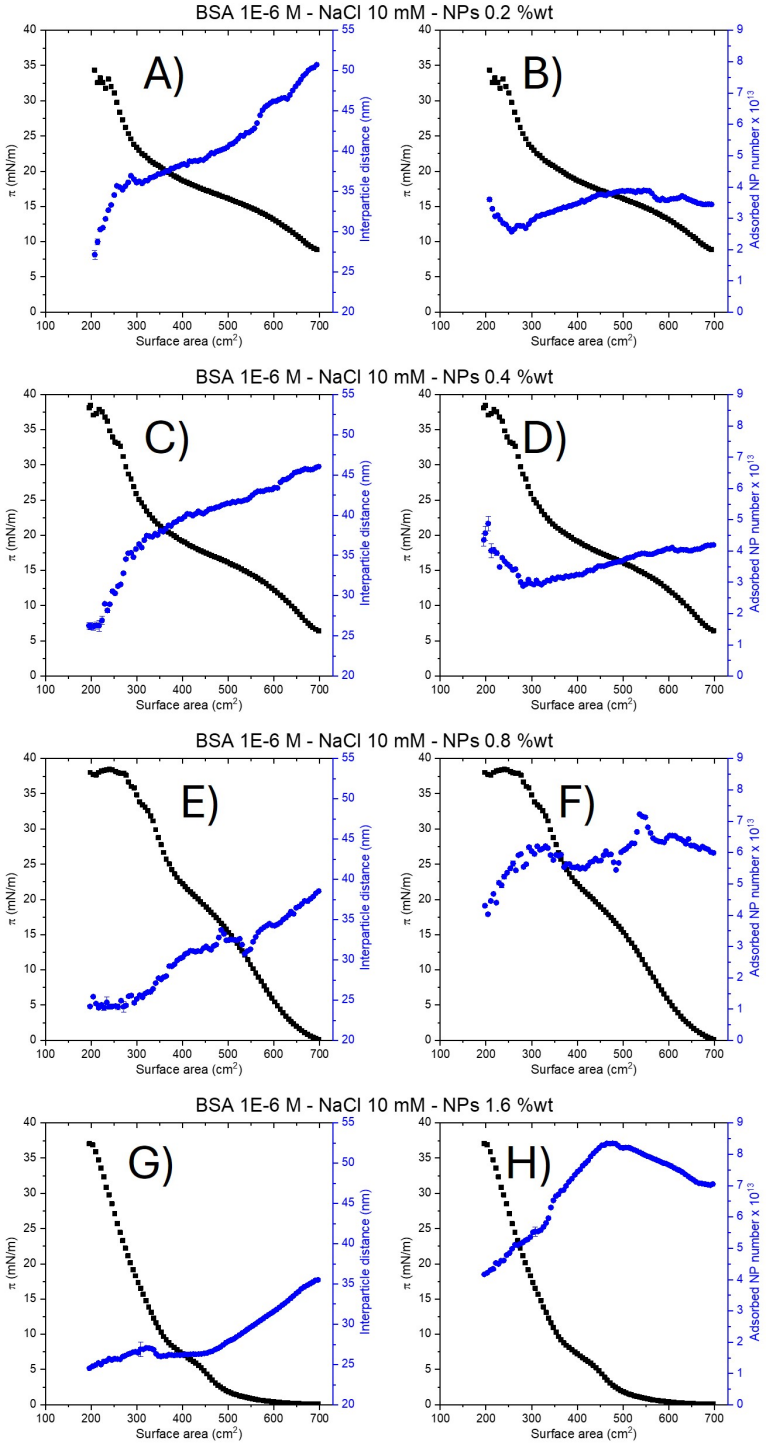

Figure D.20: *Monolayer interparticle distance (blue squares in A, C, E, G) and adsorbed NP number (blue squares B, D, F, H) evolution during compression together with the corresponding surface pressure variation (black line) for hybrid BSA–NP monolayers prepared at fixed BSA content (1 μM) in NaCl 10 mM and varying NPs bulk concentration: (A,B) 0.2 $\%_{wt}$, (C,D) 0.4 $\%_{wt}$, (E,F) 0.8 $\%_{wt}$, (G,H) 1.6 $\%_{wt}$.*

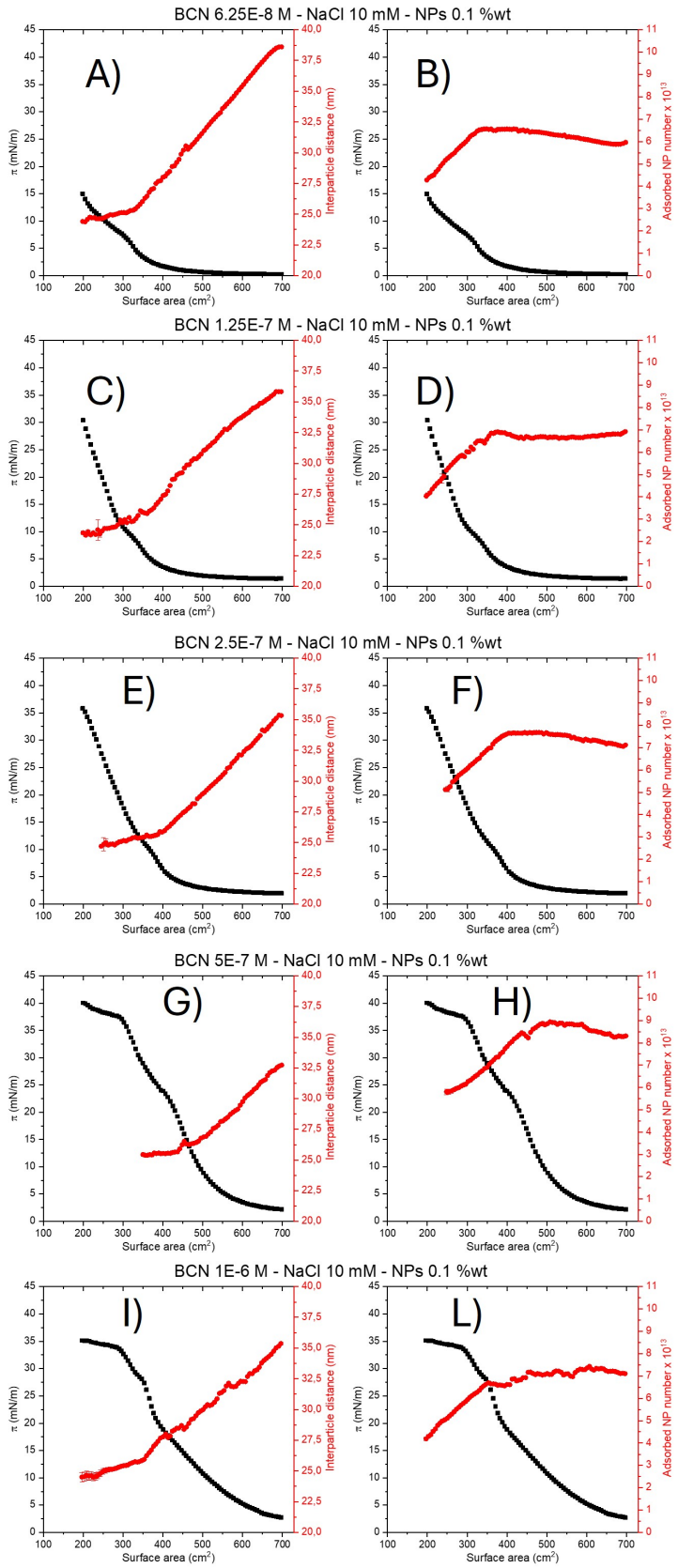

Figure D.21: *Monolayer interparticle distance (red squares in A, C, E, G, I) and adsorbed NP number (red squares B, D, F, H, L) evolution during compression together with the corresponding surface pressure variation (black line) for hybrid BCN–NP monolayers prepared at fixed NP content (0.1 $\%_{wt}$) in NaCl 10 mM and varying BCN bulk concentration: (A,B) 0.0625 μM, (C,D) 0.125 μM, (E,F) 0.25 μM, (G,H) 0.5 μM, (I,L) 1 μM.*

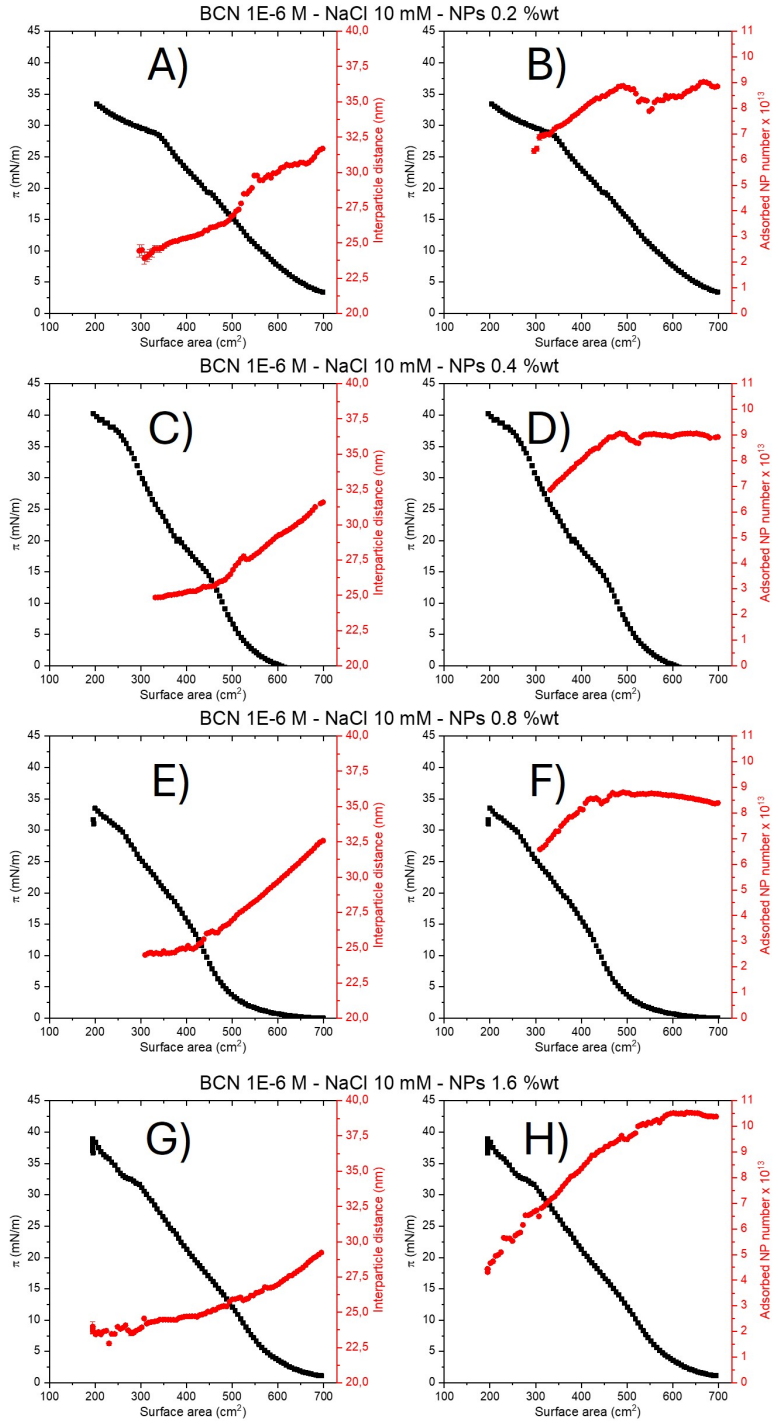

Figure D.22: *Monolayer interparticle distance (red squares in A, C, E, G) and adsorbed NP number (red squares B, D, F, H) evolution during compression together with the corresponding surface pressure variation (black line) for hybrid BSA–NP monolayers prepared at fixed BCN content (1 μM) in NaCl 10 mM and varying NPs bulk concentration: (A,B) 0.2 $\%_{wt}$, (C,D) 0.4 $\%_{wt}$, (E,F) 0.8 $\%_{wt}$, (G,H) 1.6 $\%_{wt}$.*

Table D.1: *Fitted parameters for BSA 0.125 μM at different surface pressures. Errors are reported in parentheses.*

BSA 0.125 μM - NaCl 10 mM - NPs 0.1 %wt				
	Full expanded Value (nm)	+2.5 mN/m Value (nm)	+8 mN/m Value (nm)	Full compression Value (nm)
$\sigma_{a/w}$	0.26 (0.00)	0.26 (0.00)	0.26 (0.00)	0.26 (0.00)
r_{av}	11.62 (0.00)	11.62 (0.00)	11.62 (0.00)	11.62 (0.00)
r_{dev}	2.48 (0.00)	2.48 (0.00)	2.48 (0.00)	2.48 (0.00)
h_{av}	24.22 (0.37)	24.63 (0.66)	24.75 (0.66)	23.85 (1.64)
h_{av}	0.44 (0.18)	0.27 (0.01)	0.30 (0.04)	0.43 (0.16)
s	19.20 (0.02)	9.26 (0.02)	1.39 (0.23)	0.93 (0.53)
ϕ_{np}	0.51 (0.10)	0.24 (0.07)	0.19 (0.03)	0.20 (0.14)
t_{air}	7.39 (0.32)	7.29 (0.00)	7.15 (3.20)	8.72 (1.45)
$\phi_{BSA,air}$	0.62 (0.25)	0.50 (0.00)	0.74 (0.32)	0.63 (0.26)
z_{air}	8.74 (1.45)	8.50 (0.99)	8.10 (0.83)	7.48 (2.69)
w_{air}	2.18 (1.76)	2.14 (2.23)	8.01 (1.49)	5.01 (3.24)
t_{water}	7.78 (0.08)	7.83 (0.07)	8.38 (1.30)	10.46 (2.42)
$\phi_{BSA,water}$	0.34 (0.03)	0.52 (0.02)	0.69 (0.24)	0.66 (0.19)
z_{water}	13.94 (0.80)	13.78 (2.33)	8.10 (0.29)	8.32 (0.25)
w_{water}	5.55 (3.25)	7.72 (0.98)	7.90 (2.79)	4.65 (3.91)
χ^2	42.36	37.52	48.25	54.21

Table D.2: *Fitted parameters for BSA 0.25 μM at different surface pressures. Errors are reported in parentheses.*

BSA 0.25 μM - NaCl 10 mM - NPs 0.1 %wt				
	Full expanded Value (nm)	+5 mN/m Value (nm)	+10 mN/m Value (nm)	Full compression Value (nm)
$\sigma_{a/w}$	0.26 (0.01)	0.26 (0.00)	0.26 (0.01)	0.25 (0.00)
r_{av}	11.62 (0.00)	11.62 (0.00)	11.62 (0.00)	11.62 (0.00)
r_{dev}	2.48 (0.00)	2.48 (0.00)	2.48 (0.00)	2.48 (0.00)
h_{av}	25.82 (2.18)	25.12 (2.63)	26.06 (2.24)	21.80 (3.29)
h_{av}	0.50 (0.23)	0.47 (0.15)	0.44 (0.10)	0.45 (0.24)
s	14.99 (0.33)	9.70 (0.00)	7.50 (0.00)	2.09 (1.00)
ϕ_{np}	0.75 (0.20)	0.50 (0.01)	0.47 (0.17)	0.60 (0.14)
t_{air}	8.94 (0.30)	5.59 (3.58)	6.18 (3.07)	6.65 (0.72)
$\phi_{BSA,air}$	0.30 (0.45)	0.44 (0.31)	0.38 (0.39)	0.46 (0.22)
z_{air}	8.18 (5.57)	12.81 (2.29)	10.35 (3.49)	8.09 (1.66)
w_{air}	6.25 (3.29)	3.96 (2.09)	2.73 (1.41)	6.87 (1.90)
t_{water}	8.13 (0.89)	10.62 (1.03)	9.67 (2.80)	6.22 (3.48)
$\phi_{BSA,water}$	0.37 (0.07)	0.53 (0.17)	0.90 (0.10)	0.68 (0.21)
z_{water}	11.78 (2.29)	13.51 (2.53)	12.40 (2.32)	12.29 (3.08)
w_{water}	3.98 (2.24)	5.46 (1.75)	4.67 (3.62)	3.80 (2.81)
χ^2	32.51	58.47	62.41	41.28

Table D.3: *Fitted parameters for BSA 1 μM at different surface pressures. Errors are reported in parentheses.*

BSA 1 μM - NaCl 10 mM - NPs 0.1 %wt				
	Full expanded Value (nm)	+2.5 mN/m Value (nm)	+6.5 mN/m Value (nm)	Full compression Value (nm)
$\sigma_{a/w}$	0.26 (0.01)	0.26 (0.00)	0.26 (0.00)	0.26 (0.00)
r_{av}	11.62 (0.00)	11.62 (0.00)	11.62 (0.00)	11.62 (0.00)
r_{dev}	2.48 (0.00)	2.48 (0.00)	2.48 (0.00)	2.48 (0.00)
h_{av}	24.37 (1.17)	24.94 (0.11)	24.83 (1.97)	24.73 (0.21)
h_{av}	0.41 (0.23)	0.39 (0.08)	0.54 (0.10)	0.53 (0.02)
s	24.46 (0.18)	19.06 (0.66)	11.68 (1.72)	2.75 (0.92)
ϕ_{np}	0.71 (0.02)	0.57 (0.08)	0.91 (0.12)	0.68 (0.35)
t_{air}	10.74 (0.59)	10.62 (0.21)	9.12 (1.07)	9.15 (0.15)
$\phi_{BSA,air}$	0.78 (0.15)	0.73 (0.15)	0.56 (0.24)	0.52 (0.24)
z_{air}	9.64 (0.55)	9.22 (0.14)	9.14 (1.53)	8.38 (1.11)
w_{air}	3.13 (0.71)	2.94 (0.52)	3.67 (0.91)	4.85 (1.74)
t_{water}	7.18 (0.85)	7.58 (2.90)	8.94 (0.09)	9.51 (1.01)
$\phi_{BSA,water}$	0.96 (0.06)	0.97 (0.03)	0.57 (0.20)	0.41 (0.04)
z_{water}	11.09 (0.96)	10.78 (0.44)	10.03 (0.05)	10.00 (0.00)
w_{water}	3.38 (0.59)	3.09 (0.63)	2.53 (0.05)	4.50 (2.72)
χ^2	35.74	82.54	78.25	34.21

Table D.4: *SFG fitting parameters in the water OH region for BSA 1 μM in NaCl 10 mM at different nanoparticle (NPs) concentrations. A is the band area, ϕ is the phase, w the IR mode frequency, and g full width at half maximum (FWHM). Errors are reported in parentheses.*

NPs (% wt)	OH 3250 cm^{-1}				OH 3400 cm^{-1}			
BSA 1 μM - NaCl 10 mM	A	ϕ	w	g	A	ϕ	w	g
0.00	23.71 (1.98)	0.03 (0.24)	3250.00	120.00	28.93 (1.66)	-0.33 (0.24)	3400.00	135.00
0.1 (8:1)	32.23 (3.81)	0.26 (0.38)	3250.00	120.00	42.78 (6.49)	0.00 (0.35)	3400.00	135.00
0.2 (4:1)	39.80 (4.28)	0.13 (0.55)	3250.00	120.00	37.51 (3.34)	-0.14 (0.50)	3400.00	135.00
0.33 (2.67:1)	50.44 (7.05)	0.19 (0.36)	3250.00	120.00	41.42 (5.58)	-0.17 (0.33)	3400.00	135.00
0.4 (2:1)	49.04 (6.88)	0.17 (0.36)	3250.00	120.00	40.33 (5.43)	-0.15 (0.33)	3400.00	135.00
0.67 (1.33:1)	45.07 (6.85)	0.18 (0.41)	3250.00	120.00	35.40 (5.50)	-0.14 (0.38)	3400.00	135.00
0.8 (1:1)	33.49 (5.57)	0.23 (0.38)	3250.00	120.00	26.25 (4.72)	-0.01 (0.35)	3400.00	135.00
1.6 (0.5:1)	34.09 (2.55)	0.24 (0.06)	3250.00	120.00	29.03 (2.83)	-0.02 (0.06)	3400.00	135.00

Table D.5: *SFG fitting parameters in the CH region for BSA 1 μM in NaCl 10 mM at different nanoparticle (NPs) concentrations. A is the band area, ϕ is the phase, w the IR mode frequency, and g the full width at half maximum (FWHM). Errors are reported in parentheses.*

NPs (% wt)	CH_3 ss				FR				CH aromatic				CH_2 ss				CH_3 as			
BSA 1 μM - NaCl 10 mM	A	ϕ	w	g	A	ϕ	w	g	A	ϕ	w	g	A	ϕ	w	g	A	ϕ	w	g
0.00	4.44 (0.11)	-0.09 (0.24)	2876.35	10.26	3.22 (0.24)	0.30 (0.24)	2949.27	9.95	2.89 (0.74)	-0.03 (0.24)	3055.00	25.00	3.28 (0.31)	0.02 (0.24)	2855.00	30.00	7.83 (1.03)	-1.88 (0.24)	2962.36	23.68
0.1 (8:1)	2.81 (0.18)	0.30 (0.59)	2878.43	9.83	4.12 (0.40)	0.52 (0.56)	2945.18	11.90	3.43 (0.20)	-1.25 (0.47)	3064.84	8.33	0.82 (0.13)	-0.08 (0.59)	2851.98	7.88	5.69 (0.75)	-1.07 (0.57)	2961.64	16.30
0.2 (4:1)	2.84 (0.14)	0.19 (0.74)	2878.43	9.83	5.29 (0.31)	0.46 (0.70)	2945.18	11.90	3.91 (0.16)	-1.39 (0.61)	3064.84	8.33	1.21 (0.11)	-0.15 (0.76)	2851.98	7.88	5.46 (0.57)	-1.30 (0.68)	2961.64	16.30
0.33 (2.67:1)	3.08 (0.17)	0.11 (0.58)	2878.43	9.83	5.48 (0.39)	0.44 (0.55)	2945.18	11.90	4.94 (0.15)	-1.30 (0.44)	3064.84	8.33	1.64 (0.13)	-0.08 (0.60)	2851.98	7.88	7.48 (0.89)	-1.06 (0.54)	2961.64	16.30
0.4 (2:1)	2.87 (0.19)	0.14 (0.58)	2878.43	9.83	5.00 (0.37)	0.45 (0.55)	2945.18	11.90	4.89 (0.16)	-1.33 (0.44)	3064.84	8.33	1.82 (0.13)	-0.07 (0.60)	2851.98	7.88	7.70 (0.85)	-1.12 (0.54)	2961.64	16.30
0.67 (1.33:1)	3.10 (0.19)	0.21 (0.64)	2878.43	9.83	5.36 (0.32)	0.50 (0.60)	2945.18	11.90	4.48 (0.17)	-1.33 (0.49)	3064.84	8.33	1.71 (0.13)	0.05 (0.65)	2851.98	7.88	7.14 (0.78)	-1.12 (0.59)	2961.64	16.30
0.8 (1:1)	2.49 (0.19)	0.34 (0.61)	2878.43	9.83	5.29 (0.36)	0.64 (0.59)	2945.18	11.90	3.50 (0.19)	-1.23 (0.48)	3064.84	8.33	0.93 (0.14)	-0.02 (0.61)	2851.98	7.88	4.68 (0.80)	-0.95 (0.59)	2961.64	16.30
1.6 (0.5:1)	2.32 (0.20)	0.50 (0.14)	2878.43	9.83	3.71 (0.45)	0.71 (0.14)	2945.18	11.90	3.33 (0.18)	-1.20 (0.10)	3064.84	8.33	0.74 (0.15)	0.19 (0.14)	2851.98	7.88	3.77 (0.71)	-1.00 (0.18)	2961.64	16.30

Table D.6: *SFG fitting parameters in the Amide region for BSA 1 μM in NaCl 10 mM at different nanoparticle (NPs) concentrations. A is the band area, ϕ is the phase, w the IR mode frequency, and g the full width at half maximum (FWHM). Errors are reported in parentheses.*

NPs (% wt)	$-COO^-$				CH_2 bending				Amide II				Amide I				-C=O (COOH)			
BSA 1 μM - NaCl 10 mM	A	ϕ	w	g	A	ϕ	w	g	A	ϕ	w	g	A	ϕ	w	g	A	ϕ	w	g
0.00	3.32 (0.32)	-0.01 (0.04)	1402.63	13.41	5.67 (0.52)	0.90	1450.53	29.53	6.72 (0.84)	0.98 (0.10)	1549.73	35.64	10.21 (0.48)	0.00 (0.08)	1657.98	20.44	2.33 (0.36)	-0.04 (0.09)	1730.00	23.52
0.1 (8:1)	3.82 (0.49)	0.15 (4.84)	1399.13	15.57	2.95 (0.13)	0.93	1450.53	29.53	4.76 (0.26)	0.97 (11.69)	1558.52	35.64	7.56 (0.94)	0.29 (11.97)	1650.05	22.15	2.54 (0.76)	0.27 (5.91)	1730.00	23.52
0.2 (4:1)	3.55 (0.31)	0.10 (0.06)	1399.13	15.57	3.39 (0.62)	0.93	1450.53	29.53	4.82 (0.13)	0.98 (0.11)	1558.52	35.64	6.58 (0.61)	0.23 (0.11)	1650.05	22.15	3.26 (0.39)	0.34 (0.08)	1730.00	23.52
0.33 (2.67:1)	2.91 (0.36)	0.05 (0.07)	1399.13	15.57	3.05 (0.66)	0.96	1450.53	29.53	4.49 (0.10)	1.00 (0.12)	1558.52	35.64	4.83 (0.52)	0.16 (0.12)	1650.05	22.15	4.56 (0.38)	0.34 (0.07)	1730.00	23.52
0.4 (2:1)	1.89 (0.30)	0.14 (0.07)	1399.13	15.57	3.18 (0.65)	0.89	1450.53	29.53	3.12 (0.17)	1.00 (0.15)	1558.52	35.64	3.26 (0.64)	0.43 (0.10)	1650.05	22.15	3.96 (0.51)	0.51 (0.08)	1730.00	23.52
0.67 (1.33:1)	1.28 (0.33)	0.07 (0.09)	1399.13	15.57	2.33 (0.64)	0.94	1450.53	29.53	1.74 (0.10)	1.00 (0.20)	1558.52	35.64	1.76 (0.51)	0.22 (0.11)	1650.05	22.15	3.57 (0.41)	0.47 (0.05)	1730.00	23.52
0.8 (1:1)	2.84 (0.23)	0.11 (2.98)	1399.13	15.57	2.64 (0.74)	0.97	1450.53	29.53	3.58 (0.12)	0.99 (7.17)	1558.52	35.64	5.24 (0.40)	0.21 (7.33)	1650.05	22.15	3.56 (0.66)	0.30 (3.63)	1730.00	23.52
1.6 (0.5:1)	3.52 (0.25)	0.11 (2.64)	1399.13	15.57	3.53 (0.86)	0.96	1450.53	29.53	4.55 (0.13)	0.96 (6.60)	1558.52	35.64	6.82 (0.49)	0.26 (6.73)	1650.05	22.15	2.30 (0.40)	0.31 (3.28)	1730.00	23.52

Table D.7: *SFG fitting parameters in the water OH region for BSA 1 μM and BSA 1 μM - NPs 0.8 $\%_{wt}$ at different ionic strength in NaCl. A is the band area, ϕ is the phase, w the IR mode frequency, and g the full width at half maximum (FWHM). Errors are reported in parentheses.*

Sample	OH 3250 cm^{-1}				OH 3400 cm^{-1}			
	A	ϕ	w	g	A	ϕ	w	g
BSA 1 μM - NaCl 1 mM	38.3052 (2.8862)	0.28081 (0.44151)	3250	120	38.7384 (4.2073)	-0.03031 (0.40251)	3400	135
BSA 1 μM - NaCl 5 mM	28.1717 (1.8356)	0.22221 (0.60416)	3250	120	37.5888 (1.9008)	-0.33822 (0.56547)	3400	135
BSA 1 μM - NaCl 10 mM	23.7148 (1.9814)	0.02569 (0.02432)	3250	120	28.9309 (1.6569)	-0.32837 (0.24317)	3400	135
BSA 1 μM - NaCl 50 mM	16.6773 (2.6824)	0.47869 (0.11993)	3250	120	27.8882 (1.9367)	0.20000 (0.19531)	3400	135
BSA 1 μM - NaCl 1 mM - NPs 0.8% wt	38.2192 (5.3722)	0.29550 (0.26460)	3250	120	29.2213 (4.4302)	-0.00645 (0.24189)	3400	135
BSA 1 μM - NaCl 5 mM - NPs 0.8% wt	34.6369 (4.4266)	0.58415 (0.11292)	3250	120	21.6485 (3.6569)	0.20000 (0.09806)	3400	135
BSA 1 μM - NaCl 10 mM - NPs 0.8% wt	32.5765 (3.7756)	0.39141 (0.48759)	3250	120	30.9245 (4.1531)	0.11706 (0.43870)	3400	135
BSA 1 μM - NaCl 50 mM - NPs 0.8% wt	31.6142 (3.9269)	0.38569 (0.09355)	3250	120	32.0012 (4.4822)	0.06049 (0.08732)	3400	135

Table D.8: *SFG fitting parameters in the CH region for BSA 1 μM and BSA 1 μM - NPs 0.8 $\%_{wt}$ at different ionic strength in NaCl. A is the band area, ϕ is the phase, w the IR mode frequency, and g the full width at half maximum (FWHM). Errors are reported in parentheses.*

Sample	CH_3 ss				FR				CH aromatic				CH_2 ss				CH_3 as			
	A	ϕ	w	g	A	ϕ	w	g	A	ϕ	w	g	A	ϕ	w	g	A	ϕ	w	g
BSA 1 μM - NaCl 1 mM	4.0631 (0.1870)	0.0383 (0.6093)	2882	12.27	2.3744 (0.1420)	-0.0268 (0.5754)	2948.0	9.31	0.3758 (0.1963)	1.0000 (0.5200)	3065.1	6.27	0.9286 (0.1233)	-0.5950 (0.6390)	2847.9	8.75	7.1648 (0.3612)	-2.0000 (0.5569)	2960.0	20.00
BSA 1 μM - NaCl 5 mM	4.6606 (0.1221)	-0.2447 (0.7100)	2876.5	10.48	2.6208 (0.1215)	-0.0170 (0.6991)	2947.9	9.00	2.1333 (1.4434)	0.4293 (0.6285)	3055	10.00	0.9961 (0.2357)	-0.1036 (0.7114)	2855	20.00	5.9338 (0.3899)	-2.0000 (0.6884)	2964.6	20.00
BSA 1 μM - NaCl 10 mM	4.4372 (0.1057)	-0.0941 (0.0243)	2876.4	10.26	3.2193 (0.2381)	0.2981 (0.0243)	2949.3	9.95	2.8874 (0.7439)	-0.0338 (0.0243)	3055	25.00	3.2759 (0.3144)	0.0164 (0.0243)	2855	30.00	7.8258 (1.0321)	-1.8781 (0.0243)	2962.4	23.68
BSA 1 μM - NaCl 50 mM	3.4618 (0.1062)	0.2041 (0.0878)	2872.6	9.10	7.0798 (0.2614)	0.5897 (0.1003)	2945.3	14.29	2.4542 (0.5888)	0.3446 (0.1166)	3055.5	25.00	4.4795 (0.3788)	0.4312 (0.0841)	2865	30.00	1.3107 (0.1914)	0.4827 (0.1136)	2963.3	10.30
BSA 1 μM - NaCl 1 mM – NPs 0.8% wt	1.6797 (0.1600)	0.1071 (0.4256)	2880.9	8.66	4.7140 (0.1801)	-0.0597 (0.3945)	2941.6	10.99	4.1444 (0.1395)	-1.1877 (0.3362)	3064.8	8.33	1.3035 (0.2066)	-0.3590 (0.4351)	2848.7	10.55	10.649 (0.3661)	-1.0756 (0.3872)	2977.5	18.86
BSA 1 μM - NaCl 5 mM - NPs 0.8% wt	1.7165 (0.1125)	0.2709 (0.2737)	2882.0	8.46	5.9497 (0.1678)	0.2059 (0.2443)	2943.5	12.79	4.0067 (0.1194)	-0.9128 (0.1869)	3064.8	8.33	2.2629 (0.1783)	-0.0889 (0.2841)	2851.5	13.58	11.966 (0.3822)	-0.7985 (0.2366)	2977.1	19.15
BSA 1 μM - NaCl 10 mM - NPs 0.8% wt	2.2196 (0.1646)	0.2881 (0.6928)	2881.4	10.13	4.8647 (0.1799)	0.0889 (0.6612)	2941.5	12.03	4.9850 (0.2097)	-1.1447 (0.5880)	3057.8	11.46	1.6421 (0.1803)	-0.3641 (0.7132)	2846.8	11.50	10.567 (0.5322)	-0.9796 (0.6496)	2976.6	20.94
BSA 1 μM - NaCl 50 mM - NPs 0.8% wt	3.0771 (0.1853)	0.4309 (0.1660)	2881.2	11.55	7.3462 (0.3561)	0.3633 (0.1566)	2943.3	14.66	4.3921 (0.2258)	-1.1216 (0.1622)	3057.8	11.46	1.9906 (0.1411)	0.0885 (0.1685)	2851.6	11.34	9.5508 (1.0932)	-0.8363 (0.1963)	2973.1	20.19

Table D.9: *SFG fitting parameters in the Amide region for BSA 1 μM and BSA 1 μM - NPs 0.8 $\%_{wt}$ at different ionic strength in NaCl. A is the band area, ϕ is the phase, w the IR mode frequency, and g the full width at half maximum (FWHM). Errors are reported in parentheses.*

Sample	$-COO^-$				CH_2 bending				Amide II				Amide I				–C=O (COOH)			
	A	ϕ	w	g	A	ϕ	w	g	A	ϕ	w	g	A	ϕ	w	g	A	ϕ	w	g
BSA 1 μM – NaCl 1 mM	2.5505 (0.31679)	0.07186 (0.05567)	1402.6264	13.4056	4.6763 (0.66848)	0.9137	1450.5277	29.5282	5.282 (0.71724)	0.96646 (0.12471)	1549.732	35.6422	8.1594 (0.50675)	0.12137 (0.09193)	1657.9836	20.4372	3.5395 (0.42998)	-0.00673 (0.08465)	1730	23.5161
BSA 1 μM – NaCl 5 mM	3.0823 (0.31929)	0.05848 (0.0477)	1402.6264	13.4056	5.1215 (0.66134)	0.91534	1450.5277	29.5282	6.6582 (0.69745)	0.97312 (0.09187)	1549.732	35.6422	8.2064 (0.45843)	0.20422 (0.08377)	1657.9836	20.4372	2.013 (0.47379)	0.15513 (0.12507)	1730	23.5161
BSA 1 μM – NaCl 10 mM	3.3227 (0.32120)	-0.01103 (0.04039)	1402.6264	13.4056	5.6652 (0.51612)	0.89706	1450.5277	29.5282	6.7182 (0.83672)	0.98228 (0.09779)	1549.732	35.6422	10.2101 (0.4848)	-0.00388 (0.07557)	1657.9836	20.4372	2.3347 (0.35721)	-0.03982 (0.08851)	1730	23.5161
BSA 1 μM – NaCl 50 mM	3.4482 (0.34295)	0.03705 (0.0448)	1402.6264	13.4056	5.6995 (0.58226)	0.9029	1450.5277	29.5282	7.1306 (1.2164)	1.0000 (0.11609)	1549.732	35.6422	10.8165 (0.64935)	-0.0463 (0.09777)	1657.9836	20.4372	1.989 (0.43897)	-0.10237 (0.12132)	1730	23.5161
BSA 1 μM – NaCl 1 mM – NPs 0.8% wt	0.76272 (0.2939)	-0.05202 (0.10583)	1399.1264	15.5656	1.7353 (0.48187)	1.0000	1450.5277	29.5282	1.2385 (0.91154)	0.9313 (0.24665)	1558.5249	35.6422	4.9357 (0.43048)	-0.38529 (0.07934)	1650.0473	22.1545	2.8956 (0.3008)	0.09839 (0.04127)	1730	23.8581
BSA 1 μM – NaCl 5 mM – NPs 0.8% wt	1.0674 (0.2731)	0.01225 (0.07607)	1399.1264	15.5656	2.0952 (0.46517)	0.96961	1450.5277	29.5282	1.8429 (1.1562)	1.0000 (0.22828)	1558.5249	35.6422	4.4657 (0.58505)	-0.34518 (0.13251)	1650.0473	22.1545	3.2619 (0.28851)	0.09195 (0.05384)	1730	23.8581
BSA 1 μM – NaCl 10 mM – NPs 0.8% wt	2.8445 (0.22852)	0.10991 (2.9849)	1399.1264	15.5656	2.6446 (0.7444)	0.96895	1450.5277	29.5282	3.5769 (0.12099)	0.98743 (7.1696)	1558.5249	35.6422	5.2364 (0.39676)	0.20557 (7.3314)	1650.0473	22.1545	3.5564 (0.65632)	0.30047 (3.6265)	1730	23.5161
BSA 1 μM – NaCl 50 mM – NPs 0.8% wt	3.1848 (0.68495)	-0.00519 (8.4748)	1399.1264	15.5656	3.0755 (0.22611)	0.88284	1450.5277	29.5282	4.209 (0.32779)	0.88352 (22.9905)	1558.5249	35.6422	6.3018 (0.18457)	0.19476 (24.5621)	1650.0473	22.1545	1.7978 (0.11303)	0.12728 (11.5065)	1730	23.8581

Table D.10: *SFG fitting parameters in the water OH region for BCN 1 μM in NaCl 10 mM at different nanoparticle (NPs) concentrations. A is the band area, ϕ is the phase, w the IR mode frequency, and g full width at half maximum (FWHM). Errors are reported in parentheses.*

NPs (% wt)	OH 3250 cm^{-1}				OH 3400 cm^{-1}			
BCN 1 μM - NaCl 10 mM	A	ϕ	w	g	A	ϕ	w	g
0.00	29.0669 (0.4163)	0.29906	3250	110.06	17.2439 (0.5918)	0.02749	3400	91.81
0.1 (8:1)	37.8417 (0.5133)	0.29906	3250	110.06	18.6837 (0.6464)	0.02749	3400	91.81
0.2 (4:1)	40.9066 (0.4933)	0.29906	3250	110.06	22.3758 (0.6176)	0.02749	3400	91.81
0.33 (2.67:1)	42.7961 (0.4625)	0.29906	3250	110.06	21.3878 (0.5879)	0.02749	3400	91.81
0.4 (2:1)	43.0273 (0.4815)	0.29906	3250	110.06	21.4663 (0.6152)	0.02749	3400	91.81
0.67 (1.33:1)	42.2013 (0.4449)	0.29906	3250	110.06	20.8133 (0.5602)	0.02749	3400	91.81
0.8 (1:1)	42.2284 (0.4546)	0.29906	3250	110.06	20.8243 (0.5485)	0.02749	3400	91.81
1.6 (0.5:1)	38.8278 (0.5322)	0.29906	3250	110.06	19.8636 (0.6601)	0.02749	3400	91.81

Table D.11: *SFG fitting parameters in the CH region for BCN 1 μM in NaCl 10 mM at different nanoparticle (NPs) concentrations. A is the band area, ϕ is the phase, w the IR mode frequency, and g the full width at half maximum (FWHM). Errors are reported in parentheses.*

NPs (% wt)	CH_3 ss				FR				CH aromatic				CH_2 ss				CH_3 as			
BCN 1 μM - NaCl 10 mM	A	ϕ	w	g	A	ϕ	w	g	A	ϕ	w	g	A	ϕ	w	g	A	ϕ	w	g
0.00	4.1667 (0.1157)	0.1549 (0.0192)	2876.0	11.998	4.7496 (0.0897)	0.0086 (0.0196)	2940.4	10.77	0.6865 (0.2099)	0.5748 (0.0994)	3042.8	11.35	1.6515 (0.1552)	-0.2843 (0.0382)	2849.7	15.00	3.8293 (0.2250)	0.5294 (0.0224)	2972.5	18.83
0.1 (8:1)	2.7129 (0.1436)	0.1391 (0.0269)	2876.6	11.000	5.4980 (0.1231)	-0.1405 (0.0163)	2937.5	11.80	0.6058 (0.1908)	0.0491 (0.1126)	3030.0	14.80	1.2063 (0.1678)	-0.5416 (0.0532)	2843.0	10.00	3.4227 (0.2409)	0.4599 (0.0215)	2972.5	18.83
0.2 (4:1)	2.9227 (0.1141)	-0.1056 (0.0264)	2876.6	11.000	5.0398 (0.1256)	-0.2565 (0.0162)	2937.5	11.80	0.7103 (0.1665)	0.1358 (0.0819)	3030.0	14.80	1.7147 (0.1948)	-0.6364 (0.0496)	2843.0	10.00	3.5673 (0.2354)	0.4917 (0.0185)	2972.5	18.83
0.33 (2.67:1)	3.0580 (0.1121)	-0.1170 (0.0236)	2876.6	11.000	5.2098 (0.1234)	-0.2989 (0.0144)	2937.5	11.80	0.7097 (0.1597)	0.0413 (0.0797)	3030.0	14.80	1.7026 (0.1800)	-0.6652 (0.0442)	2843.0	10.00	4.0215 (0.2267)	0.4670 (0.0159)	2972.5	18.83
0.4 (2:1)	2.9402 (0.1116)	-0.1864 (0.0275)	2876.6	11.000	5.6528 (0.1236)	-0.3553 (0.0151)	2937.5	11.80	0.5399 (0.1612)	0.0294 (0.1047)	3030.0	14.80	1.7809 (0.1768)	-0.6352 (0.0485)	2843.0	10.00	4.3068 (0.2088)	0.4393 (0.0143)	2972.5	18.83
0.67 (1.33:1)	2.9086 (0.1080)	-0.1011 (0.0227)	2876.6	11.000	5.1882 (0.1153)	-0.2763 (0.0137)	2937.5	11.80	0.6680 (0.1526)	0.0344 (0.0808)	3030.0	14.80	1.5193 (0.1591)	-0.5910 (0.0440)	2843.0	10.00	3.8815 (0.2108)	0.4577 (0.0156)	2972.5	18.83
0.8 (1:1)	2.4701 (0.1123)	-0.0498 (0.0258)	2876.6	11.000	4.7925 (0.1142)	-0.2259 (0.0143)	2937.5	11.80	0.5307 (0.1514)	0.0764 (0.0999)	3030.0	14.80	1.5171 (0.1712)	-0.5931 (0.0466)	2843.0	10.00	3.1514 (0.2106)	0.4559 (0.0191)	2972.5	18.83
1.6 (0.5:1)	2.5627 (0.1300)	-0.1572 (0.0364)	2876.6	11.000	4.8769 (0.1426)	-0.3414 (0.0187)	2937.5	11.80	0.5692 (0.1721)	0.0173 (0.1058)	3030.0	14.80	1.5130 (0.2507)	-0.7016 (0.0717)	2843.0	10.00	3.6329 (0.2391)	0.4466 (0.0187)	2972.5	18.83

Table D.12: *SFG fitting parameters in the Amide region for BCN 1 μM in NaCl 10 mM at different nanoparticle (NPs) concentrations. A is the band area, ϕ is the phase, w the IR mode frequency, and g the full width at half maximum (FWHM). Errors are reported in parentheses.*

NPs (% wt)	$-COO^-$				CH_2 bending				Amide II				Amide I				-C=O (COOH)			
BCN 1 μM - NaCl 10 mM	A	ϕ	w	g	A	ϕ	w	g	A	ϕ	w	g	A	ϕ	w	g	A	ϕ	w	g
0.00	2.0664 (0.1451)	-0.0742 (0.0207)	1391.3	18.92	0.5355 (0.0964)	0.9946	1457.5	12.38	8.576 (0.6409)	0.9627 (0.0268)	1547.6	79.99	6.964 (0.3193)	0.4580 (0.0163)	1657.6	31.87	2.4994 (0.2334)	0.0266 (0.0347)	1712.2	25.46
0.1 (8:1)	0.8643 (0.1310)	-0.0230 (0.0487)	1391.3	18.92	0.5390 (0.1026)	1.0000	1457.5	12.38	3.146 (0.6292)	0.8868 (0.0682)	1547.6	79.99	2.713 (0.3117)	0.2746 (0.0383)	1657.6	31.87	2.1264 (0.2178)	0.0331 (0.0333)	1712.2	25.46
0.2 (4:1)	1.9754 (0.1395)	-0.0250 (0.0230)	1391.3	18.92	0.5040 (0.0985)	1.0000	1457.5	12.38	3.376 (0.6512)	0.8749 (0.0676)	1547.6	79.99	3.047 (0.3155)	0.3352 (0.0346)	1657.6	31.87	2.3828 (0.2165)	0.0668 (0.0306)	1712.2	25.46
0.33 (2.67:1)	1.4376 (0.1736)	-0.0910 (0.0358)	1391.3	18.92	0.4882 (0.1206)	1.0000	1457.5	12.38	2.771 (0.8117)	0.7236 (0.0826)	1547.6	79.99	3.089 (0.3520)	0.2419 (0.0386)	1657.6	31.87	3.2183 (0.2349)	-0.0090 (0.0249)	1712.2	25.46
0.4 (2:1)	1.6005 (0.5177)	-0.2558 (0.1043)	1391.3	18.92	0.2135 (0.1772)	0.9468	1457.5	12.38	3.066 (1.1691)	0.6307 (0.1202)	1547.6	79.99	4.236 (0.4426)	0.3112 (0.0422)	1657.6	31.87	3.9382 (0.2990)	-0.0043 (0.0324)	1712.2	25.46
0.67 (1.33:1)	1.4050 (0.2294)	-0.0983 (0.0493)	1391.3	18.92	0.1711 (0.1451)	1.0000	1457.5	12.38	1.428 (0.8351)	0.2601 (0.1943)	1547.6	79.99	2.518 (0.3767)	0.0973 (0.0535)	1657.6	31.87	2.3544 (0.2535)	-0.1277 (0.0377)	1712.2	25.46
0.8 (1:1)	1.9838 (0.6599)	-0.2529 (0.1025)	1391.3	18.92	0.3095 (0.1690)	1.0000	1457.5	12.38	3.141 (1.1876)	0.5845 (0.1034)	1547.6	79.99	3.431 (0.4581)	0.1867 (0.0497)	1657.6	31.87	2.5676 (0.2989)	-0.0619 (0.0436)	1712.2	25.46
1.6 (0.5:1)	1.2682 (0.2347)	-0.1058 (0.0542)	1391.3	18.92	0.1497 (0.1445)	1.0000	1457.5	12.38	0.7754 (0.7708)	0.1725 (0.3889)	1547.6	79.99	2.007 (0.3844)	0.0595 (0.0695)	1657.6	31.87	1.8864 (0.2570)	-0.1228 (0.0472)	1712.2	25.46

Table D.13: *SFG fitting parameters in the water OH region for BLG 1 μM in NaCl 10 mM at different nanoparticle (NPs) concentrations. A is the band area, ϕ is the phase, w the IR mode frequency, and g full width at half maximum (FWHM). Errors are reported in parentheses.*

NPs (% wt)	OH 3250 cm^{-1}				OH 3400 cm^{-1}			
BLG 1 μM - NaCl 10 mM	A	ϕ	w	g	A	ϕ	w	g
0.00	40.2437 (1.2432)	0.34127	3250	110.0612	18.5618 (0.78863)	0.02519	3400	84.9579
0.1 (8:1)	34.5666 (0.97627)	0.34127	3250	110.0612	16.9184 (0.62902)	0.01301 (0.00593)	3400	84.9579
0.2 (4:1)	29.7361 (1.3399)	0.34127	3250	110.0612	15.3022 (0.87732)	0.03103 (0.00907)	3400	84.9579
0.33 (2.67:1)	32.5647 (0.99814)	0.34127	3250	110.0612	15.6166 (0.64238)	0.01590 (0.00666)	3400	84.9579
0.4 (2:1)	32.8515 (1.0423)	0.34127	3250	110.0612	16.0304 (0.66630)	0.01516 (0.00659)	3400	84.9579
0.67 (1.33:1)	32.7991 (1.1184)	0.34127	3250	110.0612	15.7138 (0.70967)	0.01295 (0.00724)	3400	84.9579
0.8 (1:1)	31.7765 (0.99485)	0.34127	3250	110.0612	16.1599 (0.64948)	0.00530 (0.00625)	3400	84.9579
1.6 (0.5:1)	30.4044 (1.1191)	0.34127	3250	110.0612	14.8495 (0.72034)	0.01095 (0.00751)	3400	84.9579

Table D.14: *SFG fitting parameters in the CH region for BLG 1 μM in NaCl 10 mM at different nanoparticle (NPs) concentrations. A is the band area, ϕ is the phase, w the IR mode frequency, and g the full width at half maximum (FWHM). Errors are reported in parentheses.*

NPs (% wt)	CH_3 ss				FR				CH aromatic				CH_2 ss				CH_3 as			
BLG 1 μM - NaCl 10 mM	A	ϕ	w	g	A	ϕ	w	g	A	ϕ	w	g	A	ϕ	w	g	A	ϕ	w	g
0.00	2.6562 (0.1379)	-0.2688 (0.0603)	2876.1	9.919	10.3212 (0.2013)	-0.2688 (0.0337)	2939.7	17.15	2.4307 (0.9123)	0.2394	3030.7	20.00	6.4282 (0.4016)	-0.4223 (0.0898)	2852.8	22.41	9.8736 (1.1996)	0.9864 (0.0213)	3001.1	37.11
0.1 (8:1)	1.4859 (0.1042)	0.0275 (0.0467)	2876.1	7.919	9.4928 (0.1662)	-0.0778 (0.0270)	2939.7	18.80	0.8102 (0.1749)	0.9642 (0.0696)	3048.0	14.48	6.9595 (0.7049)	-0.3032 (0.0722)	2852.8	28.21	5.9641 (0.5600)	1.333 (0.0359)	3001.1	37.11
0.2 (4:1)	1.8384 (0.1487)	0.1565 (0.0557)	2876.1	7.919	9.3640 (0.2341)	-0.0631 (0.0329)	2939.7	18.80	1.0690 (0.2574)	0.8589 (0.0805)	3048.0	14.48	6.1753 (1.4495)	-0.2720 (0.0846)	2852.8	28.21	6.1632 (0.7305)	1.248 (0.0451)	3001.1	37.11
0.33 (2.67:1)	1.5436 (0.1016)	0.0604 (0.0470)	2876.1	7.919	9.0608 (0.1659)	-0.0518 (0.0282)	2939.7	18.80	0.9293 (0.1812)	0.8981 (0.0635)	3048.0	14.48	7.0597 (0.7087)	-0.2983 (0.0710)	2852.8	28.21	6.2622 (0.5802)	1.343 (0.0362)	3001.1	37.11
0.4 (2:1)	1.4468 (0.1015)	-0.0421 (0.0531)	2876.1	7.919	8.9915 (0.1756)	-0.0741 (0.0308)	2939.7	18.80	0.9760 (0.1828)	0.8428 (0.0621)	3048.0	14.48	7.7715 (0.7396)	-0.2920 (0.0786)	2852.8	28.21	6.9495 (0.6132)	1.323 (0.0363)	3001.1	37.11
0.67 (1.33:1)	1.7539 (0.1053)	-0.0253 (0.0547)	2876.1	7.919	9.2407 (0.1895)	-0.0890 (0.0324)	2939.7	18.80	0.9117 (0.2011)	0.8821 (0.0724)	3048.0	14.48	8.0000 (0.7882)	-0.2793 (0.0803)	2852.8	28.21	6.3976 (0.6433)	1.284 (0.0395)	3001.1	37.11
0.8 (1:1)	1.5917 (0.1005)	0.1079 (0.0383)	2876.1	7.919	9.2717 (0.1658)	-0.0175 (0.0230)	2939.7	18.80	1.0842 (0.1872)	0.9420 (0.0564)	3048.0	14.48	7.2177 (0.5654)	-0.2295 (0.0485)	2852.8	28.21	5.8563 (0.5405)	1.360 (0.0337)	3001.1	37.11
1.6 (0.5:1)	1.8272 (0.1130)	0.1451 (0.0356)	2876.1	7.919	9.5566 (0.1943)	-0.0222 (0.0196)	2939.7	18.80	1.1443 (0.2102)	0.9066 (0.0615)	3048.0	14.48	6.4655 (0.4852)	-0.1233 (0.0382)	2852.8	28.21	6.9557 (0.5572)	1.294 (0.0304)	3001.1	37.11

Table D.15: *SFG fitting parameters in the Amide region for BLG 1 μM in NaCl 10 mM at different nanoparticle (NPs) concentrations. A is the band area, ϕ is the phase, w the IR mode frequency, and g the full width at half maximum (FWHM). Errors are reported in parentheses.*

NPs (% wt)	$-COO^-$				CH_2 bending				Amide II				Amide I				-C=O (COOH)			
BLG 1 μM - NaCl 10 mM	A	ϕ	w	g	A	ϕ	w	g	A	ϕ	w	g	A	ϕ	w	g	A	ϕ	w	g
0.00	3.776 (0.141)	-0.059 (0.012)	1391.5	16.09	2.540 (0.152)	1	1458.2	18.64	11.385 (0.910)	0.767 (0.023)	1550.0	80.00	8.439 (0.406)	0.258 (0.018)	1650.5	29.69	3.669 (0.316)	-0.447 (0.029)	1692.5	23.82
0.1 (8:1)	5.343 (0.174)	-0.059 (0.014)	1391.5	16.09	2.642 (0.166)	1	1458.2	18.64	11.152 (0.993)	0.804 (0.028)	1550.0	80.00	10.167 (0.440)	0.216 (0.016)	1650.5	29.69	3.379 (0.313)	-0.561 (0.029)	1692.5	23.82
0.2 (4:1)	4.664 (0.136)	-0.039 (0.012)	1391.5	16.09	2.380 (0.145)	1	1458.2	18.64	11.074 (0.856)	0.778 (0.025)	1550.0	80.00	9.222 (0.376)	0.253 (0.015)	1650.5	29.69	3.425 (0.274)	-0.453 (0.028)	1692.5	23.82
0.33 (2.67:1)	4.777 (0.199)	-0.089 (0.019)	1391.5	16.09	2.563 (0.171)	1	1458.2	18.64	12.017 (1.087)	0.802 (0.028)	1550.0	80.00	9.726 (0.470)	0.257 (0.019)	1650.5	29.69	2.951 (0.321)	-0.497 (0.037)	1692.5	23.82
0.4 (2:1)	4.590 (0.193)	-0.095 (0.022)	1391.5	16.09	2.196 (0.167)	0.96	1458.2	18.64	12.149 (1.116)	0.735 (0.029)	1550.0	80.00	9.709 (0.478)	0.250 (0.020)	1650.5	29.69	2.920 (0.342)	-0.431 (0.032)	1692.5	23.82
0.67 (1.33:1)	3.408 (0.141)	-0.049 (0.014)	1391.5	16.09	2.259 (0.156)	1	1458.2	18.64	9.478 (0.909)	0.785 (0.029)	1550.0	80.00	7.463 (0.412)	0.245 (0.020)	1650.5	29.69	2.815 (0.287)	-0.385 (0.037)	1692.5	23.82
0.8 (1:1)	3.321 (0.156)	-0.072 (0.016)	1391.5	16.09	1.918 (0.160)	1	1458.2	18.64	9.174 (0.952)	0.757 (0.030)	1550.0	80.00	7.224 (0.431)	0.224 (0.022)	1650.5	29.69	3.082 (0.310)	-0.411 (0.035)	1692.5	23.82
1.6 (0.5:1)	3.178 (0.260)	-0.092 (0.043)	1391.5	16.09	1.961 (0.208)	0.98	1458.2	18.64	8.830 (1.553)	0.791 (0.047)	1550.0	80.00	7.772 (0.653)	0.296 (0.038)	1650.5	29.69	2.392 (0.419)	-0.409 (0.069)	1692.5	23.82

This page intentionally left blank.

Experimental techniques

This page intentionally left blank.

G

Grazing Incidence Small Angle X-ray Scattering (GISAXS)

Grazing Incidence Small Angle X-ray Scattering (GISAXS) is a powerful and nondestructive technique widely used to characterize micro- and nano-scale density correlation and shape analysis of objects in thin films, surfaces, and buried interfaces for various classes of materials spanning from ceramics (Moritz et al., 1999), metals (Metwalli et al., 2013), semiconductors (Buljan et al., 2003) to soft-matter such as polymers (Li Destri et al., 2015), proteins (Steinhauer et al., 2014) and nanoparticles (Tomasella et al., 2025). As a result, GISAXS provides an excellent complementarity to more conventional techniques such as Atomic Force Microscopy (AFM) and Electron Microscopy (EM). Although both of them operate in real space, GISAXS gives information in reciprocal space.

In contrast to Small Angle X-ray Scattering (SAXS) which operates in transmission geometry, GISAXS experiments are performed in reflection geometry. Thus, it combines the sensitivity to nanometer scale inhomogeneities offered by SAXS with the surface sensitivity of Grazing Incidence X-ray Diffraction (GIXD) (Müller-Buschbaum, 2009). Today, the key feature that makes GISAXS an excellent technique for studying surfaces is the possibility to access:

- **structural information with sub-nm spatial resolution** of objects with dimension from ~ 1 nm to hundreds of nm, or in Grazing Incidence Ultra Small Angle X-ray Scattering (GIUSAXS) of objects in the μm scales (Hu et al., 2009);
- **averaged statistical structural information of the illuminated sample area**, which can span to some square centimeters in the most common configuration to square micrometers in the so-called μ-GISAXS where the beam size in the order of some μm enabling also for imaging (Müller-Buschbaum et al., 2007);
- **buried structure located well below the surface** and thus inaccessible to other techniques as AFM;
- **depth-dependent structural information**, by scanning the X-ray beam incidence

angle (Saito et al., 2015);

- **real-time information** enabling the investigation of kinetics and dynamic process (Jankowski et al., 2023; Hemmerle et al., 2024);
- **different environments** enabling for the study of solid-gas, solid-liquid, liquid-gas and liquid-liquid interfaces (Jankowski et al., 2023; Hemmerle et al., 2024);
- **structural information in non-invasive and non-destructive way**.

G.1 The GISAXS geometry

The GISAXS technique is based on elastic X-ray scattering, where the incoming beam interacts with fluctuations in the electron density of the sample. In the region of angles probed by the GISAXS, the influence of the periodic crystal structure of the sample component can be neglected, so the description based on the mean refractive index can be used. The X-Ray refractive index n_j of the component j can be expressed as follows:

$$n_j = 1 - \delta_j + i\beta_j \tag{G.1}$$

where δ_j represents the dispersive term

$$\delta_j(q,\lambda) = \frac{e^2\lambda^2}{8\pi^2 m_e c^2 \epsilon_0}\rho_j \sum \frac{f_k^0(q,\lambda) + f_k'(\lambda)}{M_k} \tag{G.2}$$

and β the absorption contribution.

$$\beta_j(\lambda) = \frac{e^2\lambda^2}{8\pi^2 m_e c^2 \epsilon_0}\rho_j \sum \frac{f_k''(\lambda)}{M_k} \tag{G.3}$$

where λ is the X-ray wavelength, c is the speed of light, e is the elementary charge, m_e is the electron rest mass, ϵ_0 is the vacuum permittivity, ρ_j is the mass density of the component j, M_k are the atomic weight of the atoms in component j and $f_k'(\lambda)$ and $f_k''(\lambda)$ are the dispersion correction. $f_k^0(q,\lambda)$ can be approximated by the number of electrons Z_k of the atom k and the summation is performed over all atoms k that form the component j (Lindner et al., 2024).

As a result, the X-ray refractive index for vacuum or air is generally considered to be equal 1 ($\rho_{vacuum} = 0$ and $\rho_{air} \approx 0$), while any other samples with higher electron density have a refractive index < 1. In this perspective, for any interface between two phases 1 and 2, such that $\rho_1 < \rho_2$ and thus $n_1 > n_2$, it is possible to define an incidence angle at which total external reflection occurs. This angle, usually known as the critical angle (α_c) is material-dependent and can be approximately calculated as follows:

$$\alpha_c \approx \sqrt{2\delta_2} \tag{G.4}$$

where α_c is the angle defined by the incidence beam and the xy plane (Figure G.1) and δ_2 is the absorption coefficient defined in Equation G.2 of phase 2. When the X-ray

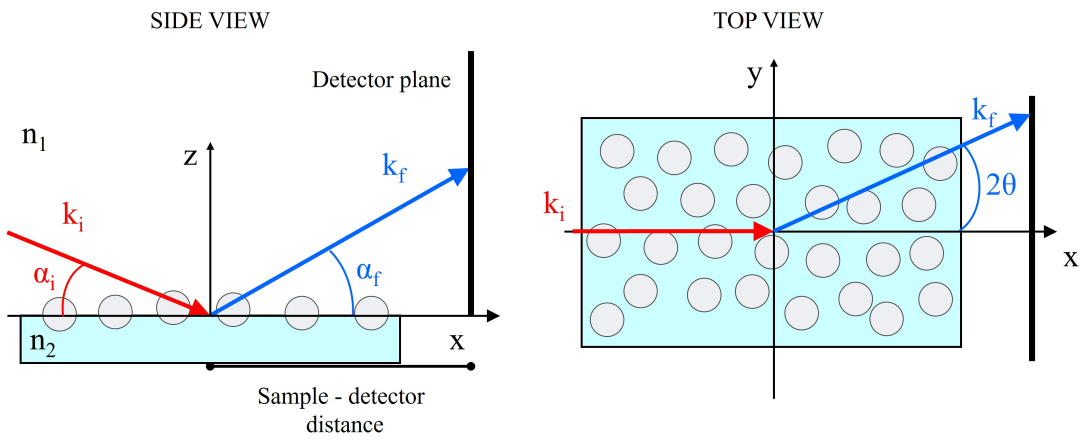

Figure G.1: *Sketch of the GISAXS configuration geometry: incident X-ray beam of wavevector k_i, is scattered with a wavevector k_f from the interface between phase 1 with n_1 and phase 2 with n_2. α_i is the incidence angle of the X-ray beam with respect to the xy, α_f is the angle of the scattered beam with respect to the xy plane and 2Θ is the angle of the scattered beam with respect to the xz plane.*

beam coming from the less dense phase 1 impinges on the interface 1-2 at an incident angle α_i close to or smaller than α_c, the beam generates an evanescent wave that penetrates only a few nanometers into the more dense phase 2. This allows GISAXS to give information coming from the objects at the interface, avoiding the scattering from the bulk phase, and thus to be highly surface-sensitive. Moreover, for a typical X-ray wavelength of around 0.1 nm, critical angles are in the range of 0.2°-1°, thus in grazing incidence geometry (Renaud et al., 2009).

The magnitude of the incidence wavevector for a monochromatic X-ray beam of wavelength λ is defined as $|k_i| = 2\pi/\lambda$. As GISAXS is an elastic scattering technique in which the scattering event causes a change in the direction of the scattered photon with respect to the direction of the incidence, by keeping its energy, and thus its wavelength, unaltered, a useful quantity to describe this process is the scattering vector. The scattering vector $\vec{q} = \vec{k}_f - \vec{k}_i$ is the vector difference between the incidence and scattered wavevector. In a tridimensional (3D) space, the scattering vector can be expressed in terms of its components along the laboratory coordinate system, as sketched in Figure G.1:

$$q_x = \frac{2\pi}{\lambda}\left[\cos(\alpha_f)\cos(2\theta) - \cos(\alpha_i)\right] \tag{G.5}$$

$$q_y = \frac{2\pi}{\lambda}\cos(\alpha_f)\sin(2\theta) \tag{G.6}$$

$$q_z = \frac{2\pi}{\lambda}\left[\sin(\alpha_f) + \sin(\alpha_i)\right] \tag{G.7}$$

For a sample that is isotropic in the xy plane, as can be for a nanoparticle monolayer adsorbed at the fluid interface, the in-plane structure is related to the $q_{xy} = q_y$ component, while the out-of-plane structure is related to the q_z (Renaud et al., 2009).

G.2 Form Factor and Structure Factor in the DWBA Theory

To quantitatively describe the scattering intensity obtained from standard SAXS experiments, it is necessary to model the interaction between the incident beam and the scattering objects within the sample. A commonly used theoretical framework is the Born Approximation (BA) (J. Li et al., 2010). The BA theory is applicable when:

- The incident beam is not significantly perturbed during its propagation through the sample (diluted sample);
- The scattered wave can be directly calculated from the incident wave, neglecting the effects of reflection, refraction, or multiple scattering within the medium.

In the BA, the intensity of the scattered beam as a function of the scattering vector can be described as:

$$I(\vec{q}) = N \cdot (\Delta\rho)^2 \cdot |F(\vec{q})|^2 \cdot S(\vec{q}) \tag{G.8}$$

where N is the number density of the scattered objects; $\Delta\rho = \rho_i - \rho_{mediuem}$ is the difference in the electron density of the scattering object i^{th} and the medium and is usually known as the scattering contrast; $F(\vec{q})$ is the form factor which describes the spatial distribution of the electron density within a single scattering object; $S(\vec{q})$ is the structure factor which describes the spatial correlations between multiple scattering objects (Renaud et al., 2009).

The form factor encodes information about the shape, size, and orientation of individual scattering objects (e.g., particles, domains, or pores) in the probed region. It is defined as the Fourier transform of the electron density contrast $\Delta\rho(\vec{r})$ within a single object:

$$F(\vec{q}) = \int_V \Delta\rho(\vec{r}) e^{i\vec{q}\cdot\vec{r}} d\vec{r} \tag{G.9}$$

where the integral extends over the volume V of the object.

The structure factor accounts for the relative spatial arrangement of the scattering objects and describes their spatial correlations. It can be expressed as:

$$S(\vec{q}) = 1 + \rho \int \left[g(\vec{r}) - 1\right] e^{i\vec{q}\cdot\vec{r}} d\vec{r} \tag{G.10}$$

where ρ is the average number density of scatterers and $g(\vec{r})$ is the radial distribution function, giving the probability of finding a second object at position $\vec{r}$ relative to a reference one. For ordered systems, $S(\vec{q})$ shows well-defined peaks, while for disordered or amorphous systems, it appears more diffuse. In contrast to the form factor, for which analytical expressions exist for simple geometries (such as spheres, cylinders, or ellipsoids), the computation of the structure factor is not straightforward and typically requires *a priori* knowledge of the spatial distribution of the scattering objects within

the sample. This information is usually obtained through complementary techniques or theoretical modeling (Glatter, 2018).

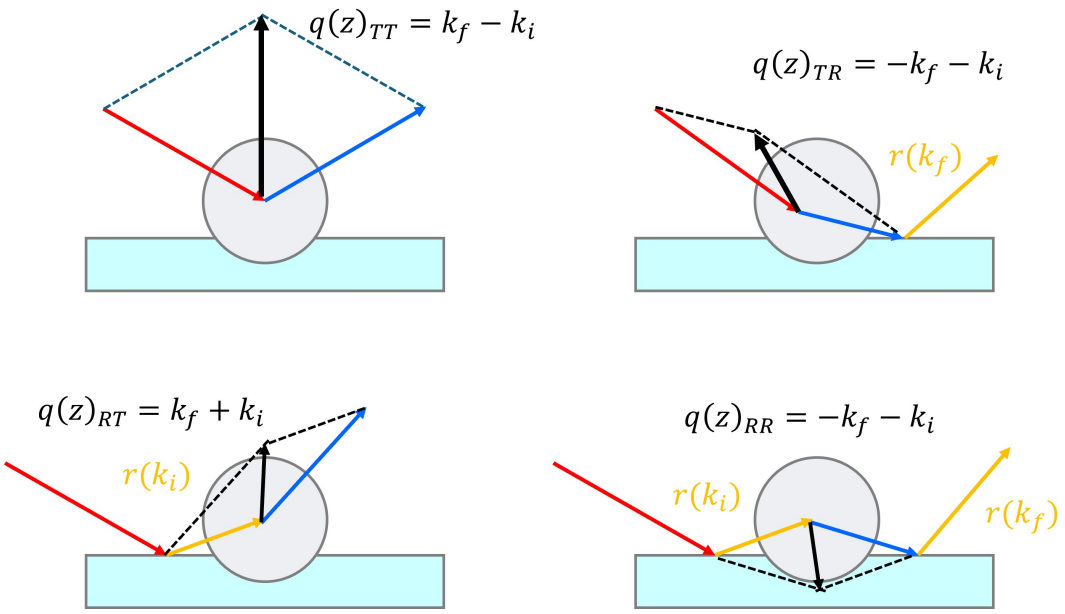

Figure G.2: *Sketch of the contribution to the Distorted Wave Born Approximation (DWBA). R stand for reflection and T stand for transmission, while $r(k_i)$ is the reflection probability according to the Fresnel reflection coefficient.*

While the Born approximation is well suited for bulk samples and thus able to describe most of the SAXS experiments in transmission geometry, it breaks down in the presence of sharp electron density discontinuities, such as interfaces between different media. In fact, at an interface, the incident X-ray beam undergoes reflection and refraction, resulting in a distorted wavefield near the surface. In this case, the local electromagnetic field that interacts with the scattering inhomogeneities is no longer just the incident plane wave but includes contributions from reflected and transmitted components Figure G.2. Moreover, at grazing incidence, evanescent waves can be generated below the critical angle, further complicating the scattering behavior. Therefore, the Born approximation becomes inadequate, and the more general Distorted Wave Born Approximation (DWBA) must be used, as it accounts for the wavefield distortion introduced by the interface and enables a more accurate description of the scattering process (Jiliang Liu et al., 2018). In this framework, a corrected form factor must be used that can be generalized as follows:

$$\begin{aligned} I_{\mathrm{DWBA}}(q_z) \approx |F_{\mathrm{DWBA}}(\vec{q})|^2 = & |T(\alpha_i)T(\alpha_f)|^2 I_R(+Q_{TT}) + \\ & |T(\alpha_i)R(\alpha_f)|^2 I_R(-Q_{TR}) + \\ & |R(\alpha_i)T(\alpha_f)|^2 I_R(+Q_{RT}) + \\ & |R(\alpha_i)R(\alpha_f)|^2 I_R(-Q_{RR}) \end{aligned} \tag{G.11}$$

where $R(\alpha_k)$ and $T(\alpha_k)$ are the reflection and transmission Fresnel coefficients, respec-

tively, and Q_{kk} are the scattering vector represented in Figure G.2 (Jiliang Liu et al., 2018).

G.3 Practical aspects of GISAXS experiment

In a standard GISAXS experiment, the scattered radiation is collected by using a two-dimensional (2D) detector, that allows for the simultaneous acquisition of the in-plane and out-of-plane scattered beam. However, the obtained image is expressed in terms of an intensity as a function of the pixel position. Thus, in order to analyze GISAXS data in reciprocal space, detector pixel coordinates must be converted into components of the scattering vector $\vec{q}$. This transformation depends on the experimental geometry and is performed separately for the in-plane (q_{xy}) and out-of-plane (q_z) components.

The in-plane scattering vector q_{xy} is calculated as:

$$q_{xy} = \frac{4\pi}{\lambda} \sin\left(\frac{1}{2} \arctan\left(\frac{(x - x_0) \cdot p}{D}\right)\right) \tag{G.12}$$

where λ is the X-ray wavelength, x is the horizontal detector pixel, x_0 is the x-coordinate of the direct beam position on the detector, p is the pixel size in mm, and D is the sample-to-detector distance in mm. This expression accounts for the angular deviation of the scattered beam in the horizontal plane and projects it into reciprocal space.

The out-of-plane scattering vector q_z is computed as:

$$q_z = \frac{4\pi}{\lambda} \sin\left(\frac{1}{2} \arcsin\left(\frac{(z_0 - z) \cdot p}{D} + \alpha_i\right)\right) \tag{G.13}$$

where z is the vertical detector pixel, z_0 is the z-coordinate of the direct beam position on the detector, p is the pixel size, D is the sample-to-detector distance, and α_i is the incidence angle expressed in radians. This formulation captures the vertical momentum transfer, incorporating both the detector geometry and the angle of incidence.

The obtained patterns are a 2D dimensional map of the intensity of the scattered beam, shown in color scale, as a function of the two components of the scattering vector. A characteristic pattern of silica nanoparticles of about 25 nm adsorbed at the air-water interface is reported in Figure G.3*A*. The GISAXS pattern shows the characteristic peaks at positive and negative values of q_{xy}, specular with respect to the direct beam plane $q_{xy} = 0$, that are diagnostic for the formation of a single nanoparticle monolayer at the interface and correspond to the in-plane GISAXS structure factor $S(q)$. The formation of a multilayered structure would lead to the appearance of characteristic features along q_z.

To extrapolate quantitative information from the 2D GISAXS pattern, a horizontal cut and integration along q_z is required (see Figure G.3*B*). The resulting 1D scattering intensity profile as a function of q_{xy} typically displays features that are symmetric with respect to the incident beam position at $q_{xy} = 0$. These features correspond to Bragg peaks, which are characteristic of the formation of a nanoparticle monolayer

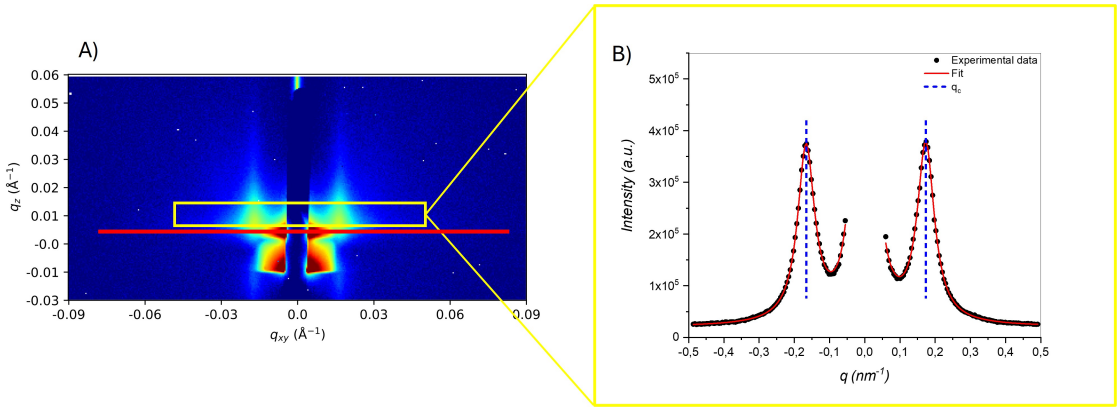

Figure G.3: *A) GISAXS pattern characteristic for the formation of a nanoparticle monolayer at the air water interface. The nanoparticle diameter was 25 nm, the X-ray wavelength was 0.56 Å(22 KeV), and the sample-to-detector distance was 4331 mm. The red horizontal line was placed at the Yoneda peak where $\alpha_f = \alpha_c$. B) 1D pattern obtained by the horizontal cut and integrated intensity along q_z in the range 0.008 Å^{-1} and 0.014 Å^{-1}.*

with hexagonal in-plane ordering.

The primary Bragg peak appears at $q_{xy} = q_c$ in reciprocal space and is associated with the (10) crystallographic direction. It is directly related to the average center-to-center interparticle distance (ID) in real space through the following expression:

$$ID = \frac{4\pi}{\sqrt{3}q_c} \tag{G.14}$$

In the case of highly ordered monolayers with hexagonal symmetry, higher-order Bragg peaks may be observed at positions corresponding to scattering vectors $\sqrt{3}q_c$, $2q_c$, $\sqrt{7}q_c$, $3q_c$, and so on (Figure G.4. These peaks are associated with higher-index crystallographic directions, following the general relation:

$$q_{hk} = q_c \cdot \sqrt{h^2 + hk + k^2} \tag{G.15}$$

where (h, k) are the two-dimensional Miller indices. Specifically, q_c corresponds to the (10) direction, $\sqrt{3}q_c$ to the (11) direction, $2q_c$ to the (20), $\sqrt{7}q_c$ to the (21), and $3q_c$ to the (30), respectively (Förster et al., 2005). The presence and sharpness of these peaks provide insight into the degree of lateral order and domain size within the monolayer.

The obtained 1D scattering profiles, corresponding to the in-plane structure factor $S(q)$, were fitted using an arbitrary function describing the background and a summation of Lorentz functions associated to the linewidth of the Bragg peaks:

$$I(q) \propto S(q) = bkg(q) + \sum_i \frac{A_i}{\pi} \cdot \frac{w_i}{(q - q_i)^2 + w_i^2} \tag{G.16}$$

where A_i is the total area under the peak, w_i is the full width at half maximum (FWHM), which defines the width of the peaks, and q_i are the peaks positions expected for a 2D hexagonal lattices as described above.

In Section G.2, it was discussed that the intensity of the scattered beam in a GISAXS

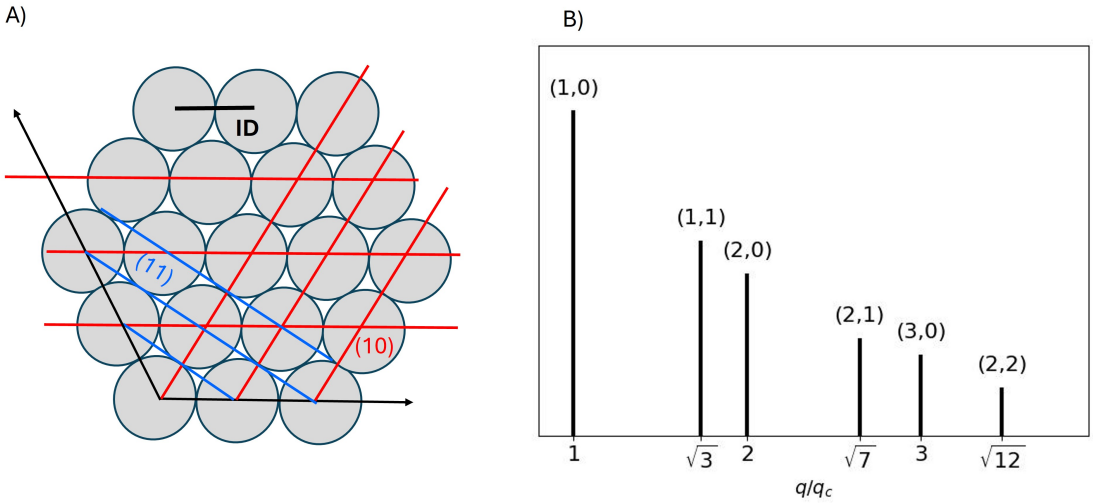

Figure G.4: *A) Schematic representation of a 2D hexagonally packed monolayer of spherical nanoparticles. The interparticle distance (1D) is defined as the center-to-center distance along the close-packed (10) direction. Red and blue lines indicate the (10) and (11) crystallographic directions in real space, respectively. B) Expected positions of Bragg peaks in reciprocal space for a 2D hexagonal lattice, plotted as a function of q/q_c, where q_c is the position of the primary peak (10). Higher-order peaks correspond to (h, k) reflections, following the relation in Equation G.15. Relative intensities are illustrative.*

experiment is a convolution of both the particle form factor $F(q)$ and the structure factor $S(q)$. However, in the case of highly ordered nanoparticle monolayers, especially those forming 2D hexagonal arrays, the structure factor dominates the scattering profile in the in-plane direction. As a result, the Bragg peaks arising from lateral interparticle correlations (encoded in $S(q)$) are clearly observed in the GISAXS intensity profile, while the form factor contribution $F(q)$ may be smooth, broad, or even negligible in comparison. This is particularly true for horizontal cuts (along q_{xy}), where lateral ordering is most pronounced. The form factor becomes more evident either in dilute systems (where $S(q) \approx 1$) or in vertical cuts (along q_z), where out-of-plane features such as particle height or layering effects can be detected. Therefore, in ordered monolayers measured under grazing incidence, the visible intensity modulations primarily reflect the structure factor, and only limited information can be directly extracted regarding the form factor unless $F(q)$ is isolated or modeled separately (Pedersen, 1997).

In the following pages, the home-built Python scripts used for the analysis of the GISAXS experiment are reported. Listing G.1 was employed to convert the 2D detector image from pixel coordinates to reciprocal space (scattering vector components). Listing G.2 was used to perform the horizontal cut and integration along q_z of the 2D pattern, yielding the corresponding 1D scattering profile. Finally, Listing G.3 was used to fit the resulting 1D intensity profile using an appropriate model function, as described in Equation G.16.

Listing G.1: *Python script used for 2D GISAXS pattern conversion from pixel to reciprocal space (q_{xy}, q_z).*

```
# Import required libraries
import h5py                              # To read .h5 data files
import os                                # For directory and file handling
import matplotlib.pyplot as plt          # For plotting 2D images
from matplotlib import colors            # For applying log scale
import numpy as np                       # Numerical operations

# ------------------------------------------
# Experimental Parameters
# ------------------------------------------

Wavelength = 0.55          # X-ray wavelength in Ångstroms
distance = 4331            # Sample-detector distance in mm
pixel_size = 0.075         # Detector pixel size in mm
angle = 0.045              # Incidence angle in degrees
theta_offset = angle * np.pi / 180  # Convert angle to radians

# ------------------------------------------
# Define reciprocal space axes (q_x and q_z)
# ------------------------------------------

# Horizontal axis: x pixels (left to right)
x = np.arange(765, 1023)
zero_x = 1022
q_x = np.round(np.sin(np.arctan((x - zero_x) * pixel_size / distance) / 2) *
               4 * np.pi / Wavelength, 4)

# Vertical axis: z pixels (top to bottom)
z = np.arange(1460, 2040)
zero_z = 2010
q_z = np.round((4 * np.pi * np.sin(
    np.arcsin(((zero_z - z) * pixel_size / distance) + theta_offset) / 2
) / Wavelength), 4)

# Print q-range for debugging
print(np.min(q_x), np.max(q_x))
print(np.min(q_z), np.max(q_z))

# Calculate z position corresponding to the critical angle
z_tr = zero_z + ((distance * theta_offset) / pixel_size)
print('z_tr =', z_tr)

# Compute corresponding q_z at the critical angle
q_z_tr = (4 * np.pi * np.sin(
    np.arcsin(((zero_z - z_tr) * pixel_size / distance) + theta_offset) / 2
) / Wavelength)
print(q_z_tr)

```

```
# ------------------------------------------
# File and figure settings
# ------------------------------------------

Name = 'Nps_BSA_1.25E-7_NaCl_50'
Name_fig = 'BSA 0.125 µM - NaCl 50 mM - NPs 0.1 %wt'
directory = 'Images'
path = f'{directory}/Protein GISAXS pattern'

# Create output directory if it does not exist
if not os.path.exists(path):
    os.makedirs(path)

# ------------------------------------------
# Load and crop GISAXS pattern
# ------------------------------------------

# Open the .h5 file and load the 2D detector image
fname = h5py.File(f'Proteina/{Name}/sc5572_{Name}.h5', 'r')
Scan = np.array(fname.get(f'/{Name}_0001_3.1/measurement/eiger4m')[1, :, :])

# Crop the region of interest from the detector image
image = Scan[1460:2040, 765:1023]

# ------------------------------------------
# Plot the 2D GISAXS pattern
# ------------------------------------------

plt.figure(figsize=(4, 6))
plt.xlabel(r'$q_{xy}$ ($\mathrm{\AA^{-1}}$)', fontsize=10)
plt.ylabel(r'$q_{z}$ ($\mathrm{\AA^{-1}}$)', fontsize=10)
plt.title(Name_fig, fontsize=11)

# Display the image with logarithmic color scale
plt.imshow(
    image,
    norm=colors.LogNorm(vmin=10, vmax=10000),
    cmap='jet',
    extent=[-np.max(q_x), -np.min(q_x), np.min(q_z), np.max(q_z)]
)
plt.locator_params(axis='x', nbins=7)
plt.locator_params(axis='y', nbins=13)
cbar = plt.colorbar()
cbar.ax.tick_params(labelsize=10)
plt.savefig(f'{path}/{Name_fig}.tif', dpi=500)
plt.show()
plt.close()
```

Listing G.2: *Python script used for 2D GISAXS patterns horizontal cut and vertical integration and isotherm extraction.*

```
1
2  # Import required libraries
3  import h5py                              # For reading .h5 data files
4  import os                                # For handling directories and paths
5  import matplotlib.pyplot as plt          # For plotting
6  import numpy as np                       # For numerical computations
7
8  # ------------------------------------------
9  # Experimental Parameters
10 # ------------------------------------------
11
12 Wavelength = 0.55       # X-ray wavelength in Ångstroms
13 Distance = 4331         # Sample-detector distance in mm
14 pixel_size = 0.075      # Detector pixel size in mm
15
16 # Define q-vector based on detector geometry
17 x = np.arange(0, 2068)  # Pixel indices (assuming detector has 2068 horizontal pixels)
18 q = np.sin(np.arctan((1022 - x) * pixel_size / Distance) / 2) * 4 * np.pi / Wavelength
19 # q is the scattering vector magnitude in Å^{-1}
20
21 # ------------------------------------------
22 # Define file paths and create output folders
23 # ------------------------------------------
24
25 # Define metadata for the sample (you should replace these with actual variable values)
26 Substance = 'Nps_BSA_1.25E-7_NaCl_50'
27 scan_name = 'sc5572'
28 Name = 'Nps_BSA'
29
30 # Construct the path for saving analysis results
31 path = f'Analisi dati proteina_Pascal/{Substance}/{scan_name}/{Name}'
32 if not os.path.exists(path):
33     os.makedirs(path)
34
35 # ------------------------------------------
36 # Load data from HDF5 file
37 # ------------------------------------------
38
39 # Open the HDF5 file
40 File = h5py.File(f'Proteina/{Substance}/{scan_name}_{Substance}.h5', 'r')
41
42 # Define sample and scan identifiers
43 Sample_name = f'{Substance}_0004'
44 Scan_number = '4.1'
45
46 # Load surface area signal (from Langmuir trough controller)
47 raw_surface_area = np.array(File.get(f'{Sample_name}_{Scan_number}/measurement/fb_A'))
48
```

```
# Calibration from spec unit to surface area in mm^2
# The conversion is done using a linear fit (slope and intercept from calibration)
Slope = 10571.59
Intercept = 9079.01
Surface_area = Slope * raw_surface_area + Intercept  # in mm^2

# Load surface pressure data in mN/m
Surface_Pressure = np.array(File.get(f'{Sample_name}_{Scan_number}/measurement/fb_Pi'))

# Save the surface area and pressure data to text file
output_isotherm = np.vstack((Surface_area / 100, Surface_Pressure)).T
np.savetxt(f'{path}/{Name}_{scan_name}.txt', output_isotherm, header='Surface_Area
↪  (cm2); Surface_Pressure (mN/m)')

# Save elapsed time for each scan
Times = np.array(File.get(f'{Scan_number}/measurement/elapsed_time'))
np.savetxt(f'{path}/Times_{Name}.txt', Times, fmt='%s')

# ------------------------------------------------
# Load 2D GISAXS data and extract line-cuts
# ------------------------------------------------

# Load the GISAXS detector data (Eiger 4M)
SAXS_data = np.array(File.get(f'{Sample_name}_{Scan_number}/measurement/eiger4m'))

# Create folder for cut profiles
cut_directory = f'{path}/Cut'
if not os.path.exists(cut_directory):
    os.makedirs(cut_directory)

# Loop through each frame in the scan
for i in range(len(SAXS_data)):
    print(f'Processing scan: {i}')

    # Select vertical slice of the detector (ROI: rows 1880 to 1915)
    image_slice = np.array(SAXS_data[i, 1880:1915, :])
    # Integrate over the ROI vertically (sum over rows)
    intensity_profile = np.sum(image_slice, axis=0)
    # Save intensity profile as .txt
    np.savetxt(f'{cut_directory}/scan_{i}.txt', np.vstack((q, intensity_profile)).T)

    # Plot the 1D intensity profile vs q
    fig = plt.figure()
    plt.yscale('log')
    plt.xlabel(r'$q$ ($\mathrm{\AA^{-1}}$)')
    plt.ylabel(r'Intensity (a.u.)')
    plt.plot(q, intensity_profile, label=f'Scan: {i}')
    plt.legend()
    plt.savefig(f'{cut_directory}/scan_{i}.png', dpi=300)
    plt.show()
    plt.close(fig)
```

Listing G.3: *Python script used to fit 1D GISAXS horizontal cuts with a model composed of three correlated Lorentzian peaks. Both right and left sides of the scattering pattern are processed independently.*

```
# Import required libraries
import os
import matplotlib.pyplot as plt
import numpy as np
from natsort import natsorted
from scipy.optimize import curve_fit
import glob

# Define the fit function: sum of 3 correlated Lorentzian peaks + background
def Fit_curve(x, A, B, n, C, D, w, xc, D1, w1, D2, w2):
    return (
        A + B / (x**2 * n) + C
        + (2 * D / np.pi) * (w / (4 * (x - xc)**2 + w**2))
        + (2 * D1 / np.pi) * (w1 / (4 * (x - np.sqrt(3) * xc)**2 + w1**2))
        + (2 * D2 / np.pi) * (w2 / (4 * (x - 2 * xc)**2 + w2**2))
    )

# Define metadata and paths
Substance = 'BSA 2.50E-7 M_NaCl 10 mM_NPs 0.1 %'
Scan_name = '0001'
Name = 'Full compression_2'

# Output directory
path = f'Analisi dati proteina_Pascal/{Substance}/{Scan_name}/{Name}/Fit'
if not os.path.exists(path):
    os.makedirs(path)

# Load intensity data from cut profiles
file = natsorted(glob.glob(f'Analisi dati
↪  proteina_Pascal/{Substance}/{Scan_name}/{Name}/Cut/scan_**.txt'))
name = np.array([((fname.split('/')[4]).split('.')[0]).split('_')[1] for fname in file])
all_file = np.array([np.loadtxt(fname, usecols=1) for fname in file]).T
q = np.loadtxt(file[0], usecols=0)  # q-axis from the first scan

# Define q-ranges for fitting
x_right = q[750:920]
x_left = q[1124:1294]
scan_number = np.arange(all_file.shape[1])

# Iterate over all scans
for i in scan_number:

# --------------------
# Fit right left side
# --------------------

    y_right = all_file[750:920, i]
    scan_id = name[i]
```

```
    print(scan_id)

    # Initial guess and bounds for right side fit
    p0 = (1000, 180, 400, 1000, 10, 0.015, 0.026, 10, 0.01, 10, 0.01)
    bounds = ((-np.inf, 0, 0, -np.inf, 0, 0.001, 0.026, 0, 0.01, 0, 0.01),
              (np.inf, np.inf, np.inf, np.inf, np.inf, 100, 0.04, 1000, 100, 1000, 100))

    popt, pcov = curve_fit(Fit_curve, x_right, y_right, p0, bounds=bounds)
    y_opt = Fit_curve(x_right, *popt)

    # Save fit parameters and errors
    popt = np.round(popt, 5)
    error = np.round(np.sqrt(np.diag(pcov)), 5)
    value_error = np.vstack((popt, error)).T
    np.savetxt(f'{path}/Fit_value_{scan_id}_right.par', value_error,
               header='A,B,n,C,Area,Width,Peak_position,D_a,w_a,D_b,w_b')
    np.savetxt(f'{path}/Only_fit_{scan_id}_right.par', y_opt)

    # Plot and save fit
    fig = plt.figure(figsize=(7.3, 5))
    plt.yscale('log')
    plt.title(f'{scan_id}')
    plt.scatter(x_right, y_right, c='k')

    I_d = np.round((4 * np.pi) / (popt[6] * np.sqrt(3) * 10), 1)
    plt.plot(x_right, y_opt, 'r', label=(
        f'scan={scan_id}\nA={popt[0]} ± {error[0]}\nB={popt[1]} ±
        ↪  {error[1]}\nn={popt[2]} ± {error[2]}\n'
        f'C={popt[3]} ± {error[3]}\nD={popt[4]} ± {error[4]}\nw={popt[5]} ±
        ↪  {error[5]}\n'
        f'xc={popt[6]} ± {error[6]}\nD1={popt[7]} ± {error[7]}\nw1={popt[8]} ±
        ↪  {error[8]}\n'
        f'D2={popt[9]} ± {error[9]}\nw2={popt[10]} ± {error[10]}\nI_d={I_d}'
    ))

    plt.xlabel(r'$q_{xy}$ ($\mathrm{\AA^{-1}}$)')
    plt.ylabel('Intensity (a.u.)')
    plt.legend()
    plt.savefig(f'{path}/Fit_{scan_id}_right.png')
    np.savetxt(f'{path}/Fit_{scan_id}_right.txt', np.vstack((x_right, y_right,
    ↪  y_opt)).T)
    plt.close(fig)

# --------------------
# Fit the left side
# --------------------

    y_left = all_file[1124:1294, i]
    p0 = (1000, 200, 600, 1000, 10, 0.015, -0.026, 10, 0.01, 10, 0.01)
    bounds = ((-np.inf, 0, 0, -np.inf, 0, 0.001, -0.04, 0, 0.01, 0, 0.01),
          (np.inf, np.inf, np.inf, np.inf, np.inf, 0.1, -0.026, 1000, 50, 1000, 100))
```

```
95
96      popt_l, pcov_l = curve_fit(Fit_curve, x_left, y_left, p0, bounds=bounds)
97      y_opt_l = Fit_curve(x_left, *popt_l)
98
99      # Save fit values
100     popt_l = np.round(popt_l, 5)
101     error_l = np.round(np.sqrt(np.diag(pcov_l)), 5)
102     value_error_l = np.vstack((popt_l, error_l)).T
103     np.savetxt(f'{path}/Fit_value_{scan_id}_left.par', value_error_l,
104                header='A,B,n,C,Area,Width,Peak_position,D_a,w_a,D_b,w_b')
105     np.savetxt(f'{path}/Only_fit_{scan_id}_left.par', y_opt_l)
106
107     fig_l = plt.figure(figsize=(7.3, 5))
108     plt.yscale('log')
109     plt.title(f'{scan_id}')
110     plt.scatter(x_left, y_left, c='k')
111
112     I_d = np.round((4 * np.pi) / (popt_l[6] * np.sqrt(3) * 10), 1)
113     plt.plot(x_left, y_opt_l, 'r', label=(
114         f'scan={scan_id}\nA={popt_l[0]} ± {error_l[0]}\nB={popt_l[1]} ±
        ↪  {error_l[1]}\nn={popt_l[2]} ± {error_l[2]}\n'
115         f'C={popt_l[3]} ± {error_l[3]}\nD={popt_l[4]} ± {error_l[4]}\nw={popt_l[5]} ±
        ↪  {error_l[5]}\n'
116         f'xc={popt_l[6]} ± {error_l[6]}\nD1={popt_l[7]} ± {error_l[7]}\nw1={popt_l[8]} ±
        ↪  {error_l[8]}\n'
117         f'D2={popt_l[9]} ± {error_l[9]}\nw2={popt_l[10]} ± {error_l[10]}\nI_d={-I_d}'
118     ))
119
120     plt.xlabel(r'$q_{xy}$ ($\mathrm{\AA^{-1}}$)')
121     plt.ylabel('Intensity (a.u.)')
122     plt.legend()
123     plt.savefig(f'{path}/Fit_{scan_id}_left.png')
124     np.savetxt(f'{path}/Fit_{scan_id}_left.txt', np.vstack((x_left, y_left, y_opt_l)).T)
125     plt.close(fig_l)
```

H

Neutron Reflectometry (NR)

Specular Neutron Reflectometry (NR) is a grazing-incidence scattering technique that provides the scattering length density (SLD) profile normal to a surface or interface. Unlike X-rays, neutrons interact with nuclei rather than electron clouds, and the interaction is strongly isotope-dependent (e.g. H vs. D). This makes NR uniquely sensitive to light elements and enables powerful contrast variation strategies via selective deuteration or solvent mixing (Cousin et al., 2018).

Thanks to this property, NR has become a key method in soft matter and biological systems, where nanoscale organization and buried interfaces are otherwise difficult to probe. Applications range from thin polymer films, coatings, and self-assembled monolayers at solid surfaces, to lipid and protein layers at aqueous interfaces, and to responsive hydrogels or supported membranes at solid–liquid interfaces (Gerelli, 2020; A. Maestro et al., 2021; Johnson et al., 2025). More recently, NR has also been applied to hybrid and complex interfaces, such as emulsions, nanoparticles, and biomolecular assemblies (Bowers et al., 2001; Scoppola et al., 2015).

This versatility makes NR indispensable not only in fundamental research on interfacial structure but also in applied contexts such as energy materials, advanced coatings, and pharmaceutical formulations (Thomas, 1996; Yeager et al., 2012). Its combination of isotope sensitivity, non-destructive probing, and sub-nanometer depth resolution explains its central role in modern interface science. With a typical depth resolution of the order of 1 nm and the ability to probe buried interfaces non-destructively, NR provides structural information that is difficult to obtain by other techniques.

H.1 From neutron–matter interaction to an effective refractive index

The interaction between neutrons and matter is described by taking into account two main interactions, the strong interaction with the nuclei and the magnetic interaction with the existing spin moments of both nuclei and electrons. However, in standard NR

experiments, cold or thermal neutrons are used. These neutrons are produced either by nuclear reactors or spallation sources and cooled down to an energy of some meV by inelastic scattering with highly hydrogenated substances, such as liquid methane. This thermal energy, corresponding to a neutron velocity of some thousands m/s, can be converted by means of the de Broglie relationship, to a wavelength of 1–25 Å. In this framework, the associated wavelength is much bigger than the characteristic nuclei dimension and also than the spatial extension of the strong interaction. Thus, ignoring the magnetic interaction, we can assume that neutrons interact with nuclei in an isotropic manner described by the Fermi pseudo-potential (Zhou et al., 1995), where the nuclei are described as punctual and isotropic scattering centers.

A neutron possessing a momentum p is characterized by a de Broglie wavelength equal to:

$$\lambda = \frac{h}{p} \tag{H.1}$$

where h is the Planck constant; an associated wave vector in vacuum

$$k_0 = \frac{2\pi}{\lambda} \tag{H.2}$$

and an energy

$$E_0 = \frac{\hbar^2 k_0^2}{2m_N} \tag{H.3}$$

where $\hbar = h/2\pi$, and m_N is the neutron rest mass.

The wavefunction of a neutron interaction with an atomic nucleus (ψ) must satisfy the Schrödinger equation which, in the specific geometry of specular reflection, is reduced to a mono-dimensional equation along the direction perpendicular to the interface (z) of the form:

$$\frac{\hbar^2}{2m_N}\frac{d^2\psi}{dz^2} + [E_0 - V_F(z)]\psi = 0 \tag{H.4}$$

where the terms $V_F(z)$ is the nuclear Fermi pseudo-potential that, within the Born approximation, is defined as:

$$V_F(z) = b(\frac{2\pi\hbar^2}{m_N})\delta(z) \tag{H.5}$$

where $\delta(z)$ is the Dirac delta function of the nuclear position and b is known as the atomic scattering length, whose value is characteristic for each isotope.

The scattering length, which defines the magnitude of the nuclear potential, is formally defined by a complex number, as follows:

$$b = b' + ib'' \tag{H.6}$$

where the real part takes into account both the coherent b'_{coh} and incoherent b'_{inc} scat-

tering lengths

$$b' = \langle |\, b \,| \rangle^2 + (\langle |\, b^2 \,| \rangle - \langle |\, b \,| \rangle^2) = b'_{coh} + b'_{inc} \tag{H.7}$$

while the imaginary part is associated with the neutron absorption process probability (Fermon et al., 2009). The incoherent contribution comes from the isotopic spatial distribution and the spin spatial disorder and generally causes an increase in the background value and thus the decrease of the signal-to-noise ratio. On the other hand, the absorption process leads to a decrease in the intensity of the scattered beam. However, both of these two terms are usually negligible with respect to the coherent contribution so, hereafter, we will refer to the coherent scattering length by means of b.

In the framework of the Fermi pseudo-potential, the scattering material can be treated as a continuum and thus the scattering potential can be characterized by a density known as scattering length density (SLD). The SLD (ρ) of a material is defined as:

$$\rho_i = \sum N_i \cdot b_i = \frac{N_A \cdot \rho_m}{MW} \sum b_i, \tag{H.8}$$

where b_i is the scattering length of the isotope i^{th}, and N_i is its volume number density calculated as the product between the Avogadro number (N_A) and the mass density of the material (ρ_m in g/cm^3) divided by its molecular weight (MW in g/mol).

As the neutron reflectometry is an elastic scattering technique, the conservation of the neutron energy requires that the wavevector outside and inside the material potential must be related by the following relationship

$$k_z^2 = k_0^2 - 4\pi\rho(z) \tag{H.9}$$

where k_z^2 is the neutron wavevector in a medium of SLD equal to $\rho(z)$. This formula can be rewritten as

$$n_z^2 = \frac{k_z^2}{k_0^2} = \left[1 - \frac{4\pi\rho(z)}{k_0^2}\right]^2 \tag{H.10}$$

and by considering that $\rho(z)$ is in the order of 10^{-6} Å^{-2}, and thus $1 - 4\pi\rho(z)/k_0^2 \simeq 1$, we can directly compute n_z as follows:

$$n_z = \frac{k_z}{k_0} = 1 - \frac{4\pi\rho(z)}{k_0^2} \tag{H.11}$$

So, we can describe the neutron-matter interaction by means of an effective neutron refractive index n that is related to the isotopic composition of the material by its scattering length density. This allows us to treat the neutron reflection from an interface by using simple light optics considerations in an analogous way as for X-rays.

H.2 Geometry of specular neutron reflectometry and fitting algorithms

In specular neutron reflectometry, the scattering geometry is constrained such that the angle of incidence equals the angle of reflection, and the scattering vector is oriented normal to the surface. The momentum transfer is thus purely out-of-plane,

$$q_z = \frac{4\pi}{\lambda} \sin\theta, \tag{H.12}$$

where λ is the neutron wavelength and θ the angle of incidence (reflection) with respect to the sample surface. Under these conditions, the reflectivity signal provides direct information on the SLD profile $\rho(z)$ along the surface normal.

Following the optical analogy above mentioned, for a single sharp interface between two homogeneous media of SLD ρ_1 and ρ_2, the reflection amplitude is given by the Fresnel coefficient.

$$r_{12} = \frac{k_{z,1} - k_{z,2}}{k_{z,1} + k_{z,2}}, \qquad R = |r_{12}|^2, \tag{H.13}$$

with $k_{z,i}$ the perpendicular component of the neutron wave vector in medium i and $R(\theta)$ is the reflectivity profile as a function of the incidence (reflection) angle or, alternatively, as a function of the momentum transfer q_z.

As already described for X-ray in Appendix G, when the neutron beam coming from a more optically dense medium characterized by ρ_1 is reflected by a less optically dense medium characterized by ρ_2, such that $\rho_1 > \rho_2$, the existence of a critical momentum transfer,

$$q_c = \sqrt{16\pi\,\Delta\rho}, \tag{H.14}$$

defines the onset of total external reflection ($R \simeq 1$ for $q_z < 1_c$) and the asymptotic Fresnel decay $R \propto q_z^{-4}$ for $q_z \gg q_c$ (Fermon et al., 2009; Cousin et al., 2020).

In the more general case of a continuous SLD profile $\rho(z)$, and under the Born approximation where multiple scattering events are neglected (J. Li et al., 2010), the reflectivity is related to the Fourier transform of the SLD gradient by the so-called *master formula*:

$$R(q_z) \approx \frac{16\pi^2}{q_z^4} \left| \int_{-\infty}^{+\infty} \frac{d\rho(z)}{dz}\, e^{iq_z z}\, dz \right|^2. \tag{H.15}$$

This expression emphasizes that reflectivity is sensitive to variations in the SLD profile rather than to its absolute value (Cousin et al., 2020).

Close to the critical edge or in multilayer systems, multiple reflections and interference must be taken into account. The exact calculation is performed using the recursive formalism introduced by Parratt (1954), or equivalently the Abélès matrix method (Abelès, 1950). Considering a stratified medium of layers with thickness d_j, perpen-

dicular wave vectors $k_{z,j}$, and single–interface reflection amplitudes

$$r_{j,j+1} = \frac{k_{z,j} - k_{z,j+1}}{k_{z,j} + k_{z,j+1}}, \tag{H.16}$$

the net reflection amplitude can be obtained recursively from the substrate ($R_{N+1} = 0$) as

$$R_j = \frac{r_{j,j+1} + R_{j+1}\, e^{2ik_{z,j+1}d_j}}{1 + r_{j,j+1}R_{j+1}\, e^{2ik_{z,j+1}d_j}}, \qquad R(Q_z) = |R_0|^2. \tag{H.17}$$

An important experimental signature in specular reflectivity is the presence of so–called Kiessig fringes, i.e. oscillations in $R(q_z)$ arising from interference between waves reflected at the top and bottom of a thin film (Kiessig, 1931). The periodicity Δq_z of these oscillations is directly related to the film thickness d through

$$\Delta q_z \approx \frac{2\pi}{d}. \tag{H.18}$$

Thus, the observation of Kiessig fringes provides a direct measure of layer thickness on the nanometer scale, while their amplitude encodes information on contrast and interfacial roughness. In multilayer systems, the superposition of different fringe patterns can be exploited to resolve complex stratification using fitting algorithms based on the Parratt recursion.

In real interfaces, deviations from the ideal case of perfectly sharp and flat boundaries must be considered: interfacial roughness and possible inter-diffusion between adjacent layers significantly affect the reflectivity profile, modifying both the fringe contrast and the overall decay of $R(q_z)$; therefore, appropriate corrections or modeling strategies are required to account for these effects in multilayer systems. Generally, interfacial roughness is described by a Gaussian root-mean-square (rms) parameter σ, which quantifies the statistical height fluctuations of the interface. In reflectivity modeling, this effect is commonly incorporated through the Nevot–Croce factor applied to each interface, effectively damping the reflection coefficients and thereby reducing the fringe contrast in $R(q_z)$ for high q_z values (Nevot et al., 1980)

$$r_{j,j+1} \longrightarrow r_{j,j+1}\, e^{-2\,k_{z,j}\,k_{z,j+1}\,\sigma^2}. \tag{H.19}$$

In practice, Equation H.17–H.19 constitute the forward model used in all modern NR fitting workflows, while Equation H.15 provides a simple but powerful conceptual picture of the relation between reflectivity and the depth derivative of the SLD.

H.3 Contrast variation

One of the intrinsic limitations of specular neutron reflectometry is the so-called phase problem: only the intensity of the reflected beam, $R(q_z) = |r_{j,j+1}|^2$, is measured experimentally, while the phase of the reflection amplitude is lost. As a result, the inversion

of the reflectivity curve into a unique SLD profile $\rho(z)$ is not straightforward, and in practice different structural models can yield reflectivity curves that fit the experimental data equally well. This non-uniqueness can complicate the interpretation, especially for complex or buried interfaces. A powerful strategy to reduce such ambiguity is the use of contrast variation.

The concept of contrast variation in neutron reflectometry originates from the fundamental property that the nuclear scattering length b can assume both positive and negative values depending on the isotope. A classical example is the case of hydrogen (H), which exhibits a negative coherent scattering length ($b = -3.74fm$), whereas deuterium (D) has a positive one ($b = +6.67fm$). This unique feature has no analogue in X-ray scattering, where the scattering length is always proportional to the number of electrons and thus strictly positive. Because the scattering length density is defined as Equation H.8, the replacement of H by D within a molecule or in a solvent leads to large, tunable changes in the effective SLD.

From the perspective of the master formula (Equation H.15), the measured reflectivity depends not on the absolute value of the SLD but on its variation across an interface, i.e. on $\Delta\rho_z$. This implies that if two adjacent media have matched SLD, their interface becomes effectively "invisible" to neutrons, as no contrast is present to generate scattering. Exploiting this principle, one can deliberately adjust the contrast of specific sample components by solvent blending. For example, by mixing H_2O and D_2O in appropriate ratios, it is possible to continuously tune the solvent SLD between -0.556×10^{-6} Å^{-2} (pure H_2O) and 6.356×10^{-6} Å^{-2} (pure D_2O). Quantitatively, the effective SLD of a mixed solvent can be expressed as a linear combination of the scattering length densities of H_2O and D_2O weighted by their respective volume fractions:

$$\rho_{\text{solvent}}(\phi) = \phi \cdot \rho_{\text{D2O}} + (1 - \phi) \cdot \rho_{\text{H}_2\text{O}}, \tag{H.20}$$

where ϕ is the D_2O volume fraction.

By matching the solvent SLD to that of a particular material, the contribution of that material to the reflectivity can be suppressed (contrast matching), allowing the selective highlighting of other components within the system. This approach is particularly powerful for complex, multi-component or buried interfaces where different SLD profiles could reproduce the same reflectivity curve due to the phase problem. Contrast variation provides independent experimental constraints that help to resolve such ambiguities and thereby enables a more robust reconstruction of the true interfacial structure.

The calculation of the scattering length density (SLD) of the silica nanoparticles was performed assuming the amorphous nature of SiO_2. A consensus mass density of 2.1 ± 0.1 g cm^{-3} was used in Equation H.8, together with the coherent scattering lengths (b) of 5.803 fm for oxygen (O) and 4.149 fm for silicon (Si).

In the case of proteins, two complications in the calculation of the molecular SLD arise. The first is due to the presence of exchangeable (labile) hydrogens, which can be

Table H.1: *Summary of the scattering length densities (SLD) of air, solvents of different H_2O/D_2O composition, and species in suspension (silica nanoparticles and BSA) under the experimental contrast conditions. Solvent compositions were chosen to provide distinct contrast matching points: SiO_2-matching water (SiO_2MW), BSA-matching water (BSAMW), and null-reflecting water (NRW).*

Substance	ϕ_{D_2O}	ϕ_{H_2O}	**SLD** (10^{-6} Å^{-2})
Air	-	-	0
Solvent			
H_2O	0	100	-0.556
D_2O	100	0	6.356
SiO_2MW	57.45	42.55	3.41
BSAMW	42.55	57.45	2.39
NRW	91.9	8.1	0
Species in suspension			
SiO_2 (amorphous)[a]	-	-	3.41
BSA in D2O[b]	100	0	3.06
BSA in SiO_2MW[b]	57.45	42.55	2.55
BSA in BSAMW[b]	42.55	57.45	2.37
BSA in NRW[b]	91.9	8.1	1.95

[a] SLD obtained by considering a SiO_2 mass density equal to 2.1 ± 0.1 g/cm^3 (Calzolari et al., 2012).
[b] SLD obtained with the biomolecular SLD calculator (`http://psldc.isis.rl.ac.uk/Psldc/`).

replaced by deuterium when the protein is dispersed in D_2O-containing medium. The second depends on the molecular volume that can be modified upon the adsorption at the interface or interaction with nanoparticles. As a consequence, the protein SLD is not a fixed value but depends on the isotopic composition of the surrounding solvent and on the location of the protein and its interaction with the surrounding species present in the suspension. To account for these effects, in our study we calculated the SLD of bovine serum albumin (BSA) using the Biomolecular SLD Calculator (`http://psldc.isis.rl.ac.uk/Psldc/`) which implements a residue-by-residue summation of coherent scattering lengths based on the protein's amino acid sequence.

For this purpose, we used the FASTA sequence of BSA deposited in the Protein Data Bank (PDB ID: 3V03, doi.org/10.2210/pdb3v03/pdb). To realistically account for H/D exchange effects, we assumed that 90% of the labile hydrogens are exchanged with deuterium under our experimental solvent conditions. This assumption is consistent with typical exchange levels observed for proteins in D_2O-based buffers and allows for a more accurate estimation of the effective scattering length density of the protein. In this framework, the calculator sums over all the amino acid scattering lengths and consensus volumes to yield the effective SLD of BSA as a function of solvent D_2O fraction, which was then used in the modeling of our reflectivity data.

In order to probe the structure of the protein–nanoparticle interface under different contrast conditions, we employed several solvent compositions obtained by mixing H_2O and D_2O in controlled ratios. These solvent contrasts were chosen to either

match or highlight specific components of the system (*e.g.*, silica nanoparticles or BSA), thereby enhancing the sensitivity of the reflectivity measurements to selected structural features. The resulting scattering length densities (SLD) of the solvents and suspended species, as calculated or derived from literature values, are summarized in Table H.1.

H.4 Slab model for BSA thin film at the air-water interface

To describe the reflectivity data of BSA adsorbed at the air-water interface, we employed a slab (or box) model representation of the interfacial structure. In this approach, the protein layer is approximated as a homogeneous slab of thickness d, scattering length density (SLD) ρ, the slab hydration ($h\%$) and the interfacial roughness σ, positioned at the air-water boundary. Each parameter has a direct physical meaning: the slab thickness corresponds to the average extension of the protein layer normal to the interface, the SLD reflects the protein composition, the hydration takes into account the solvent penetration within the layer, and the roughness accounts for height fluctuations and partial interdiffusion at the boundaries.

Formally, the model is implemented by introducing an additional layer into the Parratt recursion (Equation H.17), such that the reflectivity is calculated for a stratified system consisting of (i) air, (ii) the protein slabs, and (iii) the bulk solvent of a given contrast. The SLD of the BSA slab was treated as a fixed constant determined for each solvent composition using the Biomolecular SLD Calculator (see Section H.3). This ensures that the model correctly reflects the dependence of the protein scattering contrast on the solvent D_2O fraction.

In practice, the reflectivity fitting procedure consisted of simultaneously adjusting the slab parameters (d, $h\%$, σ) across different solvent contrasts. Such a multi-contrast fitting strategy significantly reduces model ambiguity arising from the phase problem, as discussed in Section H.3. In particular, the use of pure D_2O, SiO_2-matching water, BSA-matching water, and null reflecting water (see Table H.1) enabled us to disentangle the relative contributions of the protein and the substrate. The resulting fits provided quantitative estimates of the thickness and hydration of the adsorbed BSA layer, as well as the degree of conformational changes upon adsorption.

Overall, the slab model offers a simple yet robust framework for the analysis of BSA reflectivity data, striking a balance between physical interpretability and computational tractability. Although it neglects fine structural details such as protein orientation or lateral inhomogeneity, it nevertheless enables the extraction of important quantitative parameters. In particular, the two key quantities that we derived from slab-model fits are the surface excess, Γ, and area per molecule, APM, as it will be discussed in Chapter 5.

Thus, even when limited by the lack of orientational detail, neutron reflectivity at the air–water interface can yield direct estimates of the surface coverage and packing density of interfacial species, parameters of central importance in the characterization of adsorbed protein thin films (Kleinschmidt, 2013).

H.5 Physical model for hybrid BSA-NP monolayer at the interface

In the literature, different strategies have been employed to model the scattering length density (SLD) or electron density profiles of nanoparticle (NP) monolayers at air-liquid and solid-liquid interfaces, using both neutron and X-ray reflectivity. A first approach consists in the use of simplified slab models, where the NP layer is approximated as a single homogeneous slab characterized by an effective thickness, SLD, and roughness. This strategy has been successfully applied, for instance, to monolayers of silica nanoparticles at the air–water interface (Calzolari et al., 2012; Ang et al., 2010). A second approach, particularly adopted for NP monolayers at solid–liquid interfaces, relies on representing the spherical geometry and packing of the particles through a sequence of discrete slabs, each corresponding to a horizontal slice of the NP ensemble. In this way, the local volume fraction of solvent and nanoparticles is properly accounted for in each slice, enabling a more realistic description of the vertical density distribution (Al-Shatty et al., 2022). While these models are useful for reproducing the measured reflectivity, they do not easily yield direct physical quantities such as the lateral packing of the nanoparticles, their immersion depth relative to the interface, or the spatial partitioning of adsorbed proteins with respect to the NP surface. For this reason, in the present work, we extended the interfacial model of Calzolari et al., 2012 by explicitly including NP lateral packing, immersion depth distribution, and radius polydispersity, and an asymmetric protein corona term, thus enabling a more direct connection between the reflectivity-derived SLD profiles and the underlying structural organization of hybrid NP–protein monolayers. Figure Figure H.1 presents a sketch of the geometric construction, together with the set of geometric parameters that were employed in developing the mathematical model, which will be discussed and explained in detail in the following sections.

H.5.1 Bare air–water interface

The bare air–water interface was modeled by an error-function profile with a Gaussian roughness in order to account for capillary-waves (CWs) roughness:

$$\rho_{\mathrm{a/w}}(z) = \rho_{solvent} + \frac{\rho_a - \rho_{solvent}}{2} \operatorname{erf}\left(\frac{z}{\sqrt{2}\sigma_{\mathrm{a/w}}}\right), \tag{H.21}$$

where ρ_a is the SLD of air taken as 0, $\rho_{solvent}$ are the bulk SLD of H_2O/D_2O mixture used for each contrast (see Table H.1), and $\sigma_{\mathrm{a/w}}$ represents the interfacial roughness induced by capillary waves. z = 0 is the ideal Gibbs plane for the air-water interface, z > 0 is the water side, while z < 0 is the air side.

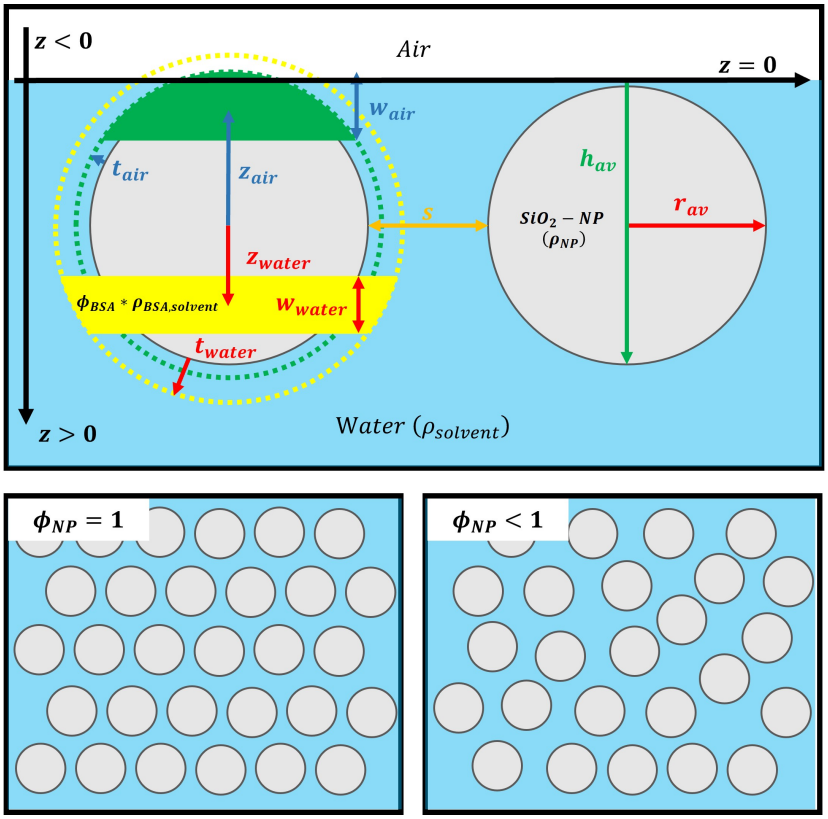

Figure H.1: *Sketch of the geometrical model for neutron reflectometry fit of NP-BSA hybrid monolayer at the air-water interface.*

H.5.2 Nanoparticle contribution

The contribution of the nanoparticle ensemble to the overall scattering length density (SLD) profile was computed as follows:

$$\rho_{\mathrm{NP}} = \int \int \frac{2\pi \cdot \left(r^2 - (z - (r+h))^2\right) \cdot [\rho_{SiO_2} - \rho_{a/w}(z)]}{\phi_{NP} \cdot \sqrt{3}(2r+s)^2} \cdot G(r) \cdot G(h)\, dr\, dh, \quad \text{(H.22)}$$

for $h < z < h + 2r$ and $\rho_{\mathrm{NP}} = 0$ elsewhere.

This expression captures, within a single framework, the geometry of spherical particles, their packing at the interface, and their statistical distributions in both size and immersion depth.

The central term, $\pi \cdot (r^2 - (z - (r + h))^2)$, represents the cross-sectional area of a sphere of radius r at a given height z, for a particle whose center lies at a depth $r + h$ below the interface plane. In other words, it quantifies how much of the nanoparticle volume contributes to the density at a specific vertical position. $h > 0$ represents the immersion depth in the water side. Multiplying this geometric term by the scattering length density of the SiO_2, ρ_{SiO_2}, yields the local contribution of the nanoparticle relative to the surrounding medium. The subtracted term $(\rho_{a/w}(z))$ takes into account the water displacement by the nanoparticle fraction immersed in the water side.

Since the particles are not isolated but arranged laterally at the interface, the expression is normalized by the effective surface area per particle in a hexagonal lattice, $\sqrt{3}(2r + s)^2/2$, where s is the mean surface-to-surface NP lateral separation distance within the monolayer. The factor $0 < \phi_{\mathrm{NP}} < 1$ accounts for the effective surface coverage, rescaling the density to reflect deviations from an ideal, fully occupied lattice, thus taking into account in-plane disorder, inhomogeneity and defects .

To account for sample polydispersity, the SLD profile is integrated over Gaussian distributions in both particle radius and immersion depth. Specifically,

$$G(x) = G(x; x_{av}, \sigma_x) = \frac{1}{\sigma_x\sqrt{2\pi}} \exp\left(-\frac{(x - x_{av})^2}{2\sigma_x^2}\right),$$

is the Gaussian distribution of the quantity x, and $G(r) = G(r; r_{\mathrm{av}}, \sigma_r)$ describes the NP size distribution with mean radius r_{av} and standard deviation σ_r, while $G(h) = G(h; h_{\mathrm{av}}, \sigma_h)$ describes the immersion depth distribution with mean h_{av} and width σ_h. This convolution ensures that the resulting profile faithfully represents the polydispersity of the nanoparticle monolayer.

Altogether, Equation H.22 provides a physically grounded description of the vertical SLD profile of nanoparticles at a liquid interface. By explicitly incorporating spherical geometry, lateral packing, interparticle spacing, and ensemble heterogeneity, this model goes well beyond the simplified slab approximation.

However, in order to avoid overfitting and to maintain the physical significance of the extracted parameters, several quantities were constrained to values obtained either from complementary experimental techniques or from physically motivated considerations. In particular, the average particle radius r_{av} and its polydispersity σ_r were determined independently from preliminary Small-Angle Neutron Scattering (SANS, see Chapter 5) measurements of the particle size distribution. The mean lateral separation distance s between neighboring nanoparticles was fixed from grazing-incidence small-angle X-ray scattering (GISAXS, see Chapter 5) measurements, while the nanoparticle SLD, $\rho_{\mathrm{SiO_2}}$, was set to the tabulated value of 3.41×10^{-6} Å^{-2}. Finally, since the distribution of immersion depths is predominantly governed by capillary waves at the liquid interface, the standard deviation of the immersion depth, σ_h, was restricted within a physically meaningful interval:

$$\sigma_{a/w} < \sigma_h < 3 \cdot \sigma_{a/w},$$

where $\sigma_{a/w}$ denotes the intrinsic roughness of the bare air–water interface.

With these constraints, the set of free fitting parameters was effectively reduced to the average immersion depth h and the packing density scaling factor ϕ_{NP}. This corresponds to no more than three free parameters, which is comparable to the degrees of freedom typically employed in simple slab models (i.e. thickness d, roughness σ, and layer hydration $h\%$), thereby ensuring both robustness and interpretability of the model.

H.5.3 Protein contribution

In order to reproduce the measured reflectivity curves, it was necessary to explicitly include the presence of a protein corona surrounding the nanoparticles. The only physically consistent way to fit the data was to model the corona as two independent concentric shells, one extending towards the air side and the other towards the water side of the interface. The thickness along the radial direction (t_i) of the two shells was treated as independent, thereby allowing for asymmetric adsorption of proteins across the interface.

Each corona shell was represented as a finite slab of constant SLD, existing only within the vertical interval:

$$\rho_{\mathrm{BSA},i}(z) \;\exists\; \text{if} \;\; z_i - \frac{w_i}{2} < z < z_i + \frac{w_i}{2}, \tag{H.23}$$

where z_i denotes the vertical position of the slab center (defined relative to the nanoparticle center along the z-axis), and w_i is its thickness projected along z. Thus, the corona contribution to the SLD profile can be expressed as:

$$\rho_{\mathrm{BSA},i}(z) = \int\int \frac{2\pi \cdot (r_{out} - r_{in})^2}{\phi_{\mathrm{NP}} \cdot \sqrt{3}(2r + s + t_i)^2} \cdot \tag{H.24}$$
$$\Big[\phi_{\mathrm{BSA},i} \cdot \rho_{\mathrm{BSA,solvent}} - (1 - \phi_{\mathrm{BSA},i}) \cdot \rho_{a/w}(z)\Big]\, G(r)\, G(h)\, dr\, dh,$$

where $r_{out} = ((r + t_i)^2 - \big(z - (r + h)\big)^2)^{1/2}$ and $r_{in} = (r^2 - \big(z - (r + h)\big)^2)^{1/2}$ are respectively the outer and the inner radii of the core-shell system.

Further, the integration runs over the two sides of the interface ($i = a$ for the shell at the air side and $i = w$ for the one at the water side), $\phi_{BSA,i}$ is the protein volume fraction within the shell, $\rho_{\mathrm{BSA,solvent}}$ is the SLD of BSA under the chosen solvent (Table H.1). This formulation guarantees that the corona extends only within a finite thickness along z, while remaining independent on the two sides of the interface.

Again, constrained parameters were used to avoid overfitting. Specifically, the shell thickness (t_i) was constrained between the lower axis and bigger axis of the triaxial ellipsoid model used to fit the SANS data for the protein (Chapter 5), and an effective thickness (t_{eff}, see Listing H.1) was used to take into account eventual shell overlap upon monolayer compression in the Langmuir trough. Thus, the full free parameters describing the protein shells were the shell position with respect to the nanoparticle center (z_i), the shell width along the z direction (w_i) and the shell hydration ($\phi_{BSA,i}$). This choice ensures that the number of degrees of freedom remains equivalent to that of the simple slab model, thereby allowing a direct comparison between the two approaches.

H.5.4 Total SLD profile

The complete SLD profile was constructed as:

$$\rho(z) = \rho_{\mathrm{a/w}}(z) + \rho_{\mathrm{NP}}(z) + \rho_{\mathrm{BSA,a}}(z) + \rho_{\mathrm{BSA,w}}(z). \tag{H.25}$$

This profile was then used within the RasCAL 2019 custom xy model to compute the reflectivity profiles by simultaneously fitting each contrast. (`https://github.com/arwelHughes/RasCAL_2019.git`). To further assess the reliability of the developed physical model, we performed simulations of reflectivity curves in which key structural parameters of the monolayer were systematically varied. In particular, we explored the effects of changing the nanoparticle packing density (s), immersion depth (h), real packing fraction (ϕ_{NP}), and protein shell thickness (t_i), width (w_i), protein dry fraction $(\phi_{BSA,i})$ position with respect to the sphere center (z_i) both in air and water on the calculated reflectivity. The results, shown in Figure H.2, clearly demonstrate that even modest variations in these parameters produce significant and characteristic changes in the reflectivity profiles. This highlights the high sensitivity of the model to the underlying interfacial structure, ensuring that the fitting procedure is not only mathematically stable but also physically meaningful. Consequently, the approach can be considered robust for the analysis of experimental data, as structural modifications at the nanoscale are directly and quantitatively reflected in the simulated scattering curves.

Finally, beyond providing a geometrical description of the monolayer structure in terms of both the nanoparticles and the surrounding protein corona, the developed model also enables the extraction of quantities that are directly relevant for the physicochemical characterization of the system. In particular, by analyzing the corona volume it is, in principle, possible to estimate the number of protein molecules adsorbed per nanoparticle, while the knowledge of the lateral packing fraction allows one to quantify the protein excess at the interface. These aspects, together with their implications for protein adsorption and desorption under compression, will be addressed in detail in Chapter 5 and 6.

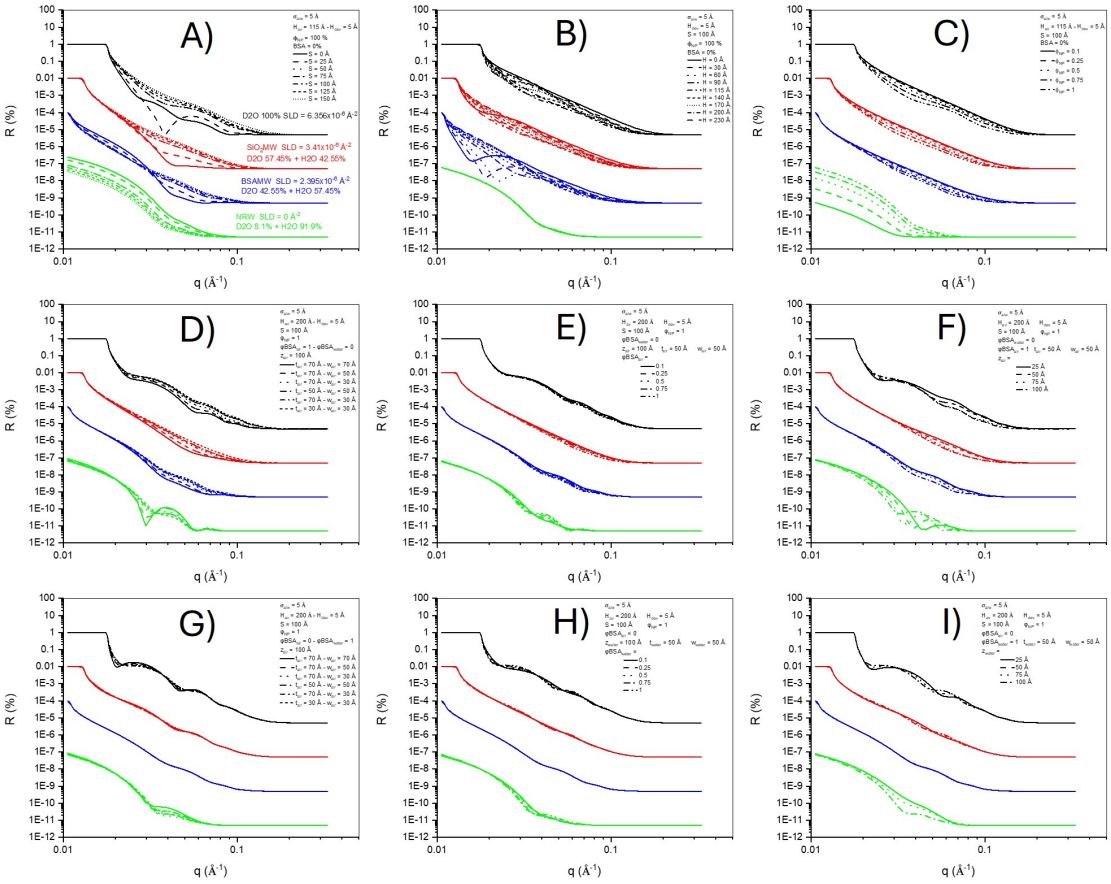

Figure H.2: *Simulated neutron reflectivity curves obtained by systematically varying key structural parameters of the model, such as A) packing density (s), B) nanoparticle immersion depth (h), C) nanoparticle packing fraction (ϕ_{NP}), and protein shell thickness (t_i) and width (w_i) in D) air and G) water, protein dry fraction ($\phi_{BSA,i}$) in E) air and H) water, and protein shell position with respect to the sphere center (z_i) in F) air and I) water. The pronounced and contrast-dependent changes observed in the reflectivity profiles upon small parameter variations demonstrate the high sensitivity of the physically motivated model to the underlying interfacial structure. This highlights the robustness and reliability of the approach for fitting experimental data, since physically meaningful differences in the organization of the monolayer translate into clear and measurable features in the reflectivity signal.*

Listing H.1: *MATLAB script used within the custom XY model of RasCAL to compute the SLD profile of the mixed protein - nanoparticle monolayers at the air-water interface.*

```
function output = SLD_NP_and_BSA_RasCAL_optimized(params, bulk_in, bulk_out, contrast)
% SLD_NP_and_BSA_RasCAL_optimized
% ------------------------------------------------------------------
% Purpose
%   Compute the 1D scattering length density (SLD) profile SLD(z)
%   for a hexagonally packed nanoparticle (NP) monolayer at a buried air-water
↪  interface,
%   including a geometrically limited BSA shell on both sides of the interface.
%
%   bulk_in   aAir SLD = 0 Å^-2
%   bulk_out  bulk SLD of the water phase for each contrast:
%   D2O = 6.356x10^-6 Å^-2
%   SiO2MW = 3.41x10^-6 Å^-2
%   BSAMW = 2.39x10^-6 Å^-2
%   NRW = 0 Å^-2
%
% ------------------------------------------------------------------

    % ------------------------------
    % Fitting scalar parameters
    % ------------------------------
    Substrate_Roughness = params(1); [Å]   %(Gaussian roughness of the interface)

    r_av   = params(2); [Å]   %(mean NP radius obtainaed with SANS - not fitted)
    r_dev  = params(3); [Å]   %(std dev of NP radius obtained with SANS - not fitted)
    h_av   = params(4); [Å]   %(mean immersion depth into water; h>0 into water -
    ↪  fitted)
    h_dev  = params(5); [Å]   %(std dev of immersion depth - fitted with constrain)
    s      = params(6); [Å]   %(lateral surface-to-surface separation distance between
    ↪  NPs obtained with GISAXS - not fitted)
    phi_np = params(7);  -    %(interfacial NP area fraction to account for imperfect
    ↪  hexagonal packing)

    t_air       = params(8);  [Å]  (max BSA shell thickness on air side - fitted with
    ↪  constrains)
    shell_phi_a = params(9);  -    (BSA volume fraction in air-side shell)
    z_air       = params(10); [Å]  (air-side shell vertical offset from NP center plane)
    w_air       = params(11); [Å]  (air-side shell slab full width)

    t_water     = params(12);  [Å]  (max BSA shell thickness on water side - fitted
    ↪  with constrains)
    shell_phi_w = params(13);   -   (BSA volume fraction in water-side shell)
    z_w         = params(14);  [Å]  (water-side shell vertical offset from NP center
    ↪  plane)
    w_w         = params(15);  [Å]  (water-side shell slab full width)

    np_sld         = params(16); [Å^-2] 3.41x10^-6 (not fitted)
    BSA_SLD_D2O    = params(17); [Å^-2] 3.06x10^-6 (not fitted)
```

```
    BSA_SLD_SiMW   = params(18); [Å^-2] 2.55x10^-6 (not fitted)
    BSA_SLD_PMW    = params(19); [Å^-2] 2.37x10^-6 (not fitted)
    BSA_SLD_NRW    = params(20); [Å^-2] 1.95x10^-6 (not fitted)

    % ------------------------------
    % Depth vectors (nm)
    % z is the computation grid; Z_end defines the exported z-axis
    % ------------------------------
    z     = (-400:7:300).';   % computation grid (column vector)
    n_z   = numel(z);
    Z_end = (-300:7:400);     % exported z-axis, paired with a flipped SLD

    % ------------------------------
    % Integration grids over NP size (r) and immersion (h)
    % Handle zero-width Gaussians gracefully.
    % ------------------------------
    Ngrid = 35;  % resolution of (r,h) quadrature

    if r_dev > 0
        r_vals = linspace(max(0, r_av - 5*r_dev), r_av + 5*r_dev, Ngrid);
        sig_r  = r_dev;
    else
        r_vals = r_av;
        sig_r  = 1; % dummy to avoid division by zero in Gaussian
    end

    if h_dev > 0
        h_vals = linspace(h_av - 5*h_dev, h_av + 5*h_dev, Ngrid);
        sig_h  = h_dev;
    else
        h_vals = h_av;
        sig_h  = 1; % dummy
    end

    [R, H] = meshgrid(r_vals, h_vals);
    if numel(r_vals) > 1
        dr = diff(r_vals(1:2));
    else
        dr = 1;  % arbitrary (will cancel with normalized weights)
    end
    if numel(h_vals) > 1
        dh = diff(h_vals(1:2));
    else
        dh = 1;
    end
    dA = dr * dh;

    % Gaussian PDF without toolbox (normalized)
    gauss = @(x,mu,sig) exp(-0.5*((x-mu)./sig).^2) ./ (sig*sqrt(2*pi));

    % Weight matrix (2D Gaussian over r and h); if dev=0, W becomes a delta.
```

```
    if r_dev>0 && h_dev>0
        W = gauss(R, r_av, sig_r) .* gauss(H, h_av, sig_h);
    elseif r_dev==0 && h_dev>0
        W = gauss(H, h_av, sig_h);
    elseif r_dev>0 && h_dev==0
        W = gauss(R, r_av, sig_r);
    else
        W = 1; % point mass at (r_av,h_av)
    end

    % -------------------------------
    % Expand to 4D tensors over z
    % -------------------------------
    Z3 = reshape(z, [1,1,1,n_z]);
    R3 = repmat(R, 1,1,1, n_z);
    H3 = repmat(H, 1,1,1, n_z);
    W3 = repmat(W, 1,1,1, n_z);

    % -------------------------------
    % Rough air-water background (error function)
    % AW(z) goes from bulk_out (z<<0) to bulk_in (z>>0).
    % -------------------------------
    AW = ((bulk_in(contrast) - bulk_out(contrast))/2) .* ...
         (1 + erf( Z3 ./ (sqrt(2)*Substrate_Roughness) )) + bulk_out(contrast);
    AW_z = squeeze(AW);  % (n_z x 1)

    % -------------------------------
    % Nanoparticle term (exact spherical cross-section between z=H..H+2R)
    % shape_np is the area of the circle at each z-slice; mask bounds the cap.
    % pref_np contains packing and contrast (np_sld - background).
    % -------------------------------
    mask_np  = (Z3 >= H3) & (Z3 <= H3 + 2*R3);
    shape_np = pi .* (-Z3.^2 + 2*(H3+R3).*Z3 - H3.*(H3 + 2*R3)); % =  [r^2 - (z -
    ↪  (H+R))^2]
    packing_np = 2 ./ (sqrt(3) * (2*R3 + s).^2); % hexagonal packing area factor
    pref_np  = phi_np .* packing_np .* (np_sld - AW);
    np_int   = pref_np .* shape_np .* W3 .* mask_np;
    np_contrib = squeeze(sum(sum(np_int,1),2) * dA); % (n_z x 1)

    % Partial SLD (background + NP)
    SLD_partial = AW_z + np_contrib;

    % -------------------------------
    % Geometric helpers for shell thickness limitation
    % -------------------------------
    % Radius of the NP cross-section at each z: sqrt(R^2 - (z - (H+R))^2)
    radius_proj = sqrt( max(0, R3.^2 - (Z3 - (H3+R3)).^2) );
    % Center-to-center pitch in hexagonal packing: 2*R + s
    I_d = 2 .* R3 + s;
    % Effective half-gap available for shell growth (per side)
    t_eff = (I_d - 2 .* radius_proj) ./ 2; % >=0 by construction
```

```
    % Inner (bare) NP cross-section area at each z
    rho_in = max(0, R3.^2 - (Z3 - (H3+R3)).^2);

    % ------------------------------
    % AIR-SIDE BSA shell (limited by t_air and by local t_eff)
    % ------------------------------
    if (s >= 0) && (s < 2*t_air)
        shell_thickness_air = max(0, min(t_eff, t_air));
    else
        shell_thickness_air = t_air;
    end
    shell_max_a   = (H3+R3) + z_air + (w_air/2);
    shell_min_a   = (H3+R3) + z_air - (w_air/2);
    shell_mask_air = (Z3 >= shell_min_a) & (Z3 <= shell_max_a);
    rho_out_air   = max(0, (R3 + shell_thickness_air).^2 - (Z3 - (H3+R3)).^2);
    shell_area_air = pi .* (rho_out_air - rho_in) .* shell_mask_air;
    packing_air    = phi_np .* (2 ./ (sqrt(3) * (2*R3 + s + shell_thickness_air).^2))
    ↪  .* shell_area_air .* W3;

    % ------------------------------
    % WATER-SIDE BSA shell (limited by t_water and by local t_eff)
    % ------------------------------
    if (s >= 0) && (s < 2*t_water)
        shell_thickness_w = max(0, min(t_eff, t_water));
    else
        shell_thickness_w = t_water;
    end
    shell_max_w   = (H3+R3) - z_w + (w_w/2);
    shell_min_w   = (H3+R3) - z_w - (w_w/2);
    shell_mask_w  = (Z3 >= shell_min_w) & (Z3 <= shell_max_w);
    rho_out_w     = max(0, (R3 + shell_thickness_w).^2 - (Z3 - (H3+R3)).^2);
    shell_area_w  = pi .* (rho_out_w - rho_in) .* shell_mask_w;
    packing_w     = phi_np .* (2 ./ (sqrt(3) * (2*R3 + s + shell_thickness_w).^2)) .*
    ↪  shell_area_w .* W3;

    % ------------------------------
    % Assemble contrast-specific total SLDs
    % For each contrast X, compute BSA SLD_X, subtract AW to get the incremental
    % shell SLD, integrate with packing_* weights, then add to SLD_partial.
    % ------------------------------
    % D2O
    BSA_sld_d2o_a    = shell_phi_a .* BSA_SLD_D2O + (1 - shell_phi_a) .* AW;
    sld_d2o_a        = (BSA_sld_d2o_a - AW);
    bsa_contrib_d2o_a = squeeze(sum(sum(packing_air .* sld_d2o_a,1),2) * dA);

    BSA_sld_d2o_w    = shell_phi_w .* BSA_SLD_D2O + (1 - shell_phi_w) .* AW;
    sld_d2o_w        = (BSA_sld_d2o_w - AW);
    bsa_contrib_d2o_w = squeeze(sum(sum(packing_w .* sld_d2o_w,1),2) * dA);

    SLD_tot_D2O = SLD_partial + bsa_contrib_d2o_a + bsa_contrib_d2o_w;

```

```
    % SiMW
    BSA_sld_simw_a    = shell_phi_a .* BSA_SLD_SiMW + (1 - shell_phi_a) .* AW;
    sld_simw_a        = (BSA_sld_simw_a - AW);
    bsa_contrib_simw_a = squeeze(sum(sum(packing_air .* sld_simw_a,1),2) * dA);

    BSA_sld_simw_w    = shell_phi_w .* BSA_SLD_SiMW + (1 - shell_phi_w) .* AW;
    sld_simw_w        = (BSA_sld_simw_w - AW);
    bsa_contrib_simw_w = squeeze(sum(sum(packing_w .* sld_simw_w,1),2) * dA);

    SLD_tot_SiMW = SLD_partial + bsa_contrib_simw_a + bsa_contrib_simw_w;

    % PMW
    BSA_sld_pmw_a    = shell_phi_a .* BSA_SLD_PMW + (1 - shell_phi_a) .* AW;
    sld_pmw_a        = (BSA_sld_pmw_a - AW);
    bsa_contrib_pmw_a = squeeze(sum(sum(packing_air .* sld_pmw_a,1),2) * dA);

    BSA_sld_pmw_w    = shell_phi_w .* BSA_SLD_PMW + (1 - shell_phi_w) .* AW;
    sld_pmw_w        = (BSA_sld_pmw_w - AW);
    bsa_contrib_pmw_w = squeeze(sum(sum(packing_w .* sld_pmw_w,1),2) * dA);

    SLD_tot_PMW = SLD_partial + bsa_contrib_pmw_a + bsa_contrib_pmw_w;

    % NRW
    BSA_sld_nrw_a    = shell_phi_a .* BSA_SLD_NRW + (1 - shell_phi_a) .* AW;
    sld_nrw_a        = (BSA_sld_nrw_a - AW);
    bsa_contrib_nrw_a = squeeze(sum(sum(packing_air .* sld_nrw_a,1),2) * dA);

    BSA_sld_nrw_w    = shell_phi_w .* BSA_SLD_NRW + (1 - shell_phi_w) .* AW;
    sld_nrw_w        = (BSA_sld_nrw_w - AW);
    bsa_contrib_nrw_w = squeeze(sum(sum(packing_w .* sld_nrw_w,1),2) * dA);

    SLD_tot_NRW = SLD_partial + bsa_contrib_nrw_a + bsa_contrib_nrw_w;

    % ------------------------------
    % Output: pair the flipped SLD(z) with Z_end to match RasCAL expectations
    % ------------------------------
    BSA_D2O  = [Z_end(:) , flipud(SLD_tot_D2O(:))];
    BSA_SiMW = [Z_end(:) , flipud(SLD_tot_SiMW(:))];
    BSA_PMW  = [Z_end(:) , flipud(SLD_tot_PMW(:))];
    BSA_NRW  = [Z_end(:) , flipud(SLD_tot_NRW(:))];

    switch contrast
        case 1, output = BSA_D2O;
        case 2, output = BSA_SiMW;
        case 3, output = BSA_PMW;
        case 4, output = BSA_NRW;
    end
end
```

Listing H.2: *MATLAB script used to estimate the number of BSA molecules per nanoparticle from the fitted structural parameters.*

```
%Parameters in [nm]

r_av   = ...   ;   r_dev  = ...
h_av   = ...   ;   h_dev  = ...
s      = ...   ;   s_err  = ...

t_air       = ...   ;   t_air_err       = ...
shell_phi_a = ...   ;   shell_phi_a_err = ...
z_air       = ...   ;   z_air_err       = ...
w_air       = ...   ;   w_air_err       = ...


t_water     = ...   ;   t_water_err     = ...
shell_phi_w = ...   ;   shell_phi_w_err = ...
z_w         = ...   ;   z_w_err         = ...
w_w         = ...   ;   w_w_err         = ...


% Depth vector (column)
z = (-40:0.1:30)';
n_z = numel(z);
dz = diff(z(1:2));

% r and h integration grids
r_vals = linspace(max(0, r_av-5*r_dev), r_av+5*r_dev, 35);
h_vals = linspace(h_av-5*h_dev, h_av+5*h_dev, 35);
[R, H] = meshgrid(r_vals, h_vals);
dr = diff(r_vals(1:2));
dh = diff(h_vals(1:2));
dA = dr * dh;

% Weight matrix (2D Gaussian PDF)
% normpdf(x,mu,sigma) returns the Gaussian PDF at x for mean mu and std sigma
W = normpdf(R, r_av, r_dev) .* normpdf(H, h_av, h_dev);
W3 = repmat(W, 1, 1, 1, n_z);
W_norm = W3 / sum(W3(:));


% Expand to 4D
Z3 = reshape(z, [1,1,1,n_z]);
R3 = repmat(R, 1,1,1, n_z);
H3 = repmat(H, 1,1,1, n_z);

%Parametri ellissoide BSA
a = 1.423;   sigma_a = 0.025;  % nm
b = 3.397;   sigma_b = 0.106;
c = 7.440;   sigma_c = 0.212;
```

```
49
50  V_BSA_mean = (4/3)*pi*a*b*c;
51  sigma_V_BSA = V_BSA_mean * sqrt((sigma_a/a)^2 + (sigma_b/b)^2 + (sigma_c/c)^2);
52
53
54  %BSA shell volume
55
56  % Shell geometry
57  radius_proj = sqrt(max(0,(R3).^2 - (Z3 - (H3+R3)).^2));
58  I_d = 2 .* R3 + s;
59  t_eff = (I_d - 2 .* radius_proj) ./ 2;
60  rho_in  = max(0, R3.^2 - (Z3 - (H3+R3)).^2);
61
62  % BSA layer in air
63
64  if (s >= 0 ) && (s < 2 * t_air)
65
66      shell_thickness_air = max(0, min(t_eff, t_air));
67
68  elseif s >= 2 * t_air
69
70      shell_thickness_air = t_air ;
71
72  end
73
74  shell_max_a = ((H3+R3) + z_air) + (w_air / 2);
75  shell_min_a = ((H3+R3) + z_air) - (w_air / 2);
76  shell_mask_air = (Z3 >= shell_min_a) & (Z3 <= shell_max_a);
77  rho_out_air = max(0, (R3 + shell_thickness_air).^2 - (Z3 - (H3+R3)).^2);
78  shell_area_air = pi .* (rho_out_air - rho_in) .* shell_mask_air;
79  V_shell_air = shell_phi_a*(sum(sum(sum(shell_area_air(:) .* W3(:),1),2) * dA))*dz;
    ↪  %[nm3]
80  Error_V_air = V_shell_air * sqrt((t_air_err/t_air)^2 + ...
81      (shell_phi_a_err/shell_phi_a)^2 + (z_air_err/z_air)^2 + ...
82      (w_air_err/w_air)^2);
83  N_BSA_air = V_shell_air / V_BSA_mean;
84  N_BSA_air_err = N_BSA_air * sqrt((sigma_V_BSA/V_BSA_mean)^2 +
    ↪  (Error_V_air/V_shell_air)^2);
85
86
87  % BSA layer in water
88
89  if (s >= 0 ) && (s < 2 * t_water)
90
91      shell_thickness_w = max(0, min(t_eff, t_water));
92
93  elseif s >= 2 * t_water
94
95      shell_thickness_w = t_water ;
96
97  end
```

```
98
99  shell_max_w = ((H3+R3) - z_w) + (w_w / 2);
100 shell_min_w = ((H3+R3) - z_w) - (w_w / 2);
101 shell_mask_w = (Z3 >= shell_min_w ) & (Z3 <= shell_max_w);
102 rho_out_w = max(0, (R3 + shell_thickness_w).^2 - (Z3 - (H3+R3)).^2);
103 shell_area_w = pi .* (rho_out_w - rho_in) .* shell_mask_w;
104 V_shell_w = shell_phi_w*(sum(sum(sum(shell_area_w(:) .* W3(:),1),2) * dA))*dz; %[nm3]
105 Error_V_w = V_shell_w * sqrt((t_water_err/t_water)^2 + ...
106     (shell_phi_w_err/shell_phi_w)^2 + (z_w_err/z_w)^2 + ...
107     (w_w_err/w_w)^2);
108 N_BSA_w = V_shell_w / V_BSA_mean;
109 N_BSA_w_err = N_BSA_w * sqrt((sigma_V_BSA/V_BSA_mean)^2 + (Error_V_w/V_shell_w)^2);
110
111 N_BSA_TOT = N_BSA_air + N_BSA_w;
112 N_BSA_TOT_err = N_BSA_air_err + N_BSA_w_err;
113
114 Interparticle_distance = s + 2*r_av;
115 ID_err = s_err + r_dev;
116
117 fprintf('\n BSA singola: %.2f ± %.2f nm^3', V_BSA_mean, sigma_V_BSA);
118 fprintf('\n Interparticle distance: %.2f ± %.2f nm^3', Interparticle_distance, ID_err);
119 fprintf('\n Volume shell air: %.2f ± %.2f nm^3', V_shell_air, Error_V_air);
120 fprintf('\n BSA molecule in air: %.2f ± %.2f nm^3', N_BSA_air, N_BSA_air_err);
121 fprintf('\n Volume shell air: %.2f ± %.2f nm^3', V_shell_w, Error_V_w);
122 fprintf('\n BSA molecule in water: %.2f ± %.2f nm^3', N_BSA_w, N_BSA_w_err);
123 fprintf('\n BSA molecule TOT: %.2f ± %.2f nm^3', N_BSA_TOT, N_BSA_TOT_err);
124
```

Listing H.3: *MATLAB script used to calculate the protein surface excess both in the air and water shells.*

```
1
2  % Parameters in [nm]
3
4  r_av   = ...  ;    r_dev  = ...;
5  h_av   = ...  ;    h_dev  = ...;
6  s      = ...;
7  phi_np = ...;
8
9  t_air       = ...;    t_w         = ...;
10 shell_phi_a = ...;    shell_phi_w = ...;
11 z_air       = ...;    z_w         = ...;
12 w_air       = ...;    w_w         = ...;
13
14 % Depth vector (column)
15 z = (-40:0.1:30)';
16 n_z = numel(z);
17 dz = diff(z(1:2));
18
19 % r and h integration grids
20 r_vals = linspace(max(0, r_av-5*r_dev), r_av+5*r_dev, 35);
21 h_vals = linspace(h_av-5*h_dev, h_av+5*h_dev, 35);
22 [R, H] = meshgrid(r_vals, h_vals);
23 dr = diff(r_vals(1:2));
24 dh = diff(h_vals(1:2));
25 dA = dr * dh;
26
27 % Weight matrix (2D Gaussian PDF)
28 W = normpdf(R, r_av, r_dev) .* normpdf(H, h_av, h_dev);
29 W3 = repmat(W, 1, 1, 1, n_z);
30 W_norm = W3 / sum(W3(:));
31
32 % Expand to 4D
33 Z3 = reshape(z, [1,1,1,n_z]);
34 R3 = repmat(R, 1,1,1, n_z);
35 H3 = repmat(H, 1,1,1, n_z);
36
37 % Shell geometry
38 radius_proj = sqrt(max(0,(R3).^2 - (Z3 - (H3+R3)).^2));
39 I_d = 2 .* R3 + s;
40 t_eff = (I_d - 2 .* radius_proj) ./ 2;
41 rho_in  = max(0, R3.^2 - (Z3 - (H3+R3)).^2);
42
43 % BSA layer in air
44 if (s >= 0 ) && (s < 2 * t_air)
45     shell_thickness_air = max(0, min(t_eff, t_air));
46 elseif s >= 2 * t_air
47     shell_thickness_air = t_air ;
48 end
49
```

```
shell_max_a = ((H3+R3) + z_air) + (w_air / 2);
shell_min_a = ((H3+R3) + z_air) - (w_air / 2);
shell_mask_air = (Z3 >= shell_min_a) & (Z3 <= shell_max_a);
rho_out_air = max(0, (R3 + shell_thickness_air).^2 - (Z3 - (H3+R3)).^2);
shell_area_air = pi .* (rho_out_air - rho_in) .* shell_mask_air;
paking_air = phi_np .* (2./((sqrt(3)*(2*R3 + s + shell_thickness_air).^2))).*
↪  shell_area_air .* W3;
V_air_BSA_per_area = sum(paking_air(:) * dA * dz); % [nm^3 / nm^2 = nm]

% Mass concentration [g/cm^2]
rho_BSA = 1.35; % g/cm^3 (typical protein density)

% Convert volume per unit area to cm^3
V_air_BSA_cm3 = V_air_BSA_per_area * 1e-7; % from nm to cm

% Surface concentration (mass per area)
conc_BSA_air_gcm2 = V_air_BSA_cm3 * rho_BSA * shell_phi_a; % [g/cm^2]

fprintf('\n BSA surface excess layer in air: %.4e', conc_BSA_air_gcm2);

% BSA layer in water
if (s >= 0 ) && (s < 2 * t_w)
    shell_thickness_w = max(0, min(t_eff, t_w));
elseif s >= 2 * t_w
    shell_thickness_w = t_w ;
end

shell_max_w = ((H3+R3) + z_w) + (w_w / 2);
shell_min_w = ((H3+R3) + z_w) - (w_w / 2);
shell_mask_w = (Z3 >= shell_min_w) & (Z3 <= shell_max_w);
rho_out_w = max(0, (R3 + shell_thickness_w).^2 - (Z3 - (H3+R3)).^2);
shell_area_w = pi .* (rho_out_w - rho_in) .* shell_mask_w;
paking_w = phi_np .* (2./((sqrt(3)*(2*R3 + s + shell_thickness_w).^2))).* shell_area_w
↪  .* W3;
V_w_BSA_per_area = sum(paking_w(:) * dA * dz); % [nm^3 / nm^2 = nm]

% Mass concentration [g/cm^2]
rho_BSA = 1.35; % g/cm^3 (typical protein density)

% Convert volume per unit area to cm^3
V_w_BSA_cm3 = V_w_BSA_per_area * 1e-7; % from nm to cm

% Surface concentration (mass per area)
conc_BSA_w_gcm2 = V_w_BSA_cm3 * rho_BSA * shell_phi_w; % [g/cm^2]

fprintf('\n BSA surface excess layer in water: %.4e', conc_BSA_w_gcm2);

```

I

Vibrational Sum Frequency Generation Spectroscopy (SFG)

Vibrational Sum Frequency Generation (SFG) spectroscopy is a second-order nonlinear optical technique widely used to probe molecular structure and dynamics at interfaces. Unlike linear spectroscopies such as IR absorption or Raman scattering, which are sensitive to bulk phases, SFG is intrinsically interface-specific because the process is forbidden in centrosymmetric media but allowed where inversion symmetry is broken. This makes SFG uniquely suited to study interfacial molecular orientation, ordering, and vibrational dynamics in systems ranging from aqueous surfaces to biological membranes and catalytic interfaces (Y. Shen, 1989; Richmond, 2002; Bonn et al., 2015).

Since its development, SFG has been applied across diverse fields: from characterizing adsorbates on catalytic metal surfaces, to probing water and ionic solutions at air/liquid interfaces, to investigating the orientation of surfactants and polymers at solid/liquid and liquid/air boundaries (Somorjai et al., 2000; Rupprechter, 2001; Fellows et al., 2024). More recently, SFG has also been extended to biological systems, providing insights into lipid and protein conformations at various interfaces (J. Wang et al., 2003; Braunschweig et al., 2016).

In summary, SFG combines vibrational specificity with intrinsic interfacial sensitivity, offering molecular-level information inaccessible to conventional bulk-sensitive spectroscopic methods.

This chapter introduces the theoretical foundations of vibrational SFG spectroscopy, based on and adapted from seminal works and comprehensive reviews Lambert et al., 2005; Hung et al., 2015; Ohno et al., 2017; Y. Shen, 1994; Y. Li et al., 2019.

I.1 Nonlinear Optical Polarization

When the electric field, E, of an electromagnetic wave (light) propagates through a medium, it exerts a force on the valence electrons of the molecules within the medium.

For low intensity and non-coherent light, and within the electric dipole approximation, this force is small and isotropic, and its effect can be described by the induced electric dipole, μ, as follows:

$$\mu = \mu_0 + \alpha E \tag{I.1}$$

where μ_0 is the static dipole of the molecule and α is its polarizability. In a condensed phase, a macroscopic quantity, the bulk polarization (P), must be considered. P is defined as the sum of the molecular electric dipole per unit volume and is related to the first-order (linear) susceptibility ($\chi^{(1)}$) of the medium, giving:

$$P = \epsilon_0 \chi^{(1)} E \tag{I.2}$$

where $\chi^{(1)}$ is the macroscopic average of α and ϵ_0 is the vacuum permittivity.

As the magnitude of the electric field increases, the non-linear contribution to the polarizability must be considered. Thus, the induced polarization $\mathbf{P}$ is generally expressed as a power series of the electric field $\mathbf{E}$:

$$P = \varepsilon_0 \left[\chi^{(1)}\mathbf{E} + \chi^{(2)}\mathbf{E}^2 \ + \chi^{(3)}\mathbf{E}^3 + \cdots \right], \tag{I.3}$$

where $\chi^{(n)}$ are the nth-order nonlinear susceptibilities. As the high-order susceptibility is always much smaller than the linear susceptibility, non-linear effects become significant only when the applied electric field has a magnitude comparable with the field experienced by the electrons in a molecule. This high magnitude is normally achieved with pulsed laser sources.

To express the frequency dependence of the polarizability, we can treat the electric field of a propagating light beam as an oscillating electric field in a semi-classical description. Further, as the SFG description is usually accounted within the electric dipole approximation, we can ignore the magnetic contribution of the light wave, thus

$$E = E_1 \, cos(\omega t) \tag{I.4}$$

where ω is the frequency of the incident light. The induced polarizability (Equation I.3) then becomes:

$$P = \varepsilon_0 \left[\chi^{(1)} \left(E_1 \, cos(\omega t)\right) + \chi^{(2)} \left(E_1 \, cos(\omega t)\right)^2 \ + \chi^{(3)} \left(E_1 \, cos(\omega t)\right)^3 + \cdots \right], \tag{I.5}$$

In an SFG experiment, two laser beams are overlapped on the sample surface, thus, by using an analogous argument, we can express the incident electric field as the sum of two different oscillating electric fields of frequency ω_1 and ω_2:

$$E = E_1 \, cos(\omega_1 t) + E_2 \, cos(\omega_2 t) \tag{I.6}$$

Considering only the first and second-order polarizability, we obtain:

$$P = \varepsilon_0 \left[\chi^{(1)}(E_1\, cos(\omega_1 t) + E_2\, cos(\omega_2 t)) + \chi^{(2)}(E_1\, cos(\omega_1 t) + E_2\, cos(\omega_2 t))^2\right], \quad \text{(I.7)}$$

which can be rewritten as:

$$\begin{aligned} P = \varepsilon_0 \Bigg[& \chi^{(1)} E_1 \cos(\omega_1 t) + \chi^{(1)} E_2 \cos(\omega_2 t) \\ & + \chi^{(2)} \Big(E_1^2 + E_2^2 + E_1^2 \cos(2\omega_1 t) + E_2^2 \cos(2\omega_2 t) \\ & + \tfrac{1}{2} E_1 E_2 \cos((\omega_1 - \omega_2)t) + \tfrac{1}{2} E_1 E_2 \cos((\omega_1 + \omega_2)t) \Big) \Bigg], \end{aligned} \quad \text{(I.8)}$$

where the first-order susceptibility $\chi^{(1)}$ terms describe linear optical processes such as absorption, reflection, and refraction of the two incident laser beams from the interface, while the second-order susceptibility $\chi^{(2)}$ terms govern second-order non-linear processes, including second harmonic generation (SHG) in $E_1^2 \cos(2\omega_1 t)$ and $E_2^2 \cos(2\omega_2 t)$, difference frequency generation (DFG) in $1/2\ E_1 E_2 \cos((\omega_1 - \omega_2)t)$, and sum frequency generation (SFG) in $1/2\ E_1 E_2 \cos((\omega_1 + \omega_2)t)$.

I.2 Sum Frequency Generation from a surface

In a typical vibrational SFG experiment, two pulsed laser beams are overlapped in both time and space at an interface between two bulk phases: a visible or near-infrared (VIS) beam with frequency ω_{vis}, and a frequency tunable infrared (IR) beam with frequency ω_{IR}. Through the second-order nonlinear interaction, a coherent beam is generated (emitted) at the sum frequency:

$$\omega_{\mathrm{SFG}} = \omega_{\mathrm{vis}} + \omega_{\mathrm{IR}}. \quad \text{(I.9)}$$

The second-order polarization responsible for SFG can be written as:

$$\mathbf{P}^{(2)}(\omega_{\mathrm{SFG}}) = \varepsilon_0 \chi^{(2)} : \mathbf{E}_{\mathrm{vis}}(\omega_{\mathrm{vis}}) \mathbf{E}_{\mathrm{IR}}(\omega_{\mathrm{IR}}), \quad \text{(I.10)}$$

and the resulting intensity of the SFG signal is:

$$I_{\mathrm{SFG}} \propto \left| \mathbf{P}^{(2)}(\omega_{\mathrm{SFG}}) \right|^2. \quad \text{(I.11)}$$

Although I.10 fully describes the SFG from a surface, it does so in a manner independent of the system coordinates. Thus, it is possible to define the relationship between the surface electric field E and the incident and generated beams using the surface bound Cartesian coordinate. In this framework, $\chi^{(2)}$ is a third-rank tensor, which has 27 different components in the Cartesian space that arise from the different combinations of the applied electric field vectors of the incident and generated beams. Thus,

a single representative (1/27th of the total description of the SF) component can be expressed as:

$$P^{(2)}_{i,SF} = \epsilon_0 \, \chi^{(2)}_{ijk} \, E_{j,VIS} \, E_{k,IR} \tag{I.12}$$

where $P^{(2)}_{i,SF}$ is the polarization component in the direction i induced by the electric field components $E_{j,VIS}$ and $E_{k,IR}$ in the directions j and k, respectively. *e.g.*, the component of the polarization along the x-axis $P^{(2)}_{x,SF}$, created by the electric field components $E_{y,VIS}$ and $E_{z,IR}$, are related by the second-order susceptibility component $\chi^{(2)}_{xyz}$.

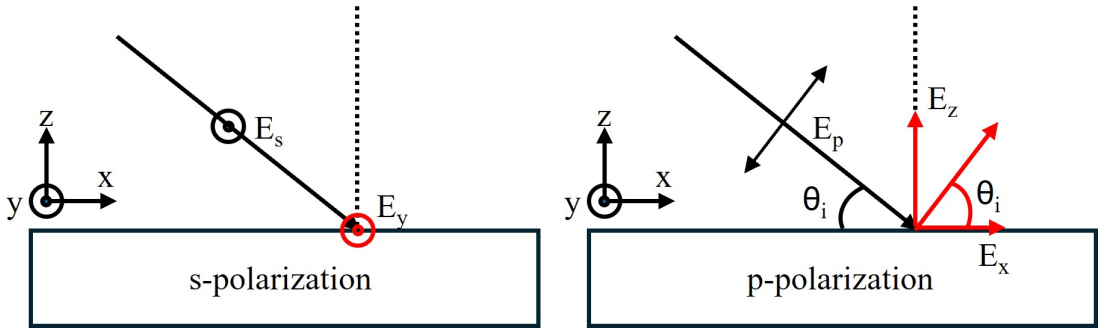

Figure I.1: *Sketch of the electric field component with respect to the surface Cartesian coordinate system for a s-polarized and a p-polarized wave.*

The different components of the second-order polarization can be probed by a selected combination of the beam polarization with respect to the surface. In fact, the orientation of the oscillation of the electric field of an electromagnetic wave can be selected in order to be parallel (s-polarized beam) and perpendicular (p-polarized beam). While the s-polarized beam has a single component with respect to the surface coordinate (y-direction in Figure I.1) the p-polarized beam can be split into two components (x and z in Figure I.1). Thus, by choosing a proper combination of the beam polarization of the SF, VIS, and IR beams, different second-order susceptibility components can be probed as reported in Table I.1.

Table I.1: *All possible polarization combinations and the elements of $\chi^{(2)}$ that contribute to the SFG spectrum.*

Polarization combination	Elements of $\chi^{(2)}_{ijk}$
pss	$\chi^{(2)}_{zyy}$
sps	$\chi^{(2)}_{yzy}$
ssp	$\chi^{(2)}_{yyz}$
ppp	$\chi^{(2)}_{zzz}$, $\chi^{(2)}_{zxx}$, $\chi^{(2)}_{xzx}$, $\chi^{(2)}_{xxz}$

Note: the beam polarizations are listed in the order SF, VIS, IR. *e.g.*, pss stands for p-SF, s-VIS, s-IR.

Noteworthy, despite the non-linear susceptibility $\chi^{(2)}$ has a maximum of 27 components, only 7 of them are reported in Table I.1. In fact, the number of unique contributing non-zero components are less due to symmetric constrains. In a centrosymmetric

medium, such as the bulk, all the directions are equivalent, and thus the value of $\chi^{(2)}$ for two opposing directions must be identical:

$$\chi^{(2)}_{ijk} = \chi^{(2)}_{-i-j-k} \tag{I.13}$$

Moreover, as $\chi^{(2)}$ is a third-rank tensor, a change in the sign of the three subscripts is equivalent to reversing the axis system; thus, the physical phenomenon described must reverse the sign:

$$\chi^{(2)}_{ijk} = -\chi^{(2)}_{-i-j-k} \tag{I.14}$$

To satisfy both Equation I.13 and Equation I.14, $\chi^{(2)}$ must be equal to 0. As a result, in a centrosymmetric medium (such as bulk solution) the SFG is forbidden. Conversely, the interface between two bulk media is inherently non-centrosymmetric and, therefore, SFG active. This is the fundamental reason why SFG spectroscopy is intrinsically interface-specific for centrosymmetric systems.

A planar surface is generally isotropic and symmetric with respect to the surface normal, thus, described by a C_∞ rotation axis corresponding with the z axis. In this framework, $z \neq -z$ but $x \equiv -x$ and $y \equiv -y$. Thus, a non-zero component of the $\chi^{(2)}$ would not change the sign upon reversing x or y axis. Only a limited number of $\chi^{(2)}$ components can satisfy this rule, and apart from $\chi^{(2)}_{zzz}$ for which reversing either x or y has no effects, only quadratic terms in either x or y contribute. *e.g.* in $\chi^{(2)}_{zyy}$ reversing the y axis must produce z-y-y, thus, $\chi^{(2)}_{z-y-y} \equiv -\chi^{(2)}_{zy-y} \equiv \chi^{(2)}_{zyy}$.

I.3 Resonant and Non-Resonant Contributions

From a molecular perspective, the macroscopic susceptibility $\chi^{(2)}$ is the orientational average of the molecular hyperpolarizabilities $\beta_{\alpha\beta\gamma}$ of interfacial molecules. While $\beta_{\alpha\beta\gamma}$ is defined in the molecular coordinate system (α, β, γ), the experiment is described in the laboratory system (x, y, z), requiring a transformation between the two via the Euler angles (ϕ, θ, ψ):

$$\chi^{(2)}_{ijk} = N \left\langle R(\phi)R(\theta)R(\psi)\,\beta_{\alpha\beta\gamma} \right\rangle \tag{I.15}$$

where N is the number density of interfacial molecules, R_{ia} the rotation matrix elements considering the three Euler angles (ϕ, θ, ψ), and $\langle \cdots \rangle$ denotes the orientational average. Noteworthy, this formalism highlights another way to appreciate the surface-specificity of SFG: in a centrosymmetric medium, such as the bulk of a liquid solution, the orientational average over all molecular orientations vanishes, leading to $\chi^{(2)} = 0$. Only at an interface, where molecular orientations are intrinsically anisotropic, can a non-zero macroscopic second-order susceptibility arise.

Close to a vibrational resonance, thus when the IR laser beam frequency (ω_{IR}) is closer to the vibrational transition, perturbation theory yields a simplified form for the

molecular hyperpolarizability:

$$\beta_{abc} = \frac{1}{2\hbar} \frac{M_{\alpha\beta} A_\gamma}{\omega_q - \omega_{IR} - i\Gamma_q} \tag{I.16}$$

with ω_q the vibrational frequency of the q-th vibration mode, ω_{IR} the frequency of the IR laser, Γ_q the damping constant correlated to the half-time of the q-th vibration mode, $M_{\alpha\beta}$ the Raman transition moment, and A_γ the IR transition moment. This expression reveals the SFG selection rule: a vibration must be simultaneously IR- and Raman-active to contribute to the resonant nonlinear susceptibility. $M_{\alpha\beta}$ and A_γ are defined as:

$$M_{\alpha\beta} = \sum_s \frac{\langle g|\mu_\alpha|s\rangle}{\hbar(\omega_{SF} - \omega_{sg})} - \frac{\langle g|\mu_\beta|v\rangle}{\hbar(\omega_{VIS} + \omega_{sg})} \tag{I.17}$$

$$A_\gamma = \langle v|\mu_\gamma|g\rangle \tag{I.18}$$

where μ_i is the electric dipole operator, $|g\rangle$ is the ground state, $|v\rangle$ is the excited vibrational state, and $|s\rangle$ is any virtual state.

Inserting the resonant $\beta_{\alpha\beta\gamma}$ dependence Equation I.14 into the averaged susceptibility Equation I.13 gives:

$$\chi^{(2)}_{ijk} = \frac{N \left\langle R(\phi)R(\theta)R(\psi)\beta_{\alpha\beta\gamma} \right\rangle}{\omega_q - \omega_{IR} - i\Gamma_q} \tag{I.19}$$

When $\omega_{\mathrm{IR}} \approx \omega_q$, the denominator approaches zero, leading to a resonant enhancement of $\chi^{(2)}$ and, consequently, of the measured SFG intensity. Scanning the infrared frequency thus yields a vibrational spectrum of the interfacial molecules.

While Equation I.19 illustrates the resonant enhancement mechanism for a single vibrational mode, the experimentally observed signal is more conveniently expressed in terms of an effective susceptibility, $\chi^{(2)}_{\mathrm{eff}}$, which accounts for multiple resonances as well as non-resonant backgrounds:

$$\chi^{(2)}_{\mathrm{eff}} = \chi^{(2)}_{\mathrm{NR}} + \sum_q \chi^{(2)}_{\mathrm{R}}(q) = \chi^{(2)}_{\mathrm{NR}} + \sum_q \frac{A_q}{\omega_{\mathrm{IR}} - \omega_q + i\Gamma_q}, \tag{I.20}$$

where $\chi^{(2)}_{\mathrm{NR}}$ is the non-resonant background, often associated with electronic responses of the molecule at the interface or plasmonic excitation in metal substrates, while $\chi^{(2)}_{\mathrm{R}}(q)$ is the resonant contribution to the susceptibility for a single vibration mode q with a resonance frequency ω_q. A_q is the denominator of Equation I.19, while the meaning of the terms in the denominator is the same as above.

So far, we have considered the SFG process as being governed exclusively by the second-order susceptibility $\chi^{(2)}$. However, at charged interfaces, the presence of a static electric field gives rise to an additional third-order contribution, which can significantly affect the measured signal. In this case, when the visible and infrared beams overlap

in space and time, the generated sum-frequency intensity depends not only on the resonant and non-resonant parts of $\chi^{(2)}$, but also on the third-order contribution, $\chi^{(3)}$, that becomes relevant for charged interfaces with non-zero surface potentials ψ_0. In this framework, the overall intensity of the SF signal can be described by the following equation:

$$I(\omega_{SF}) \propto \left| \chi^{(2)}_{NR} + \chi^{(2)}_{R} + \frac{\kappa}{\kappa + i\Delta k_z} \chi^{(3)} \psi_0 \right|^2 I_{IR} I_{vis}. \tag{I.21}$$

Here, $\chi^{(2)}_{NR}$ and $\chi^{(2)}_{R}$ are the non-resonant and the resonant contributions described in Equation I.20, κ is the inverse Debye length, Δk_z is the wave vector mismatch between all interacting beams, and I_{IR} and I_{VIS} are the intensities of the IR and visible laser beams, respectively.

I.4 Experimental Considerations

Two main approaches are used in vibrational SFG spectroscopy: *i*) the scanning configuration, where a narrow-band IR pulse is tuned stepwise across the vibrational region, and *ii*) the broadband configuration, where a femtosecond IR pulse excites a wide spectral window in a single shot.

The scanning method offers high spectral resolution but requires long acquisition times, making it less suitable for unstable systems. In contrast, broadband SFG provides rapid acquisition of entire vibrational regions with sufficient resolution, which is particularly advantageous for complex spectra.

Broadband IR pulses are generated with ultrafast laser systems. A mode-locked Ti:sapphire laser produces femtosecond near-IR pulses that are converted into tunable mid-IR radiation via an optical parametric amplifier (OPA) combined with difference frequency generation (DFG) (see Section D.1.4). Due to their short duration, femtosecond pulses span a broad spectral bandwidth (Fourier limit), allowing simultaneous coverage of vibrational ranges from a few tens to several hundred cm^{-1} depending on pulse duration and OPA configuration. This property makes broadband SFG particularly powerful for aqueous systems with strongly overlapping vibrational bands.

All spectra presented in this work were acquired in the broadband configuration. Data analysis was performed by fitting the effective susceptibility with a sum of Lorentzian functions; for the OH stretching region of water (around 3200–3400 cm^{-1}), Voigt profiles were used to account for both homogeneous and inhomogeneous broadening.

This page intentionally left blank.

References

Abelès, F (1950). "La détermination de l'indice et de l'épaisseur des couches minces transparentes". In: *Journal de Physique et le Radium* 11.7, pp. 310–314.

Abgarjan, Vahan et al. (2025). "Compression, expansion and relaxation of soft colloidal monolayers at the air/water interface". In: *Soft Matter*.

Abuillan, Wasim et al. (2012). "Quantitative determination of the lateral density and intermolecular correlation between proteins anchored on the membrane surfaces using grazing incidence small-angle X-ray scattering and grazing incidence X-ray fluorescence". In: *The Journal of chemical physics* 137.20.

Alberts, Bruce et al. (2002). "The shape and structure of proteins". In: *Molecular Biology of the Cell. 4th edition*. Garland Science.

Alkan, Mahir, Özkan Demirbaş, and Mehmet Doğan (2005). "Electrokinetic properties of kaolinite in mono-and multivalent electrolyte solutions". In: *Microporous and Mesoporous Materials* 83.1-3, pp. 51–59.

Ang, Joo Chuan et al. (2010). "Protein trapping of silica nanoparticles". In: *Soft Matter* 6.2, pp. 383–390.

Anyfantakis, Manos and Damien Baigl (2014). "Dynamic Photocontrol of the Coffee-Ring Effect with Optically Tunable Particle Stickiness". In: *Angewandte Chemie International Edition* 53.51, pp. 14077–14081.

Aoyama, Yurina et al. (2025). "Two-Dimensional Square Lattice of Colloidal Particles Formed by Electrostatic Adsorption in Confined Space". In: *Langmuir* 41.3, pp. 1948–1956.

Arnold, Owen et al. (2014). "Mantid—Data analysis and visualization package for neutron scattering and μ SR experiments". In: *Nuclear instruments and methods in physics research section a: accelerators, spectrometers, detectors and associated equipment* 764, pp. 156–166.

Asao, Hiroki and Masami Kawaguchi (2016). "Effects of salt concentration and spreading amounts on surface pressures of layers of latex particles grafted to polymer chains at interfaces between air and aqueous salt solutions". In: *Colloids and Surfaces A: Physicochemical and Engineering Aspects* 495, pp. 208–213.

Atkinson, Peter J, Eric Dickinson, and David S Horne (2007). "A Neutron Reflectivity Study of the Adsorption of □-Casein at the Air-Water". In: *Food Macromolecules and Colloids*, p. 77.

Aurbach, Doron et al. (2004). "Design of electrolyte solutions for Li and Li-ion batteries: a review". In: *Electrochimica acta* 50.2-3, pp. 247–254.

Aveyard, Robert et al. (2000). "Compression and structure of monolayers of charged latex particles at air/water and octane/water interfaces". In: *Langmuir* 16.4, pp. 1969–1979.

Baimanov, Didar, Rong Cai, and Chunying Chen (2019). "Understanding the chemical nature of nanoparticle–protein interactions". In: *Bioconjugate chemistry* 30.7, pp. 1923–1937.

Bakhshandeh, Amin, Derek Frydel, and Yan Levin (2022). "Theory of charge regulation of colloidal particles in electrolyte solutions". In: *Langmuir* 38.45, pp. 13963–13971.

Ballard, Nicholas, Adam D. Law, and Stefan A. F. Bon (2019). "Colloidal particles at fluid interfaces: behaviour of isolated particles". In: *Soft Matter* 15 (6), pp. 1186–1199. ISSN: 1744-683X. DOI: 10.1039/C8SM02048E.

Barth, Andreas and Christian Zscherp (2002). "What vibrations tell about proteins". In: *Quarterly reviews of biophysics* 35.4, pp. 369–430.

Begam, Nafisa et al. (2018). "Nanoparticle–polymer interfacial layer properties tune fragility and dynamic heterogeneity of athermal polymer nanocomposite films". In: *Soft Matter* 14.43, pp. 8853–8859.

Beierlein, Frank R et al. (2015). "Carboxylate ion pairing with alkali-metal ions for β-Lactoglobulin and its role on aggregation and interfacial adsorption". In: *The Journal of Physical Chemistry B* 119.17, pp. 5505–5517.

Beltramo, Peter J et al. (2017). "Arresting dissolution by interfacial rheology design". In: *Proceedings of the National Academy of Sciences* 114.39, pp. 10373–10378.

Berg, JC (2009). *Fluid interfaces and capillarity, an introduction to interfaces and colloids. World Sci. 936, 23-106*.

Bharti, Bhuvnesh et al. (2014). "Bridging interactions of proteins with silica nanoparticles: The influence of pH, ionic strength and protein concentration". In: *Soft Matter* 10.5, pp. 718–728.

Bhat, Mohd Younus, Tanveer Ali Dar, and Laishram Rajendrakumar Singh (2016). "Casein proteins: structural and functional aspects". In: *Milk proteins-From structure to biological properties and health aspects*. IntechOpen.

Bigioni, T. P. et al. (2006). "Kinetically driven self assembly of highly ordered nanoparticle monolayers". In: *Nature Materials* 5, pp. 265–270. DOI: 10.1038/nmat1611.

Binks, Bernard P, Jhonny A Rodrigues, and William J Frith (2007). "Synergistic interaction in emulsions stabilized by a mixture of silica nanoparticles and cationic surfactant". In: *Langmuir* 23.7, pp. 3626–3636.

Binks, Bernard P. and Stephen O. Lumsdon (2000). "Influence of particle wettability on the type and stability of surfactant-free emulsions". In: *Langmuir* 16.23, pp. 8622–8631. DOI: 10.1021/la000471y.

Bonn, Mischa, Yuki Nagata, and Ellen HG Backus (2015). "Molecular Structure and Dynamics of Water at the Water-Air Interface Studied with Surface-Specific Vibrational Spectroscopy". In: *Angewandte Chemie International Edition* 54.19, pp. 5560–5576.

Bos, Martin A and Ton Van Vliet (2001). "Interfacial rheological properties of adsorbed protein layers and surfactants: a review". In: *Advances in colloid and interface science* 91.3, pp. 437–471.

Bowers, James et al. (2001). "Neutron reflectivity studies at liquid- liquid interfaces: Methodology and analysis". In: *Langmuir* 17.1, pp. 140–145.

Braunschweig, Björn et al. (2010). "Sum-frequency generation of acetate adsorption on Au and Pt surfaces: Molecular structure effects". In: *The Journal of chemical physics* 133.23.

Braunschweig, Björn et al. (2016). "Specific effects of Ca 2+ ions and molecular structure of β-lactoglobulin interfacial layers that drive macroscopic foam stability". In: *Soft matter* 12.27, pp. 5995–6004.

Braunschweig, Björn et al. (2017). "Vibrational sum-frequency generation study of the CO2 electrochemical reduction at Pt/EMIM-BF4 solid/liquid interfaces". In: *Journal of Electroanalytical Chemistry* 800, pp. 144–150.

Buljan, Maja et al. (2003). "Analysis of 2D GISAXS patterns obtained on semiconductor nanocrystals". In: *Vacuum* 71.1-2, pp. 65–70.

Bykov, Alexey et al. (2022). "Impact of polymer nanoparticles on DPPC monolayer properties". In: *Colloids and Interfaces* 6.2, p. 28.

Cacace, MG, EM Landau, and JJ Ramsden (1997). "The Hofmeister series: salt and solvent effects on interfacial phenomena". In: *Quarterly reviews of biophysics* 30.3, pp. 241–277.

Calzolari, Davide CE et al. (2012). "Nanoscale structure of surfactant-induced nanoparticle monolayers at the oil–water interface". In: *Soft Matter* 8.45, pp. 11478–11483.

Carrillo-Carrion, Carolina et al. (2014). "Metal ions in the context of nanoparticles toward biological applications". In: *Current Opinion in Chemical Engineering* 4, pp. 88–96.

Casal, H. L., U. Kohler, and H. H. Mantsch (1988). "Structural and conformational changes of β-lactoglobulin B: An infrared spectroscopic study of the effect of pH and temperature". In: *Biochemistry* 27.8, pp. 2548–2554. DOI: 10.1021/bi00408a016.

Casal, Hector L, Ulrich Köhler, and Henry H Mantsch (1988). "Structural and conformational changes of β-lactoglobulin B: an infrared spectroscopic study of the effect of pH and temperature". In: *Biochimica et Biophysica Acta (BBA)-Protein Structure and Molecular Enzymology* 957.1, pp. 11–20.

Chai, Yu et al. (2020). "Direct observation of nanoparticle-surfactant assembly and jamming at the water-oil interface". In: *Science advances* 6.48, eabb8675.

Charykov, Nikolay A et al. (2021). "Solubility of Rare Earth Chlorides in Ternary Water-Salt Systems in the Presence of a Fullerenol—C60 (OH) 24 Nanoclusters at 25° C. Models of Nonelectrolyte Solubility in Electrolyte Solutions". In: *Processes* 9.2, p. 349.

Chen, M et al. (2018). "Foam and thin films of hydrophilic silica particles modified by β-casein". In: *Journal of colloid and interface science* 513, pp. 357–366.

Chen, Xin et al. (2007). "Specific ion effects on interfacial water structure near macromolecules". In: *Journal of the American Chemical Society* 129.40, pp. 12272–12279.

Chen, Xin et al. (2010). "Specific anion effects on water structure adjacent to protein monolayers". In: *Langmuir* 26.21, pp. 16447–16454.

Chevalier, Y. and M. A. Bolzinger (2013). "Emulsions stabilized with solid nanoparticles: Pickering emulsions". In: *Colloids and Surfaces A: Physicochemical and Engineering Aspects* 439, pp. 23–34. DOI: 10.1016/j.colsurfa.2013.02.054.

Cho, Daechul, Ganesan Narsimhan, and Elias I Franses (1996). "Adsorption dynamics of native and alkylated derivatives of bovine serum albumin at air–water interfaces". In: *Journal of colloid and interface science* 178.1, pp. 348–357.

Costa, Luca et al. (2016). "Real space imaging of nanoparticle assembly at liquid–liquid interfaces with nanoscale resolution". In: *Nano letters* 16.9, pp. 5463–5468.

Cousin, Fabrice and Alexis Chennevière (2018). "Neutron reflectivity for soft matter". In: *EPJ Web of Conferences*. Vol. 188. EDP Sciences, p. 04001.

Cousin, Fabrice and Giulia Fadda (2020). "An introduction to neutron reflectometry". In: *EPJ web of conferences*. Vol. 236. EDP Sciences, p. 04001.

Craig, VSJ, BW Ninham, and RM Pashley (1998). "Study of the long-range hydrophobic attraction in concentrated salt solutions and its implications for electrostatic models". In: *Langmuir* 14.12, pp. 3326–3332.

Creamer, LK, DAD Parry, and GN Malcolm (1983). "Secondary structure of bovine β-lactoglobulin B". In: *Archives of Biochemistry and Biophysics* 227.1, pp. 98–105.

Cruz Schneid, Andressa da et al. (2022). "Colloidal stability and degradability of silica nanoparticles in biological fluids: A review". In: *Journal of Sol-Gel Science and Technology* 102.1, pp. 41–62.

Cui, Zhenlu (2011). "Weakly sheared active suspensions: hydrodynamics, stability, and rheology". In: *Physical Review E—Statistical, Nonlinear, and Soft Matter Physics* 83.3, p. 031911.

Da, Chang et al. (2021). "Tuning surface chemistry and ionic strength to control nanoparticle adsorption and elastic dilational modulus at air-brine interface". In: *Langmuir* 37.19, pp. 5795–5809.

Damodaran, Srinivasan (2005). "Protein stabilization of emulsions and foams". In: *Journal of food science* 70.3, R54–R66.

Davies, Gary B. et al. (Oct. 2014). "Detachment energies of spheroidal particles from fluid-fluid interfaces". In: *The Journal of Chemical Physics* 141 (15). ISSN: 0021-9606. DOI: 10.1063/1.4898071.

Davies, JT (1952). "The application of the Gibbs equation to charged monolayers, and their desorption from the oil-water interface". In: *Transactions of the Faraday Society* 48, pp. 1052–1061.

Debye, Peter (1923). "The theory of electrolytes. I. Lowering of freezing point and related phenomena". In: *Physikalische Zeitschrift* 24, pp. 185–206.

Derjaguin, B. and L. Landau (1941). "A Theory of the Stability of Strongly Charged Lyophobic Sols and the Coalescence of Strongly Charged Particles in Electrolytic Solutions". In: *Acta Physicochimist URSS* 14, pp. 633–662.

Derjaguin, B. V., N. V. Churaev, and V. M. Muller (1987). *The Derjaguin—Landau—Verwey—Overbeek (DLVO) Theory of Stability of Lyophobic Colloids*. Springer US, pp. 293–310. DOI: 10.1007/978-1-4757-6639-4_8.

Deshmukh, Omkar S et al. (2015). "Hard and soft colloids at fluid interfaces: Adsorption, interactions, assembly & rheology". In: *Advances in colloid and interface science* 222, pp. 215–227.

Li-Destri, Giovanni et al. (2019). "In situ structure and force characterization of 2D nano-colloids at the air/water interface". In: *Soft Matter* 15 (42), pp. 8475–8482. DOI: 10.1039/C9SM01476D. URL: http://dx.doi.org/10.1039/C9SM01476D.

Deulgaonkar, Prashant S and VN Lad (2022). "Exploring the interfacial adsorption capability of bovine serum albumin". In: *Applied Surface Science Advances* 11, p. 100276.

Dickinson, Eric (1999). "Adsorbed protein layers at fluid interfaces: interactions, structure and surface rheology". In: *Colloids and surfaces B: Biointerfaces* 15.2, pp. 161–176.

Dickinson, Eric (Apr. 2010a). "Food emulsions and foams: Stabilization by particles". In: *Current Opinion in Colloid & Interface Science* 15 (1-2), pp. 40–49. ISSN: 13590294. DOI: 10.1016/j.cocis.2009.11.001.

Dickinson, Eric (2010b). "Food emulsions and foams: Stabilization by particles". In: *Current Opinion in Colloid & Interface Science* 15.1-2, pp. 40–49.

Dishon, Matan, Ohad Zohar, and Uri Sivan (2011). "Effect of cation size and charge on the interaction between silica surfaces in 1: 1, 2: 1, and 3: 1 aqueous electrolytes". In: *Langmuir* 27.21, pp. 12977–12984.

Donaldson Jr, Stephen H et al. (2015). "Developing a general interaction potential for hydrophobic and hydrophilic interactions". In: *Langmuir* 31.7, pp. 2051–2064.

Duan, Hongwei et al. (2004). "Directing self-assembly of nanoparticles at water/oil interfaces". In: *Angewandte Chemie International Edition* 43.42, pp. 5639–5642.

Dugyala, Venkateshwar Rao et al. (2016). "Role of electrostatic interactions in the adsorption kinetics of nanoparticles at fluid–fluid interfaces". In: *Physical Chemistry Chemical Physics* 18.7, pp. 5499–5508.

Eftekhari, Milad et al. (2020). "The influence of negatively charged silica nanoparticles on the surface properties of anionic surfactants: electrostatic repulsion or the effect of ionic strength?" In: *Physical Chemistry Chemical Physics* 22.4, pp. 2238–2248.

Eftekhari, Milad et al. (2024). "Oppositely charged surfactants and nanoparticles at the air-water interface: Influence of surfactant to nanoparticle ratio". In: *Journal of Colloid and Interface Science* 653, pp. 1388–1401.

Enders, Abigail A et al. (2023). "New Insights into Cation-and Temperature-Driven Protein Adsorption to the Air–Water Interface through Infrared Reflection Studies of Bovine Serum Albumin". In: *Langmuir* 39.15, pp. 5505–5513.

Engelhardt, Kathrin et al. (2013). "pH effects on the molecular structure of β-lactoglobulin modified air–water interfaces and its impact on foam rheology". In: *Langmuir* 29.37, pp. 11646–11655.

Fageria, NK et al. (2009). "Foliar fertilization of crop plants". In: *Journal of plant nutrition* 32.6, pp. 1044–1064.

Fellows, Alexander P et al. (2024). "Sum-Frequency Generation Spectroscopy of Aqueous Interfaces: The Role of Depth and Its Impact on Spectral Interpretation". In: *The Journal of Physical Chemistry C* 128.49, pp. 20733–20750.

Fermon, C, F Ott, and A Menelle (2009). "Neutron reflectometry". In: *X-Ray and Neutron Reflectivity: Principles and Applications*. Springer, pp. 183–234.

Fischer, Hannes, Igor Polikarpov, and Aldo F Craievich (2004). "Average protein density is a molecular-weight-dependent function". In: *Protein Science* 13.10, pp. 2825–2828.

Förster, S et al. (2005). "Scattering curves of ordered mesoscopic materials". In: *The Journal of Physical Chemistry B* 109.4, pp. 1347–1360.

Forth, Joe et al. (May 2019). "Building Reconfigurable Devices Using Complex Liquid–Fluid Interfaces". In: *Advanced Materials* 31 (18). ISSN: 0935-9648. DOI: 10.1002/adma.201806370.

Foster, Joseph F (1977). "Some aspects of the structure and conformational properties of serum albumin". In: *Albumin: Structure, function and uses*. Elsevier, pp. 53–84.

Frith, WJ et al. (2008). "Formation, stability, and rheology of particle stabilized emulsions: influence of multivalent cations". In: *Industrial & engineering chemistry research* 47.17, pp. 6434–6444.

Fujii, Syuji et al. (2017). "pH-sensitive adsorption behavior of polymer particles at the air–water interface". In: *Langmuir* 33.6, pp. 1451–1459.

Fukuto, Masa et al. (2016). "Nanoscale structure of the oil-water interface". In: *Physical review letters* 117.25, p. 256102.

Gahtori, Preeti, Vineet Gunwant, and Ravindra Pandey (2023). "How Does pH Affect the Adsorption of Human Serum Protein in the Presence of Hydrophobic and Hydrophilic Nanoparticles at Air–Water and Lipid–Water Interfaces?" In: *Langmuir* 39.44, pp. 15487–15498.

Galdino, Flávia Elisa et al. (2020). "Effect of particle functionalization and solution properties on the adsorption of bovine serum albumin and lysozyme onto silica nanoparticles". In: *Colloids and Surfaces B: Biointerfaces* 186, p. 110677.

Gao, Yan et al. (2015). "Effects of monovalent and multivalent ions on the stability of a polyelectrolyte complex with entrapped surfactants". In: *Journal of Applied Polymer Science* 132.25.

Garbin, Valeria (Oct. 2013). "Colloidal particles: Surfactants with a difference". In: *Physics Today* 66 (10), pp. 68–69. ISSN: 0031-9228. DOI: 10.1063/PT.3.2158.

Garbin, Valeria (2019). "Collapse mechanisms and extreme deformation of particle-laden interfaces". In: *Current Opinion in Colloid & Interface Science* 39, pp. 202–211.

Garbin, Valeria, John C Crocker, and Kathleen J Stebe (2012). "Forced desorption of nanoparticles from an oil–water interface". In: *Langmuir* 28.3, pp. 1663–1667.

García Rey, Natalia et al. (2018). "Quantifying double-layer potentials at liquid–gas interfaces from vibrational sum-frequency generation". In: *The Journal of Physical Chemistry C* 123.2, pp. 1279–1286.

Gennes, PrG de (1980). "Conformations of polymers attached to an interface". In: *Macromolecules* 13.5, pp. 1069–1075.

Gerelli, Yuri (2020). "Applications of neutron reflectometry in biology". In: *EPJ Web of Conferences*. Vol. 236. EDP Sciences, p. 04002.

Ghaffarkhah, Ahmadreza et al. (2024). "Chemistry, applications, and future prospects of structured liquids". In: *Chemical Society Reviews*.

Giefer, Patrick et al. (2023). "Characterization of β-lactoglobulin adsorption on silica membrane pore surfaces and its impact on membrane emulsification processes". In: *Journal of Colloid and Interface Science* 652, pp. 1074–1084.

Gilbert, R. G. (1995). "Emulsion Polymerization: A Mechanistic Approach". In: *Academic Press*.

Giner-Casares, Juan J. et al. (Jan. 2016). "Inorganic nanoparticles for biomedicine: where materials scientists meet medical research". In: *Materials Today* 19 (1), pp. 19–28. ISSN: 13697021. DOI: 10.1016/j.mattod.2015.07.004.

Glatter, Otto (2018). *Scattering methods and their application in colloid and interface science*. Elsevier.

Glotzer, Sharon C and Michael J Solomon (2007). "Anisotropy of building blocks and their assembly into complex structures". In: *Nature materials* 6.8, pp. 557–562.

Gochev, G, D Platikanov, and R Miller (2016). "Chronicles of foam films". In: *Advances in colloid and interface science* 233, pp. 115–125.

Gochev, Georgi G et al. (2024). "Exploring proteins at soft interfaces and in thin liquid films–From classical methods to advanced applications of reflectometry". In: *Advances in Colloid and Interface Science* 329, p. 103187.

González, Andrés et al. (2022). "Effects of Oil Phase on the Inversion of Pickering Emulsions Stabilized by Palmitic Acid Decorated Silica Nanoparticles". In: *Colloids and Interfaces* 6.2, p. 27.

Gonzalez-Posada, AH et al. (2024). "Interactions of human serum albumin with phosphate and Tris buffers: impact on paclitaxel binding and nanoparticles self-assembly". In: *Journal of Microencapsulation* 41.7, pp. 564–575.

Gragson, DE, BM McCarty, and GL Richmond (1997). "Ordering of interfacial water molecules at the charged air/water interface observed by vibrational sum frequency generation". In: *Journal of the American Chemical Society* 119.26, pp. 6144–6152.

Grahame, David C (1947). "The electrical double layer and the theory of electrocapillarity." In: *Chemical reviews* 41.3, pp. 441–501.

Guzmán, Eduardo and Armando Maestro (2022a). "Soft colloidal particles at fluid interfaces". In: *Polymers* 14.6, p. 1133.

Guzmán, Eduardo, Francisco Ortega, and Ramón G. Rubio (Nov. 2022b). "Forces Controlling the Assembly of Particles at Fluid Interfaces". In: *Langmuir* 38 (44), pp. 13313–13321. ISSN: 0743-7463. DOI: 10.1021/acs.langmuir.2c02038.

Hailing, Peter J and Pieter Walstra (1981). "Protein-stabilized foams and emulsions". In: *Critical Reviews in Food Science & Nutrition* 15.2, pp. 155–203.

Halder, Krishna et al. (2023). "Understanding conformational changes in human serum albumin and its interactions with gold nanorods: do flexible regions play a role in corona formation?" In: *Langmuir* 39.4, pp. 1651–1664.

Hamaker, Hugo C (1937). "The London—van der Waals attraction between spherical particles". In: *physica* 4.10, pp. 1058–1072.

Han, Yameng et al. (2023). "Pickering foams stabilized by protein-based particles: A review of characterization, stabilization, and application". In: *Trends in Food Science & Technology* 133, pp. 148–159.

Harland, JL and W Van Megen (1997). "Crystallization kinetics of suspensions of hard colloidal spheres". In: *Physical Review E* 55.3, p. 3054.

Harzallah, Besma et al. (1998). "A structural study of β-casein adsorbed layers at the air–water interface using X-ray and neutron reflectivity". In: *International journal of biological macromolecules* 23.1, pp. 73–84.

Hatlo, Marius M and Leo Lue (2008). "The role of image charges in the interactions between colloidal particles". In: *Soft Matter* 4.8, pp. 1582–1596.

Hemmerle, Arnaud et al. (2024). "Opportunities and new developments for the study of surfaces and interfaces in soft condensed matter at the SIRIUS beamline of Synchrotron SOLEIL". In: *Synchrotron Radiation* 31.1, pp. 162–176.

Heo, Jieun et al. (2024). "Stimuli-responsive nanoparticle self-assembly at complex fluid interfaces: a new insight into dynamic surface chemistry". In: *Nanoscale* 16.8, pp. 3951–3968.

Hinz, Katja (2015). "Interaction of Ln (III) and An (III)/IV/V/VI) with borate in dilute to concentrated NaCl, CaCl2 and MgCl2 solutions". PhD thesis. Karlsruhe, Karlsruher Institut für Technologie (KIT), Diss., 2015.

Hofmeister, Franz (1888). "Zur Lehre von der Wirkung der Salze". In: *Archiv für experimentelle Pathologie und Pharmakologie* 24.4, pp. 1432–1912. DOI: https://doi.org/10.1007/BF01918191.

Horne, David S (2006). "Casein micelle structure: Models and muddles". In: *Current opinion in colloid & interface science* 11.2-3, pp. 148–153.

Horvath, Attila et al. (2022). "Are casein micelles extracellular condensates formed by liquid-liquid phase separation?" In: *Febs Letters* 596.16, pp. 2072–2085.

Hsu, Jyh-Ping and Yung-Chih Kuo (1997). "The critical coagulation concentration of counterions: Spherical particles in asymmetric electrolyte solutions". In: *Journal of colloid and interface science* 185.2, pp. 530–537.

Hu, Shanshan et al. (2009). "GIUSAXS and AFM studies on surface reconstruction of latex thin films during thermal treatment". In: *Langmuir* 25.7, pp. 4230–4234.

Hua, Xiaoqing, Joelle Frechette, and Michael A Bevan (2018). "Nanoparticle adsorption dynamics at fluid interfaces". In: *Soft matter* 14.19, pp. 3818–3828.

Hughes, JV and HL Armstrong (1952). "The dielectric constant of dry air". In: *Journal of Applied Physics* 23.5, pp. 501–504.

Hung, Kuo-Kai, Ulrike Stege, and Dennis K Hore (2015). "IR absorption, raman scattering, and IR-Vis sum-frequency generation spectroscopy as quantitative probes of surface structure". In: *Applied Spectroscopy Reviews* 50.4, pp. 351–376.

Hunger, Johannes et al. (2022). "Nature of cations critically affects water at the negatively charged silica interface". In: *Journal of the American Chemical Society* 144.43, pp. 19726–19738.

Hunter, James R, Peter K Kilpatrick, and Ruben G Carbonell (1991). "β-Casein adsorption at the air/water interface". In: *Journal of colloid and interface science* 142.2, pp. 429–447.

Hunter, Timothy N. et al. (Mar. 2008). "The role of particles in stabilising foams and emulsions". In: *Advances in Colloid and Interface Science* 137 (2), pp. 57–81. ISSN: 00018686. DOI: 10.1016/j.cis.2007.07.007.

Huppertz, T, PF Fox, and AL Kelly (2018). "The caseins: Structure, stability, and functionality". In: *Proteins in food processing*. Elsevier, pp. 49–92.

Isa, Lucio et al. (2011). "Measuring single-nanoparticle wetting properties by freeze-fracture shadow-casting cryo-scanning electron microscopy". In: *Nature communications* 2.1, p. 438.

Israelachvili, Jacob and Richard Pashley (1982). "The hydrophobic interaction is long range, decaying exponentially with distance". In: *Nature* 300.5890, pp. 341–342.

Israelachvili, Jacob N (2011). *Intermolecular and surface forces*. Academic press.

Jafarlou, Amin et al. (2021). "Dynamics of adsorption of CTAB-Silica nanoparticle complexes: New experiments and modeling approach". In: *Colloids and Surfaces A: Physicochemical and Engineering Aspects* 629, p. 127448.

Jankowski, Maciej et al. (2023). "The complex systems and biomedical sciences group at the ESRF: Current status and new opportunities after extremely brilliant source upgrade". In: *Nuclear Instruments and Methods in Physics Research Section B: Beam Interactions with Materials and Atoms* 538, pp. 164–172.

Jeschull, Fabian et al. (2024). "Multivalent Cation Transport in Polymer Electrolytes–Reflections on an Old Problem". In: *Advanced Energy Materials* 14.4, p. 2302745.

Johnson, Edwin C et al. (2025). "Neutron reflectometry can capture the rapid collapse and swelling of a polymer brush". In: *Journal of Colloid and Interface Science*, p. 138248.

Jungwirth, Pavel and Douglas J Tobias (2006). "Specific ion effects at the air/water interface". In: *Chemical reviews* 106.4, pp. 1259–1281.

Kettlewell, Sarah L et al. (2007). "Is latex surface charge an important parameter for foam stabilization?" In: *Langmuir* 23.23, pp. 11381–11386.

Kiessig, Heinz (1931). "Interferenz von Röntgenstrahlen an dünnen Schichten". In: *Annalen der Physik* 402.7, pp. 769–788.

Kim, Gibum et al. (2002). "Investigations of Lysozyme Adsorption at the Air/Water and Quartz/Water Interfaces by Vibrational Sum Frequency Spectroscopy". In: *Langmuir* 18.7, pp. 2807–2811. DOI: 10.1021/la0113365. eprint: https://doi.org/10.1021/la0113365. URL: https://doi.org/10.1021/la0113365.

Kirby, Stephanie M, Shelley L Anna, and Lynn M Walker (2018). "Effect of surfactant tail length and ionic strength on the interfacial properties of nanoparticle–surfactant complexes". In: *Soft matter* 14.1, pp. 112–123.

Kleinschmidt, Jörg H (2013). *Lipid-protein interactions: methods and protocols*. Vol. 974. Springer.

Kobayashi, Motoyoshi (2008). "Electrophoretic mobility of latex spheres in the presence of divalent ions: experiments and modeling". In: *Colloid and polymer science* 286.8, pp. 935–940.

Kopp, Mathis, Sebastian Kollenda, and Matthias Epple (2017). "Nanoparticle–protein interactions: therapeutic approaches and supramolecular chemistry". In: *Accounts of chemical research* 50.6, pp. 1383–1390.

Kralchevsky, Peter A and Kuniaki Nagayama (2000). "Capillary interactions between particles bound to interfaces, liquid films and biomembranes". In: *Advances in colloid and interface science* 85.2-3, pp. 145–192.

Kundu, Simanta and Amitava Patra (Jan. 2017). "Nanoscale Strategies for Light Harvesting". In: *Chemical Reviews* 117 (2), pp. 712–757. ISSN: 0009-2665. DOI: 10.1021/acs.chemrev.6b00036.

Kurtz-Chalot, Andréa et al. (2017). "Impact of silica nanoparticle surface chemistry on protein corona formation and consequential interactions with biological cells". In: *Materials Science and Engineering: C* 75, pp. 16–24.

Kuwata, Kazuo et al. (1999). "Solution structure and dynamics of bovine β-lactoglobulin A". In: *Protein Science* 8.11, pp. 2541–2545.

Lambert, Alex G, Paul B Davies, and David J Neivandt (2005). "Implementing the theory of sum frequency generation vibrational spectroscopy: A tutorial review". In: *Applied Spectroscopy Reviews* 40.2, pp. 103–145.

Lamm, Gene (Oct. 2003). *The Poisson–Boltzmann Equation*. Wiley, pp. 147–365. DOI: 10.1002/0471466638.ch4.

Lee, Hyunsu et al. (2021). "Comparative analysis of salt cleaning and osmotic backwash on calcium-bridged organic fouling in nanofiltration process". In: *Desalination* 507, p. 115022.

Lee, Jin Gyun et al. (Dec. 2018). "Binding of Lignin Nanoparticles at Oil–Water Interfaces: An Ecofriendly Alternative to Oil Spill Recovery". In: *ACS Applied Materials & Interfaces* 10 (49), pp. 43282–43289. ISSN: 1944-8244. DOI: 10.1021/acsami.8b17748.

Lee, KS and VM Starov (2007). "Spreading of surfactant solutions over thin aqueous layers: Influence of solubility and micelles disintegration". In: *Journal of colloid and interface science* 314.2, pp. 631–642.

Lee, Sangyoup and Menachem Elimelech (2007). "Salt cleaning of organic-fouled reverse osmosis membranes". In: *Water research* 41.5, pp. 1134–1142.

Li, Chunchun et al. (2020). "Unexpected dual action of cetyltrimethylammonium bromide (CTAB) in the self-assembly of colloidal nanoparticles at liquid-liquid interfaces". In: *Advanced Materials Interfaces* 7.14, p. 2000391.

Li, Jianbing, Xuesong Wang, and Tao Wang (2010). "On the validity of Born approximation". In: *Progress In Electromagnetics Research* 107, pp. 219–237.

Li, Ming, Scott K Cushing, and Nianqiang Wu (2015). "Plasmon-enhanced optical sensors: a review". In: *Analyst* 140.2, pp. 386–406.

Li, Tianchen et al. (2023). "From fundamental amyloid protein self-assembly to development of bioplastics". In: *Biomacromolecules* 25.1, pp. 5–23.

Li, Yingmin, Bo Xiang, and Wei Xiong (2019). "Heterodyne transient vibrational SFG to reveal molecular responses to interfacial charge transfer". In: *The Journal of Chemical Physics* 150.11.

Li Destri, Giovanni, Antonio A Malfatti Gasperini, and Oleg Konovalov (2015). "The link between self-assembly and molecular conformation of amphiphilic block copolymers monolayers at the air/water interface: the spreading parameter". In: *Langmuir* 31.32, pp. 8856–8864.

Liao, Zhengzheng et al. (2011). "Protein assembly at the air–water interface studied by fluorescence microscopy". In: *Langmuir* 27.21, pp. 12775–12781.

Liggieri, L et al. (2011). "Wide-frequency dilational rheology investigation of mixed silica nanoparticle–CTAB interfacial layers". In: *Soft Matter* 7.17, pp. 7699–7709.

Lindner, Peter and Julian Oberdisse (2024). *Neutrons, X-rays, and light: scattering methods applied to soft condensed matter*. Elsevier.

Liu, Jiliang and Kevin G Yager (2018). "Unwarping GISAXS data". In: *IUCrJ* 5.6, pp. 737–752.

Liu, Juan et al. (2024). "Heterogeneous catalysis for the environment". In: *The Innovation Materials* 2.3, p. 100090.

Liu, Yuwei, Joshua Jasensky, and Zhan Chen (2012). "Molecular interactions of proteins and peptides at interfaces studied by sum frequency generation vibrational spectroscopy". In: *Langmuir* 28.4, pp. 2113–2121.

Liu, Zilong et al. (2020). "Understanding the stability mechanism of silica nanoparticles: The effect of cations and EOR chemicals". In: *Fuel* 280, p. 118650.

Loescher, Sebastian et al. (2025). "Tunable mechanical properties and phase transitions in nanoconfined polyzwitterionic UCST hydrogels". In: *Soft Matter* 21.20, pp. 4003–4009.

Loglio, G et al. (2001). "Drop and bubble shape analysis as a tool for dilational rheological studies of interfacial layers". In: *Studies in interface science*. Vol. 11. Elsevier, pp. 439–483.

López-León, Teresa et al. (2003). "Hofmeister effects in the stability and electrophoretic mobility of polystyrene latex particles". In: *The Journal of Physical Chemistry B* 107.24, pp. 5696–5708.

Lorenz-Fonfria, V. A. (2020). "Infrared difference spectroscopy of proteins: From bands to bonds". In: *Chemical Reviews* 120.7, pp. 3466–3576. DOI: 10.1021/acs.chemrev.9b00449.

Lu, JR, TJ Su, and J Penfold (1999a). "Adsorption of serum albumins at the air/water interface". In: *Langmuir* 15.20, pp. 6975–6983.

Lu, JR, TJ Su, and RK Thomas (1999b). "Structural conformation of bovine serum albumin layers at the air-water interface studied by neutron reflection". In: *Journal of Colloid and Interface Science* 213.2, pp. 426–437.

Lucassen, J and M_ Van Den Tempel (1972). "Dynamic measurements of dilational properties of a liquid interface". In: *Chemical Engineering Science* 27.6, pp. 1283–1291.

Lundqvist, Martin, Ingmar Sethson, and Bengt-Harald Jonsson (2004). "Protein adsorption onto silica nanoparticles: conformational changes depend on the particles' curvature and the protein stability". In: *Langmuir* 20.24, pp. 10639–10647.

Maestro, A. et al. (2014). "Contact angle of micro- and nanoparticles at fluid interfaces". In: *Langmuir* 30, pp. 6979–6987. DOI: 10.1021/la501192j.

Maestro, Armando (Feb. 2019). "Tailoring the interfacial assembly of colloidal particles by engineering the mechanical properties of the interface". In: *Current Opinion in Colloid & Interface Science* 39, pp. 232–250. ISSN: 13590294. DOI: 10.1016/j.cocis.2019.02.013.

Maestro, Armando and Philipp Gutfreund (2021). "In situ determination of the structure and composition of Langmuir monolayers at the air/water interface by neutron and X-ray reflectivity and ellipsometry". In: *Advances in Colloid and Interface Science* 293, p. 102434.

Maestro, Armando, Eva Santini, and Eduardo Guzmán (Aug. 2018). "Physico-chemical foundations of particle-laden fluid interfaces". In: *The European Physical Journal E* 41 (8), p. 97. ISSN: 1292-8941. DOI: 10.1140/epje/i2018-11708-6.

Maestro, Armando et al. (2012). "Wettability of silicananoparticle–surfactant nanocomposite interfacial layers". In: *Soft Matter* 8 (3), pp. 837–843. ISSN: 1744-683X. DOI: 10.1039/C1SM06421E.

Malmberg, Cyrus G and Arthur A Maryott (1956). "Dielectric constant of water from 0 to 100 C". In: *Journal of research of the National Bureau of Standards* 56.1, pp. 1–8.

Marinova, Krastanka G et al. (2013). "Co-adsorption of the proteins β-casein and BSA in relation to the stability of thin liquid films and foams". In: *Colloid and interface chemistry for nanotechnology*. CRC Press Boca Raton, FL, pp. 439–458.

Matheus, Girotto, P dos Santos Alexandre, and Levin Yan (2016). "Interaction of Charged Colloidal Particles at the Air–Water Interface". In: *The Journal of Physical Chemistry B* 120.26, pp. 5817–5822.

McBride, Sean P. and Bruce M. Law (Nov. 2012). "Influence of Line Tension on Spherical Colloidal Particles at Liquid-Vapor Interfaces". In: *Physical Review Letters* 109 (19), p. 196101. ISSN: 0031-9007. DOI: 10.1103/PhysRevLett.109.196101.

Meier, W et al. (1990). "Molecular dynamics studies of lanthanum chloride solutions". In: *Journal of Physical Chemistry* 94.11, pp. 4672–4682.

Mendoza, Alma J et al. (2014). "Particle laden fluid interfaces: Dynamics and interfacial rheology". In: *Advances in colloid and interface science* 206, pp. 303–319.

Metwalli, Ezzeldin et al. (2013). "Cobalt nanoparticles growth on a block copolymer thin film: A time-resolved GISAXS study". In: *Langmuir* 29.21, pp. 6331–6340.

Mileti, Olga et al. (2024). "Interfacial rheological study of β-casein/pectin mixtures at the air/water interface". In: *Gels* 10.1, p. 41.

Miller, R et al. (2000). "Dynamics of protein and mixed protein/surfactant adsorption layers at the water/fluid interface". In: *Advances in colloid and interface science* 86.1-2, pp. 39–82.

Min, Younjin et al. (2008). "The role of interparticle and external forces in nanoparticle assembly". In: *Nature materials* 7.7, pp. 527–538.

Mishra, Himanshu et al. (2012). "Brønsted basicity of the air–water interface". In: *Proceedings of the National Academy of Sciences* 109.46, pp. 18679–18683.

Moll, Carolyn J, Jan Versluis, and Huib J Bakker (2021). "Bulk response of carboxylic acid solutions observed with surface sum-frequency generation spectroscopy". In: *The Journal of Physical Chemistry B* 126.1, pp. 270–277.

Moritz, T et al. (1999). "Characterization of thin ceramic layers with a graded pore structure". In: *Materials science forum*. Vol. 308. Trans Tech Publ, pp. 884–889.

Müller-Buschbaum, P (2009). "A basic introduction to grazing incidence small-angle X-ray scattering". In: *Applications of Synchrotron Light to Scattering and Diffraction in Materials and Life Sciences*. Springer, pp. 61–89.

Müller-Buschbaum, P et al. (2007). "Large-scale and local-scale structures in polymer-blend films: a grazing-incidence ultra-small-angle X-ray scattering and sub-microbeam grazing-incidence small-angle X-ray scattering investigation". In: *Applied Crystallography* 40.s1, s341–s345.

Murayama, Koichi and Mihoko Tomida (2004). "Heat-induced secondary structure and conformation change of bovine serum albumin investigated by Fourier transform infrared spectroscopy". In: *Biochemistry* 43.36, pp. 11526–11532.

Nairi, Valentina et al. (2018). "Interactions between bovine serum albumin and mesoporous silica nanoparticles functionalized with biopolymers". In: *Chemical Engineering Journal* 340, pp. 42–50.

Nevot, 11_L and P Croce (1980). "Caractérisation des surfaces par réflexion rasante de rayons X. Application à l'étude du polissage de quelques verres silicates". In: *Revue de Physique appliquée* 15.3, pp. 761–779.

Nguyen, P. and S. J. Neethling (2011). "The effect of surfactant concentration on the recovery of oil from a water-wet porous medium using foam and surfactant flooding". In: *Journal of Petroleum Science and Engineering* 78, pp. 164–172. DOI: 10.1016/j.petrol.2011.05.004.

Noskov, BA et al. (2010). "Bovine serum albumin unfolding at the air/water interface as studied by dilational surface rheology". In: *Langmuir* 26.22, pp. 17225–17231.

Ohno, Paul E, Hong-fei Wang, and Franz M Geiger (2017). "Second-order spectral lineshapes from charged interfaces". In: *Nature communications* 8.1, p. 1032.

Park, Sangkwon and Hyun-Bo Lee (2012). "Effect of pH on monolayer properties of colloidal silica particles at the air/water interface". In: *Colloid and Polymer Science* 290.5, pp. 445–455.

Parratt, Lyman G (1954). "Surface studies of solids by total reflection of X-rays". In: *Physical review* 95.2, p. 359.

Pedersen, Jan Skov (1997). "Analysis of small-angle scattering data from colloids and polymer solutions: modeling and least-squares fitting". In: *Advances in colloid and interface science* 70, pp. 171–210.

Pérez-Fuentes, Leonor et al. (2017). "Adsorption of milk proteins (β-casein and β-lactoglobulin) and BSA onto hydrophobic surfaces". In: *Materials* 10.8, p. 893.

Pickering, Spencer Umfreville (1907). "CXCIV.—The interaction of metallic sulphates and caustic alkalis". In: *J. Chem. Soc., Trans.* 91 (0), pp. 1981–1988. ISSN: 0368-1645. DOI: 10.1039/CT9079101981.

Qazi, Mohsin J et al. (2020). "Dynamic surface tension of surfactants in the presence of high salt concentrations". In: *Langmuir* 36.27, pp. 7956–7964.

Qiao, Xiuying et al. (2022). "Adsorption, Surface Viscoelasticity, and Foaming Properties of Silk Fibroin at the Air/Water Interface". In: *Colloids and Interfaces* 6.3, p. 40.

Qing, Weihua et al. (2020). "In situ silica growth for superhydrophilic-underwater superoleophobic Silica/PVA nanofibrous membrane for gravity-driven oil-in-water emulsion separation". In: *Journal of Membrane Science* 612, p. 118476.

Quesada-Pérez, M, A Martın-Molina, and R Hidalgo-Álvarez (2004). "Simulation of electric double layers with multivalent counterions: Ion size effect". In: *The Journal of chemical physics* 121.17, pp. 8618–8626.

Ramesh, Manickam et al. (2022). "Nanotechnology-enabled biosensors: a review of fundamentals, design principles, materials, and applications". In: *Biosensors* 13.1, p. 40.

Ramsden, W. (Jan. 1904). "Separation of solids in the surface-layers of solutions and 'suspensions' (observations on surface-membranes, bubbles, emulsions, and mechanical coagulation).—Preliminary account". In: *Proceedings of the Royal Society of London* 72 (477-486), pp. 156–164. ISSN: 0370-1662. DOI: 10.1098/rspl.1903.0034.

Ravera, Francesca et al. (2006). "Effect of nanoparticles on the interfacial properties of liquid/liquid and liquid/air surface layers". In: *The Journal of Physical Chemistry B* 110.39, pp. 19543–19551.

Razavi, Sepideh et al. (2015). "Collapse of particle-laden interfaces under compression: buckling vs particle expulsion". In: *Langmuir* 31.28, pp. 7764–7775.

Renaud, Gilles, Rémi Lazzari, and Frédéric Leroy (2009). "Probing surface and interface morphology with grazing incidence small angle X-ray scattering". In: *Surface Science Reports* 64.8, pp. 255–380.

Rey, Marcel et al. (2018). "Amphiphile-induced anisotropic colloidal self-assembly". In: *Langmuir* 34.34, pp. 9990–10000.

Richert, Manuela E, Georgi G Gochev, and Björn Braunschweig (2019). "Specific ion effects of trivalent cations on the structure and charging state of β-lactoglobulin adsorption layers". In: *Langmuir* 35.35, pp. 11299–11307.

Richert, S., E. Schneck, et al. (2020). "Charge inversion of β-lactoglobulin at interfaces induced by trivalent ions studied with vibrational sum-frequency generation spectroscopy". In: *arXiv preprint*. eprint: 2007.07784.

Richmond, GL (2002). "Molecular bonding and interactions at aqueous surfaces as probed by vibrational sum frequency spectroscopy". In: *Chemical reviews* 102.8, pp. 2693–2724.

Roach, Lucien et al. (2022). "Controlling disorder in self-assembled colloidal monolayers via evaporative processes". In: *Nanoscale* 14.9, pp. 3324–3345.

Royall, C Patrick, Wilson CK Poon, and Eric R Weeks (2013). "In search of colloidal hard spheres". In: *Soft Matter* 9.1, pp. 17–27.

Ruffino, Roberta et al. (2022). "Direct Measurement of Surfactant-Mediated Picoforces among Nanoparticles in a Quasi-Two-Dimensional Environment". In: *Langmuir* 38.40, pp. 12281–12291.

Rupprechter, Günther (2001). "Surface vibrational spectroscopy from ultrahigh vacuum to atmospheric pressure: adsorption and reactions on single crystals and nanoparticle model catalysts monitored by sum frequency generation spectroscopy". In: *Physical Chemistry Chemical Physics* 3.21, pp. 4621–4632.

Safouane, M, D Langevin, and BP Binks (2007). "Effect of particle hydrophobicity on the properties of silica particle layers at the air- water interface". In: *Langmuir* 23.23, pp. 11546–11553.

Sah, Bijay K and Sarathi Kundu (2017). "Modification of hysteresis behaviors of protein monolayer and the corresponding structures with the variation of protein surface charges". In: *Colloids and Surfaces B: Biointerfaces* 159, pp. 696–704.

Saito, Itsuki, Tsukasa Miyazaki, and Katsuhiro Yamamoto (2015). "Depth-resolved structure analysis of cylindrical microdomain in block copolymer thin film by grazing-incidence small-angle X-ray scattering utilizing low-energy X-rays". In: *Macromolecules* 48.22, pp. 8190–8196.

Santini, Eva et al. (2011). "Study of the monolayer structure and wettability properties of silica nanoparticles and CTAB using the Langmuir trough technique". In: *Colloids and Surfaces A: Physicochemical and Engineering Aspects* 382.1-3, pp. 186–191.

Schaefer, DW et al. (1985). "Structure of random materials". In: *Physics of Finely Divided Matter: Proceedings of the Winter School, Les Houches, France, March 25–April 5, 1985*. Springer, pp. 31–37.

Schmidt, Matthias and Hartmut Löwen (1997). "Phase diagram of hard spheres confined between two parallel plates". In: *Physical Review E* 55.6, p. 7228.

Schultz, David G et al. (2006). "Structure, wrinkling, and reversibility of Langmuir monolayers of gold nanoparticles". In: *The Journal of Physical Chemistry B* 110.48, pp. 24522–24529.

Schvartz, Marion et al. (2023). "Role of the protein corona in the colloidal behavior of microplastics". In: *Langmuir* 39.12, pp. 4291–4303.

Scoppola, E et al. (2015). "Structure of a liquid/liquid interface during solvent extraction combining X-ray and neutron reflectivity measurements". In: *Physical Chemistry Chemical Physics* 17.23, pp. 15093–15097.

Seshadri, Kannan et al. (1997). "Synthesis of Crystalline, Nanometer-Scale,-(CH2) x- Clusters and Films on Gold Surfaces". In: *Journal of the American Chemical Society* 119.20, pp. 4698–4711.

ShamsiJazeyi, Hadi et al. (2014). "Polymer-coated nanoparticles for enhanced oil recovery". In: *Journal of applied polymer science* 131.15.

Al-Shatty, Wafaa et al. (2022). "Interaction of surface-modified alumina nanoparticles and surfactants at an oil/water interface: a neutron reflectometry, scattering, and enhanced oil recovery study". In: *ACS Applied Materials & Interfaces* 14.17, pp. 19505–19514.

Shen, YR (1989). "Surface properties probed by second-harmonic and sum-frequency generation". In: *Nature* 337.6207, pp. 519–525.

Shen, YR (1994). "Surfaces probed by nonlinear optics". In: *Surface Science* 299, pp. 551–562.

Shen, Yuen Ron and Victor Ostroverkhov (2006). "Sum-frequency vibrational spectroscopy on water interfaces: polar orientation of water molecules at interfaces". In: *Chemical reviews* 106.4, pp. 1140–1154.

Shourni, Sara et al. (2022). "Characterization of protein corona formation on nanoparticles via the analysis of dynamic interfacial properties: Bovine serum albumin-silica particle interaction". In: *Colloids and Surfaces A: Physicochemical and Engineering Aspects* 638, p. 128273.

Siegel, Henrik et al. (2025). "The effect of charge screening for cationic surfactants on the rigidity of interfacial nanoparticle assemblies". In: *Journal of Colloid and Interface Science* 678, pp. 201–208.

Silvera Batista, Carlos A, Ronald G Larson, and Nicholas A Kotov (2015). "Nonadditivity of nanoparticle interactions". In: *Science* 350.6257, p. 1242477.

Singh, Amarjeet and Oleg Konovalov (2013). "Measuring elastic properties of a protein monolayer at water surface by lateral compression". In: *Soft Matter* 9.10, pp. 2845–2851.

Socrates, George (2004). *Infrared and Raman characteristic group frequencies: tables and charts*. John Wiley & Sons.

Somorjai, Gabor A and Keith R McCrea (2000). "Sum frequency generation: Surface vibrational spectroscopy studies of catalytic reactions on metal single-crystal surfaces". In: *Advances in catalysis*. Vol. 45. Elsevier, pp. 385–438.

Son, HA et al. (2015). "The potential applications in oil recovery with silica nanoparticle and polyvinyl alcohol stabilized emulsion". In: *Journal of Petroleum Science and Engineering* 126, pp. 152–161.

Srivastava, A et al. (2017). "Effects of silica nanoparticles and polymers on foam stability with sodium dodecylbenzene sulfonate in water–liquid paraffin oil emulsions at high temperatures". In: *Journal of Molecular Liquids* 241, pp. 1069–1078.

Stamou, Dimitris, Claus Duschl, and Diethelm Johannsmann (2000). "Long-range attraction between colloidal spheres at the air-water interface: The consequence of an irregular meniscus". In: *Physical Review E* 62.4, p. 5263.

Steinhauer, Tim, Ulrich Kulozik, and Ronald Gebhardt (2014). "Structure of milk protein deposits formed by casein micelles and β-lactoglobulin during frontal microfiltration". In: *Journal of Membrane Science* 468, pp. 126–132.

Strazdaite, S et al. (2020). "Structure determination of hen egg-white lysozyme aggregates adsorbed to lipid/water and air/water interfaces". In: *Langmuir* 36.17, pp. 4766–4775.

Strazdaite, Simona, Konrad Meister, and Huib J Bakker (2017). "Reduced acid dissociation of amino-acids at the surface of water". In: *Journal of the American Chemical Society* 139.10, pp. 3716–3720.

Suttiprasit, Prasert, Viwat Krisdhasima, and Joseph McGuire (1992). "The surface activity of α-lactalbumin, β-lactoglobulin, and bovine serum albumin: I. Surface tension measurements with single-component and mixed solutions". In: *Journal of colloid and interface science* 154.2, pp. 316–326.

El-Tawargy, AS et al. (2018). "Multiple structural transitions in Langmuir monolayers of charged soft-shell nanoparticles". In: *Langmuir* 34.13, pp. 3909–3917.

Ter Minassian-Saraga, L (1956). "Recent work on spread monolayers, adsorption and desorption". In: *Journal of Colloid Science* 11.4-5, pp. 398–418.

Thijssen, Job HJ and Jan Vermant (2017). "Interfacial rheology of model particles at liquid interfaces and its relation to (bicontinuous) Pickering emulsions". In: *Journal of Physics: Condensed Matter* 30.2, p. 023002.

Thomas, Robert K (1996). "Neutron reflectometry in solid state and materials science". In: *Current Opinion in Solid State and Materials Science* 1.5, pp. 636–644.

Tian, Rui et al. (2014). "Activation energies of colloidal particle aggregation: towards a quantitative characterization of specific ion effects". In: *Physical Chemistry Chemical Physics* 16.19, pp. 8828–8836.

Tiraferri, Alberto, Plinio Maroni, and Michal Borkovec (2015). "Adsorption of polyelectrolytes to like-charged substrates induced by multivalent counterions as exemplified by poly (styrene sulfonate) and silica". In: *Physical Chemistry Chemical Physics* 17.16, pp. 10348–10352.

Tomasella, Pascal et al. (2025). "Time-resolved study of nanoparticle adsorption at liquid surfaces: structure, thermodynamics and kinetics". In: *Journal of Colloid and Interface Science*, p. 137978.

Tran, Lisa and Martin F Haase (2019). "Templating interfacial nanoparticle assemblies via in situ techniques". In: *Langmuir* 35.26, pp. 8584–8602.

Tyrode, Eric et al. (2005). "A vibrational sum frequency spectroscopy study of the liquid- gas interface of acetic acid- water mixtures: 2. Orientation analysis". In: *The Journal of Physical Chemistry B* 109.1, pp. 329–341.

Ulaganathan, V., A. Paananen, T. Åkesson, et al. (2017). "Adsorption of β-lactoglobulin at the air–water interface studied by tensiometry, ellipsometry, and vibrational sum frequency spectroscopy". In: *Colloids and Surfaces B: Biointerfaces* 153, pp. 152–160. DOI: 10.1016/j.colsurfb.2016.12.001.

Uttinger, Maximilian J et al. (2022). "Determination of specific and non-specific protein–protein interactions for beta-lactoglobulin by analytical ultracentrifugation and membrane osmometry experiments". In: *Soft Matter* 18.35, pp. 6739–6756.

Van Den Berg, Merel EH et al. (2018). "Nonlinear shear and dilatational rheology of viscoelastic interfacial layers of cellulose nanocrystals". In: *Physics of Fluids* 30.7.

Varga, Noémi et al. (2016). "Comprehensive study on the structure of the BSA from extended- to aged form in wide (2–12) pH range". In: *International journal of biological macromolecules* 88, pp. 51–58.

Vasquez-Montes, Victor et al. (2022). "Ca2+ and Mg2+ influence the thermodynamics of peptide-membrane interactions". In: *Journal of molecular biology* 434.21, p. 167826.

Vegso, Karol et al. (2011). "In situ GISAXS monitoring of Langmuir nanoparticle multilayer degradation processes induced by UV photolysis". In: *physica status solidi (a)* 208.11, pp. 2629–2634.

Verwey, Evert Johannes Willem (1947). "Theory of the stability of lyophobic colloids." In: *The Journal of Physical Chemistry* 51.3, pp. 631–636.

Vialetto, Jacopo and Manos Anyfantakis (2021). "Exploiting Additives for Directing the Adsorption and Organization of Colloid Particles at Fluid Interfaces". In: *Langmuir* 37.29, pp. 8656–8671. DOI: 10.1021/acs.langmuir.1c01029.

Vialetto, Jacopo et al. (2019). "Photoswitchable Dissipative Two-Dimensional Colloidal Crystals". In: *Angewandte Chemie International Edition* 58.27, pp. 9145–9149.

Vialetto, Jacopo et al. (2020). "From bulk crystallization of inorganic nanoparticles at the air/water interface: tunable organization and intense structural colors". In: *Nanoscale* 12.11, pp. 6279–6284.

Vogel, Nicolas et al. (July 2015). "Advances in Colloidal Assembly: The Design of Structure and Hierarchy in Two and Three Dimensions". In: *Chemical Reviews* 115 (13), pp. 6265–6311. ISSN: 0009-2665. DOI: 10.1021/cr400081d.

Vorobiev, Alexey et al. (2015). "Substantial difference in ordering of 10, 15, and 20 nm iron oxide nanoparticles on a water surface: in situ characterization by the grazing incidence X-ray scattering". In: *Langmuir* 31.42, pp. 11639–11648.

Wahlgren, Marie and Thomas Arnebrant (1990). "Adsorption of β-lactoglobulin onto silica, methylated silica, and polysulfone". In: *Journal of Colloid and Interface Science* 136.1, pp. 259–265.

Wang, Jie, Sarah M Buck, and Zhan Chen (2002). "Sum frequency generation vibrational spectroscopy studies on protein adsorption". In: *The Journal of Physical Chemistry B* 106.44, pp. 11666–11672.

Wang, Jie, Sarah M Buck, and Zhan Chen (2003). "The effect of surface coverage on conformation changes of bovine serum albumin molecules at the air–solution interface detected by sum frequency generation vibrational spectroscopy". In: *Analyst* 128.6, pp. 773–778.

Wang, Jie et al. (2005). "Molecular studies on protein conformations at polymer/liquid interfaces using sum frequency generation vibrational spectroscopy". In: *Surface Science* 587.1-2, pp. 1–11.

Wang, Tingting et al. (2023). "Bridging attraction of condensed bovine serum albumin solution in the presence of trivalent ions: A SANS study". In: *Biochimica et Biophysica Acta (BBA)-General Subjects* 1867.12, p. 130487.

Ward, AFH and L Tordai (1946). "Time-dependence of boundary tensions of solutions I. The role of diffusion in time-effects". In: *The Journal of Chemical Physics* 14.7, pp. 453–461.

Webster, JRP et al. (2011). "Reflectometry techniques on the Second Target Station at ISIS: Methods and science". In: *The European Physical Journal Plus* 126.11, p. 112.

Weeks, Eric R (2017). *Introduction to the colloidal glass transition*.

Wen, Tianlong and Sara A Majetich (2011). "Ultra-large-area self-assembled monolayers of nanoparticles". In: *ACS nano* 5.11, pp. 8868–8876.

Williams, David F and John C Berg (1992). "The aggregation of colloidal particles at the air—water interface". In: *Journal of colloid and interface science* 152.1, pp. 218–229.

Wu, Haimei et al. (2020). "Rapid 3-dimensional shape determination of globular proteins by mobility capillary electrophoresis and native mass spectrometry". In: *Chemical science* 11.18, pp. 4758–4765.

Xie, Danhua and Yulong Jiang (2022). "The mediated rheological properties of emulsions stabilized by thread-like mesoporous silica nanoparticles in combination with CTAB". In: *Soft Matter* 18.40, pp. 7782–7793.

Xue, Zheng et al. (2016). "Viscosity and stability of ultra-high internal phase CO2-in-water foams stabilized with surfactants and nanoparticles with or without polyelectrolytes". In: *Journal of colloid and interface science* 461, pp. 383–395.

Yadav, Indresh, Vinod K Aswal, and Joachim Kohlbrecher (2016). "Size-dependent interaction of silica nanoparticles with lysozyme and bovine serum albumin proteins". In: *Physical Review E* 93.5, p. 052601.

Yampolskaya, Galina and Dimo Platikanov (2006). "Proteins at fluid interfaces: adsorption layers and thin liquid films". In: *Advances in colloid and interface science* 128, pp. 159–183.

Yan, Linglong et al. (2000). "pH value and ionic strength effects on the adsorption kinetics of protein/phospholipid at the chloroform/water interface". In: *Colloids and Surfaces A: Physicochemical and Engineering Aspects* 175.1-2, pp. 61–66.

Yang, Seon-Ah et al. (2018). "Silica nanoparticle stability in biological media revisited". In: *Scientific reports* 8.1, p. 185.

Yeager, John D et al. (2012). "Probing interfaces between pharmaceutical crystals and polymers by neutron reflectometry". In: *Molecular pharmaceutics* 9.7, pp. 1953–1961.

Yi, Qinpiao, Liang Liu, and Ganhua Xie (2024). "Recent Advances of Stimuli-Responsive Liquid–Liquid Interfaces Stabilized by Nanoparticles". In: *ACS nano* 18.47, pp. 32364–32385.

Yu, Kai et al. (2018). "The rheology of polyvinylpyrrolidone-coated silica nanoparticles positioned at an air-aqueous interface". In: *Journal of colloid and interface science* 527, pp. 346–355.

Yuan, Shurui, Xiankun Lin, and Qiang He (2022). "Reconfigurable assembly of colloidal motors towards interactive soft materials and systems". In: *Journal of Colloid and Interface Science* 612, pp. 43–56.

Zanini, Michele and Lucio Isa (Aug. 2016). "Particle contact angles at fluid interfaces: pushing the boundary beyond hard uniform spherical colloids". In: *Journal of Physics: Condensed Matter* 28 (31), p. 313002. ISSN: 0953-8984. DOI: 10.1088/0953-8984/28/31/313002.

Zhang, Haozhen et al. (2022). "Thoroughly review the recent progresses in improving O/W interfacial properties of proteins through various strategies". In: *Frontiers in Nutrition* 9, p. 1043809.

Zhou, Xiao-Lin and Sow-Hsin Chen (1995). "Theoretical foundation of X-ray and neutron reflectometry". In: *Physics Reports* 257.4-5, pp. 223–348.

Zigelman, Anna and Ofer Manor (May 2020). "The Electrical Double Layer Force between Spherical Particles Which Are Partially Submerged in Water". In: *Langmuir* 36 (18), pp. 4942–4954. ISSN: 0743-7463. DOI: 10.1021/acs.langmuir.0c00384.

Finanziato dall'Unione europea NextGenerationEU | Ministero dell'Università e della Ricerca | Italiadomani PIANO NAZIONALE DI RIPRESA E RESILIENZA

UNIVERSITÀ degli STUDI di CATANIA

This work was carried out within the PhD Program in **Chemical Sciences (International)**, **38th cycle**, at the **University of Catania**, Department of Chemical Sciences. The doctoral fellowship (ID **1514**) was funded by the *Italian National Recovery and Resilience Plan (PNRR)*, Mission 4 – Component 1, Investment **I.4.1 "General Doctoral Scholarships for PNRR Research"**, CUP **E61I22000340002**.